Interactions Between Channel Topography and Hydrokinetic Turbines: Sediment Transport, Turbine Performance, and Wake Characteristics

A DISSERTATION
SUBMITTED TO THE FACULTY OF THE GRADUATE SCHOOL
OF THE UNIVERSITY OF MINNESOTA
BY

Craig Steven Hill

IN PARTIAL FULFILLMENT OF THE REQUIREMENTS
FOR THE DEGREE OF
Doctor of Philosophy

Michele Guala, Fotis Sotiropoulos

August, 2015

Acknowledgements

There are many people that deserve acknowledging for the support they have provided along the way during my time at St. Anthony Falls Laboratory (SAFL). Most importantly, I would like to thank my advisers, Dr. Michele Guala and Dr. Fotis Sotiropoulos, for their encouragement, advice, direction, and support in my decision to pursue my Ph.D. and throughout the course of my studies and research program. In addition to my co-advisers, I would like to thank the other two professors on my Ph.D. committee, Dr. Chris Paola and Dr. Jiarong Hong. I would like to thank many people on the SAFL Technical and Engineering Staff who have helped me over the years, including Jeff Marr, Ben Erickson, Mike Plante, Erik Steen, Jim Tucker, Jessica Kozarek, Dick Christopher, Matt Lueker, Chris Milliren, and Sara Mielke. Engineers Dr. Chris Ellis and Jim Mullin deserve special acknowledgment for their creativity, ingenuity, and state-of-the-art instrumentation systems they have designed, built, and made an integral part of research at SAFL. Without their tremendous work, much of the research and high-resolution data presented in this work, and at SAFL in general, would not be possible. They have provided continued support and encouragement while challenging me to learn in all areas of engineering and think outside the box when approaching research problems. Additionally, I would like to thank Dr. Leonardo Chamorro from the University of Illinois (formerly from SAFL) for his support and involving me early on in hydrokinetic energy research at SAFL, providing me the groundwork and collaborative experience that paved the way for my research program. Additionally, many thanks to the graduate students (Toni Calderer, Nick Evans, Mohammad Hajit, Mirko Musa, Gerard Salter, Jon Schwenk, Abby Tomasek, Anne Wilkinson, and Dr. Adam Witt) and many undergraduate students at SAFL who volunteered to recirculate sediment during the Outdoor StreamLab experiments (Chapter 4). My career at SAFL would likely not have started if it weren't for my undergraduate professor, Dr. Tom Hickson at the University of St. Thomas Geology Department, introducing me to SAFL in 2003. Finally, I would like to acknowledge Dr. Brian Polagye and Dr. Alberto Aliseda from the University of Washington, Dr. Martin Wosnik from the University of New Hampshire, and Dr. Vincent Neary from Sandia National Laboratories for their continued support and discussions of my research over the years and

willingness to share research experience, advice, and discussion on future research challenges, needs, and collaborations.

The research during my Ph.D. tenure was funded through several sources, including the Initiative for Renewable Energy and the Environment (IREE) at the University of Minnesota (UMN), the National Science Foundation (NSF) Career Grant Geophysical Flow Control (Dr. Michele Guala), NSF Partnership For Innovation (PFI) grant IIP-1318201 and the Department of Energy (DOE), Office of Energy Efficiency and Renewable Energy (EERE), Wind and Water Power Technologies Office (WWPTO), primarily through Sandia National Laboratories (SNL), the National Renewable Energy Laboratory (NREL), and Oak Ridge National Laboratories (ORNL). Special thanks is needed for the families of Edward Silberman for selecting me to receive the Edward Silberman Fellowship Award during my 2nd year of Ph.D. study, as well as the Frank and Julie Tsai Travel Award and the SAFL Graduate Student Travel Fund Award.

Dedication

This work is dedicated to my family, especially my parents, Steve and Betsy Hill, who have encouraged opportunities over the years that have in one way or another, led me towards this endeavor. Exposing me early to the outdoors, my father's demonstration and teaching of hard work, handiness, and curiosity with how things work, and my mother's introduction and fascination with the sciences have all fostered the growth of my education, curiosity, and fascination with the mechanics of the environment. Opportunities they have provided, from the years I spent at Camp Widjiwagan and my undergraduate studies in Geology at the University of St. Thomas, to my recent years at St. Anthony Falls Laboratory at the University of Minnesota, have enabled me to narrow my focus towards Earth surface processes and pursue a combination of mechanical systems in renewable energy and their interactions with the environment, and most importantly, provided a way to constantly challenge me and continue exploring my fascination with rivers, lakes, and environmental fluid mechanics. Thank you!

Abstract

Accelerating marine hydrokinetic (MHK) renewable energy development towards commercial viability requires investigating interactions between the engineered environment and its surrounding physical and biological environments. Complex and energetic hydrodynamic and morphodynamic environments desired for such energy conversion installations present difficulties for designing efficient yet robust sustainable devices, while permitting agency uncertainties regarding MHK device environmental interactions result in lengthy and costly processes prior to installing and demonstrating emerging technologies. A research program at St. Anthony Falls Laboratory (SAFL), University of Minnesota, utilized multi-scale physical experiments to study the interactions between axial-flow hydrokinetic turbines, turbulent open channel flow, sediment transport, turbulent turbine wakes, and complex hydro-morphodynamic processes in channels. Model axial-flow current-driven three-bladed turbines (rotor diameters, $d_T = 0.15$m and 0.5m) were installed in open channel flumes with both erodible and non-erodible substrates. Device-induced local scour was monitored over several hydraulic conditions and material sizes. Synchronous velocity, bed elevation and turbine performance measurements provide an indication into the effect channel topography has on device performance. Complimentary experiments were performed in a realistic meandering outdoor research channel with active sediment transport to investigate device interactions with bedform migration and secondary turbulent flow patterns in asymmetric channel environments. The suite of experiments undertaken during this research program at SAFL in multiple channels with stationary and mobile substrates under a variety of turbine configurations provides an in-depth investigation into how axial-flow hydrokinetic devices respond to turbulent channel flow and topographic complexity, and how they impact local and far-field sediment transport characteristics. Results provide the foundation for investigating advanced turbine control strategies for optimal power production in non-stationary environments, while also providing a robust data-set for computational model validation for further investigating the interactions between energy conversion devices and the physical environment.

Contents

Acknowledgements i

Dedication iii

Abstract iv

List of Tables viii

List of Figures x

1 Introduction, Overview, & Motivation 1

1.1 Overview . . . 1

1.2 Marine Renewable Energy: A Review . . . 3

1.3 Motivation: Turbine interactions with turbulence & the environment . . . 10

1.3.1 MHK device impacts on the environment . . . 10

1.3.2 Interactions between turbulence and axial-flow turbines . . . 14

2 Local scour near an axial-flow hydrokinetic turbine 22

2.1 Introduction . . . 22

2.2 Experimental Setup . . . 24

2.2.1 Clear Water Experiments . . . 24

2.2.2 Live Bed Experiments . . . 28

2.3 Results . . . 29

2.3.1 Clear Water Experiments . . . 29

2.3.2 Live Bed Experiments . . . 40

2.4 Summary & Conclusions . . . 43

2.5 Notation used in Chapter 2 . . . 44

3 Interactions between large-scale bedforms and axial-flow turbines 46
3.1 Introduction . . . 46
3.2 Experimental Setup . . . 49
3.3 Methods of Analysis . . . 54
3.3.1 Bedform Tracking . . . 54
3.3.2 Cross Correlation . . . 56
3.4 Results . . . 57
3.4.1 Effects of sediment transport on turbine performance . . . 57
3.4.2 Effects of turbine on sediment transport . . . 63
3.5 Discussion . . . 68
3.5.1 Effects of sediment transport on turbine performance . . . 68
3.5.2 Effects of turbines on sediment transport . . . 69
3.5.3 Scaling between model and prototype . . . 70
3.5.4 Further applications . . . 71
3.6 Summary & Conclusions . . . 72
3.7 Notations used in Chapter 3 . . . 74

4 Hydrokinetic turbine operating in meandering asymmetric channels 76
4.1 Introduction . . . 76
4.2 Experimental Facility . . . 79
4.3 Results . . . 82
4.3.1 Baseline Experiment . . . 82
4.3.2 Turbine Experiment . . . 91
4.4 Discussion . . . 99
4.4.1 Channel bathymetry and sediment transport . . . 99
4.4.2 Flow field and wake characteristics . . . 101
4.4.3 Applications within MHK industry . . . 103
4.5 Conclusion . . . 104
4.6 Notation used in Chapter 4 . . . 106

5 Morphodynamic impact of a hydrokinetic turbine 108
5.1 Introduction . . . 108
5.2 Experimental Setup . . . 110
5.3 Results & Discussion . . . 114
5.3.1 Turbine Performance . . . 114
5.3.2 Wake Recovery . . . 120
5.3.3 Near-Wake Vortices . . . 121

5.3.4 Morphodynamics: Average characteristics . . . 123
5.4 Summary & Conclusion . . . 129
5.5 Notation used in Chapter 5 . . . 130

6 U.S. Department of Energy Reference Model 1 132
6.1 Introduction . . . 132
6.2 Experimental Setup . . . 133
6.3 Data Reduction Methods . . . 140
6.4 Results & Discussion . . . 142
6.4.1 Inflow Characteristics . . . 142
6.4.2 Turbine Performance . . . 144
6.4.3 Wake Characteristics . . . 146
6.5 Summary & Conclusions . . . 152
6.6 Notation used in Chapter 6 . . . 153

7 Additional Results and Future Directives 154
7.1 Additional Results . . . 154
7.1.1 Axial-flow turbine arrays & sediment transport . . . 154
7.1.2 Verdant Power and the RITE site . . . 160
7.1.3 U.S. Department of Energy Reference Model 2 . . . 173
7.1.4 Particle Image Velocimetry (PIV) using bedform topography . . . 178
7.2 Future Directives . . . 181

8 Summary & Conclusions 185

References 191

List of Tables

1.1 Three components of turbulence intensity I_{u_i} ($= \sigma_{u_i}/U_{hub}$) of the wake flow at the turbine lateral tip, one rotor diameter downstream of the turbine, with and without the large cylinder placed at x/d_c = -3 and -8 [1]. 19

2.1 Turbine, flow, channel, and sediment parameters used during the small-scale and large-scale experiments. Note: (#) indicates slope and corresponding shear velocity used from previous experiments with equivalent depth, but $Fr = 0.12$ and $Re_b = 4.7\text{x}10^5$ ($Re_T = 2.0\text{x}10^5$). 29

2.2 Factors used for bridge scour comparison analysis. 40

3.1 Turbine, flow, channel, and sediment parameters. See Chapter 2 for additional information. 54

3.2 Summary of the hub height velocity, U_{hub}, mean voltage, $\bar{V}$, and the voltage intensity, $v'/\bar{V}$, for each of the four experiments from clear water conditions and three experiments during live bed transport conditions. The two columns at the right indicate the percentage variation of each experiment-specific variable with respect to the corresponding experiment-specific baseline value (Single turbine). . 59

3.3 Comparison of depth of scour downstream of each turbine during clear water and live bed single and multi-turbine experiments. Scour depths normalized by rotor diameter ($d_T = 0.15$m). 65

3.4 Summary of bedform geometric characteristics, $\bar{\lambda_b}$ and h_b, for each of the experiments found using two methods: Bedform Tracking and Interface Width. 67

4.1 Summary of the mean ($\bar{U}$,$\bar{V}$,$\bar{W}$), fluctuating (σ_u,σ_v,σ_w), turbulent kinetic energy (k), and the integral time ($\mathcal{T}$) and length ($\mathcal{L}$) scales from the baseline (B) and turbine (T) experiments from three locations (US = upstream ($x/d_T \approx$ -2.9); Turb. = turbine ($x/d_T \approx 0.4$), and DS = downstream ($x/d_T \approx 4.4$)) at the same elevation as the turbine hub height, h_{hub}. Statistics were calculated from 45 minute ADV records at each location. No data are available for the Turbine location during the Turbine experiment because model turbine was in the way of the ADV. 87

4.2 Summary of the horizontal (ϕ), vertical (θ), and relative change in angle ($\Delta\phi$) of the velocity magnitude vector (U_{mag}) from the 3 ADV locations. Cross-correlation coefficients for lag zero (ρ_0) are summarized from the correlation analysis between bed elevations and velocity magnitude and direction. 88

5.1 Performance measurement data during Q_1(○), Q_2(★), and Q_3(◁). Data refer to points plotted in Figure 5.5. U_∞ during Q_1 comes from hub height ADV measurement during vertical inflow profile measured during Baseline-Q_1 experiments (Figure 5.4). U_∞ during Q_2 and Q_3 is calculated from the cross-sectional area bulk velocity, $U_\infty = Q_w/(hb)$. 117

5.2 Hydraulic and bedform characteristics estimated using the interface width approach for each phase of the experiments. Reynolds number, $Re = (U_\infty h)/\nu$. [2]. 126

6.1 Geometric and experimental parameters for RM1 experiments. 137

6.2 Characteristics of the RM1 turbine blades (NACA-4415). 139

List of Figures

1.1 Comparison of 2012 (left) and 2015 (right) marine hydrokinetic project permit maps issued by the Federal Energy Regulatory Commission (FERC). 11

1.2 Generalized stressor/receptor matrix for MHK projects. Color indicates degree of significance (green = low significance; red = high significance). Symbols denote degree of uncertainty (□ = low, OO = medium, ΔΔΔ = high) [3]. 12

1.3 Complex channel topography with large-scale stationary and mobile features. (Top left) Bathymetry of non-mobile rock ledges at Roosevelt Island Tidal Energy (RITE) site, New York, NY, USA; (Top right) Mobile bedforms within Scroby Sands offshore wind farm in the North Sea, a potential future MHK device installation site with existing infrastructure; (Bottom left) Sediment dunes in the Lower Mississippi River [4]; (Bottom right) Gravel dunes in Minas Passage, Bay of Fundy, Nova Scotia at tidal power demonstration site. 14

1.4 Left: photograph of the turbine and cylinder partially submerged with the ADV array; Right: experimental set-up of turbine, cylinder, ADV array and measurement location [1]. 16

1.5 a) Spectra of the approach flow (u-velocity component) at hub height and $1d_T$ upstream of the turbine; b) Spectra of the turbine power. Large cylinder case (d_c/d_T = 0.65, x/d_c = -6). Dashed lines indicate the region where the structure of the power is affected [1]. 17

1.6 Spectra of the v-velocity at the lateral tip (ADV1 of Figure 1.4) $1d_T$ downstream of the turbine with the large cylinder installed (d_c = 0.325m, x/d_c = -3 and -8) [1]. 19

1.7 a) Spectral coherence between the turbine power and the streamwise velocity component measured at the lateral tip, $1d_T$ downstream of the turbine. Large cylinder: d_c = 0.325m, x/d_c = -3; medium cylinder: d_c = 0.115m, x/d_c = -10. b) Spectral coherence between the streamwise velocity component at both lateral tips. Flow velocities are measured at $1d_T$ downstream of the turbine [1]. 20

1.8 Mean velocity deficit at hub height with and without the medium cylinder [1]. . . 21

2.1 Schematic of large-scale experiment setup and instrumentation. Turbine rotor diameter $d_T = 0.5$m. Base support platform is a concrete cone 0.15m tall with upper and lower diameters of 0.1m and 0.43m, respectively. 25
2.2 Photo of 1:10 model and instrumentation. 25
2.3 Photograph of the 1:33 model hydrokinetic turbine used during the small-scale clear water and live bed experiments, shown here with the ADV and sonar device. Flow is left to right. 27
2.4 End topography from large-scale clear water experiments with the a) turbine support tower only, b) nacelle and support tower, and c) fully operational turbine. Flow is left to right. 31
2.5 End topography from small-scale clear water experiments with the a) turbine support tower only, b) rotor on downstream side of tower, and c) rotor on upstream side of tower. Flow is left to right. 32
2.6 Contour lines showing region of scour (enclosed boundaries nearest turbine to the left) and deposition (lines to the right side of image) for three cases: large-scale experiments (solid line), small-scale downstream rotor (dash-dot line), and small-scale upstream rotor (dashed line). Scour contour lines show extent of 5% d_T scour depth, while deposition contour lines show extent of 5% d_T deposition height. 34
2.7 Evolution of scour in time comparison between rotor position on upstream (filled circles) versus downstream (open circles) side of the support tower from the small-scale clear water experiments. Inset axes show location with respect to turbine rotor from which data were taken. 35
2.8 Laser and camera topography renderings from large-scale experiment bed topography corresponding to time $t = 30$ minutes (a), 60 minutes (b), and 90 minutes (c). Time span between successive scans is approximately 73 seconds (sub-Figures a–c show scan passes 25, 50, and 75, respectively). 36
2.9 Evolution of scour formation in time from the large-scale clear water experiment, shown for various lateral positions normalized by the turbine rotor diameter. Maximum scour depths occurred at $y/d_T = \pm 0.2$. Open symbols are from the positive (river right) side of the nacelle. Filled symbols are from the negative (river left) side of the nacelle. Similar symbol shapes indicate equivalent distances on either side of the turbine nacelle. 36
2.10 Normalized temporal evolution of the scour hole downstream of the small-scale and large-scale turbines. Data taken from $x/d_T = 0.66$ and $y/d_T = 0$ for all cases. 38

2.11 Normalized temporal evolution of the downstream distance, x_p/d_T, to the location of the peak of deposition, z_p, during the small-scale (circles: downstream rotor; squares: upstream rotor) and large-scale (diamonds) clear water experiments. . . 38
2.12 (a) Comparison between final bed topography from the live bed experiments from baseline conditions and (b) with a single turbine installed. 41
2.13 Examples of instantaneous (thin light background lines) and average bed surface (solid) and water surface (dotted) elevations from the single turbine live bed small-scale experiment. The bold dot-dashed lines indicate overall maximum and minimum bed elevation surfaces. 42
2.14 Comparison between average water surface and ending channel topography from the small-scale clear water experiments and the time-averaged water surface and bed elevation from the live bed experiments with a single turbine installed. Bed elevations have been zeroed by removing the mean bed profile slope from the data. Hub height during the clear water experiment was approximately 1 cm higher than during live bed experiments. 42
3.1 Schematic of the experimental setup. Coordinate system origin (x = 0m) is located approximately 8m downstream of channel inlet and vertical cylinder baffles. Flow is from left to right. 50
3.2 Photo of single turbine with bedforms. Inset image shows close-up of the 1:33 scale turbine used during experiments. Rotor direction is counter-clockwise. . . . 51
3.3 Sample from 200Hz instantaneous voltage signal acquired from the turbine motor. Darker dashed line and circles illustrate filtered signal to match sampling frequency of bed elevation data for analysis described later. 52
3.4 Spectral plot comparing inflow hub-height velocity, U_{hub} (dotted line), to the turbine voltage signal (solid line). The dashed vertical line indicates the turbine rotational frequency, f_T. 53
3.5 Definitions of various bedform geometric parameters calculated during bedform tracking methods employed for this analysis. 55
3.6 Demonstration of the assumption that correlation analysis between a voltage timeseries and BEP can focus on only lag $k = 0$. Solid line shows BEP as a function of time at position, x_1. When BEP at position x_2 (dotted line) is shifted by k = -3 lags, it closely resembles BEP at x_1 (dashed line). The correlation between BEP x_1 and BEP x_2 at k = -3 is $\rho = 0.92$. Inset figure shows the correlation between two cross-correlation signals: $\rho_{z(x1):\bar{V}}$ and $\rho_{z(x2):\bar{V}}$. Here, the maximum correlation is $\rho = 0.95$, confirming that at lag k = -3 is the appropriate lag shift that validates this assumption. 57

3.7 Sample of normalized voltage timeseries for each of the cases investigated during clear water (CW) and live bed (LB) experiments. Data from experiments with two turbines present are recorded from the downstream turbine. 58
3.8 Dimensionless relationships between normalized mean voltage vs. bedform peak distance (top-left), bedform peak height vs. normalized mean voltage (top-right), voltage intensity ($v'/\bar{V}$) vs. bedform peak distance (bottom-left) and bedform peak height vs. voltage intensity ($v'/\bar{V}$) (bottom-right). Points have been grouped by normalized dune height (z_p/d_T): 0-10% = white diamonds; 11-20% = dark gray circles; 21-30% = light gray squares; and 31-40% = black triangles. 60
3.9 Top image: Correlation coefficients plotted along the streamwise axis for each of the 3 cases. Vertical dashed lines show locations of turbine(s). Bottom 3 images: Close-up of correlation coefficient plots in the region near the turbine for single turbine (top image pair), two turbines with $4d_T$ spacing (middle image pair), and two turbines with $7d_T$ spacing (bottom image pair). Images on left highlight correlation coefficient values and peaks (triangle = mean voltage; circle = RMS voltage), while images on the right show mean bed elevation profile (solid bold line) with 3 bed profiles with approximately $\Delta t = 10$ minutes between each profile to show migration and passage of dune crest past turbine location. Solid scale bar indicates the median bedform length, $\bar{\lambda}_b$. 62
3.10 Final topography for the clear water experiments (left): single (top), $4d_T$ (middle), and $7d_T$ (bottom). Flow is from left to right. Color scale represents normalized scour (dark colors) and deposition (light colors), $\Delta z_b/d_T$. Final topography for the live bed experiments (right): single (top), $4d_T$ (middle), and $7d_T$ (bottom). Flow is from left to right. Color scale represents flume z-coordinate system bed elevations, z_b, in mm. Turbine hub height, $h_{hub} \approx$ -382mm. 64
3.11 Close-up view of the mean bed and water surface elevations for the four live bed experiments: Baseline (solid blue), single turbine (dashed red), two turbines with $4d_T$ spacing (dotted magenta), and two turbines with $7d_T$ spacing (dashed-dot green). Turbine hub height represented by horizontal black dashed line at $z/d_T \approx$ 0.88. 65
3.12 Interface width, w_i, plots for each of the turbine configurations investigated under live bed conditions. 66
3.13 Scatter diagram comparing wavelength, λ_b (m), and bedform height, h_b (m) among each of the four live bed scenarios. Symbols represent median values. Lines represent ± 1 standard deviation for the corresponding variable. 67

4.1 (a) Photograph of the St. Anthony Falls Laboratory (SAFL) Outdoor StreamLab (OSL). (b) OSL data acquisition (DAQ) carriage used for data collection. (c) Hydrokinetic turbine model ($d_T = 0.15$m) mounted near the apex of the middle meander bend. Arrows in photos indicate flow direction. 80
4.2 (a) OSL channel topography mapped in 2010. Location of turbine indicated by red diamond at (X,Y) $\approx$ (19.7m,19.3m). (b) Topography of middle meander bend outlined by box in (a) showing channel topography from 2010 (light gray contour lines), turbine location (A, red diamond), streamwise sonar transect location (B), spanwise sonar transect location (C), final near-turbine sonar topography zone (D), boundary of data acquisition (DAQ) carriage (E) from which sensors were mounted (see Figure 4.1), and the channel bank edges (F). Flow is left to right is both images. 80
4.3 (a) Ending topography after baseline experiment and (b) after turbine (circled) experiment. Flow is left to right is both images. 82
4.4 Instantaneous (light gray) and mean bed (solid black) and water surface (solid blue) elevation data in the cross-stream (top) and streamwise (bottom) directions collected during the baseline experiment. 84
4.5 Space vs. time contours of the cross-stream sonar bed elevation data from the baseline (a) and turbine (b) experiments. Arrows at $y/d_T = 0$ indicate cross-stream location where bed elevation timeseries data are taken from and plotted in Figure 4.6. 85
4.6 Bed elevation, z_b, timeseries comparison between baseline (dotted line) and turbine (solid line) experiments at $x/d_T \approx 1.4$ and $y/d_T = 0$. 86
4.7 (a) Schematic of the ADV coordinate system and calculated velocity magnitude and direction ϕ (horizontal angle) and θ (vertical angle). (b) Schematic of the relative change in ϕ between baseline (subscript, B) and turbine (subscript, T) experiments, summarized in Table 4.2. 88
4.8 45 minute timeseries of velocity magnitude, U_{mag} (top), horizontal ϕ (black) and vertical θ (red) angles (middle), and bed elevations z_b (bottom) from the future turbine location during the baseline experiment. Bed elevations were measured 0.13m downstream of ADV location. Raw data (dotted line) and shifted data (solid line) are presented as though the elevations were collected simultaneously directly under the ADV sampling location. Timeseries has been shifted using the mean bedform velocity, $\overline{U_b} \approx 0.0016\text{ms}^{-1}$ assuming minor bedform geometry distortion under relatively short travel times and lengths. 90

4.9 Temporal cross-correlation curves between the bed elevations and the velocity magnitude and direction timeseries presented in Figure 4.8. Data from baseline experiments at the location where the turbine was placed. 91
4.10 Velocity spectrum from the ADV measurements under baseline conditions at three locations: upstream (red), future turbine location (black), and downstream (blue). $S(f)$ is the calculated energy spectrum [m^2s^{-1}]. The energy spectrum are normalized by the mean flow depth at the location of the turbine during baseline experiments ($\overline{h} = 0.306$m) and the turbulent kinetic energy velocity scale, u_k, from the upstream baseline timeseries data. 91
4.11 Instantaneous (light gray) and mean bed (solid black) and water surface (solid blue) elevation data in the cross-stream (top) and streamwise (bottom) directions collected during the turbine experiment. Turbine rotor area is represented gray circle at $y/d_T = 0$ in the top figure and by the solid black vertical line at $x/d_T = 0$ in the bottom figure. 93
4.12 Comparison between the cross-stream mean bed and water surface elevations (top) and the root-mean squared elevations (bottom) for the baseline (dashed lines) and turbine (solid lines) experiments. Turbine rotor area is represented by the gray circle in the top figure. The X-axis is presented in both dimensional (m) and non-dimensional (y/d_T) units. The Y-axis is presented in both dimensional (m) and non-dimensional (z/d_T) units with $z/d_T = 0$ corresponding to the turbine hub height, h_{hub}. 94
4.13 Comparison between the streamwise mean bed and water surface elevations (top) and the root-mean squared elevations (bottom) for the baseline (dashed lines) and turbine (solid lines) experiments. Turbine rotor area is represented by the vertical solid black line in the top figure. The X-axis is presented in both dimensional (m) and non-dimensional (x/d_T) units. The Y-axis is presented in both dimensional (m) and non-dimensional (z/d_T) units with $z/d_T = 0$ corresponding to the turbine hub height, h_{hub}. 95
4.14 Comparison between the U, V, and W velocity spectrum from the downstream ADV measurements during the baseline (blue) and turbine (red) experiments. $S(f)$ is the calculated energy spectrum [m^2s^{-1}]. The energy spectrum are normalized by the mean flow depth at the location of the turbine during baseline experiments ($\overline{h} = 0.306$m) and the turbulent kinetic energy velocity scale, u_k, from the upstream baseline timeseries data. 97

4.15 Comparison of the collected moving average window data (red, -) and the low-pass filtered data (black, –) for (a) the mean streamwise velocity, $\overline{U}$, and (b) the streamwise velocity fluctuations, u', in the wake of the turbine ($x/d_T = 1.4$) collected during the ADV moving traverse measurements. 98
4.16 (a) Mean streamwise velocity, $\overline{U}$, (b) streamwise velocity fluctuations, u', and (c) turbulent kinetic energy, k, in the wake of the turbine ($x/d_T = 1.4$ to 5.4) collected during the ADV moving traverse measurements. The model turbine, $d_T = 0.15$m, is visible in each image at $(X, Y) \approx$ (19.7m,19.3m). Channel topography from the end of the turbine experiment is shown in gray-scale contoured background region. Moving traverse ADV transect locations illustrated by black lines spanning the velocity contour regions. 99
4.17 Comparison between the streamwise mean bed elevation from the OSL turbine experiments and the clear water and live bed experiments presented by [5]. . . . 101
4.18 Comparison of the streamwise bed elevation root-mean squared values from baseline (dashed) and turbine (solid) experiments in both a straight laboratory channel (red) and the meandering natural channel in the OSL (black). 101
4.19 Comparison of the wake velocity deficit downstream of the axial flow turbine ($d_T = 0.15$m) from a straight non-erodible channel (black) and the meandering natural channel in the OSL (red). 103
5.1 (a) Photograph of the St. Anthony Falls Laboratory (SAFL) main channel and turbine model. (b) Data acquisition (DAQ) carriage collecting spatio-temporal bedform topography data in SAFL main channel. Arrows indicate flow direction. 111
5.2 Volumetric flow rate hydrograph used during the experiments. Baseline experiments started at $t = 0$hrs. Turbine was installed at $t = 19.5$hrs. 111
5.3 Schematic of the turbine installed in SAFL main channel. (A) Torque transducer, (B) rotor angular velocity speed control motor, (C) rotary encoder, and (D) manual blade pitch angle adjustment. Rotor diameter, $d_T = 0.5$m, average hub height, $\bar{h}_{hub} = 0.425$m, and average sediment depth, $\bar{h}_{sed} = 0.43$m. 112
5.4 Vertical profiles of (a) U/U_{hub} and (b) u'/u_* from the concrete channel experiments (O) and sediment transport experiments (△). Normalization factors U_{hub} (concrete, $U_{hub} = 0.45\text{ms}^{-1}$; sediment, $U_{hub} = 0.52\text{ms}^{-1}$) and u_* are specific to each experiment (concrete, $u_* = 0.033\text{ms}^{-1}$; sediment, $u_* = 0.04\text{ms}^{-1}$). Data collected $x/d_T =$ -5 and -10 upstream of the turbine for concrete channel and sediment transport experiments, respectively. The turbine rotor plane extends from $h/d_T =$ -0.5 to 0.5, with the turbine hub height at $h/d_T = 0$. 113

5.5 Turbine performance curve, C_p vs. λ for fixed bed concrete rectangular channel experiments without ($\square$) and with cylinders (small = $\diamond$; medium = $\triangle$; large = $\triangleright$) and erodible sediment transport experiments (Q_1 = $\circ$; Q_2 = $\bigstar$; Q_3 =$\triangleleft$). Numbers by points refer to sonar traces in Figure 5.6 and data in Table 5.1. . . . 116
5.6 Sonar centerline bed elevation profiles t_1 to t_7 associated with numbered points 1 ($Q_2, \bigstar$) and 2 ($Q_3, \triangleleft$) through 7 ($Q_3, \triangleleft$) in the turbine performance curve in Figure 5.5. . . . 118
5.7 Turbine torque power spectra for the concrete channel, medium cylinder, and sediment channel experiments. The $x-$axis has been normalized by the experiment specific turbine rotational frequency ($f_T = 1.5$ for cylinder experiment; $f_T = 2.0$ for concrete channel and sediment experiments). Vertical dashed lines at $f/f_T =$ 1 and 3 correspond to the turbine (f_T) and blade passing (f_B) frequency, respectively. Data from cylinder experiment presented in [1]. . . . 119
5.8 Velocity deficit comparison aligned with the hub center for fixed and erodible channels at several tip-speed ratios. . . . 121
5.9 (a) Power spectra of the cross-stream velocity, v, at hub height $0.5d_T$ (red) and $1d_T$ (blue) downstream of the turbine aligned with the blade tip $y/d_T = 0.5$ for sediment transport experiments. (b) Pre-multiplied spectra of the cross-stream velocity, v, at hub height $0.5d_T$ downstream of the turbine. Turbine rotational frequency, $f_T = 2.0$hz ($\omega \approx 12.6$rad s^{-1}). Spectra peak at $f_H \approx 0.51$hz identifies hub vortex signature. . . . 122
5.10 Timeseries of the fluctuating cross-stream, v, and vertical, w, velocity components at hub height $0.5d_T$ downstream of the turbine illustrating spiraling motion around the mean, $\bar{V}$ and $\bar{W}$. . . . 123
5.11 Normalized channel topography for (a) baseline ripples, (b) turbine with ripples, and (c) turbine with dunes experiments. Streamwise, x, cross-stream, y coordinates and vertical bed elevation z_b are normalized by the turbine rotor diameter, $d_T = 0.5$m. Turbine location ($x/d_T = 0$, $y/d_T = 0$) indicated by circle. Flow is left to right. . . . 125
5.12 Interface width roughness characterization for the sediment transport experiments. 126
5.13 Space-time plot of bed elevations during the bedform transitional regime phase from ripples to dunes (Q_2 from $t \approx 0$min to 125min; Q_3 from $t \approx 125$min to 265min). Streamwise x coordinate is normalized by the turbine rotor diameter, $d_T = 0.5$m. Turbine located at $x/d_T = 0$. Flow is left to right. . . . 127

5.14 End topography of Turbine Q_1 (a) and Turbine Q_3 (b) experiments, normalized by characteristic bedform wavelength, λ_b, from each experiment. The turbine zone of influence length, $I_L \approx 7\lambda_b$ for each case, while the influence width, $I_B \approx 4\lambda_b$ for each case. The zone of influence spreading angle is consistent between the two cases, $I_\theta \approx 42°$. Triangular areas outlined by white dashed lines are equivalent zones in (a) and (b). Contour scale is normalized bedform height, z/h_b. Turbine location outlined by white dashed circle. Flow is left to right. . . . 128
5.15 Centerline bed elevation profiles aligned with the turbine center plotting mean elevations and scour depth for a range of Reynolds numbers. 128
6.1 Experimental setup schematic of RM1 in the SAFL Main Channel Facility. . . . 135
6.2 (a) Photo of RM1 installed in the SAFL Main Channel Facility. (b) CAD image showing internal instrumentation setup for data acquisition of turbine performance. 135
6.3 Detailed dimensions of the 1:40 scale RM1 turbine tested at SAFL. 136
6.4 Comparison between full-scale blade geometric characteristics for the original RM1 blade design (NACA 63-series) and the modified design (NACA 44-series) for lower Reynolds number testing at SAFL. 138
6.5 Inflow vertical profile characteristics in the center of the channel at $3d_T$ upstream of the RM1 rotors: mean streamwise velocity, $\bar{U}$ (left), streamwise velocity root-mean squared, u' (center), and streamwise turbulence intensity, I_u (right). Area between dashed lines -0.25m $\leq Z \leq$ 0.25m indicates RM1 rotor energy extraction plane. Mean water surface elevation (WSE) indicated by dashed line at $Z = 0.5$m. 143
6.6 Inflow horizontal profile characteristics at hub height, h_{hub}, from $3d_T$ upstream of the RM1 rotors: mean streamwise velocity, $\bar{U}$ (top), streamwise velocity root-mean squared, u' (center), and streamwise turbulence intensity, I_u (bottom). Y-axis distance shows full channel width, $b = 2.75$m. 144
6.7 Calculated C_p vs. λ (coefficient of power vs. tip-speed ratio) for the left (blue) and right (red) RM1 rotors. Vertical error bars represent mean C_p value measurement uncertainty. Maximum C_p occurs near $\lambda \approx 5.1$ (right rotor $C_p = 0.48$; left rotor $C_p = 0.43$). Results have not been corrected for channel blockage; therefore, maximum C_p may slightly decrease after blockage corrections have been applied. 145
6.8 Instantaneous torque (light gray dots) measurements, τ_i vs. instantaneous rotor blade angular position, $\theta_i(°)$. Solid black line illustrates mean torque value, $\bar{\tau}$ vs. rotor blade angular position, $\theta(°)$. Measurements collected from right rotor while turbine was operating at $\omega = 3.4$rps ($\lambda \approx 5.1$). RM1 blades are offset 180° on each rotor but were rotating in symmetry. 146

6.9 Velocity deficit horizontal (XY) and vertical (XZ) plane contours upstream and downstream of RM1 in the SAFL Main Channel. Vertical plane y-axis, z/d_T, shows full water depth during the experiment ($h = 1.0$ m). Horizontal plane y-axis, y/d_T, shows full channel width ($b = 2.75$ m). Horizontal and vertical dotted black lines indicate actual ADV measurement profile locations. ADV vertical point spacing $\Delta z = 0.025$ m ($z/d_T = 0.05$). Horizontal spacing varied. Measurements collected at $\lambda \approx 5.1$ ($\omega = 3.4$ rps). Flow is left to right. 149

6.10 Normalized turbulent kinetic energy, k/k_∞, horizontal (XY) and vertical (XZ) plane contours upstream and downstream of RM1 in the SAFL Main Channel. Vertical plane y-axis, z/d_T, shows full water depth during the experiment ($h = 1.0$ m). Horizontal plane y-axis, y/d_T, shows full channel width ($b = 2.75$ m). Horizontal and vertical dotted black lines indicate actual ADV measurement profile locations. ADV vertical point spacing $\Delta z = 0.025$ m ($z/d_T = 0.05$). Horizontal spacing varied. Measurements collected at $\lambda \approx 5.1$ ($\omega = 3.4$ rps). Flow is left to right. 150

6.11 Hub height velocity deficit. RM1 rotors located at $x/d_T = 0$. Measurements collected at $\lambda \approx 5.1$ ($\omega = 3.4$ rps). 151

6.12 Hub height streamwise root-mean squared ($\sigma_u = \sqrt{\overline{u'^2}}$). RM1 rotors located at $x/d_T = 0$. Measurements collected at $\lambda \approx 5.1$ ($\omega = 3.4$ rps). 151

6.13 Hub height streamwise turbulence intensity, I_u. RM1 rotors located at $x/d_T = 0$. Measurements collected at $\lambda \approx 5.1$ ($\omega = 3.4$ rps). 152

7.1 Topography of seven turbine staggered array installed in migrating sand ripple topography ($d_{50} = 0.42$mm). Inset shows photograph of experiment. Flow is left to right (top to bottom in inset image). 155

7.2 Instantaneous (light gray lines) and mean bed elevation profiles (solid black lines) along three streamwise sonar transects (top: right side of channel; center: middle of channel; bottom: left side of channel) during the seven turbine staggered array experiments. Vertical red dashed lines indicate locations of the seven turbines. Flow is left to right. 156

7.3 Cross-correlation coefficients, ρ_0, between bed elevation, z_b, and turbine voltage as a function of normalized streamwise distance x/d_T. Black lines shows relationships from ripples experiment, while the red line shows results from dunes experiments presented for a single turbine in Chapter 3. 157

7.4 Voltage spectra from Turbine 1 (upstream center turbine in seven turbine array) for both fixed bed and erodible channel experiments. Light gray lines show 5-minute interval voltage spectra during the erodible channel experiments, while the solid black line illustrates the average of those instantaneous spectral functions. The dashed black line shows the voltage spectra from the same turbine during fixed bed experiments. Spectra have been normalized using the corresponding hub height velocity, U_{hub}, rotor diameter $d_T = 0.15$m, and timeseries variance, σ_v^2. 158

7.5 Voltage spectra from Turbine 7 (downstream center turbine in seven turbine array) for both fixed bed and erodible channel experiments. Light gray lines show 5-minute interval voltage spectra during the erodible channel experiments, while the solid purple line illustrates the average of those instantaneous spectral functions. The dashed purple line shows the voltage spectra from the same turbine during fixed bed experiments. Spectra have been normalized using the corresponding hub height velocity, U_{hub}, rotor diameter $d_T = 0.15$m, and timeseries variance, σ_v^2. 159

7.6 Pre-multiplied voltage spectra from the seven turbine staggered array experiment during fixed bed conditions for the three turbines in the center of the channel (Turbine 1 = upstream; Turbine 4 = middle; Turbine 7 = downstream). Dark blue lines shows pre-multiplied spectra of the hub height flow velocity at seven rotor diameters ($7d_T$) downstream of a single turbine during fixed bed experiments. 160

7.7 Mean streamwise velocity, U, normalized by the hub height velocity, U_{hub}, in a vertical plane aligned with the turbine center from -2 < x/d_T < 15. Measurements collected using a Nortek Vectrino+ acoustic Doppler velocimeter (ADV) at locations indicated by black dots (18 vertical profiles x 41 measurements locations each profile = 738 total points). Data collected with turbine operating at optimal condition ($C_p \approx 0.45$ at $\lambda = 5.8$) [6]. 162

7.8 Mean cross-stream velocity, V, normalized by the hub height velocity, U_{hub}, in a vertical plane aligned with the turbine center from -2 < x/d_T < 15. Measurements collected using a Nortek Vectrino+ ADV at locations indicated by black dots. Data collected with turbine operating at optimal condition ($C_p \approx 0.45$ at $\lambda = 5.8$) [6]. 162

7.9 Mean vertical velocity, W, normalized by the hub height velocity, U_{hub}, in a vertical plane aligned with the turbine center from -2 < x/d_T < 15. Measurements collected using a Nortek Vectrino+ ADV at locations indicated by black dots. Data collected with turbine operating at optimal condition ($C_p \approx 0.45$ at $\lambda = 5.8$) [6]. 163

7.10 Root-mean squared (RMS) streamwise velocity, u', normalized by the hub height velocity, U_{hub}, in a vertical plane aligned with the turbine center from -2 < x/d_T < 15. Measurements collected using a Nortek Vectrino+ ADV at locations indicated by black dots. Data collected with turbine operating at optimal condition ($C_p \approx$ 0.45 at $\lambda = 5.8$) [6]. 163
7.11 RMS cross-stream velocity, v', normalized by the hub height velocity, U_{hub}, in a vertical plane aligned with the turbine center from -2 < x/d_T < 15. Measurements collected using a Nortek Vectrino+ ADV at locations indicated by black dots. Data collected with turbine operating at optimal condition ($C_p \approx 0.45$ at $\lambda =$ 5.8) [6]. 164
7.12 RMS vertical velocity, w', normalized by the hub height velocity, U_{hub}, in a vertical plane aligned with the turbine center from -2 < x/d_T < 15. Measurements collected using a Nortek Vectrino+ ADV at locations indicated by black dots. Data collected with turbine operating at optimal condition ($C_p \approx 0.45$ at $\lambda =$ 5.8) [6]. 164
7.13 Reynolds stress, $u'w'$, normalized by the hub height velocity squared, U_{hub}^2, in a vertical plane aligned with the turbine center from -2 < x/d_T < 15. Measurements collected using a Nortek Vectrino+ ADV at locations indicated by black dots. Data collected with turbine operating at optimal condition ($C_p \approx 0.45$ at $\lambda =$ 5.8) [6]. 165
7.14 Velocity deficit, $U_{def} = (U_\infty - U_x)/U_\infty$, within a plane at hub height from 1 < x/d_T < 10 downstream of a single turbine, $d_T = 0.15$m operating at $\lambda \approx$ 4.5-4.6. 166
7.15 Velocity deficit, $U_{def} = (U_\infty - U_x)/U_\infty$, within a plane at hub height from 1 < x/d_T < 10 downstream of a tri-frame turbine arrangment, $d_T = 0.15$m operating at $\lambda \approx$ 4.5-4.6. 167
7.16 Spanwise comparison of velocity deficit, $U_{def} = (U_\infty - U_x)/U_\infty$, between a single turbine wake (O) and a tri-frame turbine configuration wake (Δ) at $x/d_T =$ 1(a), 4(b), 7(c), and 10(d). 168
7.17 Velocity deficit, $U_{def} = (U_\infty - U_x)/U_\infty$, comparison at hub height in the streamwise direction between five configurations: Single turbine (O), tri-frame turbines (Δ), and two turbines spaced at $4d_T$ ($\square$), $7d_T$ ($\diamond$), and $10d_T$ ($\triangleright$). 169
7.18 Normalized turbulent kinetic energy, k/u_*^2, within a plane at hub height from 1 < x/d_T < 10 downstream of a single turbine, $d_T = 0.15$m operating at $\lambda \approx$ 4.5-4.6. 170
7.19 Normalized turbulent kinetic energy, k/u_*^2, within a plane at hub height from 1 < x/d_T < 10 downstream of a tri-frame turbine arrangment, $d_T = 0.15$m operating at $\lambda \approx$ 4.5-4.6. 171

7.20 Normalized turbulent kinetic energy, k/u_*^2, comparison in the spanwise direction at hub height between a single turbine wake (O) and a tri-frame turbine configuration wake (Δ) at $x/d_T = 1$(a), 4(b), 7(c), and 10(d). 172
7.21 Normalized turbulent kinetic energy, k/u_*^2, comparison at hub height in the streamwise direction between five configurations: Single turbine (O), tri-frame turbines (Δ), and two turbines spaced at $4d_T$ ($\square$), $7d_T$ ($\diamond$), and $10d_T$ ($\triangleright$). 173
7.22 Photo of the RM2 dual-rotor model in the SAFL Main Channel. 174
7.23 Schematic of the RM2 experimental setup and ADV collection locations in the SAFL Main Channel facility. Flow is from left to right. 175
7.24 Velocity deficit downstream of RM2 in the SAFL Main Channel in a plane parallel to the channel bottom at turbine center height. Turbine location indicated by the two circles at $x/d_T = 0$. Vertical axis, y/d_T, shows full SAFL Main Channel width ($b = 2.75$m). Black dots indicate actual ADV measurement locations. Measurements collected with dual-rotors in-phase and $\lambda \approx 2.2$ ($\omega = 2.0$rps). Flow is left to right. 175
7.25 Velocity deficit upstream and downstream of RM2 in the SAFL Main Channel in vertical planes aligned with the right rotor (top), midway between the two rotors (middle), and the left rotor (bottom). Turbines located at $x/d_T = 0$. Vertical axis, z/d_T, shows full water depth during experiments ($h = 1.0$m). Black dots indicate actual ADV measurement locations. Measurements collected with dual-rotors in-phase and $\lambda \approx 2.2$ ($\omega = 2.0$rps). Flow is left to right. 176
7.26 Normalized turbulent kinetic energy, k/k_∞, downstream of RM2 in the SAFL Main Channel in a plane parallel to the channel bottom at turbine center height. Turbine location indicated by the two circles at $x/d_T = 0$. Vertical axis, y/d_T, shows full SAFL Main Channel width ($b = 2.75$m). Black dots indicate actual ADV measurement locations. Measurements collected with dual-rotors in-phase and $\lambda \approx 2.2$ ($\omega = 2.0$rps). Flow is left to right. 177
7.27 Normalized turbulent kinetic energy, k/k_∞, upstream and downstream of RM2 in the SAFL Main Channel in vertical planes aligned with the right rotor (top), midway between the two rotors (middle), and the left rotor (bottom). Turbines located at $x/d_T = 0$. Vertical axis, z/d_T, shows full water depth during experiments ($h = 1.0$m). Black dots indicate actual ADV measurement locations. Measurements collected with dual-rotors in-phase and $\lambda \approx 2.2$ ($\omega = 2.0$rps). Flow is left to right. 178

7.28 Demonstration of particle image velocimetry being applied to sediment topography data. Instantaneous bed elevation data for (a) $t_1$and (b) t_2 can be used to determine local areas of (c) erosion and deposition (i.e. $\Delta z_b = t_2 - t_1$). Using elevation nodes as particles, the correlation between the data from (a) and (b) can be analyzed using PIV algorithms to calculate instantaneous local bedform velocities (d). Averaging all time-steps together enables determining a regional map of average bedform velocities (e). Flow is left to right in all images. 180
7.29 Feedback and feed-forward loop diagram schematic for advanced control strategies for the next generation MHK devices. 183
7.30 Schematic experimental setup for future studies on the interactions between dune generated turbulence and axial-flow hydrokinetic turbines to study to role dune size and location has on turbine performance and the associated near and far-wake characteristics. 184

Chapter 1

Introduction, Overview, & Motivation

1.1 Overview

Research within marine hydrokinetic (MHK) energy aims to integrate industry, government, and academic expertise to rapidly develop the understanding of device operations and interactions with the physical and ecological environments. This relatively new industry currently faces challenging regulatory permitting processes, often times resulting in developers abandoning their ideas. With continued and focused research, regulatory agencies can continually update adaptive management practices and provide open avenues for industry development and demonstration, ultimately leading to industry expansion, competitive cost of energy from marine renewable sources, and movement towards the U.S. Department of Energy's (DOE) goals of energy security and independence. The breadth of research in MHK covers areas spanning individual device performance and wake characteristics, interactions between device(s) and the physical and ecological environments, multi-turbine interactions, turbine(s) response to turbulent and complex inflow environments, device control strategies, and more. These issues are critical to the rapid and continued advancement of the MHK industry.

To date, few studies exist on the interactions between MHK devices and the physical environment, for instance, on how these devices modify erodible channels nearby or at farther distances downstream in the channel, or how complex topography impacts device performance and structural fatigue. At the foreground of MHK research lies the interactions of devices with the ecological environment; however, there is a strong interaction between the physical environment (i.e. channel geometry, sediment distributions, turbulence levels, etc.) and the ecological

environment (i.e. species diversity and behavior, benthic organisms and diversity, etc.). Because of this, it is imperative to better understand device interactions with the physical environment, both in terms of structural stability and performance, but also to develop a holistic understanding as to how these devices impact all aspects of the environment.

The research program pursued during my Doctoral studies at the University of Minnesota included a suite of experiments that aimed to address uncertainties surrounding device impacts on erodible channels in both near and far-field locations, as well as how complex topography influences device performance and wake characteristics. The natural environments MHK devices are installed in are complex and contain turbulent eddies covering large time and length scales. Not only do coherent turbulent motions in the flow impact turbine performance, but wake turbulence from individual turbines and/or turbine farms will modulate the downstream hydrodynamic and morphodynamic environment. For this reason, it is imperative to understand the interactions between the large-scale coherent motions within a turbine wake and how they modulate the turbulence and kinetic energy near the boundary, especially as the MHK industry aims to expand installations towards larger arrays mounted in erodible channels with active sediment transport.

Through a combined multi-scale approach using laboratory experiments, numerical models, and field-scale investigations, uncertainty surrounding the MHK industry can be minimized, thereby decreasing the cost of energy through advanced development towards large-scale grid-connected installations. My Doctoral research program, summarized in the bullet points below and described in depth in the following chapters, focused on scaled laboratory experiments and contributes to an area that currently remains relatively unexplored in MHK research: the interactions between complex topography and sediment transport and its influence on the performance and wake characteristics of axial-flow hydrokinetic energy devices.

- Chapter 1 provides an overview of research and development in current-driven hydrokinetic devices (i.e. tidal, river, etc.) and motivation for the research undertaken during this Doctoral research program.
- Chapter 2 provides results on the spatial and temporal evolution of turbine-induced local scour in erodible channels.
- Chapter 3 addresses the interactions between large-scale mobile sediment dunes and an axial-flow hydrokinetic turbine model, both in terms of turbine performance response to mobile topography, as well as turbine influence on sediment transport.
- Chapter 4 investigates the interactions between an axial-flow hydrokinetic turbine and the hydrodynamics and morphodynamics in a meandering channel with an asymmetric channel cross-section and sand bedload sediment transport.

- Chapter 5 focuses on high-resolution monitoring of the kinematic and geometric characteristics of bedforms as they migrate past a turbine, as well as detailed, synchronous measurements of turbine power and turbulent wake characteristics in erodible channels.
- Chapter 6 highlights experimental results on the performance and wake characteristics of the U.S. Department of Energy's Reference Model 1, a dual-rotor axial-flow turbine aimed at providing high-resolution, open-source data for numerical model validation and rapid MHK industry advancement.
- Chapter 7 discusses opportunities for future research problems and additional work I have been involved with in MHK research before concluding with a summary of key results from this Doctoral research program in the Summary & Conclusions section, Chapter 8.

1.2 Marine Renewable Energy: A Review

Development of renewable energy technologies continues to gain attention across many industries, including wind, solar and hydropower. The U.S. Department of Energy annually injects millions of dollars towards research and development aimed at advancing these industries in light of the national goal of increasing its renewable energy portfolio to make strides towards energy security and independence [7]. As regulatory agencies struggle to keep up with rapidly advancing technologies within each industry, collaboration among industry, government and academia is a critical component of supplying data to enable these regulatory agencies to adjust permitting regulations and incorporate updated research findings into adaptive management practices. Among the newest of renewable energy industries is marine hydrokinetics (MHK), a diverse group of technologies capable of harnessing kinetic energy from naturally occurring currents such as tides, rivers, waves, ocean currents and thermal gradients [8, 9, 10]. This subset of hydropower has gained attention in recent years as conventional hydropower practices requiring dams, despite their efficiency, have gained negative attention given several undesired harmful environmental impacts (e.g. fish blockage prohibiting spawning, trapping sediment, decreasing dissolved oxygen and overall water quality, among others) (e.g. [11]). As MHK industry strives to develop quickly and learn from more advanced renewable technologies (e.g. wind energy), the list of regulatory agencies managing permitting applications within this broad field is lengthy given the locations where industry developers wish to pursue field-scale deployments. Examples of such agencies are BOEM (Bureau of Ocean Energy Management), FERC (Federal Energy Regulatory Commission), NOAA (National Oceanic and Atmospheric Administration), U.S. FWS (Fish & Wildlife Service), and individual state government agencies, to name just a few [12]. Complicating their job, there are a multitude of designs currently being pursued in

the MHK industry, for example axial-flow two and three bladed turbines (Marine Current Turbines, Verdant Power, OpenHydro, Andritz Hydro, among others), cross flow turbines (ORPC (Ocean Renewable Power Company), for example), oscillating hydrofoils, vortex induced vibrating devices and a myriad of wave energy conversions (WEC) systems (OPT (Ocean Power Technologies), for example) ([9, 13, 14, 15], among others). While European countries are leading the way in field-scale deployments, the U.S. currently has three companies with full-scale devices in the water (Verdant Power, ORPC, and OPT).

Uncertainty surrounding MHK devices impact on the biological and morphological ecosystems in tidal and river environments continues to rank highly as an area needing further investigation [8, 16, 17, 18, 19, 20]. Often this uncertainty is an insurmountable barrier for companies in this emerging field; however, in recent years, progress in full-scale demonstrations and grid-connected licensed projects have started providing data as to how such devices interact with the environment. In January 2012, FERC issued its first license to Verdant Power for their Roosevelt Island Tidal Energy site development, marking the first grid connected licensed project in the United States. More recently, Verdant Power has received permission to further develop the site, aiming to install 30 of their devices within the project boundaries. In March 2014, FERC issued a license for a 600-kilowatt Admiralty Inlet Project in Puget Sound, WA, providing government agencies, academic research institutions, utility providers, and device developers another field scale installation to study, monitor, and evaluate the environmental and economic effects of hydrokinetic energy systems. Unfortunately, despite these recent success stories in the burgeoning MHK industry, many developers fall short, burdened by the costly and lengthy environmental permitting process for project site development. A striking example of this is illustrated by comparing the FERC MHK permit maps between the years of 2012 and 2013. During this span, 98% of wave energy device permits, 94% of tidal energy device, and 99% of in-stream river current device permits were retracted from FERC. Through ongoing research, industry developers hope to compete with the cost of energy by lowering the financial risks and costs associated with implementing these new technologies [21, 20].

Research and development in MHK has focused on many aspects of devices, including performance, wake characteristics, interactions with both the physical and biological environments, power take off systems and more. These studies, performed experimentally, computationally and at field-scales, have resulted from extensive collaborations among national and international academic, government and industry based organizations [8]. Previously, experiments and numerical studies have focused mainly on characterizing the mean wake structure and wake turbulence [22, 23, 24, 25, 26, 27, 28, 29, 30, 31], power production capabilities [32, 33, 1, 34, 35], and turbine response to turbulent flow conditions [6]. For example, [32] and [33] performed detailed performance measurements around a 0.8m diameter axial-flow turbine, looking at the

effects of blade pitch angle, rotor yaw angle, submergence and tip speed ratio on the resulting thrust (C_T) and power (C_P) coefficients in both a cavitation tunnel and towing tank. Additionally, studies have focused on surface wave loading on blades and MHK structures [36, 37, 38]. [39] and [38] both studied the effect of surface waves on turbine performance, finding a minimal effect on mean power and torque coefficients; however, this is dependent on the submergence depth of the turbine. The authors did see a relationship between phase of the surface waves and instantaneous power and torque values. As described by [28], the persistence and spreading of a turbine wake above a smooth channel bottom depends on the hub height. However, these experiments used circular porous discs to vary thrust coefficients, prohibiting true turbine wake characteristics and development and did not allow for investigations into estimated turbine power output. The power and wake characteristics will undoubtedly change as channel roughness changes. Optimization of this problem can lead to minimized fatigue loading and impacts on device rotors, maximum mean power production, and shorten wake momentum recovery allowing for increased device density when considering multi-turbine deployments.

Interactions between hydrokinetic turbines and the near-field and far-field regions of sediment are often identified as a critical area for assessment [17, 19, 40, 3]; however, to date, limited research has been published to address this concern. [41] reiterate the need for scour estimation procedures by summarizing numerous existing scour estimation procedures around submerged pilings; however, local scour induced by a single small-scale axial-flow turbine model was investigated under clear water and live bed transport conditions and compared to standard bridge scour prediction methods and showed little success using existing guidelines [5]. Other experiments have suggested armoring the near-field region with a rigid approach platform, thereby accelerating flow and reducing local scour, yet no data were collected on turbine-sediment interactions [40]. [42] recently completed experiments showing the interactions between axial-flow turbines and large-scale 2D bedforms, reporting on both bedform impacts on turbine performance as well as turbine effects on near-field and far-field modulations to sediment transport. Additionally, other investigations have been reported resulting from numerical studies on the effects arrays of tidal turbines have on far-field sediment characteristics [43, 44, 45, 46, 47]; however, large computational domains did not provide the resolution to investigate the local or channel-scale effects on scour and sediment transport. The advancements in CFD capabilities in recent years have provided unprecedented results regarding flow structure interaction around hydrokinetic devices [24, 48]. Large-eddy simulations are now capable of solving problems in arbitrarily complex natural geometries [49, 50]. With the available computational tools, the advancement in turbine-sediment interactions has the capability to progress rapidly, and will likely do so in the coming years through an integrated experimental, computational and field-scale scientific approach.

Numerical models ranging in complexity from simple BEM (Blade Element Momentum) codes, to more complex 2D models and fully-coupled 3D hydrodynamic and morphodynamic CFD codes have been used to simulate flow over single and multiple turbines [51, 52, 53, 54, 55, 56, 57, 58, 59, 60]. Models incorporating large-scale domains often parametrize turbines as a momentum sink in the grid, whereas high-resolution models can fully resolve complex rotating turbine blades and static foundation components. Three distinct regions of wake flow were first simulated and reported by [24]. Here, the CURVIB (**CURV**ilinear **I**mmersed **B**oundary) method Large-Eddy Simulations (LES) were employed, and provided a systematic approach at investigating turbine wake and performance characteristics at various grid resolution and full vs. partially resolved turbine geometry against field data for the Verdant Turbine at the East River RITE site in New York. This report highlighted the near-turbine tip vortex and spiraling inner-core vortex co-rotating in the same direction as the rotor and bounding the counter-rotating outer core wake vortex. Ongoing work using these methods are demonstrating the utility of these computational methods for simulating single and multi-turbine wake characteristics in the near field and far-field regions while discussing the importance of resolving the turbines as actuator disks, actuator lines, vs. fully-resolved turbine geometries [48]. Until these studies, most reported CFD investigations utilize submerged actuator disks to model the blockage of turbines. While this approach may work on a basic level for large-scale turbine deployment and far-field wake interactions studies, they miss the crucial physics occurring the near-field wake regions, which ultimately effect tip vortex breakdown, wake momentum recovery, wake meandering characteristics, and therefore far-field interactions in some cases. Recent methods such as an immersed boundary method allow fluid-structure interactions to be modeled accurately for moving bodies such as turbine rotors [61]. Other examples include studies by [62] who discussed the model SNL-EFDC (Environmental Fluid Dynamics Code) developed at Sandia National Laboratories and its utility in modeling MHK device interactions with the environment and potential changes they might induce. Single and twin-rotor vertical axis cross-flow MHK turbines have also been investigated using numerical models [63, 64, 65, 66].

The U.S. Department of Energy (DOE) and Sandia National Laboratories (SNL) have extended their code CACTUS (**C**ode for **A**xial and **C**ross-flow **TU**rbine **S**imulation), a vortex wake method, from the wind industry into the MHK research & development program [67]. This code, among many others, provides an method of assessing axial-flow and cross-flow turbine geometries and the performance characteristics. Continued efforts within the DOE MHK R&D program Reference Model Project (RMP) collaborates with a number of research universities around the US to develop robust databases on performance and wake measurements for a reference axial-flow and cross-flow turbine, providing open-source access for CFD method

validation and verification for continued design and development of MHK devices [68]. Cross-flow MHK devices also continue to be a focus of detailed laboratory and computational studies [69, 70, 71]. Understanding these devices is complex given the continuously changing angle of attack during rotation, variations in dynamic stall conditions, and blade wake interactions on the leeward side of the rotational axis. These challenging interactions are being investigated experimentally, computationally and at field-scales. [72] recently investigated large-scale turbulent motion effects on performance of a 25kW field-scale vertical axis device.

Turbulence levels at potential MHK sites can greatly impact the performance and fatigue loading of a device, therefore, it is critical to properly assess site conditions prior to field deployment [73, 74, 75, 68, 76, 77, 78, 79]. [74] demonstrated how incorporating the turbulent fluctuations into power calculations can increase the available and harnessed power of a device, an exercise that can be demonstrated numerically, yet the full-scale implications of this have yet to be fully understood, reiterating the need to properly measure and characterize turbulent inflow to determine resource availability, mean annual power production, as well as potential fatigue loading on devices.

Commercial scale MHK projects will be installed in natural and complex topographical environments. Because the flow within these environments in greatly impacted by the scale of roughness and asymmetry within the natural channel, well defined open channel flow simulations and experiments do not necessarily indicate true device response to complex topography and unsteady large-scale coherent turbulent motions shed from these geometries. Previous experiments by [1] begin to shed light on these interactions, demonstrating scale-to-scale interactions in turbulent eddies and resulting turbine performance power spectral characteristics. Research in wind energy has also examined the response of wind turbines installed in complex terrain [80, 81, 82, 83]. Simplifying the complexity of topography both experimentally and numerically can provide an initial look at turbine response and resulting wake structure. [81] used experiments in a wind tunnel using a sinusoidal hill upwind of a model axial-flow turbine to investigate differences in downwind turbine response between a topographic form compared to an additional turbine. Others have used numerical simulations to investigate arrays of turbines and their response in power production and wake characteristics for turbine farms installed in complex terrain. Further understanding of the wake above complex geometries is of critical importance because it impacts wake meandering characteristics which are important for downstream turbine fatigue loading and power production [84]. Additionally, large-scale structures in the outer regions of the flow can modify the spectral characteristics and the turbulence in the near wall region [85]. For this reason, it is imperative to understand the interactions between the large-scale coherent motions within a turbine wake and how they modulate the turbulence and kinetic energy near the boundary, especially when MHK devices will eventually be installed

in mobile channels.

Integral to understanding the interactions between turbulent channel flow and turbine wake flow, is understanding turbulence generated by roughness along channel boundaries. One are of this relates to the mean and fluctuating velocity fields above laboratory and field subaqueous dunes which have been extensively studied during recent decades [86, 87, 88, 89, 90, 91, 92] and in more recent years using computational fluid dynamics (CFD) ([93, 94], for example). From the research work of [95], five main flow regions above dunes have been identified: **a)** maximum velocity, **b)** shear layer, **c)** separation zone, **d)** internal boundary layer, and **e)** wake region. The region of maximum velocity occurs along the top portion of a dune above the crest where the cross-sectional flow area is at a minimum. Downstream of the crest, the shear layer creates a zone of high turbulence intensity and instability. This region can often contain high concentrations of suspended sediment and other abrasive material [96], a potential problem for the longevity of MHK device blades. The separation zone, located immediately downstream of the dune crest, creates a highly turbulent zone and often has recirculating, upstream velocities interacting with the lee-side slope of the dune. This region extends downstream up until the point of reattachment, typically located a horizontal distance of approximately five times the bedform height, H_b [96]. Downstream of the reattachment point, a new boundary layer begins to develop along the low-angle stoss side of the dune. Located between the growing internal boundary layer and the turbulent shear layer is the wake region [95, 97]. In summary, flow characteristics, such as mean values, turbulence intensity and turbulent kinetic energy, vary depending on the region above a dune where measurements are made. This spatial variability of the turbulent flow around bedforms is expected to add temporal variability to the incoming flow perceived by instream MHK devices due to both bedform migration and deformation (see e.g. [98, 99, 100, 91]).

Large rivers around the world (e.g. Mississippi River) are characterized by large meanders, asymmetric channels and mobile substrates that respond differently during various flood stages. The complexity of channel topography introduces a broad range of large turbulent scales into the flow environment that must be taken into account in the design and performance evaluation of MHK devices and project site development. For instance, field data of bedforms indicate that areas within the Mississippi River can have small-scale bedforms ($H_b \approx$ 0.5m-3m and $\lambda_b \approx$ 5m-50m) migrating up the stoss side of larger-scale dunes ($H_b \approx$ 1m-6m and $\lambda_b \approx$ 100m-300m) in flow depths of $h \approx$ 15m-20m [101]. Other studies have reported similar findings [102, 4], and in general, it is not uncommon to find mobile topographic features on the scale of the rotor diameters (i.e. $d_T \approx$ 5m-10m) of proposed hydrokinetic devices this day in age. Regardless, whether mobile or stationary large-scale topographic features exist at proposed projects sites, these features will introduce a broad range of turbulence scales into the flow that need to

be properly characterized during pre-project site assessment. Also integral to understanding MHK device interactions with the morphodynamic environment will be incorporating studies on sediment transport and scour around hydraulic structures in bi-directional flows with mobile substrates (i.e. tidal channels).

Although not a major focus of this work, perhaps the largest barrier to the MHK industry is the lack of understanding surrounding the device interactions and impacts on marine life, both through physical interactions with organisms as well as electrical and acoustic frequency interference underwater [16, 18, 103, 3, 104]. The US DOE recognizes this uncertainty within the industry and research continues to be heavily focused on these issues [105]. It is worth acknowledging the strong interaction between the physical environment (i.e. channel geometry, sediment distributions, turbulence levels, etc.) and the ecological environment (i.e. species diversity and behavior, benthic organisms and diversity, etc.) [106]. European and U.S. MHK field-scale projects continue to develop an understanding of the interactions between marine life and these devices, for example, environmental assessment reports have been filed by MeyGen Tidal Energy Project in the United Kingdom, Marine Current Turbine's SeaGen Turbine System at Strangford Lough in Northern Ireland, or the US Based Verdant Power's East River RITE site. While research should focus in-depth on individual device interactions with either the physical or ecological environment, the industry needs to also collaborate with institutions on developing relationships on the co-evolution of these environments, both under anthropogenic modifications stemming from MHK industry development, but also climatic changes in the aquatic environments where these devices will be installed.

Despite the MHK industry being relatively new, development of active and passive control strategies can and should co-evolve with the understanding of device interactions with their natural environments. Device geometry and operating principles will influence control strategies, for example, whether it is an axial-flow device with asymmetric, lift generating blades, or a cross-flow device utilizing symmetric blades in either a straight-bladed or helical (i.e. Gorlov) arrangement. The MHK industry will benefit from previous research in control strategies and implementation in the wind industry [107, 108, 109, 110, 111]. In the case of axial-flow devices, possible active control strategies could aim to achieve maximum power point tracking for specific devices. Additionally, control strategies may focus on minimizing individual blade, rotor, or entire turbine and support structure fatigue. Due to the scale of laboratory devices, these goals may be achievable purely through controlling rotational velocity of the rotor. With larger scale rotors having a much larger moment of inertia, such as at field scale, the likelihood of active control based on a feed-forward approach using in-situ measurements of turbulent flow-fields may be less feasible, and approaches may shift to focus on slower response control when large-scale topographic changes occur or sensors indicate a local presence of marine life or

other structures (i.e. ships) moving nearby. At field-scale, active pitching of blades will likely be incorporated into designs, similar to what is used in the wind industry. In environments where the dominant approach flow direction changes (i.e. tidal flows, mobile channel substrates with 3D bedforms), incorporating yaw control will improve performance [112]. To date, little work has been completed for active control of MHK devices. [113] experimented with closed-loop PI (Proportional Integral) and H_∞ LPV (Linear Parametric Varying) speed control of a straight-bladed vertical axis hydrokinetic turbine. Here, the authors attempted to incorporate a maximum power point tracking feedback control system and had reasonable success. Unlike wind energy systems, MHK systems typically operated at lower tip speed ratios, λ, a possible benefit for the control systems community. Regardless, non-linearities in the MHK systems (i.e. C_P or C_T vs. λ) often introduce complexity when considering control operations, and the inherent energy in environments these devices are designed for will require both low-pass and high-pass filters to reduce noise from environmental variables.

As shown, the breadth of research in MHK covers areas spanning individual device performance and wake characteristics, interactions between device(s) and the physical and ecological environments, multi-turbine interactions, turbine(s) response to turbulent and complex inflow environments, device control strategies, and more. These issues are critical to the rapid and continued advancement of the MHK industry. Through a combined multi-scale approach using laboratory experiments, numerical models, and field-scale investigations, uncertainty surrounding the MHK industry can be minimized, thereby decreasing the cost of energy through advanced development towards large-scale grid-connected installations. My proposed research, outlined below, contributes to an area that currently remains relatively unexplored in MHK research. As discussed, the interactions between complex topography and wind energy devices has been more frequently studied, yet this area needs to be systematically addressed for the MHK community. Through my proposed laboratory experiment approach, I will contribute an improved understanding of turbine interactions with the morphological environment.

1.3 Motivation: Turbine interactions with turbulence & the environment

1.3.1 MHK device impacts on the environment

Emerging hydrokinetic device companies face many challenges as they design and develop their energy harvesting technologies. These challenges often prove too costly and become insurmountable barriers. Designing robust devices capable of operating efficiently with minimal maintenance in extremely energetic and harsh environments is one of many challenges these companies face.

Additionally, the permitting process and list of regulatory agencies ensures that each company will endure a lengthy and costly process in order to get a single device into the water during the pilot project and demonstration phase, let alone a grid-connected multi-device installation. Examples of such agencies are the Bureau of Ocean Energy Management (BOEM), Federal Energy Regulatory Commission (FERC), National Oceanic and Atmospheric Administration (NOAA), U.S. Fish & Wildlife Service (FWS), and individual state government agencies, to name just a few [12]. Due to these barriers, among others, many preliminary MHK project licenses have been forfeited over recent years, as illustrated in Figure 1.1 showing a map of the U.S. FERC issued site licenses for 2012 and 2015. All preliminary permits on the Lower Mississippi River are no longer being pursued, and many along coastal areas have lapsed over the past three years. One reason many of these permits have been dropped by companies that originally pursued them is due to the lengthy and costly pre-project site Environmental Impact Statement (EIS) and assessment. Due to the nature of this young industry, the uncertainties regarding the interactions between the devices and its surrounding environment are high.

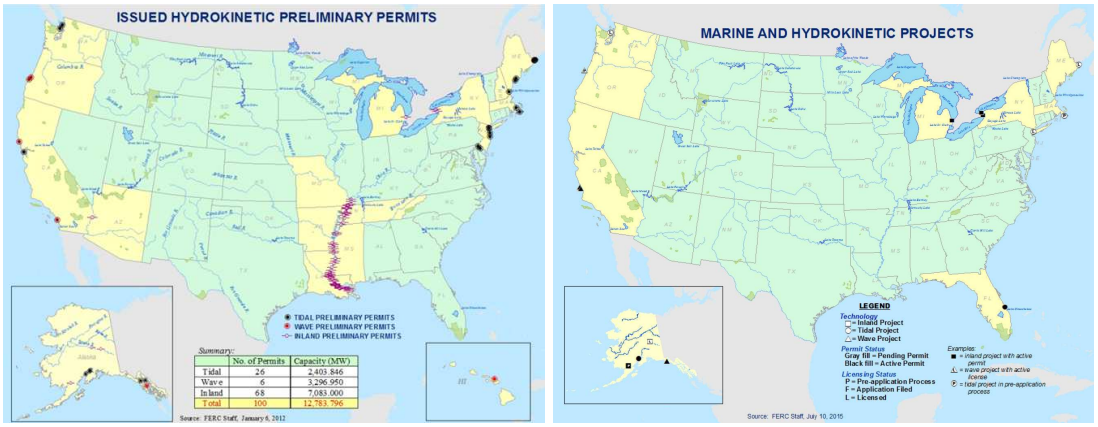

Figure 1.1: Comparison of 2012 (left) and 2015 (right) marine hydrokinetic project permit maps issued by the Federal Energy Regulatory Commission (FERC).

Uncertainties surrounding the interactions between MHK devices and the surrounding ecological and physical environments were categorized based on their relative level of significance and uncertainty surrounding each category [3]. Figure 1.2 illustrates these levels of significance and uncertainty. Here, the color scale indicates degree of significance (green = low significance; red = high significance), while the symbols denote degree of uncertainty regarding the problem ($\square$ = low uncertainty, OO = medium uncertainty, $\Delta\Delta\Delta$ = high uncertainty). As shown, the most significant categories with high uncertainty relate to fish and marine life and the impacts that moving MHK devices and large-scale installations will have on these communities. What

is not shown by the matrix in Figure 1.2 are the complex interconnections between the physical sediment environment and the biological communities that rely on the upper layers of sediment for feeding and reproducing. Researching the interactions between MHK devices and the near and far-field sediment environment will provide further indication as to how these devices may impact marine life communities (both plants and fish). Additionally, developing a greater understanding of how devices modify local scour compared to other hydraulic structures (i.e. bridge piers and abutments) is important for designing robust foundations to minimize structure instability. Minimizing these uncertainties provided motivation for developing this research program presented in Chapters 1 through 8.

	Device Presence: Statis Effects	Device Presense: Dynamic Effects	Chemical effects	Acoustic effects	Electromagnetic effects	Energy Removal	Cumulative Effects
Physical Environment: Near-field	ΔΔΔ	OO	ΔΔΔ	□	□	ΔΔΔ	ΔΔΔ
Physical Environment: Far-field	OO	OO	□	□	□	ΔΔΔ	ΔΔΔ
Habitat	OO	ΔΔΔ	OO	□	OO	ΔΔΔ	ΔΔΔ
Invertebrates	OO	OO	OO	ΔΔΔ	ΔΔΔ	ΔΔΔ	ΔΔΔ
Fish: Migratory	OO	ΔΔΔ	OO	ΔΔΔ	ΔΔΔ	ΔΔΔ	ΔΔΔ
Fish: Resident	OO	ΔΔΔ	OO	ΔΔΔ	ΔΔΔ	ΔΔΔ	ΔΔΔ
Marine mammals	ΔΔΔ	ΔΔΔ	OO	ΔΔΔ	□	□	ΔΔΔ
Seabirds	OO	ΔΔΔ	OO	□	□	□	ΔΔΔ
Ecosystem interactions	OO	OO	OO	OO	ΔΔΔ	ΔΔΔ	ΔΔΔ

Figure 1.2: Generalized stressor/receptor matrix for MHK projects. Color indicates degree of significance (green = low significance; red = high significance). Symbols denote degree of uncertainty (□ = low, OO = medium, ΔΔΔ = high) [3].

While present day pilot projects, such as the Verdant Power RITE site, are installed in

areas with little to no sediment transport (Figure 1.3) and therefore little risk of local scour and structural instability issues, the future of MHK technologies relies heavily on the ability to successfully expand and operate in a variety of environments with arbitrarily complex terrain. As illustrated in Figure 1.1, the Lower Mississippi River previously was an area sought after for MHK installations, and likely will be a desirable location in the future for harnessing energy from Mississippi River flows due to its proximity to major metropolitan areas (i.e. New Orleans, LA). In this environment, it is common for large-scale dunes to migrate along the river bottom (Figure 1.3). These bedforms, which scale with depth and flood stage, modify the turbulent boundary layer and will cause time-varying turbulent structures to impact the turbine rotor. Additionally, the Bay of Fundy, Nova Scotia, Canada, is actively being developed for MHK device demonstration, as it provides some of the highest energy density in the world in the tidal flows passing through the Bay. Bathymetric sonar data from this location show large-scale gravel dunes actively migrating through the targeted project area (Figure 1.3). Other examples of fields sites that may become attractive for future MHK installations are places where electrical transmission infrastructure already exists, such as existing offshore wind turbine farms. As MHK devices become more efficient and target areas with lower peak energy availability, yet predictable and persistent currents, these existing energy farms may provide an attractive location for installing wave, tidal, and ocean current MHK devices. Within these sites, there will likely be both small and large-scale bedforms as well as locally modified topography due to wind turbine foundation structures (Figure 1.3). Regardless of the location, researching the interactions between MHK devices and the sediment environment remains critical and served as additional motivation for the development of this research program.

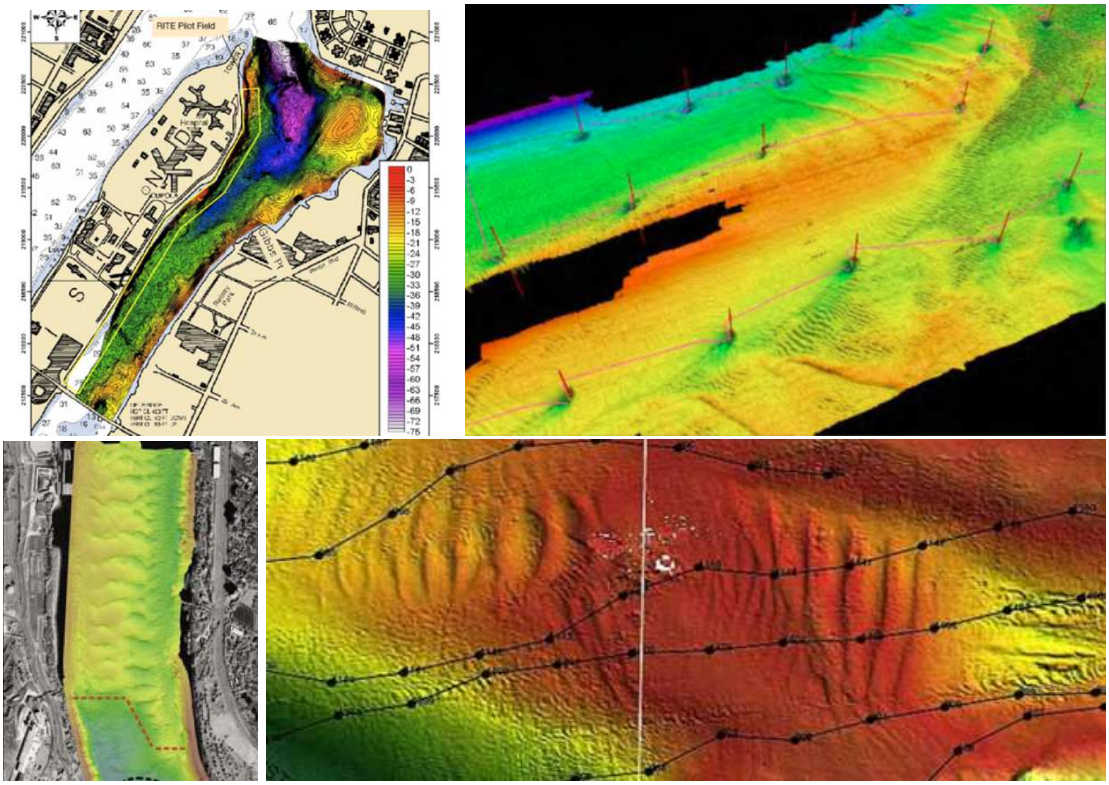

Figure 1.3: Complex channel topography with large-scale stationary and mobile features. (Top left) Bathymetry of non-mobile rock ledges at Roosevelt Island Tidal Energy (RITE) site, New York, NY, USA; (Top right) Mobile bedforms within Scroby Sands offshore wind farm in the North Sea, a potential future MHK device installation site with existing infrastructure; (Bottom left) Sediment dunes in the Lower Mississippi River [4]; (Bottom right) Gravel dunes in Minas Passage, Bay of Fundy, Nova Scotia at tidal power demonstration site.

1.3.2 Interactions between turbulence and axial-flow turbines

Prior to my Doctoral research program, I worked as a Research Engineer at St. Anthony Falls Laboratory (SAFL) at the University of Minnesota (UMN) on MHK device related research. In collaboration with Dr. Leonardo P. Chamorro (currently at the University of Illinois Urbana-Champaign) and Oak Ridge National Laboratories (ORNL), we investigated the interactions between large-scale coherent turbulent eddies and axial-flow hydrokinetic turbines. The results of this project are summarized below, while a complete description is published in the peer-reviewed journal, *Physics of Fluids*. Please refer to the published article for additional information and future citations.

Chamorro, L. P., Hill, C., Neary, V. S., Gunawan, B., Arndt, R. E. A., and Sotiropoulos, F., (2015), Effects of energetic coherent motions on the power and wake of an axial-flow turbine, *Phys. Fluids*, 27, 055104, doi: 10.1063/1.4921264 (PDF).

Experimental Setup

The experiments were conducted in the SAFL main channel, a concrete channel supplied by Mississippi River water that is 85m long, 2.75m wide, and 1.8m deep. A model axial-flow 3-bladed hydrokinetic model turbine with rotor diameter $d_T = 0.5$m and hub height $h_{hub} = 0.425$m was mounted approximately 40m downstream from the channel inlet. The model turbine was operated at its optimal efficiency point, where the power coefficient, C_p, was approximately 0.45. The tip-speed ratio, λ, under this condition was 5.8, where $\lambda = \omega d_T / (2U_{hub})$, and ω is the angular velocity of the turbine in radians per second. More details on the turbine hardware, controls and instrumentation are found in [6]. The bulk flow velocity, $\overline{U}$, was regulated at 0.4ms^{-1}, which approximated the mean velocity at the turbine hub height (U_{hub}). The flow depth, h, was 1.15m at the turbine location, leading to a top-tip height submergence of $1d_T$. The details of the approach flow statistics for the same flow conditions are reported in [6].

Three cylinders of different sizes were placed upstream of the turbine in the central plane of the flume to introduce energetic periodic motions of frequencies within the responsive region of the turbine [6]. These structures shed vortices, known as von Kármán vortices, at frequencies given by the relationship [114]:

$$\frac{f_K d_c}{U} = S_t^* + \frac{m}{\sqrt{Re_{d_c}}}$$

where $f_K d_c/U$ is the Strouhal number, f_K is the von Kármán shedding frequency, U is the flow velocity, $Re_{d_c} = U d_c/\nu$ is the Reynolds number based on the cylinder diameter d_c, S_t^* and m are coefficients that depend on the Re_{d_c}. The cylinders considered have diameters $d_c =$ 0.055m, 0.115m and 0.325m (hereon referred to as a small, medium and large cylinder) and associated shedding frequencies $f_K \approx$ 1.44Hz, 0.69Hz and 0.24Hz. The small cylinder diameter was chosen to induce a shedding frequency similar to that of the frequency of the turbine ($f_T =$ 1.5Hz). Each cylinder was placed at three locations upstream of the turbine. The small and medium cylinders were placed at $x/d_c =$ -7.5, -10, and -15, while the large cylinder was located at $x/d_c =$ -3, -6, and -8. As indicated in Figure 1.4, the x-axis origin coincides with the plane of the turbine rotor, and positive direction points downstream. In addition to the three scenarios for each cylinder, a scenario with the turbine operating under undisturbed conditions is included as a base case.

An array of three acoustic Doppler velocimeters (ADVs) was used to obtain high-resolution and simultaneous measurements of the three-velocity components (streamwise u, cross-stream

v, and vertical w) of the flow. The ADVs were aligned in the cross-stream direction at a height coincident with the turbine hub. The central ADV was located on the rotor axis and the other two ADVs one half rotor diameter away from each side of the central one (see Figure 1.4). For each scenario, measurements were acquired every $1d_T$ downstream of the turbine from x/d_T = 1 to 10. Additionally, two profiles were collected upstream of the turbine at x/d_T = -1 and -2 (with the medium and large cylinders in the flume) and x/d_T = -0.5 and -1 (with the small cylinder). In all the cases, the three ADV velocity measurements were collected synchronously with the turbine torque at a rate of 200Hz for a sampling period ranging between ΔT = 300s to 600s.

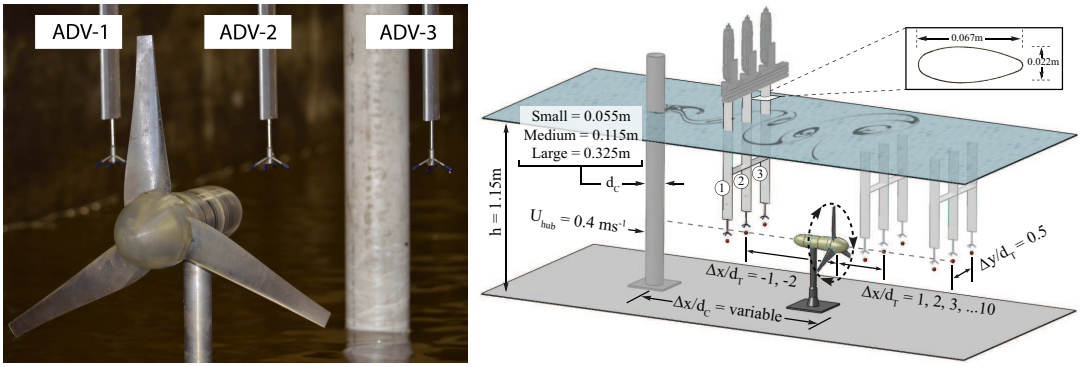

Figure 1.4: Left: photograph of the turbine and cylinder partially submerged with the ADV array; Right: experimental set-up of turbine, cylinder, ADV array and measurement location [1].

Results & Discussion

As shown by [6], the power generated by an axial-flow turbine responds to the flow turbulence in the low frequency range. Here, we look in detail at the turbine power response to various energetic and periodic flow motions induced by the vertical cylinders. The cylinder sizes were selected to address specific objectives. The large cylinder, with a diameter similar to the turbine rotor (d_c/d_T = 0.65, d_c/c = 7.43), produced a wake that affected the entire turbine rotor swept area and modified the turbulence characteristics of the approach flow in a broad range of scales. In contrast, the small cylinder introduced periodic energetic motions predominantly within a narrow frequency band into the approach flow. To investigate the effects of the coherent motions induced by the various cylinders on the turbine power fluctuations, Fourier analysis on the approach flow and turbine power was performed. Figure 1.5a illustrates the spectra of the streamwise velocity component of the approach flow at hub height and $1d_T$ upstream of the turbine, with and without the large cylinder placed six rotor diameters (x/d_c = -6) upstream

of the turbine. In this setup, the cylinder wake turbulence covered the turbine rotor area. As inferred from this figure, the cylinder modified the structure of the approach flow in a broad and well defined band of frequencies ranging from roughly 0.06Hz to 0.7Hz, which contains the von Kármán shedding frequency of the vortices generated by the cylinder ($f_K \approx 0.24$Hz). The corresponding spectra of the turbine power for these two scenarios (with and without cylinder) are depicted in Figure 1.5b. This illustrates the effect of the re-organized turbulence structure of the flow on the turbine power. The spectral distribution of the turbine power is modified essentially in the same frequency range where the cylinder altered the turbulent structure of the approach flow. It evidences the strong scale-to-scale interaction between the flow and the turbine. Similar phenomena are observed under other scenarios using the medium and large cylinders placed at other locations. This scale-to-scale character of the flow and turbine power interaction was also observed in the scenario with the small cylinder. This cylinder modified the spectral content of the approach flow locally and induced strong vortices shed at a frequency ($f_K \approx 1.44$Hz) similar to that of the turbine ($f_T \approx 1.5$Hz). In this case, the spectral structure of the turbine power was only locally affected around a frequency coincident with that of the vortex shedding from the small cylinder. Otherwise, the turbine power spectral characteristics were virtually unchanged through the entire frequency band. Despite the von Kármán frequency f_K and the turbine frequency f_T being very similar, distinctive peaks were observed, thereby stressing the scale-to-scale and localized character of the interaction.

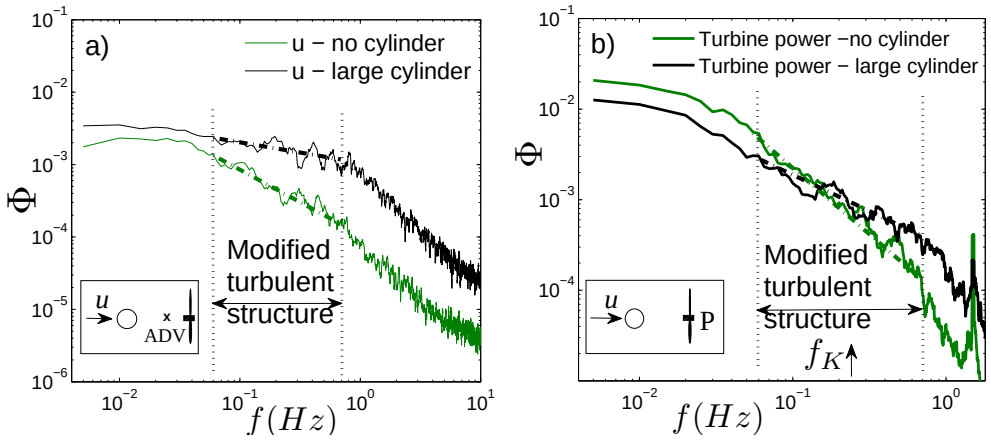

Figure 1.5: a) Spectra of the approach flow (u-velocity component) at hub height and $1d_T$ upstream of the turbine; b) Spectra of the turbine power. Large cylinder case (d_c/d_T = 0.65, x/d_c = -6). Dashed lines indicate the region where the structure of the power is affected [1].

The energetic and coherent motions induced by the cylinders can potentially trigger important changes in the characteristics of the turbine wake. The specific mechanisms involved in

this process can be controlled by the breakdown of the tip vortices (see [115] for details). The phenomenon is particularly relevant in the very near wake region ($x/d_T < 1$–2), where the tip vortices are the dominant structures of the flow. To quantify the effects induced by energetic motions on the tip vortices and mean wake statistics, the spectral structure and turbulence levels of the flow at the turbine lateral tips and at the central axis of the turbine (see Figure 1.4) were analyzed with and without the cylinders.

The spectral characteristics of the flow downstream of the turbine at the lateral tip show that the energetic motions induced by the cylinders in fact disrupt and dampen the tip vortices. An example of this phenomenon is illustrated in Figure 1.6a, which shows the spectra of the cross-stream velocity component at the lateral tip, one rotor diameter downstream of the turbine, with and without the medium cylinder placed at x/d_c = -7.5. The spectra are normalized by the cross-stream velocity variance to aid comparison. As observed from this figure, the tip vortices are the dominant flow structures in the wake when the cylinder is not present. The von Kármán vortices generated by the cylinder, which are still coherent at that location, completely disrupt and dampen the tip vortices. This suggests that the mechanism triggering the tip vortex breakdown is essentially the interaction between these two vortical and dominant flow structures, the von Kármán and tip vortices. Further analysis with the large cylinder placed at x/d_c = -3 and -8 also suggests that enhanced levels of turbulence does not necessarily induce the tip vortex breakdown. This notable phenomenon is quantified in Table 1 and illustrated in Fig. 1.6b. Table 1 shows the turbulence intensity of each velocity component ($I_{u_i} = \sigma_{u_i}/U_{hub}$, i = 1, 2, 3) at the same locations of Figure 1.6b for the cases with and without the large cylinder. The turbulence levels are the greatest with the cylinder located at x/d_c = -3. However this case did not substantially dampen the tip vortices, as depicted in Figure 1.6b. There, the tip vortices are not perceptible with the large cylinder located at x/d_c = -8, which has lower turbulence levels compared to those present with the cylinder located at x/d_c = -3. In Figure 1.6b, the tip vortices without the large cylinder (green plot) and with the cylinder at x/d_c = -3 (black plot) are evident in the spectral decomposition. In contrast, the tip vortices are absent from the case with the large cylinder at x/d_c = -8 (red plot). It is important to note that the von Kármán vortices at the lateral tips are the most energetic motions of the flow approaching the turbine in this scenario. This is illustrated in the sub-plot of Figure 1.6b with the cylinder located at x/d_c = -8 (red sub-plot). The energy of the von Kármán vortices with the cylinder located at x/d_c = -3 (black sub-plot) does not dominate above that present in the channel flow without the cylinder. This could explain why they are not able to disrupt tip vortex stability. The vortices shed from the cylinder at x/d_c = -3 may not reach the lateral tips due to its proximity to the turbine.

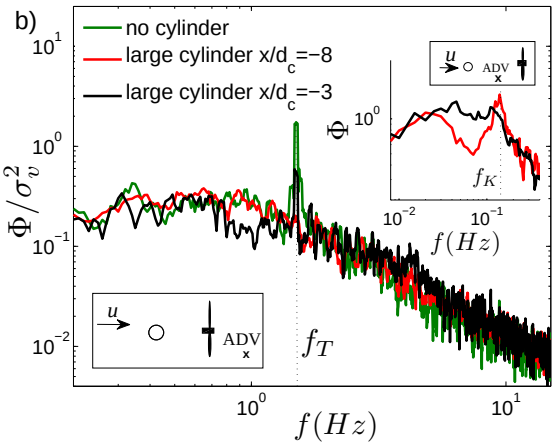

Figure 1.6: Spectra of the v-velocity at the lateral tip (ADV1 of Figure 1.4) $1d_T$ downstream of the turbine with the large cylinder installed (d_c = 0.325m, x/d_c = -3 and -8) [1].

Turbulence Intensity	**No Cylinder**	x/d_c = **-3**	x/d_c = **-8**
I_u	0.16	0.26	0.20
I_v	0.15	0.21	0.19
I_w	0.11	0.13	0.13

Table 1.1: Three components of turbulence intensity I_{u_i} ($= \sigma_{u_i}/U_{hub}$) of the wake flow at the turbine lateral tip, one rotor diameter downstream of the turbine, with and without the large cylinder placed at x/d_c = -3 and -8 [1].

Additional insights about the effect of strong coherent motions on the vortex dynamics can be obtained from the spectral coherence between two quantities. The magnitude squared coherence, C_{xy}, is a real-valued function defined as:

$$C_{xy} = \frac{|\Phi_{xy}(f)|^2}{\Phi_{xx}(f)\,\Phi_{yy}(f)}$$

where $\Phi_{xy}(f)$ denotes the cross-spectral density between the quantities x and y; $\Phi_{xx}(f)$ and $\Phi_{yy}(f)$ are the spectral densities of x and y, respectively.

The coherence between the turbine power and the tip vortices is affected by the presence of a cylinder at the frequency coincident with that of the turbine frequency (f_T = 1.5Hz). Figure 1.7a shows the spectral coherence between the turbine power and streamwise velocity component at the lateral tip, $1d_T$ downstream of the turbine under 3 different flow conditions: the base case (no cylinder) and two perturbed flows using the medium and large cylinders. With no cylinders

present, high spectral coherence is observed at a frequency coincident with that of the turbine, giving distinct evidence of strong tip vortices. This coherence is substantially reduced when the cylinders are placed in the flow. In this case, the cylinders have a direct impact on the coherence between the turbine power and flow. Furthermore, the spectral coherence at both lateral tips at $1d_T$ downstream of the turbine is depicted in Figure 1.7b). The high coherence at a frequency coincident with the turbine frequency is an indication of the continuous and helical character of the tip vortices; their 3D structure, however, is completely dampened with the presence of a cylinder.

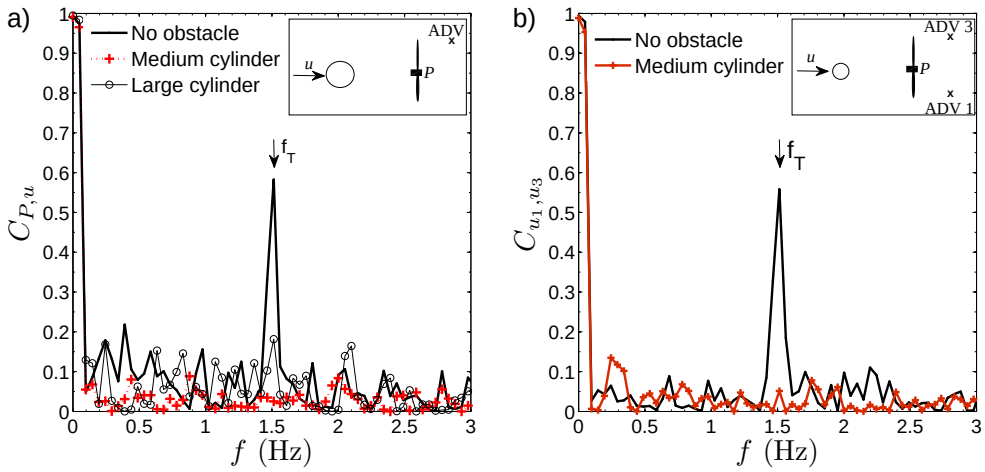

Figure 1.7: a) Spectral coherence between the turbine power and the streamwise velocity component measured at the lateral tip, $1d_T$ downstream of the turbine. Large cylinder: d_c = 0.325m, x/d_c = -3; medium cylinder: d_c = 0.115m, x/d_c = -10. b) Spectral coherence between the streamwise velocity component at both lateral tips. Flow velocities are measured at $1d_T$ downstream of the turbine [1].

The mean statistics and dynamics of the turbine wake are sensitive to, and modulated by, the tip vortices. One direct consequence of the breakdown of tip vortices is an accelerated wake recovery in the near-wake region of the turbine ($x/d_T < 5$). The mean velocity, or the velocity deficit, with respect to the undisturbed conditions along the rotor axis is a classic measure for describing the wake evolution or flow recovery in the wake. The mean velocity deficit, $\Delta U_x = U_{hub} - U\,(x, y = 0, z = 0)$ at the rotor axis, normalized by that of the approach flow U_{hub}, is shown in Figure 1.8. The figure reveals that the recovery of the mean velocity is accelerated with the cylinders. The scenario with the medium cylinder shows a wake with accelerated velocity recovery within roughly the first eight rotor diameters, with the greatest

changes occurring between three and five rotor diameters. The wake also shows an accelerated recovery with the cylinder closer to the turbine. These changes could be modulated mostly by the breakdown of tip vortices. Overall, these results provide empirical and quantitative evidence of the active role of the tip vortices in modulating the wake dynamics of axial-flow turbines.

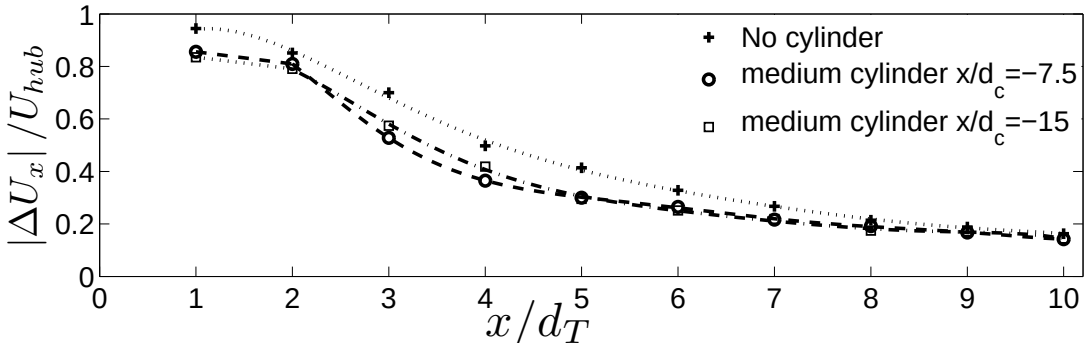

Figure 1.8: Mean velocity deficit at hub height with and without the medium cylinder [1].

Applications for Turbine-Topography interactions

The results of this preliminary study into the impact of energetic coherent turbulent motions on the power and wake characteristics of an axial-flow hydrokinetic turbine provided the groundwork for moving forward in studying the interactions between complex channel topography and MHK devices. As summarized in [95, 97], the turbulent flow field above bedforms will create time-varying zones of turbulent flow and a range of scales of turbulent structures. When mounted with the turbulent boundary layer and near the channel boundary, MHK devices will undoubtedly be impacted by these bedform-induced coherent structures. By developing an understanding of turbine-sediment interactions, this research program will provide details on how MHK devices will modify near and far-field sediment transport, impact the biological communities that rely on the upper layers of the sediment, provide guidelines for designing scour resistant foundations, and inform device developers on performance response to large-scale stationary and mobile bathymetric features, thereby providing a foundation for future development of advanced control strategies capable of maintaining peak operational conditions and minimize structural fatigue.

Chapter 2

Local scour near an axial-flow hydrokinetic turbine

The following chapter has been published in its current form in the *Journal of Hydraulic Engineering*. Please refer to the published article for future citations.

Hill, C., Musa, M., Chamorro, L. P., Ellis, C., and Guala, M., (2014), Local scour around a model hydrokinetic turbine in an erodible channel, *J. Hydraul. Eng.*, 140(8):04014037 (PDF).

2.1 Introduction

With increasing license requests for the deployment of marine hydrokinetic (MHK) devices in natural rivers, tidal and estuarine environments, it is impelling to assess the long term ecological and morphodynamic equilibrium of those ecosystems and their resilience under such anthropogenic perturbations [19]. Assessment of turbine interaction with the local sediment environment has been identified as a key environmental issue needing investigation for MHK device design and development [17]. In particular for erodible channel environments, the interaction between an MHK device and the evolution of the bed topography must be monitored in order to avoid both the structural failure of the device support structure and/or the propagation of amplified scour or deposition features within the channel. Since axial-flow MHK turbines have been observed to alter the flow field for more than 15 rotor diameters (d_T) downstream of the device [6, 116], the evolution of the induced scour and/or deposition has to be quantified both in the near and far wake regions.

As MHK projects advance toward multi-turbine deployments in environments with mobile

sediment beds, interactions with actively transporting substrates needs to be understood. For example, future installations along major US river systems, such as the Lower Mississippi River, may encounter actively migrating dunes with amplitudes greater than 1m in height [4]. In such regions, sediment transport will continually reshape the river bottom geometry, thereby adding complexity and currently unknown interactions for MHK device development and installations. Full-scale multi-unit deployments may have an overall effect that is different than a simple accumulation of effects typical for a single unit, both in terms of local sediment transport as well as channel-scale morphodynamic behavior. For this reason, benchmark experiments are needed to address the mechanisms of interaction between a turbine and the resulting near-field and far-field morphological changes.

To date, few experiments and simulations have investigated turbine effects on sediment erosion and deposition in the near and far wake environments. [43] and [44] used large grid-cell (km-scale) simulations to estimate the impact of an MHK array on the headland sand banks off the Northern coast of France. The study investigated a tidal channel many kilometers long, therefore lacking the resolution to simulate both the near-field and far-field effects. Previously, experiments and numerical studies have focused mainly on characterizing the wake structure and turbulence [22, 26, 25, 24, 116], power production capabilities of these devices [34, 32], and turbine response to turbulent flow conditions [6]. The experiments presented here provide benchmark data to quantify interactions between hydrokinetic turbines, an open channel flow and the erodible sediment layer. First studied, under clear water and live bed conditions, was the local scour associated with individual static turbine components, such as the tower and nacelle, and compared to bridge pier scour results (for example, [117, 118, 119]). Second, a three bladed axial flow rotor was used to quantify the deformation on bed topography induced by a fully operational model turbine.

A series of laboratory experiments at two scales under both clear water and live bed sediment transport were performed at the St. Anthony Falls Laboratory (SAFL) at the University of Minnesota. The turbine model used during these experiments was a three bladed axial flow turbine with rotor diameter $d_T = 0.15$m and 0.5m for the small-scale and large-scale experiments, respectively. Clear water scour experiments were performed at both scales, while live bed sediment transport conditions with relatively large bedforms were only investigated at the small scale. Time-resolved measurements of bed topography were obtained non-intrusively using SAFL data acquisition carriages, providing $z = z(x, y, t)$. During small-scale experiments, repeated scans along selected longitudinal and cross-stream transects were obtained. During large-scale experiments, a novel optical scanning device developed at SAFL was used. A detailed description of the experimental setup for both small-scale and large-scale experiments is

presented below. Following discussion of the experimental setup, results and discussion highlight the spatial and temporal evolution of localized scour under both clear water and live bed conditions at two scales.

2.2 Experimental Setup

2.2.1 Clear Water Experiments

Two sets of experiments were completed under clear water conditions (i.e. local bed shear stress below the critical value). Large-scale and small-scale experiments were completed in the main channel and tilting bed flume, respectively, at SAFL. Experimental conditions are summarized in Table 2.1. The flow depth, h, was set to provide Froude similarity between small-scale, large-scale, and field-scale, as well as ensure approach section bed shear stress at the sediment surface was below the critical entrainment value ($u_* < u_{cr*} = 0.034\text{ms}^{-1}$ for $d_{50} = 1.8$mm sand, based on Shields curve and the sediment critical mobility parameter [120]. Both scales of experiments included a series of test cases to investigate the effects of individual turbine components on channel topography.

Large-Scale Experiments

Experiments were conducted in the SAFL main channel (2.75m wide, 1.8m deep, and 85m long). The test section consisted of approximately 6m of nearly uniform sediment material ($d_{50} = 1.8$mm) distributed and flattened to match the SAFL main channel slope of approximately 0.17% before the start of each test case. A three-bladed axial-flow turbine model with rotor diameter, $d_T = 0.5$m, was anchored to the concrete bed approximately 0.25m below the sediment surface and $4d_T$ downstream from the beginning of the erodible layer. The base of the turbine tower is of conical shape 0.15m tall extending from a diameter of 0.1m to 0.43m at the interface between the sediment layer and the concrete channel bottom. Additional details of the model turbine, including fabrication, materials, instrumentation, control methods, performance and flow field interactions can be found in [6]. Figures 2.1 and 2.2 show a schematic and photo of the test section, turbine and instrumentation used during experiments. Four test cases were investigated: Case I: no structure; Case II: turbine support tower only; Case III: support tower and nacelle; and Case IV: fully operational turbine with spinning rotor.

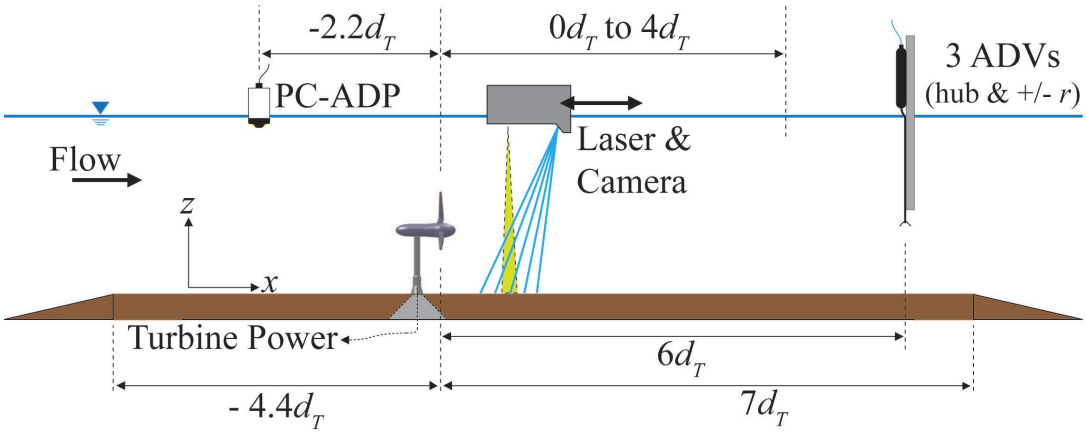

Figure 2.1: Schematic of large-scale experiment setup and instrumentation. Turbine rotor diameter $d_T = 0.5$m. Base support platform is a concrete cone 0.15m tall with upper and lower diameters of 0.1m and 0.43m, respectively.

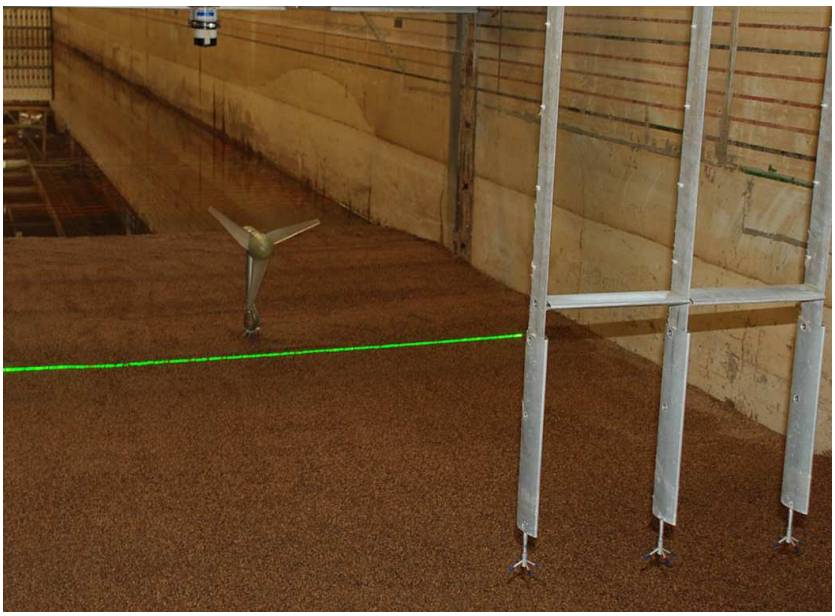

Figure 2.2: Photo of 1:10 model and instrumentation.

Spatial-temporal measurements of bed elevation, $z = z(x, y, t)$, were obtained using a computer automated data acquisition (DAQ) carriage designed at SAFL consisting of a high-speed camera and continuous laser sheet projected onto the surface of the sediment. The imaging components were assembled in a waterproof enclosure and submerged slightly below the water

surface while the carriage accurately and repeatedly traversed the test section in the longitudinal (streamwise) direction. The calibrated high-speed camera captured images when triggered by the DAQ carriage positioning encoder, mapped the location of the projected laser line, and recorded bed elevations to the corresponding horizontal coordinates on a 0.002m x 0.002m grid across the test section. Scans repeated continuously from $x = 0d_T$ to $4d_T$ during each test case every 73s, providing high-resolution spatial and temporal measurements within a domain approximately $1.5d_T$ wide by $4d_T$ long. The relatively slow sediment transport processes allowed reconstruction of the full spatial-temporal structure of the bed topography throughout the course of each test case. Additionally, at the end of each experiment, the channel was drained and a sub-aerial topography scan from approximately x = -$1.5d_T$ to $4d_T$ and y = -$1.5d_T$ to $1.5d_T$ was recorded. Net erosion and deposition was mapped by differencing before and after topographic scans. Test section mean inflow velocities were characterized using a Sontek PC-ADP located approximately $2d_T$ upstream of the turbine location. Test section outlet flow velocities were monitored using three synchronized Nortek Vectrino velocimeters located $6d_T$ downstream of the turbine at hub height and at cross-stream locations y = -$d_T/2$, 0, $d_T/2$, corresponding to the left tip, center hub and right tip of the turbine. These 200Hz measurements provided a method of tracking changes in mean and turbulent inflow conditions for possible additional downstream turbines as bed morphology changed during the course of each test case. Average flow rate during all large-scale test cases was kept constant at $Q_w = 1.765\text{m}^3\text{s}^{-1}$. Instantaneous discharge measurements were recorded at 1Hz using a Massa M5000 ultrasonic sensor and end weir elevation to measure depth of flow passing over the calibrated sharp-crested weir at the outlet of the channel. Channel flow depth was also controlled by the weir, while the discharge was controlled by an intake gate upstream of the channel and flow straightening grid.

Small-Scale Experiments

Experiments were conducted in the tilting bed flume (15m long and 0.9m wide) with the turbine model positioned 6m downstream of the channel inlet ($x = 0$m). Incoming flow was conditioned using an aluminum honeycomb grid and a matrix of 27 closely spaced vertical cylinders to break turbulent structures created from the pump and supply pipes, thereby providing uniform flow before entering the test section. The turbine position and test section were selected to be within a domain where the flow and the underlying bed topography were sufficiently far from inlet and outlet boundary conditions, thus ranging between 4m and 13m.

The small-scale model turbine with rotor diameter, $d_T = 0.15$m, was outfitted with a miniature DC motor for instantaneous voltage measurements. Three copper coils within the motor enabled calculation of the turbine rotational frequency and tip speed ratio, λ, from the voltage timeseries data [81]. No additional loading of the motor was used, and the internal frictional

torque of the device allowed for reasonable tip-speed ratios. The turbine base, support tower and nacelle were made from aluminum, while the turbine rotor was fabricated via rapid prototyping using a resin material (Figure 2.3). The diameters of the cylindrical turbine base and support tower were 0.02m and 0.01m, respectively. Three cases were investigated: a) turbine support tower only; b) fully operational turbine with the rotor on the downstream side of the support tower (consistent with the large-scale clear water experiments); and c) fully operational turbine with the rotor on the upstream side of the rotor.

Figure 2.3: Photograph of the 1:33 model hydrokinetic turbine used during the small-scale clear water and live bed experiments, shown here with the ADV and sonar device. Flow is left to right.

A Nortek Vectrino velocimeter was positioned 1m (approximately $7d_T$) upstream of the turbine to monitor inflow conditions. Velocity measurements were recorded at 200Hz at turbine hub height. The shear velocity, u_*, was estimated and confirmed by three independent methods: a) $u_* = \sqrt{gRS_w}$ using Massa M5000 ultrasonic sensor measurements of the free surface slope, S_w, and the calculated hydraulic radius, R, b) $u_* = \sqrt{-\left(u'w'\right)_{max}}$ using fluctuating velocity measurements along a vertical profile 1m upstream of the test section, and c) by fitting the mean velocity profile with the log-law formulation.

Spatial and temporal measurements of bed and water surface elevations were made using an Olympus Panametrics C305-SU immersible transducer and Massa M5000 ultrasonic range sensor, respectively. These instruments were controlled and positioned using an automated data acquisition carriage capable of traversing the entire length of the flume while simultaneously

positioning and acquiring data from multiple instruments and ensuring accurate and precise synchronization of measurement spatial coordinate locations. During each experiment, bed and water surface elevation data were collected along a single streamwise transect and a cross-stream section location immediately downstream of the turbine location. Measurements were recorded at 0.005m increments along the length of each transect. Measurements were repeated continuously for the duration of the experiment, providing a full record of bed and water surface evolution.

2.2.2 Live Bed Experiments

Small-Scale Experiments

Investigations into the effect migrating bedforms have on turbine performance and the corresponding effects that rotating turbines have on local and far-field sediment transport characteristics were completed at small-scales in the tilting bed flume at SAFL. A similar setup was used as in the clear water experiments, however, boundary conditions were changed slightly to provide actively transporting bedforms along the entire flume length (Table 2.1). A sediment recirculation system enabled continuous feed and propagation of dunes. The focus of these experiments was to investigate extreme scenarios when bedform dimensions do not necessarily scale appropriately with respect to the turbine rotor diameter. Experiments examined the local scour and bedform characteristics between a) baseline transport conditions with no turbine installed and b) a single turbine positioned in the center of the channel (Figure 2.3). The turbine location was moved downstream to 8m from the inlet to allow for adequate distance for bedform development before the test section.

Similar to the clear water experiments, reference inflow velocity measurements were collected at hub height approximately 1–2m upstream of the turbine location using a Nortek Vectrino velocimeter (ADV) sampling at 200Hz for the duration of the experiment. Bed elevation measurements were collected along three longitudinal transects and along at least one section perpendicular to flow using the same sonar measuring device previously discussed in the small-scale clear water experiment section. Spatial resolution was decreased such that bed and water surface elevation measurements were recorded every 0.010m along each transect, thereby reducing the time between repeated measurements at each position. Spatial and temporal elevation measurements allow for continuous monitoring of bedform development, migration characteristics, and both local and far-field turbine interactions with passing bedforms.

Variable	Clear Water *Large scale*	Clear Water *Small scale*	Live Bed *Small scale*
Turbine Parameters			
d_T	0.5m	0.15m	0.15m
h_{hub}/d_T	0.85	0.86	0.88 (average)
S	$0.95d_T$	$0.5d_T$	$0.5d_T$
λ	7.1	6.3	6.5
σ	12.9%	8.1%	8.1%
η	6.2%	6.8%	6.8%
Flow, Channel and Sediment parameters			
h	1.15m	0.28m	0.27m
Q_w	$1.765\text{m}^3\text{s}^{-1}$	$0.114\text{m}^3\text{s}^{-1}$	$0.130\text{m}^3\text{s}^{-1}$
S_w	$^{\#}1.2\text{x}10^{-4}$	$5.0\text{x}10^{-4}$	$3.0\text{x}10^{-3}$
b	2.75m	0.9m	0.9m
Fr	0.20	0.27	0.33
Re_b	$6.44\text{x}10^5$	$1.26\text{x}10^5$	$1.43\text{x}10^5$
Re_T	$3.30\text{x}10^5$	$6.75\text{x}10^4$	$7.95\text{x}10^4$
U_{hub}	0.66ms^{-1}	0.45ms^{-1}	0.53ms^{-1}
U_∞	0.56ms^{-1}	0.45ms^{-1}	0.53ms^{-1}
u_*	$^{\#}0.027\text{ms}^{-1}$	0.020ms^{-1}	0.070ms^{-1}
u_{cr*}	0.034ms^{-1}	0.034ms^{-1}	0.034ms^{-1}
d_{50}	1.8mm	1.8mm	1.8mm

Table 2.1: Turbine, flow, channel, and sediment parameters used during the small-scale and large-scale experiments. Note: (#) indicates slope and corresponding shear velocity used from previous experiments with equivalent depth, but $Fr = 0.12$ and $Re_b = 4.7\text{x}10^5$ ($Re_T = 2.0\text{x}10^5$).

2.3 Results

2.3.1 Clear Water Experiments

Spatial Evolution

The final bed topography from the large-scale experiments is shown in Figure 2.4(a–c) for the cases investigating the effects of various turbine components on near-field sediment stability characteristics. Baseline conditions (no turbine components) are compared to three additional

cases (support tower only, tower and nacelle, and fully operational turbine, respectively). Each axis has been normalized by the turbine rotor diameter. For each case, the initial flat topographic surface has been subtracted from the final bed topography and normalized by the turbine rotor diameter, enabling visualization of regions where erosion (negative values) and deposition (positive values) have occurred.

During baseline condition, no sediment transport occurred, confirming that the local shear stress, τ_b, is below the critical (Shields) value for the given grain size, $\tau_{cr} = 1.15$Pa. Additionally, the scour locally induced by the support tower (Figure 2.4a) is quantitatively similar to the scour produced by the combined support tower and nacelle (Figure 2.4b), yet both are sensibly smaller than the scour induced by the fully operational turbine (Figure 2.4c). This suggests that the typical mechanisms governing bridge pier scour have a minimal effect on the bed configuration downstream of the turbine under the investigated conditions. Instead, the obstruction induced by the spinning rotor and the resulting acceleration of the flow between the bottom rotor tip and the erodible bed surface dominates the changes evident during clear water conditions. During each case, no sediment motion was observed upstream of the tower and turbine location, confirming clear-water scour conditions and local scour and deposition induced by the hydrokinetic turbine. Sediment eroded from the scour region was deposited in a symmetric, chevron shaped dune ranging from $2d_T$ to approximately $6d_T$ (beyond scanned domain). Maximum scour depths approached approximately 30–35% of the rotor diameter, d_T, or 13–15% of the flow depth, h. In most cases presented herein, the resulting scour and deposition has been normalized by the turbine rotor diameter; however, the flow depth, h, can also be considered as a potential normalization factor.

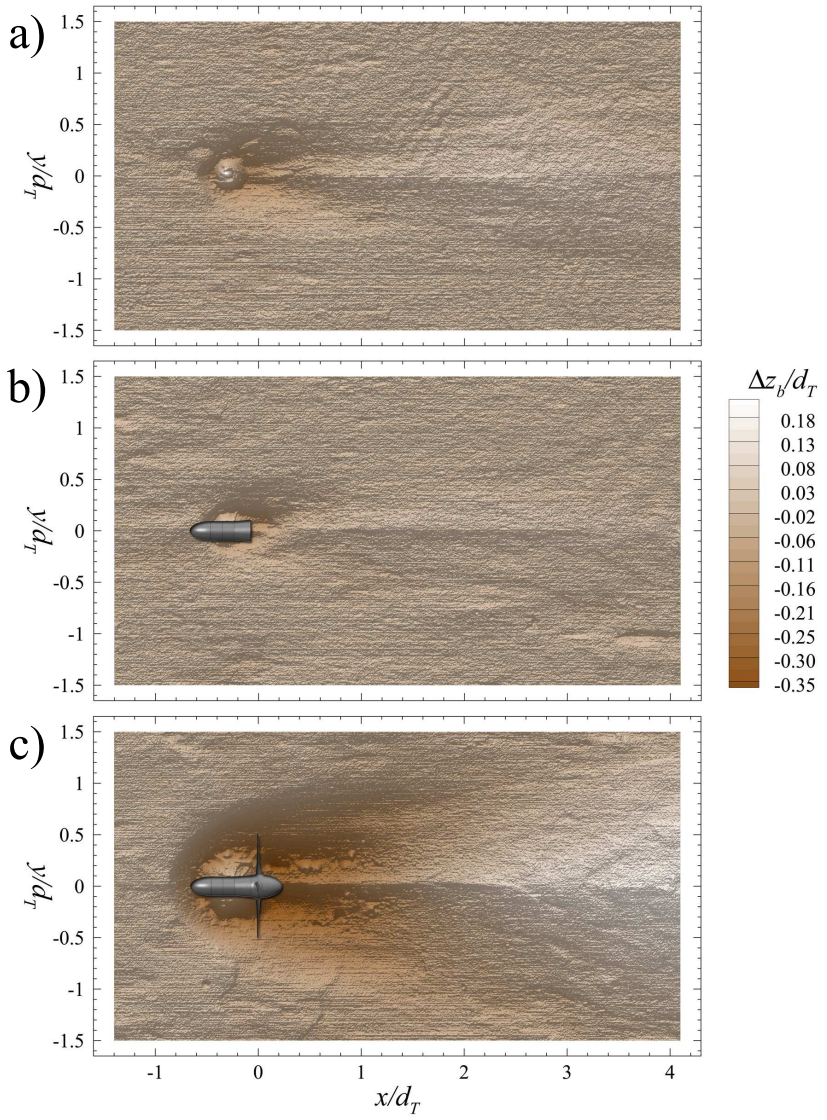

Figure 2.4: End topography from large-scale clear water experiments with the a) turbine support tower only, b) nacelle and support tower, and c) fully operational turbine. Flow is left to right.

Results from the corresponding experiments completed at small scales are qualitatively similar to those performed at large-scales (Figure 2.5a–c). In all cases, upstream of the turbine or support tower location, no transport of sediment is observed indicating conditions were properly set to maintain sub-critical bed shear stress ($\tau_b < \tau_{cr}$) providing clear water transport conditions. Minimal scour is observed when only the turbine support tower is present (Figure 2.5a).

However, with the addition of a fully operational turbine, increased local scour and formation of a downstream migrating depositional feature is observed. In the case with the turbine rotor positioned upstream of the support tower (Figure 2.5c), maximum scour reached depths of approximately 15% of the rotor diameter (8% of flow depth), while the peak of the depositional wedge reached elevations of approximately 10% of the rotor diameter (5% of flow depth). In the case of the downstream rotor, maximum scour reached depths of approximately 13% of the rotor diameter (7% of flow depth) (Figure 2.5b).

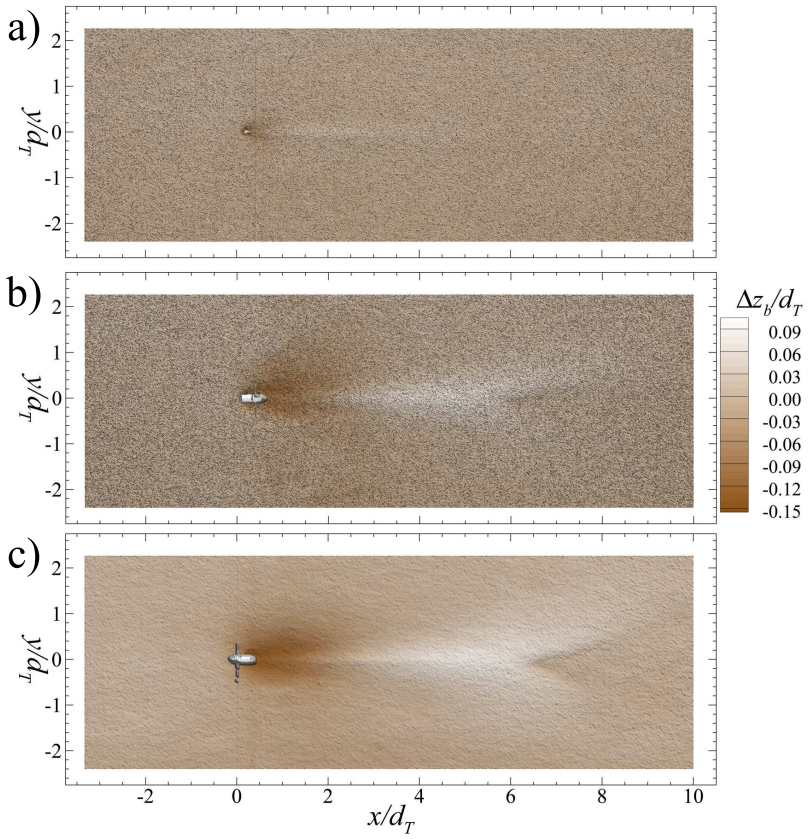

Figure 2.5: End topography from small-scale clear water experiments with the a) turbine support tower only, b) rotor on downstream side of tower, and c) rotor on upstream side of tower. Flow is left to right.

A closer look at the geometry of the scour and depositional patterns between the small-scale and large-scale single turbine clear water experiments reveals several differences (Figure 2.6). First, when normalizing all three axes by the respective turbine rotor diameter, the horizontal

expanse of the scour is larger in the large-scale experiments. We infer that the different shapes of the turbine base (within the sediment layer) could be playing a role: the conical base of the large-scale model reduces the availability of sediment in the proximity of the support tower and provides a rigid surface for flow acceleration near the sediment, thereby enhancing vertical erosion and enforcing stronger spanwise erosion. Additionally, when the rotor was on the upstream side of the turbine support tower in the small-scale experiments, a slightly larger region was eroded. Finally, the transition from the net erosion region into the net depositional region is more gradual during the small-scale experiments compared to the large-scale experiment. A closer examination into the evolution of scour reveals that there may be different mechanisms influencing scour whether the turbine rotor is positioned on the upstream versus the downstream side of the vertical support tower. The difference in scour depths and horizontal extent could result from the location of flow contraction due to the presence of the rotor. With the rotor on the upstream side of the tower, the flow converges between the bottom tip and the erodible bed upstream of the support tower. This acceleration increases the local shear stress, and when combined with typical bridge scour phenomena, may act to amplify scouring mechanisms. However, with the rotor on the downstream side of the tower, flow acceleration and convergence presumably occur later, potentially after the location of the vertical support tower. The depth of scour increased more quickly in the case with the rotor on the upstream side of the tower, and yet, both cases reached a quasi-equilibrium scour depth after approximately 2–2.5hrs of run time (Figure 2.7).

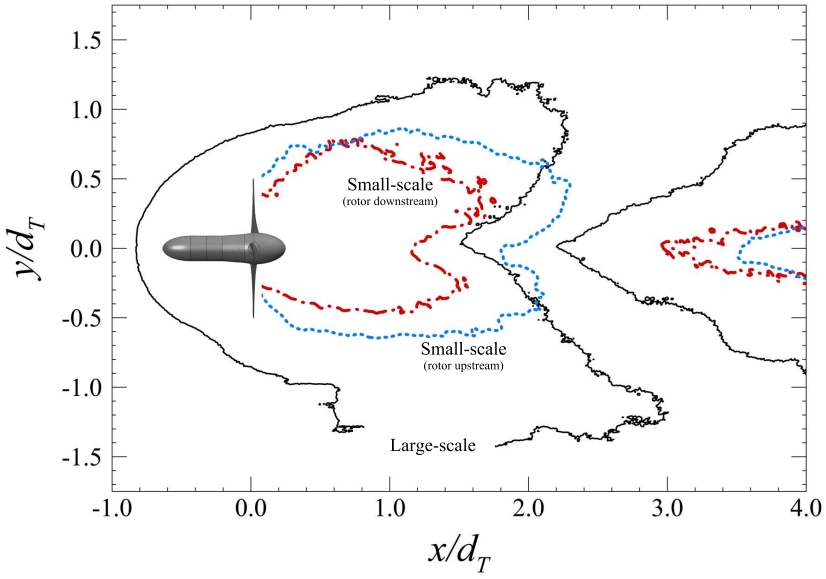

Figure 2.6: Contour lines showing region of scour (enclosed boundaries nearest turbine to the left) and deposition (lines to the right side of image) for three cases: large-scale experiments (solid line), small-scale downstream rotor (dash-dot line), and small-scale upstream rotor (dashed line). Scour contour lines show extent of 5% d_T scour depth, while deposition contour lines show extent of 5% d_T deposition height.

In general, results confirm that, despite the limited solidity, σ, of the rotor, the scour remains dominated by the flow acceleration and the local augmentation of shear stress in the proximity of the turbine. It is worth noting that the horizontal spatial extent of the scour and deposition seems to scale well with the rotor diameter. Conversely, the maximum scour still exhibits appreciable differences when scaled with the turbine rotor diameter, d_T, stressing that the excess shear stress induced by the rotor does not only depend on the geometrical properties of the turbine rotor (i.e. solidity, diameter, etc.), but also on device performance (tip speed ratio, $\lambda = \omega r/U_{hub}$), on sediment characteristics of the bed (i.e. grain size, distribution sorting, etc.) and likely on the vertical location of the rotor within the flow depth. Additionally, the transition point between net erosion and net deposition (see Figure 2.6) may indicate a relationship between the wake of the turbine and the sediment surface. Coincidentally, this is the region noted by [6] where the most rapid velocity deficit recovery begins, the turbine wake coherence begins to break down and wake meandering begins.

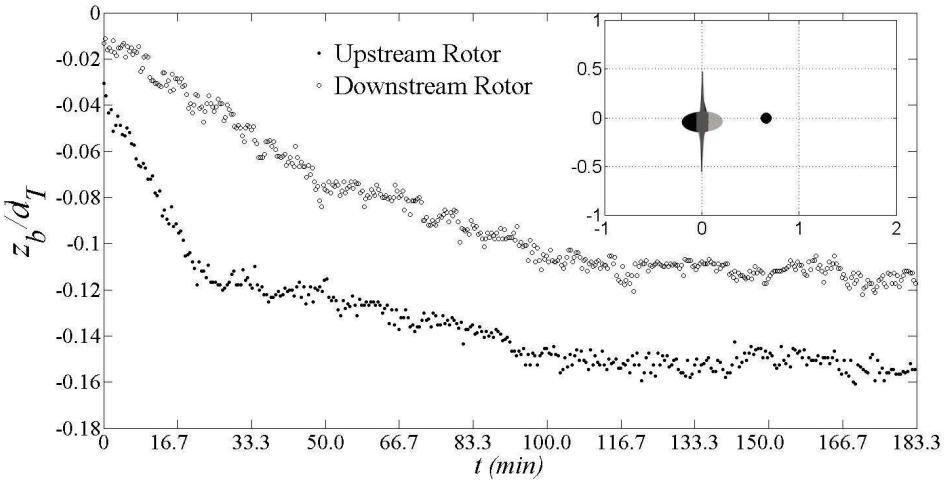

Figure 2.7: Evolution of scour in time comparison between rotor position on upstream (filled circles) versus downstream (open circles) side of the support tower from the small-scale clear water experiments. Inset axes show location with respect to turbine rotor from which data were taken.

Temporal Evolution

The subaqueous imaging system utilized during the large-scale clear water experiments enabled the mapping of the three-dimensional (3D) spatial and temporal evolution of scour and deposition downstream of the turbine. Because the time-scale of the sediment transport characteristics was much longer than the individual scan passes, renderings of each scan act as a snapshot, as illustrated in Figure 2.8 (a–c) at 30, 60, and 90 minutes. Similar renderings exist for the duration of the experiment at intervals of approximately 73s. Looking closely at the temporal evolution of scour at various lateral positions directly downstream of the turbine, it can be seen that the large-scale experiments did not reach equilibrium scour depths over the duration of the experiment (Figure 2.9). Additionally, maximum scour occurs at approximately $y/d_T = \pm 0.2$.

In the small-scale clear water experiments, near-equilibrium conditions were reached after approximately 2.5hrs, as evidenced previously in Figure 2.7. Here, it is evident that the majority of the scour occurs in the first 30 minutes. It is speculated that as sediments are eroded in the rotor cross-section vicinity, the effective blockage ratio, $\eta = A_r/A$, of the turbine rotor progressively decreases. This increase in the local cross-sectional area and widening of the gap between the rotor bottom tip elevation and the sediment surface has a two-fold effect: a) the constricted region between the rotor and sediment surface is widened thereby decreasing the local acceleration and local shear stress initially responsible for erosion in the near-field region, and

b) the increase in local flow cross-sectional area effectively reduces the incoming flow velocity, thereby presumably decreasing the available power for the turbine. As the turbine blockage ratio, η, decreases, the latter effect becomes negligible.

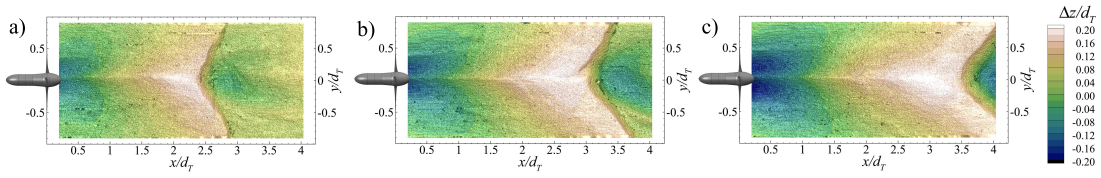

Figure 2.8: Laser and camera topography renderings from large-scale experiment bed topography corresponding to time $t = 30$ minutes (a), 60 minutes (b), and 90 minutes (c). Time span between successive scans is approximately 73 seconds (sub-Figures a–c show scan passes 25, 50, and 75, respectively).

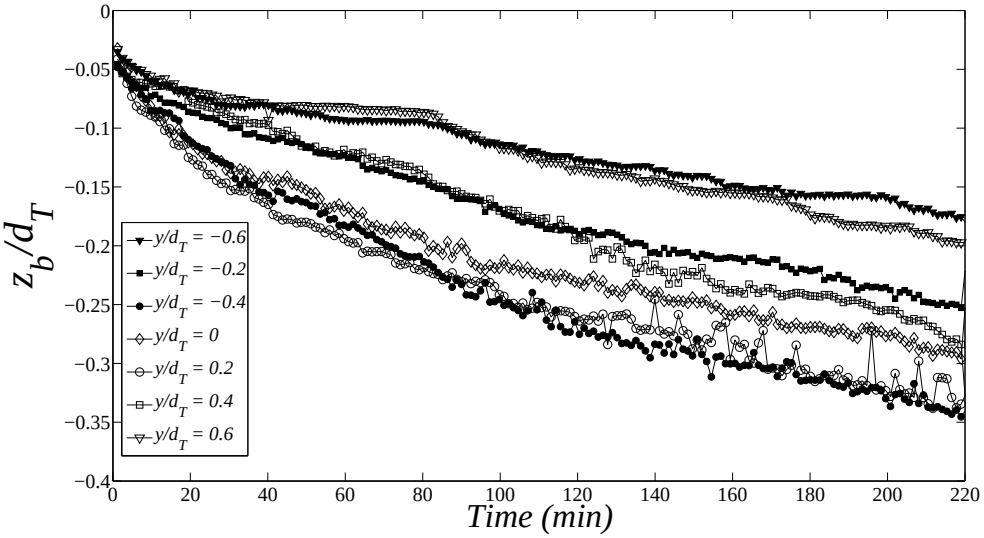

Figure 2.9: Evolution of scour formation in time from the large-scale clear water experiment, shown for various lateral positions normalized by the turbine rotor diameter. Maximum scour depths occurred at $y/d_T = \pm 0.2$. Open symbols are from the positive (river right) side of the nacelle. Filled symbols are from the negative (river left) side of the nacelle. Similar symbol shapes indicate equivalent distances on either side of the turbine nacelle.

A comparison between the small-scale and large-scale temporal evolution of the scour at equivalent distances downstream of the rotor plane ($x/d_T = 0.66$) is considered in Figure 2.10.

Here, the time has been normalized using the corresponding hub height velocity, U_{hub}, and rotor diameter, d_T. Again, it is evident that the large-scale experiment did not approach equilibrium scour depths as in the small-scale experiments with the rotor positioned either on the upstream or downstream side of the support tower. The amplified scour that occurred during the large-scale experiments is possibly a result of the difference in base geometry used between the small-scale and large-scale experiments. The conical base used in the large-scale experiments may have locally affected the scouring capacity as discussed in the comparison of the spatial topographic evolution. Temporal similarities between the two scales of experiments are evident through maximum depositional wedge crest elevation tracking, x_p/d_T (Figure 2.11). Here, the downstream location of the maximum dune elevation during single turbine clear water experiments at both scales is tracked through time. Similarly, the data have been normalized using the turbine rotor diameter and the corresponding hub height velocity. The streamwise evolution of the resulting depositional feature scales well between experiments; however, the temporal scaling of vertical scour led to inconclusive results (Figure 2.10). Here, the flow time scale, d_T/U_{hub}, does not appear to be the appropriate factor to use for normalizing the temporal evolution of the scour or depositional peak (not shown). The Exner equation [121] provides an alternative method of developing temporal relations for bed elevation evolution (scour and/or deposition); however, this time-scale normalization factor, hb^2/q_s, requires an influx of sediment, q_s, to determine the time rate-of-change for the bed elevation [122]. In clear water conditions, there is no influx of sediment, making this method difficult to apply. Both Shields parameter similarity and Froude similarity were considered for temporal scaling as well. At both scales, experiments used similar grain sizes and were in clear water conditions (i.e. similar u_*), therefore Shields parameter similarity scaling did not provide additional insights. Froude number time scaling used the length scale ratio, yet presented a time-scale ratio representative of a flow scale process, not a sediment transport process.

[123] and [124] proposed a method for predicting the temporal evolution of scour around bridge piers and abutments in clear water conditions incorporating both hydraulic and sediment characteristics in developing a reference time scale. [125] expanded on that work by providing a more generalized approach for scour in clear water conditions. In these previous cases, the limitations to the scour estimation techniques were clearly outlined, and to no surprise, unsuccessful attempts were made to incorporate this method into hydrokinetic turbine induced scour, reiterating that there are indeed more complex processes occurring when a rotor is present. These results indicate the need for further investigation into the temporal evolution and normalization of the scouring and depositional processes associated with a fully operational turbine in erodible substrates.

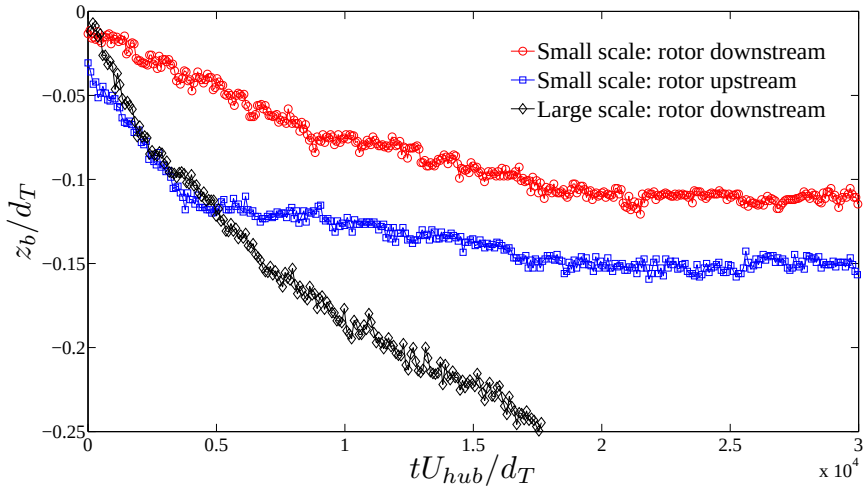

Figure 2.10: Normalized temporal evolution of the scour hole downstream of the small-scale and large-scale turbines. Data taken from $x/d_T = 0.66$ and $y/d_T = 0$ for all cases.

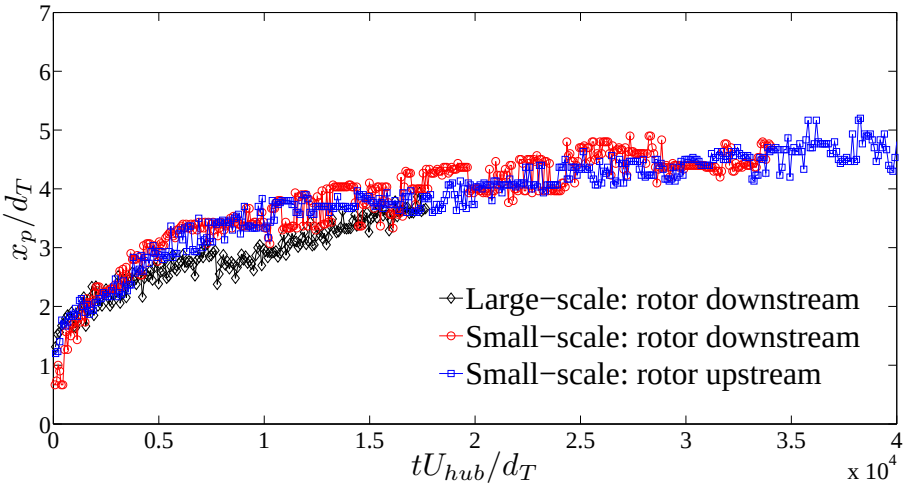

Figure 2.11: Normalized temporal evolution of the downstream distance, x_p/d_T, to the location of the peak of deposition, z_p, during the small-scale (circles: downstream rotor; squares: upstream rotor) and large-scale (diamonds) clear water experiments.

Comparison with Bridge Scour

To demonstrate that the presence of a fully operational rotor modified local scour and deposition characteristics, a test case using only the turbine support tower was performed at both small-scale (Figure 2.5a) and large-scale (Figure 2.4a), providing results analogous to a submerged bridge pier. Local scour depths occurring near bridge piers can be estimated by

$$d_s = K_{yW} K_I K_d K_{sh} K_\theta K_G$$

where K = empirical expressions accounting for the various influences on the scour depth; K_{yW} = depth size; K_I = flow intensity; K_d = sediment size; K_{sh} = pier or abutment shape; K_θ = pier or abutment alignment; and K_G = channel geometry [126]. [127] found variations in scour depths between surface-piercing and submerged piers; therefore, they proposed an additional submergence ratio factor, K_{sb}, to provide an updated estimate of the local scour depth. The above parameters for the small-scale and large-scale experiments are listed in Table 2.2. The two cases monitoring scour adjacent to the turbine support tower resulted in actual scour depths slightly less than the predicted values suggested by standard bridge pier scour prediction guidelines. The addition of the submergence proposed by [127] improved the estimations to within 17% of the observed maximum scour depths. Additionally, the large-scale experiment adding the turbine nacelle (no rotor) produced very similar scour and deposition results to the tower only case (Figure 2.4b). The close agreement between the observed and predicted values during the experiments without the rotor indicates that the different foundation geometries did not play a significant role in the ability to reasonably predict pier-like scour depths. The small-scale experiment support pile consisted of a 0.01m diameter pier above the sediment surface and a 0.02m diameter cylindrical pier beneath the sediment surface which was used in scour depth estimation. The large-scale experiment, as mentioned above, utilized a conical frustum base beneath the initial flat sediment surface elevation. Methods proposed by [126] were used to approximate an equivalent diameter for use in scour depth estimation for the cone-shaped foundation. In the large-scale experiments with the operating rotor, the foundation was progressively exposed to the flow resulting in enhanced vertical and lateral scour patterns when compared (in dimensionless form) to the equivalent scenario at small-scales. Unfortunately, we are not able to distinguish the separate effects of the larger rotor versus the different foundation structures.

Scaling Factor	Small scale	Large scale
K_{yW} (cm)	4.8	19.0
K_I	0.72	0.73
K_d	0.80	1
K_{sh}	1	1
K_θ	1	1
K_G	1	1
K_{sb}	0.71	0.65
d_s (cm)	1.9	9.1
Actual (cm)	1.6	7.5
% error	17.8%	17.2%

Table 2.2: Factors used for bridge scour comparison analysis.

2.3.2 Live Bed Experiments

Spatial Evolution

Live bed experiments were conducted using the small-scale turbine model in the tilting bed flume at SAFL using the same sediment distribution used in the clear water experiments presented above. To allow for bedform development, the turbine rotor was positioned 8m downstream of the channel inlet. Similar to the clear water experiments, spatial and temporal topography measurements were made during the course of each experiment under live bed conditions for a) baseline conditions with no turbine installed and b) a single turbine. Final bed topography measurements for a portion of the flume are shown in Figure 2.12. The x and y axes have been normalized by the turbine diameter, while the vertical axis is presented in dimensional units (mm) referenced to an arbitrary flume coordinate system origin. The signature of the local scour and deposition patterns that were clearly visible in the equivalent clear water experiments are still present, however, they have been mitigated or entirely disrupted by the passage of relatively large dunes ($\approx$ 0.05–0.01m amplitudes). When the crest of passing dunes coincides with the location where maximum scour occurred in the clear water experiments, the signature of the local scour is erased due to the filling by the passing sediments. However, when the trough of a passing dune aligns with this location, minimum elevations tend to be lower into the sediment bed compared to the clear water scour conditions. In order to estimate net scour and deposition induced by a single turbine, bedform fluctuations were filtered using a temporal average along the central streamwise transect, as shown in Figure 2.13, and compared to the same single turbine configuration in the clear water case in Figure 2.14. Here, it is evident

that the maximum downstream scour depth is approximately 1.5 times deeper when the turbine is installed in live-bed transport channel conditions (Δz_b = -0.24d_T) compared to clear water transport conditions (Δz_b = -0.16d_T). Additionally, peak deposition values resulting from the turbine are similar between cases. It should be noted that the hub height differed slightly between the clear water and live bed experiments. Not only was the hub-height continuously changing during live-bed experiments due to the passage of dunes, but also the flume contained more total sediment volume to accommodate for sediment recirculation. This resulted in a mean bed elevation increase of ≈0.01m, similarly resulting in a decrease of flow depth between cases and the resulting hub-height elevation difference. Although small, this hub-height difference may have accounted for the smaller overall scour depths observed during the clear water experiments. Additionally, it is evident that the turbine has an effect on the free surface. Mean water surface elevations indicate a maximum peak-to-trough oscillation at the rotor location of approximately 2–3% of the flow depth under live bed conditions (Figures 2.13 and 2.14). This feature continues to be present until approximately 4d_T before surface effects due to the turbine are eliminated. Interestingly, the free surface disturbance seems to be dampened under clear water conditions (approximately 1% of flow depth), perhaps indicating the interplay between the relatively large bedforms and the presence of the turbine has a greater effect on the free surface.

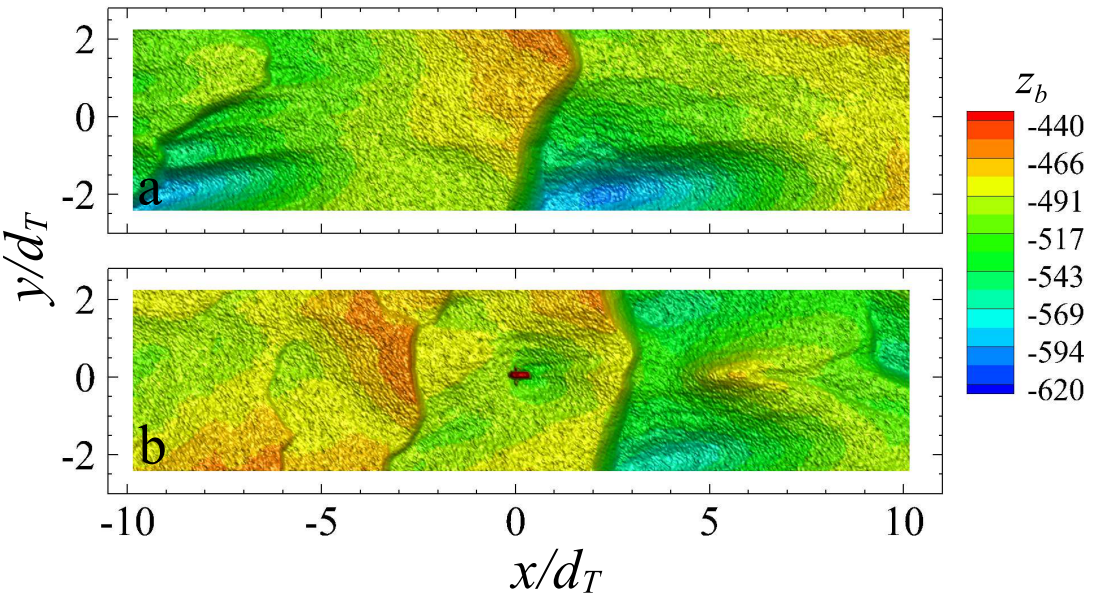

Figure 2.12: (a) Comparison between final bed topography from the live bed experiments from baseline conditions and (b) with a single turbine installed.

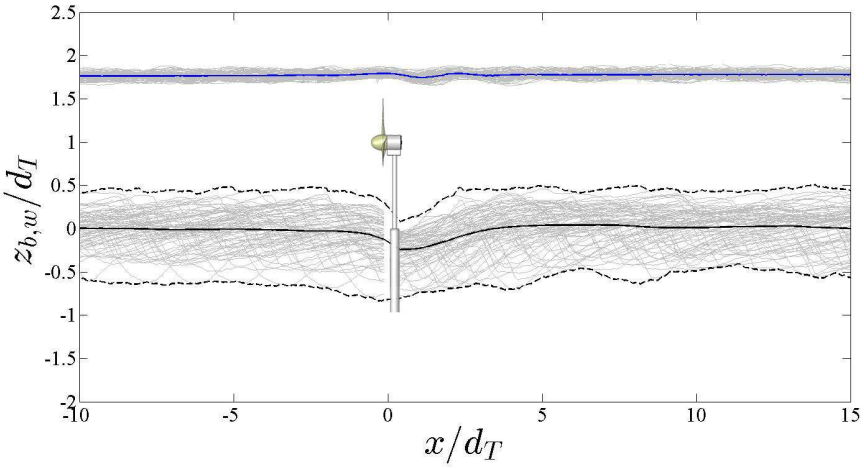

Figure 2.13: Examples of instantaneous (thin light background lines) and average bed surface (solid) and water surface (dotted) elevations from the single turbine live bed small-scale experiment. The bold dot-dashed lines indicate overall maximum and minimum bed elevation surfaces.

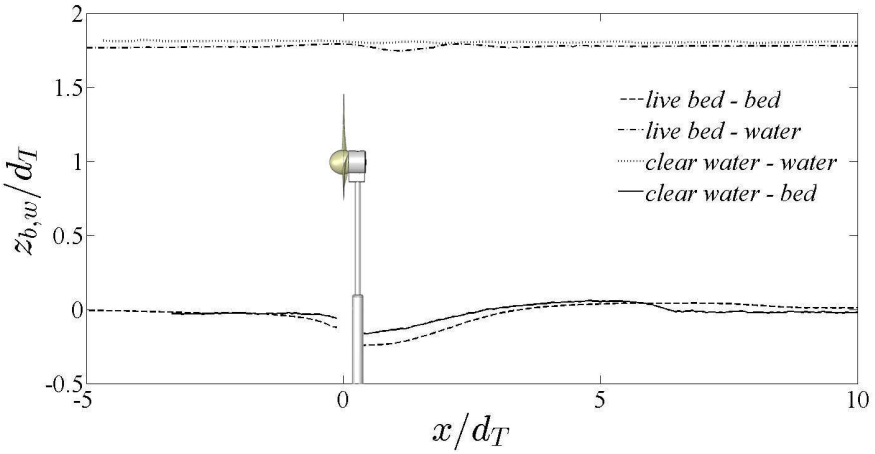

Figure 2.14: Comparison between average water surface and ending channel topography from the small-scale clear water experiments and the time-averaged water surface and bed elevation from the live bed experiments with a single turbine installed. Bed elevations have been zeroed by removing the mean bed profile slope from the data. Hub height during the clear water experiment was approximately 1 cm higher than during live bed experiments.

2.4 Summary & Conclusions

Both small-scale and large-scale clear water experiments provided key insights into the scour and deposition resulting from the presence of a hydrokinetic turbine in an erodible channel. The presence of a rotor increases the local shear stress directly downstream of its location and greatly enhances scour formation and depth as compared to the experiments where only the support tower was tested. With the rotor present, flow accelerates between the rotor bottom tip and the erodible surface, thereby amplifying the local shear stress and scouring capabilities when compared to typical bridge pier scour mechanisms. In turn, a rapidly developing scour hole and downstream migrating depositional feature are observed. Results indicate that areas susceptible to scour scale with the rotor diameter, and typically persist up to $2d_T$ downstream and up to $1.5d_T$ to either side of the turbine nacelle center location. Within this region, results show scour depths approaching 12–15%d_T from the small-scale experiments and 30–35%d_T from the large-scale experiments; however, the large-scale experiment did not reach equilibrium scour depths. Such differences may have resulted from using different base geometries between the small-scale and large-scale experiments. The conical base in the large-scale experiments provided insignificant alteration to scouring mechanisms during the turbine tower experiments (i.e. bridge pier scour); however, the increased local bed shear induced by the rotor resulted in amplified spatial scour.

Live bed conditions add complexity to the local scour induced by a turbine. Results indicate that under the conditions examined, dune crests did not interfere with the rotor blades. This is due to the local flow acceleration resulting from flow constriction between the rotor bottom tip and the approaching dune crest. This acceleration increases local shear stresses and transport capacity, thereby decreasing the dune crest elevation. When past the turbine, dune crests will act to fill in scour zones, while dune troughs can increase local scour depths beyond those reached during clear water conditions. The latter mechanism could cause greater likelihood of turbine support structure instability. Additionally, when spatial and temporal variability from migrating bedforms is averaged, the resulting bed surface shows greater maximum scour during live bed conditions (24%d_T) when compared to the clear water experiments (16%d_T), indicating that the turbine has varying effects on the local geomorphic conditions under different transport regimes. Further research is needed to understand the temporal evolution of hydrokinetic device scour processes and how they relate and differ from the currently available bridge scour temporal analysis and prediction.

The experiments discussed above provide preliminary insights into the interaction between hydrokinetic turbines and the surrounding geomorphic environment. Continued assessment of these interactions is a critical prerequisite for accelerating the environmental permitting processes currently acting as a barrier towards continued implementation of such devices. The

ability to identify critical zones susceptible to scour or unwanted deposition will inform future developers for ways to mitigate these effects. Additionally, one can imagine situations where previously armored channel material can be re-mobilized to create an active channel substrate. In other fields of engineering, circumstances exist where there is a desire to both stabilize as well as mobilize channels, therefore the use of hydrokinetic devices may provide a previously unforeseen approach to meeting desired engineering goals. Ongoing studies aim to investigate the influence of turbine geometry, hub height and spacing configurations and the interactions they have with various sediment and bedform sizes.

2.5 Notation used in Chapter 2

A = flow cross-sectional area, m^2
A_b = turbine blade cross-sectional area, m^2
A_r = turbine rotor cross-sectional area, m^2
b = channel width, m
d_s = scour depth, m
d_T = turbine rotor diameter, m
d_{50} = mean sediment grain diameter, m
Fr = Froude number $\left(Fr = u/\left(gh\right)^{1/2}\right)$, [-]
g = gravitational acceleration, ms^{-2}
h = flow depth, m
h_{hub} = turbine hub height, m
K_d = sediment size factor, [-]
K_G = channel geometry factor, [-]
K_l = flow intensity factor, [-]
K_{sb} = submergence ratio factor, [-]
K_{sh} = pier or abutment shape factor, [-]
K_{yW} = depth size factor, m
K_θ = pier or abutment alignment factor, [-]
n_b = number of blades, #
q_s = sediment discharge per unit width, $\mathrm{m}^2\mathrm{s}^{-1}$
Q_w = flow discharge, $\mathrm{m}^3\mathrm{s}^{-1}$
r = turbine rotor radius, m
R = hydraulic radius, m
Re = Reynolds number ($Re = 4RU_{hub}/\nu$), [-]
S = turbine submergence, m

S_w = channel water surface slope, %
t = time, s
U_{hub} = hub-height flow velocity, ms^{-1}
u_* = shear velocity, ms^{-1}
u_{cr*} = critical shear velocity, ms^{-1}
u = streamwise velocity fluctuations, ms^{-1}
w = vertical velocity fluctuations, ms^{-1}
x = longitudinal (streamwise) direction, m
x_p = longitudinal distance of deposition peak, m
y = lateral (spanwise) direction, m
z = vertical direction, m
z_b = bed elevation, m
z_p = elevation of deposition peak, m
z_w = water surface elevation, m

Greek symbols
η = turbine rotor blockage ($\eta = A_{rotor}/A$), %
λ = tip speed ratio, ($\lambda = \omega r/U_{hub}$), [-]
ν = kinematic viscosity of water, $\mathrm{m}^2\mathrm{s}^{-1}$
σ = turbine rotor solidity ($\sigma = (BC_L)/(2\pi R)$), %

Chapter 3

Interactions between large-scale bedforms and axial-flow turbines

The following chapter has been accepted for publication in *Renewable Energy*.

Hill, C., Musa, M., and Guala, M., (2015), Interaction between instream axial-flow hydrokinetic turbines and uni-directional flow bedforms, accepted for publication, *Ren. Energy*.

3.1 Introduction

Uncertainty surrounding the impact that marine hydrokinetic (MHK) devices have on the ecology and morphodynamics of riverine and tidal environments has been highlighted as an area needing further investigation [19, 17]. For instance, [128] discussed in detail the potential hydrodynamic effects and resulting influences on the marine physical and ecological environments resulting from tidal and wave energy device installations. This uncertainty is often an insurmountable barrier for companies in this emerging field. Over the past decade, the Federal Energy Regulatory Commission (FERC) had issued preliminary hydrokinetic permits for sites along the Mississippi River. Unfortunately, the current cost of energy for MHK devices and barriers present during the environmental review and assessment process have slowed the realization of many of these sites (for example, Free Flow Power recently withdrew their permits along the Mississippi River). As MHK research and development continues forward, the cost of energy is expected to decrease, as well as existing hesitations regarding potential environmental impacts of instream power plants. To continue development progress, MHK devices need to operate efficiently in a variety of channel conditions, both with and without mobile substrates,

and minimize their impact on the surrounding ecological and morphological environment.

Large rivers around the world (i.e. Mississippi River) are characterized by large meanders, asymmetric channels and mobile substrates that respond differently during various flood stages. The complexity of channel topography (see [129] and references therein) introduces a broad range of large turbulent scales into the flow environment that must be taken into account in the design and performance evaluation of MHK devices and project site development. For instance, field data of bedforms indicate that areas within the Mississippi River can have small-scale bedforms ($h_b \approx$ 0.5m–3m and $\lambda_b \approx$ 5m–50m) migrating up the stoss side (upstream side, see Figure 3.1) of larger-scale dunes ($h_b \approx$ 1m–6m and $\lambda_b \approx$ 100m–300m) in flow depths of $h \approx$ 15m–20m [101]. Other studies have reported similar findings [4, 102], and in general, it is not uncommon to find mobile topographic features on the scale of the rotor diameters (i.e. $d_T \approx$ 5m–10m) of proposed hydrokinetic devices this day in age. Regardless, whether mobile or stationary large-scale topographic features exist at proposed project sites, these features will introduce a broad range of turbulence scales into the flow that need proper characterization during pre-project site assessment.

Axial-flow hydrokinetic turbines have been shown to be responsive to a specific range of turbulence scales present in the approaching flow [6]. The cut-off frequency beyond which the turbine power is no longer influenced by inflow turbulence is governed by the turbine operational control (i.e. tip speed ratio, λ). This means that as the tip speed ratio increases, the minimum turbulence scales able to influence the instantaneous turbine power become smaller. In natural environments, the tip speed ratio is dictated by the shape of the turbine blades and by the mean cross sectional velocity. Based on these characteristics, optimal operating parameters are set to achieve maximum performance in the given environment. However, the addition of multi-scale roughness (i.e. ripples, dunes, mega-dunes, boulders, and meanders) along the channel boundaries introduces turbulence into the flow which is expected to directly effect turbine performance. Characterizing this turbulence is crucial, and thankfully the mean and fluctuating velocity fields above laboratory and field subaqueous dunes have been extensively studied during recent decades [90, 86, 88, 89, 129, 130] and in more recent years using computational fluid dynamics (CFD) [94, 93].

From the research work of [95, 97], five main flow regions above dunes have been identified: a) maximum velocity, b) shear layer, c) separation zone, d) internal boundary layer, and e) wake region. The region of maximum velocity occurs along the top portion of a dune above the crest where the cross-sectional flow area is at a minimum. Downstream of the dune crest (lee side, see Figure 3.1), the shear layer creates a zone of high turbulence intensity and instability. This region can often contain high concentrations of suspended sediment and other abrasive material [96], a potential problem for the longevity of MHK device blades. The separation zone,

located immediately downstream of the dune crest, creates a highly turbulent zone and often has recirculating, upstream velocities interacting with the lee side slope of the dune. This region extends downstream up until the point of reattachment, typically located a horizontal distance of approximately five times the bedform height, h_b [96]. Downstream of the reattachment point, a new boundary layer begins to develop along the low angle upstream side (stoss side) of the dune. Located between the growing internal boundary layer and the turbulent shear layer is the wake region [95, 97].

Flow characteristics vary depending on the region above a dune where measurements are made. For example, streamwise turbulence intensity, I_u, is at a maximum in the recirculating separation zone between the dune lee slope and the reattachment point. Slightly elevated values of I_u persist in the wake region, but are lowest above the dune crest due to the maximum velocities found here where cross-sectional area is at a minimum. Turbulent kinetic energy (TKE) values are at a maximum in the shear layer region closest to the crest of a dune. These values decrease further downstream from the dune crest and approach lower values typical to other regions, such as directly above the crest or in the internal boundary layer [95, 97]. This spatial variability of the turbulent flow around bedforms is expected to add temporal variability to the incoming flow perceived by instream MHK devices due to both bedform migration and deformation (see e.g. [100, 99, 98]).

Interactions between hydrokinetic turbines and the near-field and far-field regions of sediment are often identified as a critical area for assessment [19, 17]; however, to date, limited research has been published to address this concern. This may be because, at present, many MHK targeted project areas are located in highly energetic regions with heavily armored channels or limited large scale bedforms, yet as next generation devices become a reality, projects will target areas with active sediment transport and mobile substrates. Local scour induced by a single small-scale axial-flow turbine model was investigated under clear water and live bed transport conditions and compared to standard bridge scour prediction methods in the work leading up to the results presented here [5]. Other experiments have suggested armoring the near-field region with a rigid approach platform, thereby accelerating flow and reducing local scour, yet no data were collected on turbine-sediment interactions [40]. Additionally, other investigations have been reported resulting from numerical studies on the effects that tidal turbine arrays have on far-field sediment characteristics [43, 44, 45]; however, large computational domains did not provide enough resolution to investigate the local or channel-scale effects on scour and sediment transport. The advancements in CFD capabilities in recent years have provided unprecedented results regarding flow structure interaction around MHK devices [24, 116]. Large-eddy simulations are now capable of solving problems in arbitrarily complex natural geometries [49, 50]. With the available computational tools, the advancement in turbine-sediment interactions has

the capability to progress rapidly, and will likely do so in the coming years through an integrated experimental, computational and field-scale scientific approach.

The experiments presented here investigate both local and far-field effects of axial-flow hydrokinetic turbines and expand upon initial investigations into the local scour phenomena caused by a single axial-flow device [5]. Results highlight how the interactions between turbines and channel morphology are coupled, indicating how turbine performance can respond to complex mobile topography, and how the presence of single or multiple turbines can influence the local and far-field sediment transport characteristics. Potential implications extend to the design of scour-protection foundation structures, to potential control strategies based on incoming bedforms and on optimal siting for the mitigation of bedform induced unsteady loads. Although results presented within this paper are from unidirectional flow experiments with relatively large-scale roughness features, they provide an indication of the interactions MHK devices will have in bi-directional (i.e. tidal) flows with either stationary or mobile substrates containing arbitrarily complex topographic features. The turbulent flow and length scales evolving over dune-specific bathymetry are much shorter than the bedform period and wavelength; therefore, whether the channel roughness features occur in uni-directional or bi-directional flow environments, they can be considered quasi-stationary with regards to the dune specific flow field affecting the turbine performance. However, the dunes modulate large-scale turbulence organization near bedform-specific regions, implying that bedform migration exposes the turbine to slowly changing yet significant variations of the incoming flow. The results provide insight into these interactions both in terms of the device performance response to the channel roughness, but also in how the device may impact the downstream physical environment.

3.2 Experimental Setup

Two sets of experiments were completed to investigate the interactions between bedforms and axial-flow hydrokinetic turbines. Experiments were carried out at St. Anthony Falls Laboratory at the University of Minnesota in an open channel flume with dimensions $b = 0.9$m wide and $L = 15$m long, slope adjustment capabilities from -1% to 6%, a sediment recirculation system, and a 3-axis flume-traversing Data Acquisition (DAQ) Carriage. Flow entered the flume via a valve-controlled 0.3m diameter supply pipe, passed through a 0.1m wide cobble wall and three rows of vertically-oriented cylindrical baffles (diameter = 0.05m, spacing = 0.05m) to break up large-scale flow structures induced by the supply pipe before entering the main flume test section and evenly distribute the recirculated sediment across the flume inlet. The upstream turbine in these experiments was always placed more than 5m downstream of the baffle rows. Baseline conditions were established during a series of clear water scour experiments in which

flow parameters were set to ensure a bed shear stress just below the critical state. Experiments were repeated under live bed sediment transport conditions with a substrate of uniform coarse sediment (d_{50} = 0.0018m) that produced relatively large-scale two-dimensional (2D) bedforms migrating the length of the flume. Single turbine effects on local scour in both clear water and live bed conditions are presented in [5]. In this paper, investigations look into the coupled behavior between bedform characteristics and turbine voltage production (i.e. performance) for both single and aligned two turbine configurations. For two turbine experiments, a streamwise spacing of $4d_T$ and $7d_T$ was used for both the clear water and live bed experiments. An additional spacing of $10d_T$ was used in the clear water experiments. A schematic of the experimental setup is shown in Figure 3.1.

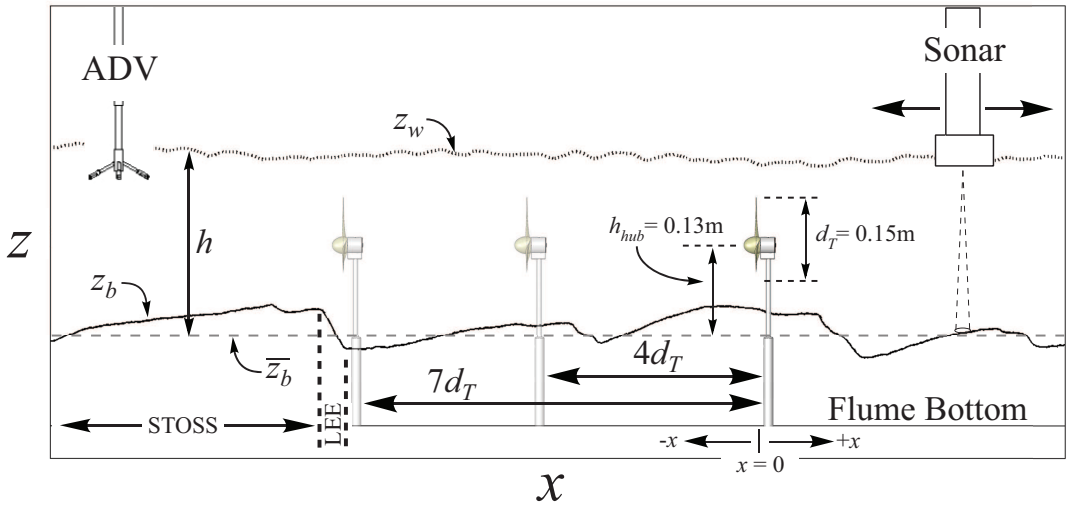

Figure 3.1: Schematic of the experimental setup. Coordinate system origin (x = 0m) is located approximately 8m downstream of channel inlet and vertical cylinder baffles. Flow is from left to right.

Figure 3.2: Photo of single turbine with bedforms. Inset image shows close-up of the 1:33 scale turbine used during experiments. Rotor direction is counter-clockwise.

Instrumentation was mounted to the DAQ Carriage and scripted to continuously move and record measurements throughout the flume. During experiments, subaqueous bed topography measurements, $z_b = z_b(x, y, t)$, were collected using an Olympus Panametrics C305-SU submersible transducer. For most experiments, data were collected along three streamwise passes (y/d_T = -1.5, 0, +1.5) and 1 or 2 spanwise passes located $0.67d_T$ downstream of the turbine(s) for the single and two-turbine experiments, respectively. Water surface elevations, $z_w = z_w(x, y, t)$, were collected simultaneously along the same transects using a Massa M5000 ultrasonic sensor. Inflow 3D velocity (u, v, w) characteristics were monitored using a Nortek Vectrino acoustic Doppler velocimeter (ADV) positioned approximately $20d_T$ upstream of the primary turbine located at $x = 0$m.

The model turbine used in these experiments was a scaled three-bladed axial-flow turbine with rotor diameter, $d_T = 0.15$m, and hub height, $h_{hub} = 0.13$m (Figure 3.2). Hub height is defined as the elevation above the mean bed elevation linear trendline directly below the hub location. A small DC motor (model #RK-370CA-14420) was mounted in the nacelle of the turbine. Nacelle and motor diameter was equal to the hub diameter ($d_h = 0.027$m). Motor

length, l_m, was 0.031m. The hub and rotor mounted directly to the motor shaft and was held secure using a set screw. A Measurement Computing MiniLAB 1008 USB data acquisition board logged instantaneous voltage measurements at 200Hz continuously throughout the experimental run time (Figure 3.3). In the experiments with a second turbine installed upstream, voltage measurements were only collected from the downstream turbine located at $x = 0$, referred to as the primary turbine from this point forward. Fast Fourier Transformation (FFT) analysis of the instantaneous voltage measurements provided an indication of the turbine operating characteristics (i.e. tip-speed ratio), as illustrated in Figure 3.4. The first spectral peak indicates the turbine rotational frequency, while resonant peaks are present at higher frequencies [81]. Instantaneous and time-averaged measurements of turbine voltage output were used as a proxy for turbine performance and how it responded to relatively large-scale bedforms. Turbine, sediment, and hydraulic parameters are summarized in Table 3.1 (see also [5]). Clear water experiments ran for a minimum of 3.5 hours, while live bed experiments ran for a minimum of 13.5 hours to allow passage of several bedforms past the turbines.

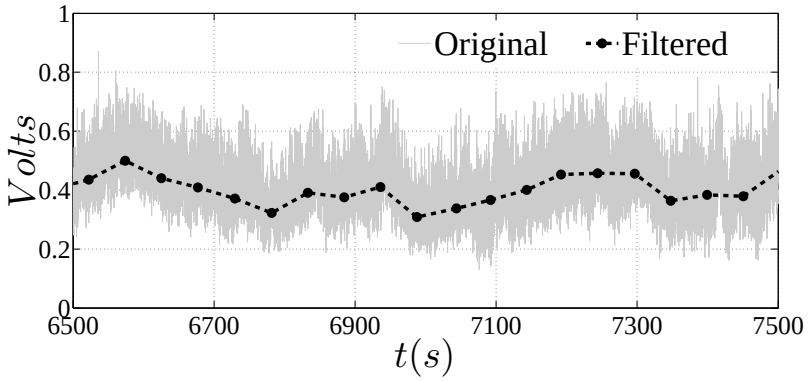

Figure 3.3: Sample from 200Hz instantaneous voltage signal acquired from the turbine motor. Darker dashed line and circles illustrate filtered signal to match sampling frequency of bed elevation data for analysis described later.

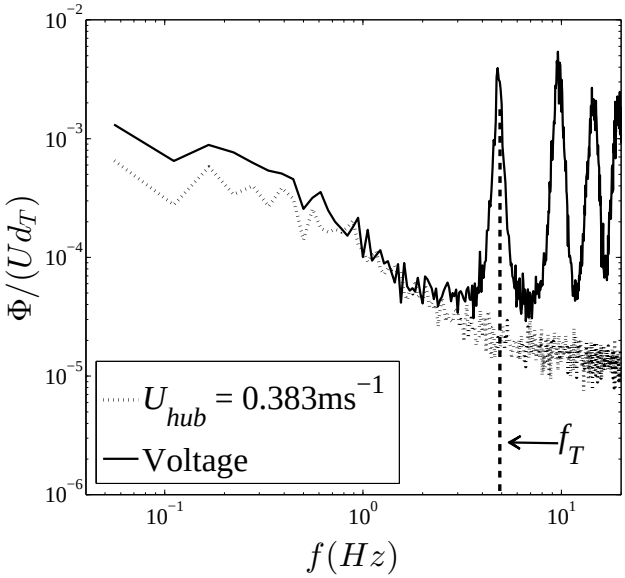

Figure 3.4: Spectral plot comparing inflow hub-height velocity, U_{hub} (dotted line), to the turbine voltage signal (solid line). The dashed vertical line indicates the turbine rotational frequency, f_T.

	Clear Water	Live Bed
Turbine Parameters		
d_T	0.15m	0.15m
h_{hub}/d_T	0.86	0.88 (average)
S	$0.5d_T$	$0.5d_T$
λ	6.3	6.5
σ	8.1%	8.1%
η	7%	7%
Flow, Channel and Sediment Parameters		
d_{50}	1.8mm	1.8mm
h	0.28m	0.27m
b	0.9m	0.9m
Q_w	$0.114\text{m}^3\text{s}^{-1}$	$0.130\text{m}^3\text{s}^{-1}$
U_∞	0.45ms^{-1}	0.53ms^{-1}
u^*	0.02ms^{-1}	0.07ms^{-1}
u^*_{cr}	0.034ms^{-1}	0.034ms^{-1}
S_w	$5.0\text{x}10^{-4}$	$3.0\text{x}10^{-3}$
Fr	0.27m	0.33m
Re	$1.26\text{x}10^5$	$1.43\text{x}10^5$

Table 3.1: Turbine, flow, channel, and sediment parameters. See Chapter 2 for additional information.

3.3 Methods of Analysis

3.3.1 Bedform Tracking

Tracking bedform crests, troughs and other characteristics during experiments was possible using sonar measurements of bed elevation, $z_b = z_b(x, y, t)$. Individual bed elevation profiles (BEPs) serve as a snapshot in time where "frozen" bedforms can be geometrically identified and classified. As noted by [131], there are several methods to select the crests and troughs of bedforms to enable geometric characterization of the channel bottom. Several methods were employed to gauge the robustness and ability of each algorithm in identifying bedforms while minimizing erroneous identification. The method employed here was similar to that described by [131]. Analysis focused on a 5m ($\approx 33d_T$) long region located downstream of the primary turbine

at $x = 0$ for all four cases examined (baseline, single turbine, and two turbines apart at $4d_T$ and $7d_T$). First, individual BEPs were removed of any outliers and detrended so that elevations fluctuated around zero. Three detrending methods were compared: a) a streamwise linear trend, b) the mean BEP from the entire experiment, and c) the mean bed elevation from each individual BEP. Second, trough-to-crest (T-C) and crest-to-trough (C-T) crossings were located. Finally, maximum and minimum elevations between the successive T-C and C-T crossings were defined as bedform crests and troughs, respectively. The corresponding geometric parameters, λ_C = crest-to-crest wavelength, λ_T = trough-to-trough wavelength, h_b = bedform height, η_C = crest elevation, and η_T = trough elevation were then calculated from these benchmarks (Figure 3.5). An additional method was employed by tracking the depositional front of each dune, however, this method was less accurate in tracking bedforms throughout the experiments.

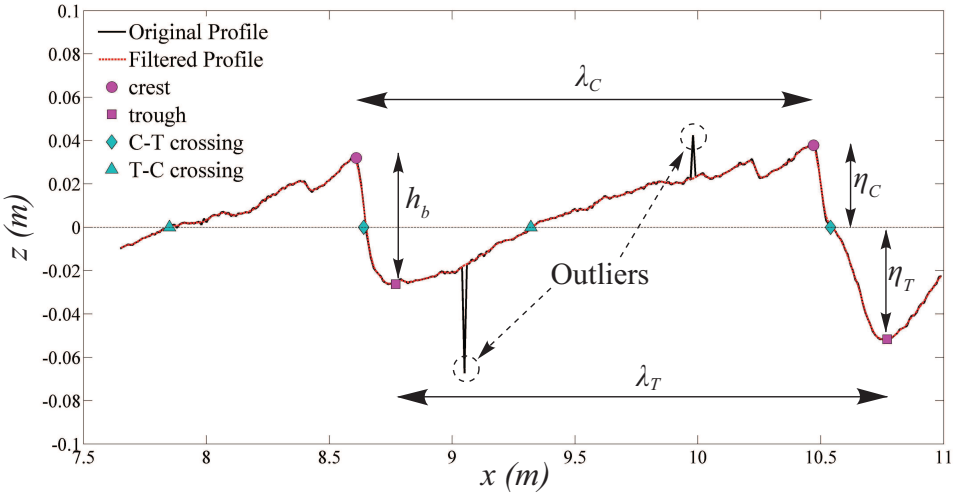

Figure 3.5: Definitions of various bedform geometric parameters calculated during bedform tracking methods employed for this analysis.

An alternative method for characterizing bedform parameters in a mobile channel uses a parameter called the interface width, w_i [2]. This method provides a way of quantifying various scales of roughness within a channel by calculating the root mean squared value of elevations within the channel by increasing the observation window size from twice the data resolution up

to the channel scale. The interface width, w_i, is defined as:

$$w_i = \left[\frac{1}{N} \sum_{i=1}^{N} (\eta_i - \overline{\eta})^2 \right]^{1/2}$$

where N is the number of observations over the window size considered. After iteratively calculating the interface width for the entire BEP data series from each experiment and plotting on a log-log scale, a measure of the dominant largest roughness elements of the channel topography can be determined [2, 2]. To verify bedform tracking and identification algorithms, bedform statistics were compared with the longitudinal roughness scale estimated by the interface width method.

3.3.2 Cross Correlation

The correlation between voltage and BEP time series provides an indication of critical distances upstream of the turbine rotor location at which large-scale bedforms have a direct relation to the voltage output of the model turbine. The 200Hz voltage signal was down-sampled to provide a time series with the same sampling period as the bed elevation time series ($\Delta t \approx$ 51.5s, 110.7s, 110.8s for the single, $4d_T$ and $7d_T$ experiments, respectively) (see Figure 3.3). In doing so, no voltage measurements were discarded, only averaged within the time window ranging from +/- $0.5\Delta t$ centered around each bed elevation measurement.

The cross-correlation between voltage and bed elevation signals focused on the correlation values at lag zero for each location in the streamwise direction along the flume. This provides a simplified understanding of bedform elevation and turbine voltage correlation. An assumption was made that bedforms are primarily translated, not distorted, as they move in the streamwise direction. Although modifications to bedform geometry occur as they migrate downstream and the local propagation velocity is bedform size dependent [100, 98], a study of the spatial correlation between turbine voltage and channel topography can be carried out neglecting the variability of the propagation velocity for small lags. For example, one may consider two BEPs in time at two streamwise locations, $z_{x1(t)}$ and $z_{x2(t)}$, which correspond to the bed elevation time series used for cross-correlation analysis for streamwise positions, x_1 and x_2, respectively. During correlation analysis, the BEP is shifted for a range of lags and correlated to the turbine voltage time series. As shown in Figure 3.6, when BEP $z_{x2(t)}$ is shifted by small lags (in this case k = -3), it closely resembles BEP $z_{x1(t)}$. Therefore, it is reasonable to assume that $z_{x1(t)}$ at lag zero closely resembles $z_{x2(t)}$ at some lag $t \pm \Delta T$ for small lags and negligible bedform deformation, and so analysis herein focuses on the correlation coefficient values only at lag k = 0.

The correlation coefficient, ρ, is defined as,

$$\rho\left(i\right) = \frac{1}{N}\sum_{i=1}^{N\pm k}\frac{\left(V_k - \bar{V}\right)\left(z_k - \bar{z}\right)}{\sqrt{\sigma_V^2\sigma_z^2}}$$

where N is the length of the signal, k is the number of lags (k = -(N-1) to N-1), the over-bar represents the mean of the signal, and σ_V^2 and σ_z^2 are the signal variances for the voltage and bed elevations, respectively.

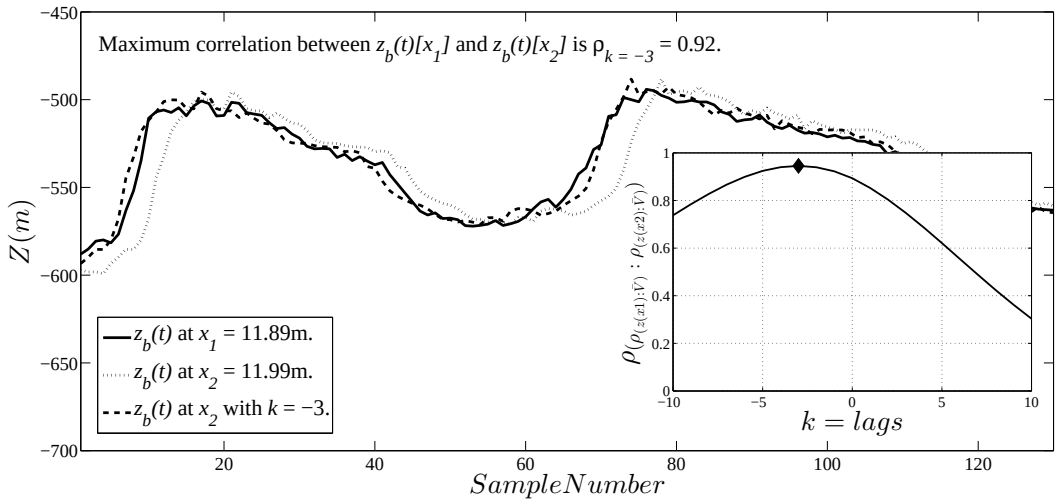

Figure 3.6: Demonstration of the assumption that correlation analysis between a voltage time-series and BEP can focus on only lag k = 0. Solid line shows BEP as a function of time at position, x_1. When BEP at position x_2 (dotted line) is shifted by k = -3 lags, it closely resembles BEP at x_1 (dashed line). The correlation between BEP x_1 and BEP x_2 at k = -3 is ρ = 0.92. Inset figure shows the correlation between two cross-correlation signals: $\rho_{z(x1):\bar{V}}$ and $\rho_{z(x2):\bar{V}}$. Here, the maximum correlation is ρ = 0.95, confirming that at lag k = -3 is the appropriate lag shift that validates this assumption.

3.4 Results

3.4.1 Effects of sediment transport on turbine performance

Mean and RMS voltage

Examples of voltage time series from clear water and live bed experiments are presented in Figure 3.7 and summarized in Table 3.2. For clear water experiments, values have been normalized by the single turbine experiment mean voltage. Hub height velocities were approximately

$U_{hub} = 0.45\text{ms}^{-1}$. When an additional turbine was positioned upstream of the primary turbine, the mean voltage values decreased, consistent with the induced blockage and the wake recovery behind the upstream unit. Interestingly, a relative increase in the mean voltage was observed during the $7d_T$ experiment ($V/\bar{V} = 57\%$) as compared to the $4d_T$ ($V/\bar{V} = 47\%$) and $10d_T$ ($V/\bar{V} = 43\%$) experiments. The fluctuations in voltage followed a similar trend. During the two turbine experiments ($4d_T$, $7d_T$, and $10d_T$ spacing upstream of the primary turbine), the voltage intensity, $v'/\bar{V}$ (analogous to turbulence intensity, I_u, for velocity data), increased compared to the single turbine clear water case; however, among the three cases with a second turbine present, the primary turbine's voltage intensity, $v'/\bar{V}$, when a second turbine was located $7d_T$ upstream was closest to that of the single turbine baseline experiment.

Despite a higher mean hub height flow velocity during live bed experiments ($U_{hub} = 0.63$m/s), and therefore, higher expected voltage output, mean voltage values were lower than the reference case found during the single turbine clear water experiment (Figure 3.7 and Table 3.2). There is also an increased variation in range of voltages resulting from migrating bedforms. All cases show an increase in the voltage intensity, $v'/\bar{V}$, compared to the clear water experiments. When a second turbine was installed, voltage intensity values were 2 to 3 times greater than observed for the similar configuration during clear water experiments.

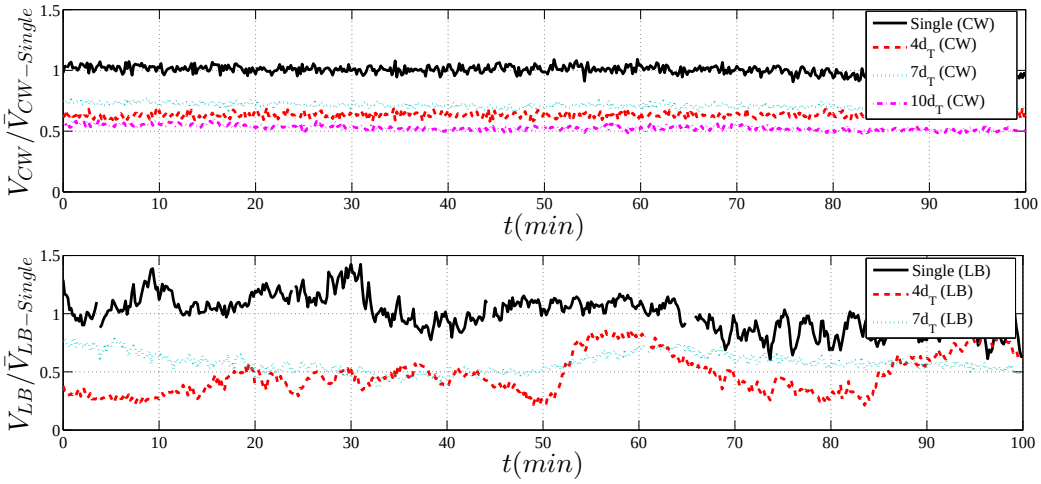

Figure 3.7: Sample of normalized voltage timeseries for each of the cases investigated during clear water (CW) and live bed (LB) experiments. Data from experiments with two turbines present are recorded from the downstream turbine.

		Measured			$\bar{V}$	$v'/\bar{V}$
Experiment	**Turbine(s)**	U_{hub} **(ms^{-1})**	$\bar{V}$	$v'/\bar{V}$	**%ST**	**%ST**
Clear Water	Single	0.45	0.81	0.14	n/a	n/a
Clear Water	$4d_T$	0.45	0.47	0.17	58%	126%
Clear Water	$7d_T$	0.45	0.57	0.15	71%	108%
Clear Water	$10d_T$	0.44	0.43	0.17	53%	121%
Live Bed	Single	0.63	0.47	0.22	n/a	n/a
Live Bed	$4d_T$	0.61	0.30	0.40	64%	186%
Live Bed	$7d_T$	0.63	0.30	0.37	65%	171%

Table 3.2: Summary of the hub height velocity, U_{hub}, mean voltage, $\bar{V}$, and the voltage intensity, $v'/\bar{V}$, for each of the four experiments from clear water conditions and three experiments during live bed transport conditions. The two columns at the right indicate the percentage variation of each experiment-specific variable with respect to the corresponding experiment-specific baseline value (Single turbine).

Using the single turbine live bed case, the relationships between the location of the closest upstream sediment dune crest and the corresponding voltages measured from the turbine could be examined. Peak identification and tracking was performed using the previously mentioned methods. Figure 3.8 illustrates the relationships between normalized streamwise distance, x_p/d_T, normalized dune peak height, z_p/d_T, normalized mean voltage, $V/\bar{V}$, and the voltage intensity $v'/\bar{V}$. Data have been binned according to their relative percentage of maximum dune height (white diamond: $0 \leq z_p/d_T \leq 0.1$; dark gray circle: $0.1 \leq z_p/d_T \leq 0.2$; light gray square: $0.2 \leq z_p/d_T \leq 0.3$; and, black triangle: $0.3 \leq z_p/d_T \leq 0.4$). Dune peak elevation averaged $0.2d_T$, corresponding to approximately $h_b = 0.06$m dune heights. The relationship between dune peak dimensionless distance upstream from the turbine energy extraction plane (EEP) and the normalized voltage, $V/\bar{V}$, indicate that as the dune peak moves within the region of $2d_T$ ($\approx 0.2\bar{\lambda}_b$) or closer, the turbine can produce up to 1.5 times the mean voltage, $\bar{V}$, measured during the course of the experiment. Additionally, as dune peak elevation increases to between $z_p = 0.2d_T$ and $0.4d_T$, the turbine can produce up to 1.5 times the mean voltage measured during the course of the experiment.

Similar analysis was done using the voltage intensity, $v'/\bar{V}$, from the single turbine live bed experiment (Figure 3.8). There is noticeable scattering of $v'/\bar{V}$ around approximately x_p/d_T = -4 ($\approx 0.4\bar{\lambda}_b$), however, a similar trend as found with the mean voltage is observed when the crest of the dune moves closer than x_p/d_T = -2 ($\approx 0.2\bar{\lambda}_b$) to the EEP. Additionally, as dune crest peak elevation increase above $z_p/d_T = 0.2$, an increase in voltage intensity is observed.

The authors acknowledge that the normalization of the streamwise distance by the rotor diameter, d_T, proposed here, is consistent with the quantification of turbine spacing and with the extension of the perturbed sediment layer obtained from clear water experiments [5]. However, while studying turbine-bedform interaction, the dominant length scale can not exclusively be chosen as the rotor diameter, as the evolution of different flow regions around the bedforms is statistically described as a function of the bedform wavelength (λ_b) and height (h_b). Key results are described using both normalization x/λ_b and x/d_T.

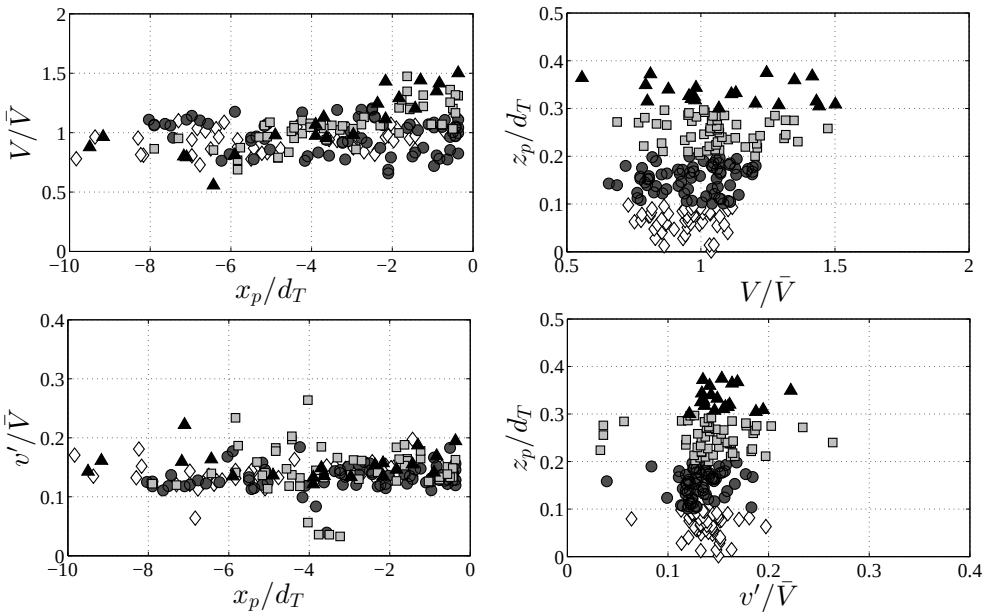

Figure 3.8: Dimensionless relationships between normalized mean voltage vs. bedform peak distance (top-left), bedform peak height vs. normalized mean voltage (top-right), voltage intensity ($v'/\bar{V}$) vs. bedform peak distance (bottom-left) and bedform peak height vs. voltage intensity ($v'/\bar{V}$) (bottom-right). Points have been grouped by normalized dune height (z_p/d_T): 0-10% = white diamonds; 11-20% = dark gray circles; 21-30% = light gray squares; and 31-40% = black triangles.

Cross-correlation

Results from cross-correlation analysis between bed elevation, $z_b = z_b(x, y, t)$ and the turbine motor voltage are presented in Figure 3.9. For the single turbine experiment, mean voltage peak correlation at lag-zero occurs at x/d_T = -1.23 ($\approx 0.12\bar{\lambda_b}$) with ρ_0 = 0.34. Maximum

bed-RMS correlation occurs at x/d_T = -0.77 ($\approx 0.07\bar{\lambda}_b$) with $\rho_0 = 0.24$, indicating a slight out-of-phase lag between the two correlation plots. For the experiment with two turbines spaced at $4d_T$, mean voltage peak correlation at lag-zero occurs at x/d_T = -0.57 ($\approx 0.09\bar{\lambda}_b$) with $\rho_0 =$ 0.42. Maximum bed-RMS correlation does not occur until downstream of the primary turbine. For the experiment with two turbines spaced at $7d_T$, peak correlation at lag-zero occurs at x/d_T = -2.43 ($\approx 0.29\bar{\lambda}_b$) with $\rho_0 = 0.43$. Maximum bed-RMS correlation occurs at $x/d_T =$ -1.1 ($\approx 0.13\bar{\lambda}_b$) with $\rho_0 = 0.47$, again indicating a slight out-of-phase lag between the two correlation plots upstream of the primary turbine located at $x = 0$. Although voltages were not actually measured from the turbine located at x/d_T = -7, the relative upstream distance between the correlation peaks and the turbine location are approximately the same for both locations, indicating that for this arrangement, the upstream turbine was also responding in a similar manner to the approaching topography as was the downstream turbine. A comparison of the correlation between the bed elevation and the mean voltage output along the length of the flume for each of the three cases is provided as well (Single turbine - black; Two turbines $4d_T$ - red; Two turbines $7d_T$ - green).

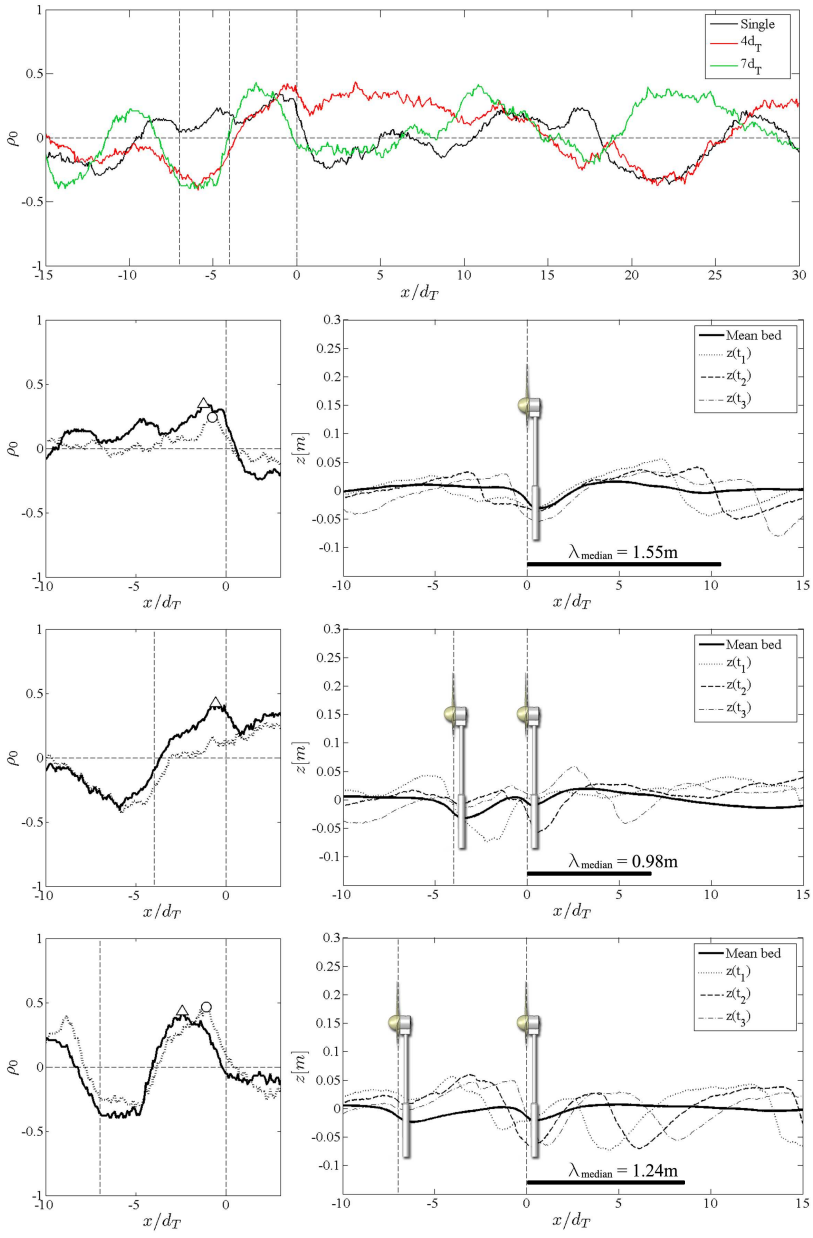

Figure 3.9: Top image: Correlation coefficients plotted along the streamwise axis for each of the 3 cases. Vertical dashed lines show locations of turbine(s). Bottom 3 images: Close-up of correlation coefficient plots in the region near the turbine for single turbine (top image pair), two turbines with $4d_T$ spacing (middle image pair), and two turbines with $7d_T$ spacing (bottom image pair). Images on left highlight correlation coefficient values and peaks (triangle = mean voltage; circle = RMS voltage), while images on the right show mean bed elevation profile (solid bold line) with 3 bed profiles with approximately $\Delta t = 10$ minutes between each profile to show migration and passage of dune crest past turbine location. Solid scale bar indicates the median bedform length, $\bar{\lambda_b}$.

3.4.2 Effects of turbine on sediment transport

Mean bed and water surface elevation

As discussed in [5], the presence of a single turbine in an erodible channel enhances local scour. It was observed that scour depths were slightly greater when relatively large-scale bedforms were present, likely a fact of the increased local bed shear and transport capacity with an increased bulk velocity. Further investigations looked into the local scour and channel scale sediment transport effects from two turbines aligned in the axial, streamwise direction. First, two turbines were studied under clear water conditions, similar to those presented in [5] for a single turbine. Ending topography for experiments with a single turbine and two turbines spaced at $4d_T$ and $7d_T$ is shown in Figure 3.10. With a second turbine at x/d_T = -4, little deposition resulted between the two turbines, and scour only occurred in the near-wake region of the upstream turbine. Interestingly, the case with turbines spaced at $7d_T$ produced the least change in maximum scour depths and peak deposition values compared to the other cases.

A second set of experiments were studied under live sediment transport conditions with relatively large-scale bedform. Analysis was performed to monitor the geometric characteristics of these bedforms. Ending topography for these experiments considered (single turbine and two turbines spaced at $4d_T$ and $7d_T$) is also shown in Figure 3.10. Despite the scale of the bedforms, similar signatures in local scour and deposition between the clear water and live bed experiments are visible. When bed elevations over the duration of the experiments are averaged to determine mean bed elevation, the effects are more noticeable (Figure 3.11). Maximum scour depths during live bed experiments occurred during the single turbine experiment. With a second turbine positioned $4d_T$ upstream, very little scour occurred immediately downstream of the second turbine, yet amplified deposition resulted in this downstream region. Scour downstream of the first turbine was reduced when compared to the single turbine case. Results from turbines spaced at $7d_T$ show that scour and deposition were both reduced compared to the single turbine and $4d_T$ spaced turbine experiments. Maximum scour depths downstream of each turbine are summarized for comparison in Table 3.3 for both clear water and live bed experiments.

The average water surface elevation shows that a single turbine has a local effect on the free surface up to approximately $4d_T$ downstream of the turbine location (Figure 3.11). When two turbines are present and spaced at $4d_T$, the same result is observed, and the unsteadiness in the free surface resulting from the upstream turbine extends to the location of the downstream turbine, thereby impacting a total length of approximately $8d_T$ along the free surface. In the case of $7d_T$ turbine spacing, the oscillations introduced to the surface from the upstream turbine extinguish approximately $3d_T$ upstream of the downstream turbine, resulting in a relatively steady free surface elevation in the near-field approach region of the next turbine.

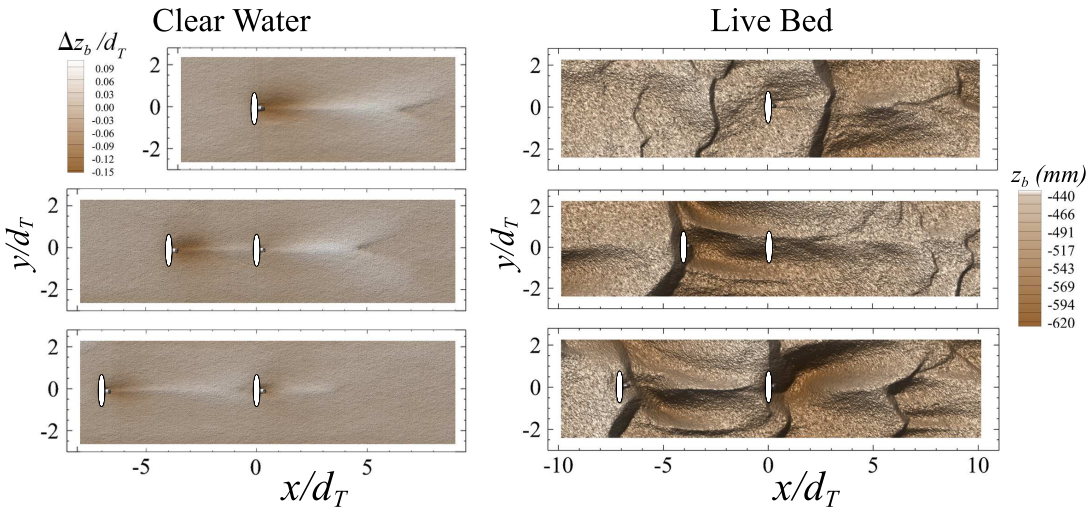

Figure 3.10: Final topography for the clear water experiments (left): single (top), $4d_T$ (middle), and $7d_T$ (bottom). Flow is from left to right. Color scale represents normalized scour (dark colors) and deposition (light colors), $\Delta z_b/d_T$. Final topography for the live bed experiments (right): single (top), $4d_T$ (middle), and $7d_T$ (bottom). Flow is from left to right. Color scale represents flume z-coordinate system bed elevations, z_b, in mm. Turbine hub height, $h_{hub} \approx$ -382mm.

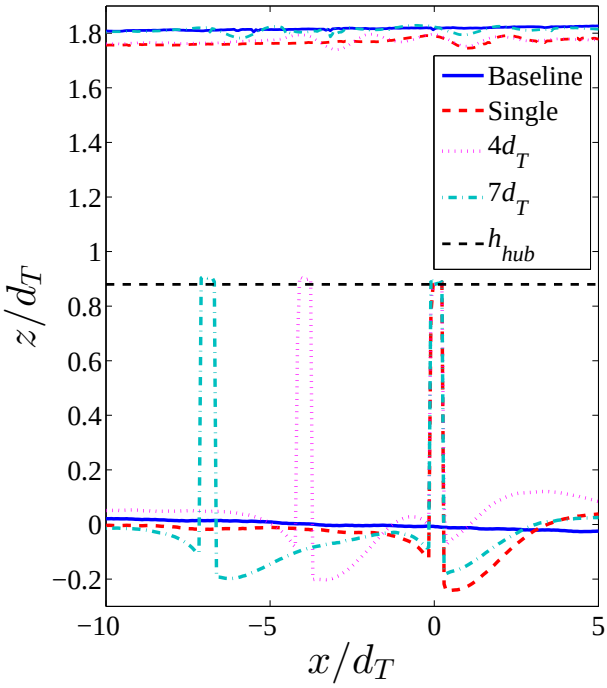

Figure 3.11: Close-up view of the mean bed and water surface elevations for the four live bed experiments: Baseline (solid blue), single turbine (dashed red), two turbines with $4d_T$ spacing (dotted magenta), and two turbines with $7d_T$ spacing (dashed-dot green). Turbine hub height represented by horizontal black dashed line at $z/d_T \approx 0.88$.

	Turbine	**Clear Water**	**Live Bed**
Single	US	n/a	n/a
	DS	12.4%	24.4%
$4d_T$	US	12.0%	20.2%
	DS	5.2%	7.4%
$7d_T$	US	10.6%	19.9%
	DS	8.3%	18.0%
$10d_T$	US	10.2%	n/a
	DS	8.8%	n/a

Table 3.3: Comparison of depth of scour downstream of each turbine during clear water and live bed single and multi-turbine experiments. Scour depths normalized by rotor diameter (d_T = 0.15m).

Bedform characteristics

Channel-scale effects from the presence of operating axial-flow turbines were assessed based on bedform geometric parameters estimated in the channel reach downstream of the device(s) ($0d_T$ to $33d_T$). Primary focus was placed on bedform wavelengths, λ_b, and height, h_b. Bedform length and height were calculated using results from both the interface method as well as the bedform tracking methods. Figure 3.12 shows the results from calculating the interface width, w_i. The intersection between power-law fit equations for the small-scale linear portion on a log-log plot and the large-scale saturation lengths is typically used to find the characteristic bedform length and roughness amplitude, or half of the bedform height. In general, results agree with values for bedform length and height calculated with the crest tracking method primarily used for this analysis and reported within this paper.

Figure 3.13 presents results from tracking individual dune crests throughout each experiment. Due to potential side wall effects, analysis was focused on the center bed elevation profile ($y/d_T = 0$). To maintain a constant analysis domain, bedform geometric characteristics were monitored in the section from $x = 8$m to 13m, a 5m section downstream of the primary turbine. A summary of bedform wavelengths and heights calculated during analysis is presented in Table 3.4.

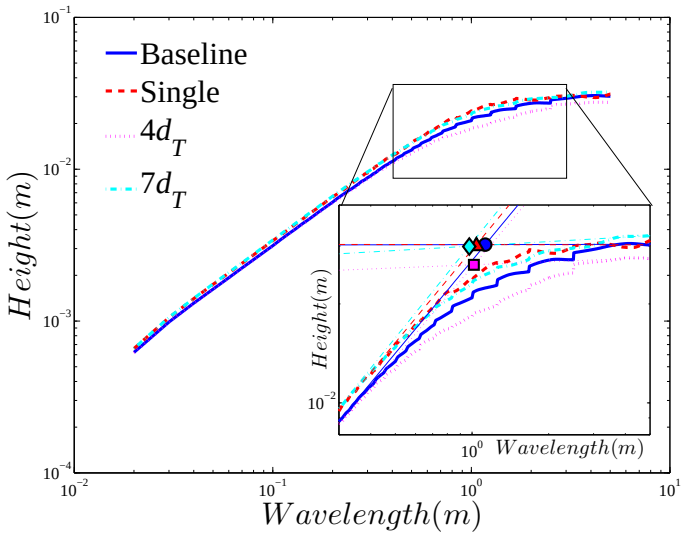

Figure 3.12: Interface width, w_i, plots for each of the turbine configurations investigated under live bed conditions.

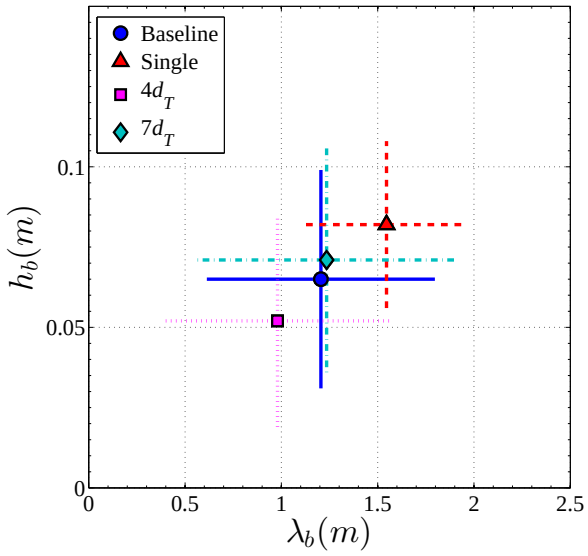

Figure 3.13: Scatter diagram comparing wavelength, λ_b (m), and bedform height, h_b (m) among each of the four live bed scenarios. Symbols represent median values. Lines represent ± 1 standard deviation for the corresponding variable.

		Bedform Tracking	**Interface Width**
Baseline	$\bar{\lambda_b}$	1.21m	1.13m
	h_b	0.07m	0.06m
Single	$\bar{\lambda_b}$	1.55m	1.04m
	h_b	0.08m	0.06m
$4d_T$	$\bar{\lambda_b}$	0.98m	1.02m
	h_b	0.05m	0.05m
$7d_T$	$\bar{\lambda_b}$	1.24m	0.98m
	h_b	0.07m	0.06m

Table 3.4: Summary of bedform geometric characteristics, $\bar{\lambda_b}$ and h_b, for each of the experiments found using two methods: Bedform Tracking and Interface Width.

3.5 Discussion

The authors acknowledge that the scale of the bedforms present in this study is extreme (h_b/d_T $\approx$ 0.3 to 0.5), and to date, locations where pilot projects and current turbine installations are present do not have such large-scale mobile features. As technologies advance and permitting barriers are reduced in this field, it may become feasible to target locations with active bedload transport for MHK turbine and/or multi-turbine power plant installations. Regardless, an understanding into the role large-scale structures, whether stationary or mobile, have on device performance and the impact such devices can have on the downstream sediment transport is critical.

3.5.1 Effects of sediment transport on turbine performance

Mean and fluctuating voltage from the primary turbine was effected both by the presence of an additional turbine upstream of its location as well as the passage of large-scale bedforms. The range of voltage fluctuations with bedforms was on the order of 2 to 3 times greater than during clear water experiments. The greatest influence on mean power, however, was the proximity to the turbine rotor plane that the peak of the dune was located. Within approximately $2d_T$ ($\approx 0.2\bar{\lambda}_b$), turbine mean voltage increased, as did the fluctuations. This could provide both benefits and possible difficulties for turbine power production. On one hand, the increase in power is likely due to the increase in velocity resulting from the decrease in cross sectional area above the dune. On the other, the turbine energy extraction plane (EEP) of the turbine may be directly intercepted by the shear layer extending downstream from the dune crest. Interestingly, the optimal turbine spacing when aligned in the axial, streamwise direction seems to be $7d_T$. At this spacing in clear water conditions, voltage output was most similar to that of a single turbine installation. In the case of live bed transport, this spacing had a slight decrease in voltage intensity, possible being a benefit for turbine structural integrity.

The results from the cross-correlation analysis provide an indication that the turbine performance (i.e. voltage) is affected by the upstream proximity of large-scale bedforms. In relation to the five zones of flow characteristics presented in the introduction and summarized by [95, 97], the peak in bed elevation correlation with mean voltage or RMS voltage indicates the zone of which the EEP is operating in. The single turbine experiment (Figure 3.9), the peak correlation between the bed elevation and the mean voltage occurs when peak elevation, z_p, is located at x/d_T = -1.2 ($\approx 0.12\bar{\lambda}_b$). That is, the mean turbine voltage output is at a maximum when maximum bed elevation occurs at this location. At this spacing, the flow is acting as a jet off the top of the dune crest, providing maximum velocities and available energy for the turbine. Additionally, the shear layer extending downstream from the dune crest may interact with the

EEP, potentially affecting the turbine by: a) exposure to high TKE values, and b) potential exposure to elevated levels of suspended sediments. In general, maximum mean voltage output occurred when the bedform peak was in this near-field upstream region, and these findings are corroborated in the results shown in Figure 3.8. The downstream shift towards the turbine for the peak correlation between bed elevation and RMS voltage possibly indicates that the lower portion of the EEP is interacting with either the highly turbulent separation zone near the lee-side slope of the dune face, or the wake zone characterized by increased levels of turbulence intensity.

In contrast to the single turbine experiment, with a second turbine located $4d_T$ upstream, the turbine at $x/d_T = 0$ was positioned in the near-wake region of the turbine at x/d_T = -4. Lower available energy and increased wake turbulence levels decreased the overall voltage output from the primary turbine at $x/d_T = 0$. Local scour and deposition created by the upstream turbine influenced maximum voltage output was increased only when the dune crest was very close to the turbine. This is possibly a result of the decrease in cross-sectional flow area and a relative increase in available energy in the flow compared to the typical flow field the turbine is exposed to in the wake of another turbine. Additionally, since the turbine faces high levels of turbulence from the wake of the upstream turbine, no substantial peak in bed-RMS correlation occurred upstream of the primary turbine. As the upstream turbine was moved even further upstream to x/d_T = -7, peak values in the correlation plots moved upstream, returning to locations similar to that found from the single turbine experiment. This indicates a decoupling of the effects of the wake from the upstream turbine and the voltage output of the primary turbine at x/d_T = 0, and reestablishment of a stronger correlation between the bed elevations and the voltage output. Similar to the case with the single turbine, the EEP of the turbine is likely feeling the effects of various flow zones above the dunes as they migrate past its location. What seems to be the case is that bedform geometry effects the turbine performance, yet only when the scale of the bedforms are large enough (i.e. on the scale of the blade length). Presumably, as the hub height and EEP are elevated further above the bed, the influence of channel bottom roughness is minimized. Regardless, the small-scale roughness features may only impact the turbine performance by changing the channel roughness, thereby changing the approach flow profile. It is only the largest scales of bedforms that directly impact the turbine performance, and when located within 1-2d_T ($\approx$ 0.1-0.2$\bar{\lambda}_b$).

3.5.2 Effects of turbines on sediment transport

Continuous sonar measurements provided the possibility of tracking bedform geometric characteristics during each experiment. Results from both clear water and live bed experiments show that turbine(s) have a local effect on scour and deposition. In nearly all cases, scour depths were

greater during live bed transport conditions when compared to the equivalent configuration for clear water experiments. These results have direct implications for turbine foundations and assumptions made for maximum scour depths in the field. In general, results did indicate that there is not an appreciable systematic modification to the channel-scale bedform characteristics when turbine(s) are present, as the observed changes are within the typical bedform variability of undisturbed erodible channels. Interestingly, the case with only a single turbine installed resulted in longer bedforms with an increase in bedform height compared to the baseline experiment. What remains potentially interesting for a full scale power plant deployment, yet to be fully understood from a fluid mechanics perspective, is the case with turbines spaced at $7d_T$. Bedform geometric characteristics remained most similar to the baseline case, local scour was minimized near both turbines, and the mean voltage output was highest from that of all other multi-turbine experiments.

Additionally, the results from time-averaged water surface elevations show that spacing turbines at $7d_T$ provides a brief section of relatively undisturbed flow that could result in improved structural integrity for nearby turbines. The presence of surfaces waves that interact with the EEP of the turbine can cause a cyclic loading on the rotor and have significant impacts on power production. Performance coefficients, however, have been shown to only be slightly impacted by surface waves [132, 37, 38].

3.5.3 Scaling between model and prototype

It is commonly known that it is not possible to match both field scale Reynolds number and Froude number for model studies of hydrokinetic turbine systems. Reynolds number is an important non-dimensional parameter to match when focusing directly on the power production of a device, as it influences the lift and drag characteristics along the blade. This study focuses more closely on the interactions between the turbine device(s) and the physical channel environment and sediment transport; therefore, Froude number scaling is more appropriate to achieve similarity between model and prototype scales. As reported above, $Fr \approx 0.27$ for the Clear Water experiments and $Fr \approx 0.33$ for the Live Bed experiments (see Table 3.1). Froude numbers at field scale are slightly lower, but in a very similar sub-critical range when compared to the model scale studies. For example, at the New York Roosevelt Island Tidal Energy (RITE) site in New York where Verdant Power has turbines installed (although no sediment transport occurs due to no supply of sediment), the hub height velocities range between 1.5ms^{-1} to 3.0ms^{-1} with a depth of 10m to 12m or more, resulting in $Fr \approx 0.14$ to 0.27. In the lower Mississippi River, a region where preliminary MHK permits have been sought after, similar Froude numbers exist. For the tidal energy site in Strangford Lough where the SeaGen-S 16m diameter turbine has been installed, design flow depths (< 38m) and expected velocities (> 2.5ms^{-1}) result in field

scale Froude numbers approximately 0.13 and higher.

Geometrically scaled sediment would result in a field scale grain size of approximately 59mm. Although this is possible, these sediments would not be representative of the model scale transport rates and bedform sizes that developed. To scale actual field scale bedform sediments to this model scale, cohesive forces between sediment grains could influence transport characteristics. This said, turbulent flow characteristics over migrating dunes are governed by the bedform shape (i.e. recirculation region, flow acceleration on the dune stoss slope, etc.) rather than by grain roughness. As dunes scale with the flow depth, the experimental conditions investigated here reproduce the large scale turbulent motions impinging on an instream turbine at prototype scale, resulting from a dominant form drag contribution (see e.g., [95, 97, 133].

An additional consideration when investigating model scale hydrokinetic turbines is top tip submergence. At full scale, this parameter ultimately governs the available navigational clearance above the turbine. The top tip submergence used in these experiments is similar to the Verdant Power RITE site deployment (5m full-scale rotor diameter); however, those turbines are installed outside of an active navigation channel. For larger scale devices installed in tidal environments, such as the SeaGen 16m diameter 1.2MW rotor in Strangford Lough (soon to be 20m diameter, 2.0MW), a similar top tip submergence would be approximately 8m (10m) below the free surface. This device is designed for depths up to approximately 38-40m; therefore, the hub height and top tip submergence ratios used in these experiments are on the order of full-scale deployments. Presumably any full-scale deployments would be well-marked with surface buoys to avoid navigation directly above the device, unless the devices are installed well below the required under-keel clearance levels for the channel.

As it could potentially have varying effects on local scour and far-field sediment transport, future studies should investigate additional geometries (and axial-flow vs. cross-flow devices), foundation characteristics and inter-array turbine spacing. Additionally, top tip submergence and bottom tip clearance above mean bed elevation are important parameters to investigate. Increasing top tip submergence will minimize navigational concerns; however, to do so requires lowering the bottom tip and rotor clearance above the mean bed elevation. This may alter local scour patterns and far field sediment transport characteristics.

3.5.4 Further applications

The work presented here provides insight that can be incorporated into future work on active control of devices installed with continuously changing boundary conditions due to large-scale geomorphic features (and stationary man-made structures) that introduce coherent eddies into the flow environment. Theoretically, an increase in individual device performance can be realized through either rotor angular velocity control or individual blade pitch control. To date, in

practice individual pitch control is often difficult to realize and achieve the theoretical increase in power performance because of the stochastic nature of turbulence in the environment introduced by either natural or man-made structures. Optimal control can, however, filter out the higher-frequency fluctuations and provide mid-level control that can account for fluctuations in the large-scale coherent eddies introduced in natural waterways (i.e. from large-scale sediment dunes, channel meander patterns and asymmetry, etc.). Further understanding of the interactions MHK devices have with the upstream and downstream geomorphic environment can, and should, coordinate with the development of device control. In terms of required input to the control strategy, this investigation provided a measure of effective bedform distance that can be technically feasible and affordable to implement with in-situ sonar sensors.

3.6 Summary & Conclusions

The work presented here expands on the limited literature available today on interactions between hydrokinetic turbines and erodible channels (see [5] and references therein). Experiments were conducted in both clear water and live bed transport conditions in a laboratory flume with recirculating sediment. Primary focus was on the interactions between large-scale bedforms and axial-flow hydrokinetic turbine(s).

The authors acknowledge that only a limited portion of the wide parameter space has been explored so far. In particular, we did not vary the sediment size ($d_{50}/h = 0.0067$) and sorting, the size of the rotor ($d_T/h = 0.56$) and the mean hub elevation above the sediment layer ($h_{hub}/h = 0.48$); the latter two define a blockage ratio of $\eta = 6.8\%$ and an average gap of $0.37d_T$ between the lower blade tip and the sediment surface, which is expected to be relevant in terms of local flow acceleration and local increase of wall shear stress. Additionally, experiments were performed in the same morphodynamic conditions with one dominant bedform type, roughly scaling with the turbine rotor as $\lambda_b/d_T \approx 6$ to 10 and $h_b/d_T \approx 0.3$ to 0.5.

For the conditions tested in our experiments the following indications can be outlined:

- Single and aligned turbine configurations were observed to only locally influence the bed topography in an area approximately $6d_T$ by $2d_T$ in the streamwise and spanwise direction, respectively (also see [5]).

- In general, i) the presence of both additional turbines and/or bedforms results in decreased performance of the turbine, ii) turbine-bedform interactions are expected to be amplified by higher or steeper bedforms, or by a larger rotor positioned closer to the sediment layer.

- Approaching bedforms reach a critical zone within approximately $2d_T$ ($\approx 0.2\bar{\lambda}_b$) upstream

of the turbine, where the bed elevation profile is closely correlated to the turbine performance (in terms of voltage output). Within this nearby region, mean voltage output tend to increase, as well as voltage intensity levels. These effects are likely related to the evolution of specific turbulent flow regions along with bedform migration. These findings can inform possible control strategies for axial-flow MHK devices.

- Downstream of the turbine(s) location in a region spanning from near-field (approximately $1d_T$ ($\approx 0.1\bar{\lambda}_b$)) to far-field (approximately $33d_T$ ($\approx 4.1\bar{\lambda}_b$)), a bedform detection technique revealed that median values for bedform wavelength, $\bar{\lambda}_b$, and bedform height, h_b, only slightly vary within the range of values encountered in the undisturbed baseline case; therefore, the presence of turbine(s) does not seem to impact the far-field sediment transport or morphodynamic characteristics of the channel under the aligned turbine configuration tested thus far.

- Regardless of the relatively large bedforms with respect to the turbine hub height, no blade damage was observed in any of the experiments, implying that the annular shear layer and local acceleration below the bottom tip responsible for the increased scour surrounding the device also acts to protect the rotor from potential impacts with the incoming bedforms.

- Further investigations are suggested, including but not limited to cases with $7d_T$ turbine spacing to confirm and explain the reduced scour in clear water and live bed experiments and increased performance with respect to other aligned multi-turbine spacings. Both preliminary findings support $7d_T$ is the optimal spacing for aligned axial-flow hydrokinetic devices.

As MHK device installations move towards medium to large arrays of turbines, the interactions between erodible environments and turbines may display more complex bathymetric changes as compared to those observed in this study for two aligned turbines; however, these results still provide an indication of the individual interactions between turbines and large-scale roughness features within natural and complex topographic channels. The local blockage of the turbine rotor and presence of the support structure will induce local scour that needs to be taken into account during foundation design and rotor height placement. Larger arrays of turbines may decrease the transport capacity in the channel, possibly impacting inter-array transport, near-by channel bank stability, and far-field sediment transport characteristics, more so than a single or two turbine array will. As the MHK development community improves its understanding of turbine-sediment interactions, studies should continue to quantify potential inter-array and far-field channel impacts imposed by medium and large arrays of turbines.

3.7 Notations used in Chapter 3

A = flow cross-sectional area, m^2
B = number of blades, #
b = channel width, m
C_L = blade chord length, m
d_{50} = mean sediment grain diameter, m
d_h = turbine hub diameter, m
d_m = turbine motor diameter, m
d_T = turbine rotor diameter, m
f_T = turbine rotational frequency, Hz
Fr = Froude number $\left(Fr = u/(gh)^{1/2}\right)$, [-]
h = flow depth, m
h_b = bedform height, m
$\bar{h_b}$ = median bedform height, m
h_{hub} = turbine hub height, m
l_m = turbine motor length, m
I_u = streamwise turbulence intensity ($I_u = u'/u$), %
L = channel length, m
N = number of samples, #
Q_w = flow discharge, m^3s^{-1}
R = turbine rotor radius, m
Re = Reynolds number ($Re = (U_\infty h)/\nu$), [-]
S = turbine hub height submergence, m
S_w = water surface slope, %
t = time, s
u = streamwise velocity, ms^{-1}
u' = streamwise velocity fluctuations, ms^{-1}
u^* = shear velocity, ms^{-1}
u^*_{cr} = critical shear velocity, ms^{-1}
U_{hub} = hub height velocity, ms^{-1}
U_∞ = bulk velocity, ms^{-1}
v = spanwise velocity, ms^{-1}
V = turbine motor voltage, volts
$\bar{V}$ = mean voltage, volts
v' = voltage fluctuations, volts
w = vertical velocity, ms^{-1}

w_i = interface width, m
x = streamwise coordinate, m
y = spanwise coordinate, m
z = vertical coordinate, m
z_b = bed surface elevation, m
z_p = bedform peak elevation, m
z_w = water surface elevation, m

Greek symbols
λ = tip speed ratio ($\lambda = \Omega R/U_{hub}$), [-]
λ_b = bedform wavelength, m
$\bar{\lambda_b}$ = median bedform wavelength, m
λ_C = bedform crest-to-crest wavelength, m
λ_T = bedform trough-to-trough wavelength, m
η = turbine rotor blockage $\big(\eta = (\pi d_T^2)/(4A)\big)$, %
η_C = bedform crest elevation, m
η_T = bedform trough elevation, m
ν = kinematic viscosity of water, $\mathrm{m^2 s^{-1}}$
Ω = turbine rotor tip speed, rad $\mathrm{s^{-1}}$
Φ = power spectral density, $(\text{quantity})^2/\mathrm{Hz}$
σ = turbine rotor solidity ($\sigma = (BC_L)/(2\pi R)$), %
ρ_0 = correlation coefficient at lag zero, [-]

Chapter 4

Hydrokinetic turbine operating in meandering asymmetric channels

The following chapter has been submitted for publication and is currently under review in *Water Resources Research*.

Hill, C., Kozarek, J., Sotiropoulos, F., and Guala, M., (2015), Hydrodynamics and sediment transport in a meandering channel with a model axial-flow hydrokinetic turbine, under review in *Water Resour. Res.*.

4.1 Introduction

Marine hydrokinetic (MHK) energy technologies provide an opportunity to broaden the renewable energy portfolio in an effort to meet local energy demand, reduce carbon footprint, and minimize fossil fuel consumption. Advancing these technologies requires both rapid development and deployment into natural environments of increasing hydrodynamic and morphodynamic complexity. Unfortunately, uncertainty surrounding potential environmental impacts poses a challenge for emerging companies to adequately address the concerns raised by overseeing agencies during all steps of site development, from environmental permitting to pilot project monitoring. It thus remains critically important for the growth of the MHK industry and for the development of sustainable riverine and coastal communities that researchers elucidate the interactions between single or multiple energy harnessing devices and the surrounding environment, including both ecological and geomorphic response [8, 3, 19]. While a growing effort has been focused on understanding the effects of MHK deployments on fish habitat and population

diversity and safety [134, 135, 136], an often overlooked, key impact area is the morphodynamics of erodible substrates and the connections between sediment transport, hydrodynamics, and the aquatic biota [128]. Compared to straight channels with non-erodible beds, natural waterways are characterized by a broad range of large scale flow structures modulated by bedform evolution and migration as well as by channel curvature and point bar configuration [137]. The link between topographic complexity and flow complexity is important to predict the optimal deployment location in terms of mean velocity U (note that the device power production, $P \propto U^3$) and also in terms of reduced variability of the flow field (limiting unsteady loads on blades, shaft and support tower of MHK devices). For multi-turbine array deployments, the same requirements apply, adding the design parameter of the optimal distance between MHK devices, a criteria based on mean velocity recovery in the wake of the rotor.

Many recent laboratory experiments and simulations have focused on the hydrodynamics of MHK turbines and downstream wake recovery in straight rectangular flumes or tow tanks. For example, [26, 138, 139] characterized the near-wake environment (less than 10 rotor diameters, d_T) while [6] and [31] have shown detailed wake recovery up to $15d_T$. [140] used porous disks to investigate wake recovery up to $\approx 25d_T$ and lateral wake velocity deficit to establish lateral spacing requirements in multi-turbine arrays. [29] reports on the far-field wake of a 3-bladed axial-flow turbine ($d_T = 0.5$m), showing wake velocity deficit remains at approximately 10–15% up to $35d_T$ downstream of the rotor location. Numerically, [24] and [116] have demonstrated the benefits of utilizing state-of-the-art large eddy simulations for investigating wake characteristics of a full-scale and model axial-flow turbine, and for identifying governing mechanisms of wake meandering, providing new insight into the physics of marine turbines, their performance, and characteristics of the near and far-field wake. Additional numerical work investigated far-field wake effects within multi-turbine array configurations [141, 142, 54], demonstrating how numerical approaches are advantageous for investigating many configurations to determine optimal layout of arrays.

Despite some newer companies targeting man-made flood diversion and irrigation canals for hydrokinetic energy production, in reality, most installations will not occur in rectangular or trapezoidal channels. In fact, for economic viability and long-term renewable and reliable energy contribution, hydrokinetic turbine arrays must target deep tidal and river channels or off-shore coastal regions with strong ocean or tidal currents. For horizontal axis turbines, $P \propto d_T^2$, implying that the channel depth represents the tightest constraint. While providing large cross-sectional area, natural sites are typically characterized by abrupt changes in topography, channel roughness, bedform induced roughness, channel sinuosity, submerged obstacles, and a number of other physical constraints that directly impact the turbulent hydrodynamic environment. These geometric inhomogeneities such as large submerged obstacles (i.e. boulders, rock ledges)

or man-made structures (i.e. bridge piers, abutments, upstream turbines) introduce periodic large-scale coherent eddies that may intersect a turbine's rotor, causing undesired unsteady structure loading and decreased energy production. Recent work by [1] examined the effects such coherent eddies have on turbine performance and wake characteristics using vertically oriented cylinders to introduce eddies of various sizes.

Until recently, investigations into the morphodynamic impact resulting from single and multi-turbine arrays remained unstudied. Numerical investigations have been undertaken by [43], [44] and [45], where they investigated the far-field effects of large-scale arrays in areas such as coastal England and the Irish Sea. At this scale, computational costs prohibit studying local effects and allow for generalized representations of each turbine or the turbine array. Regardless, such studies have indicated that large-scale conversion of kinetic energy to electrical energy using hydrokinetic turbine devices will likely alter sediment transport and depositional patterns in the far-field. More recently, advancements in computational methods and super-computing resources have allowed integration of high-resolution hydrodynamic and morphodynamic processes to simulate coupled turbulent flow and sediment transport in natural waterways around rotating hydrokinetic turbines and other hydraulic structures [48, 50].

In the work leading up to this study, a straight channel with an erodible bed was used to investigate the local and far-field effects of axial-flow hydrokinetic turbine(s) on sediment transport, and the role that large-scale migrating bedforms have on turbine performance [5, 42]. These experiments showed only locally enhanced scour and deposition induced by a small-scale turbine. Measurements also indicated how bedform features located within a critical zone approximately 2–3d_T upstream of the turbine location were able to impact performance as a result of the time varying flow characteristics imposed by (migrating) dune geometry [95].

The interactions between axial-flow turbines and meandering channels with asymmetric channel cross-section geometry have yet to be investigated. To address these interactions, an experiment was conducted in the Outdoor StreamLab (OSL) research basin at the University of Minnesota's St. Anthony Falls Laboratory (SAFL). The OSL has been the subject of recent research demonstrating novel bedform morphodynamic measurement techniques ([143]) and advanced numerical methods capable of simulating turbulent flow and sediment transport in arbitrarily complex channel topography [137, 144, 24, 145, 50, 146]. The results of these studies provide key insights into the complex flow patterns and coherent structures occurring within the asymmetric cross-section developing in a meandering channel. Of key interest for the present study is the effect of a MHK turbine on the morphodynamics and hydrodynamics of a meandering river, in particular on the longitudinal and transverse sediment transport along the meander point bar, on dune migration and deformation along the meander, and on the variability of the flow impinging on the turbine rotor. The experiments and facility are described in Section

4.2. Results from data collected during the Baseline and Turbine experiments are presented in Sections 4.3.1 and 4.3.2, respectively. Finally, discussion (Section 4.4) and concluding remarks (Section 4.5) summarize the interactions between sediment transport, complex flow patterns, and a model hydrokinetic turbine operating in a meandering channel, including implications for development of MHK devices and comparison with results obtained in a straight channel.

4.2 Experimental Facility

The experiments were conducted in the OSL Riparian Basin research facility located at SAFL at the University of Minnesota (UMN). The OSL is a field-scale meandering stream research facility with control of bulk flow (Q_w) and sediment supply (q_s) rates (Figure 4.1a). A transportable data acquisition (DAQ) carriage provides researchers the ability to collect high-resolution, spatially referenced data, including channel and floodplain topography, water surface elevation, and three-dimensional (3D) velocity measurements (Figure 4.1b). The 40m by 20m Riparian Basin, once an emergency spillway for St. Anthony Falls on the Mississippi River, contains the OSL channel, a $\overline{b} \approx 2.7$m wide, $\overline{h} \approx 0.3$m deep (bankfull conditions) meandering channel (sinuosity, $SI \approx 1.3$, and average channel bed slope, $\bar{S}_b \approx 0.007$). The sand-bed channel ($d_{50} = 0.7$mm coarse sand) has been continuously supplied with Mississippi River water since 2008. The channel banks remain relatively stable through the use of coconut fiber matting and well established vegetation. Coarse sand transports as bedload through the system, bypassing riffle zones comprised of coarse cobbles and depositing as point bars on the inside of each meander bend creating the asymmetric channel cross-section topography typical of sand-bed meandering systems. Transported bedload sediment is captured in a downstream settling basin and hydraulically transported upstream to a sediment holding tank, where a variable-speed auger system feeds sediment into the channel at a constant, user-defined rate. In this case, $q_s \approx 6.9$kg/min (dry sand). The DAQ carriage location is surveyed by a total station Sokkia X30RK. Using the DAQ carriage reference points, all data can be converted from local carriage coordinates to global OSL coordinates, providing a method for referencing current data to historic topographic and flow data collected within OSL. Through a series of overlapping DAQ carriage topography data scans, the OSL channel topography was mapped along its entire length in 2010 (Figure 4.2a). A closer view of the middle meander bed (Figure 4.2b) highlights locations of the hydrokinetic turbine model, data collections zones, and recently surveyed channel banks during these experiments. The model turbine used in the OSL experiments was a 1:33 scale three-bladed axial-flow turbine with rotor diameter, $d_T = 0.15$m, and was mounted near the apex of the middle meander bend (Figure 4.1c,d). The turbine was installed in the channel such that the rotor plane was parallel to the channel cross-section. Turbine hub height was $h_{hub} = 0.147$m, resulting in an approximate channel blockage ratio of

4%. For additional details on the turbine geometry, operating characteristics, and previous work using the same turbine, the readers are directed towards [5, 42].

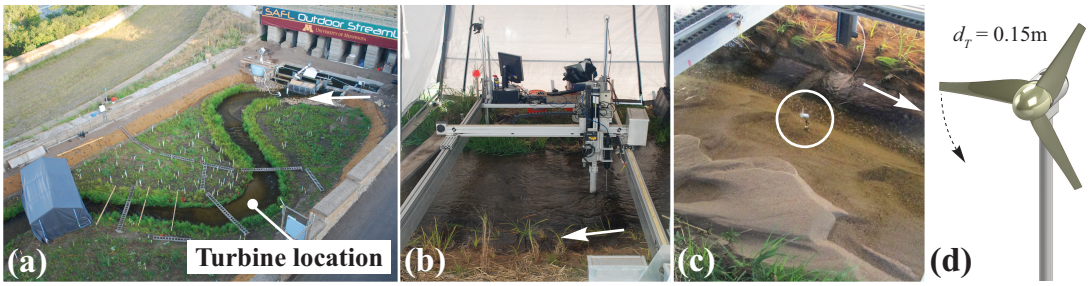

Figure 4.1: (a) Photograph of the St. Anthony Falls Laboratory (SAFL) Outdoor StreamLab (OSL). (b) OSL data acquisition (DAQ) carriage used for data collection. (c) Hydrokinetic turbine model ($d_T = 0.15$m) mounted near the apex of the middle meander bend. Arrows in photos indicate flow direction.

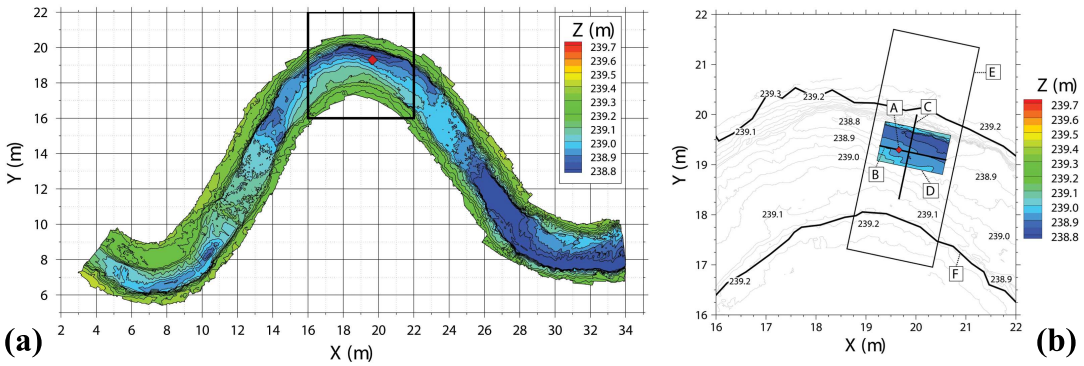

Figure 4.2: (a) OSL channel topography mapped in 2010. Location of turbine indicated by red diamond at (X,Y) ≈ (19.7m,19.3m). (b) Topography of middle meander bend outlined by box in (a) showing channel topography from 2010 (light gray contour lines), turbine location (A, red diamond), streamwise sonar transect location (B), spanwise sonar transect location (C), final near-turbine sonar topography zone (D), boundary of data acquisition (DAQ) carriage (E) from which sensors were mounted (see Figure 4.1), and the channel bank edges (F). Flow is left to right is both images.

For both the baseline and turbine experiments, the bulk flow rate was set to $\bar{Q_w} \approx 280$ L/s (bankfull channel conditions). The OSL channel was run at bankfull conditions for 2 days leading up to the testing period to ensure the channel had reached quasi-equilibrium transport conditions

for the flow and sediment supply rates used. Then, the baseline experiment (10/09/2014) ran for approximately 8 hours, while the turbine experiment (10/10/2014) ran for approximately 7 hours. A sonar transducer repeatedly traversed a streamwise and a cross-stream transect. Referring to Figure 4.2b, the streamwise transect (B) passed over the top of the turbine (location A) and collected bed elevation data from $x/d_T \approx$ -2.6 to $x/d_T \approx 6.4$ at $\Delta x = 0.01$m spacing. The cross-stream transect (C) traversed the channel at $x/d_T \approx 1.4$ downstream of the turbine and collected bed elevation data from $y/d_T \approx$ -6.3 (right bank) to $y/d_T \approx 5$ (left bank) at $\Delta y = 0.01$m spacing. The time intervals between sequential transects was $\Delta t \approx 12.3$s and 12.7s for the streamwise and cross-stream sections, respectively. At the end of both the baseline and turbine experiments, flow was decreased to baseflow conditions ($Q_w \approx 25$ L/s), and a sonar patch scan measured ending channel topography for a region within the meander (see monitored area (D) in Figure 4.2b). Figures 4.3a and 4.3b show the final topography from the baseline and turbine experiments, respectively. Note that topographic data in the OSL reference system report elevation above the sea level.

A Nortek Vectrino+ acoustic Doppler velocimeter (ADV) was used to measure 3D velocity at 3 locations along the same streamwise transect (B) used for time-resolved bed elevation data (Figure 4.2b). The ADV sampled instantaneous U_i, V_i, and W_i values at the same elevation of the turbine hub height, $z_{hub} = 239.086$m (with the hub height defined with respect to the averaged bed elevation, $h_{hub} = 0.147$m), at streamwise locations $x/d_T =$ -2.9 (upstream), 0 (turbine), and 4.4 (downstream). Velocity data were collected at 100Hz for $t = 45$ minutes at each location. Additionally, a series of cross-stream velocity profiles were collected at hub height in the turbine wake using a moving ADV sampling and averaging method, described in Section 4.3.2. The five profiles were located downstream of the turbine from $x/d_T = 1.4$ to 5.4 at $1d_T$ streamwise spacing. The ADV was traversed from $y/d_T =$ -1.5 to 1.2 at a speed of $U_{adv} = 1$mm/s.

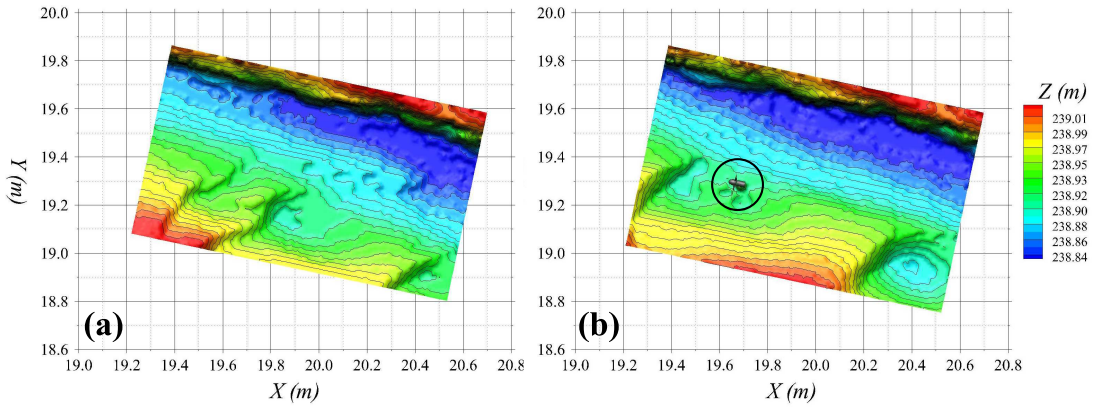

Figure 4.3: (a) Ending topography after baseline experiment and (b) after turbine (circled) experiment. Flow is left to right is both images.

4.3 Results

4.3.1 Baseline Experiment

Baseline data were collected to determine bedform characteristics and velocity statistics within the investigated region in the middle meander bend of the OSL. The following presents results on dune geometry, migration, orientation and variability, and mean velocity and turbulent fluctuations before installing the model hydrokinetic turbine in the channel.

Morphodynamics

At the end of the baseline experiment, a rectangular section of the channel bed topography was mapped prior to installing the model hydrokinetic turbine (Figure 4.2b area (D), consistent with the scan in Figure 4.3a). These data provide channel geometry initial conditions for the turbine experiment. The kinematics of migrating bedforms along the meander bend results in a distortion of the bedform geometry with appreciable effects on the bedform crest orientation. This distortion largely reflects the channel boundary shear stress imposed on the sediment, and therefore results in varying bedform migration velocities in the cross-stream direction [147]. Acknowledging the curvature of bedform crests, Figure 4.3 allows for an estimate of the bedform approach angle within a range of approximately 35°-40° with respect to the turbine rotor plane (in a straight channel, the approach angle of a 2D dune would be $\sim 0°$). Channel cross-section variability in depth, bedform height, migrating bedform velocity and local mean flow velocity results in steady and unsteady loads on turbine components that horizontal axis turbines are

not subject to in a straight, non-erodible channel.

Repeated streamwise and cross-stream bed and water surface elevation scans reveal the range of instantaneous bed surface elevations and provide a method for calculating the mean bed surface over the span of approximately 2 hours during cross-stream profile data collection and over 2.25 hours during streamwise profile data collection (Figure 4.4). During the two hour period of cross-stream profile data collection, approximately 15 bedforms migrated past this location within the meander, as evidenced by the space-time contour illustrated in Figure 4.5a. The timeseries of bed elevations at the cross-stream location where the turbine was eventually placed is provided in Figure 4.6 (location referenced by arrows at $y/d_T = 0$ in Figure 4.5), showing bedform heights, $\overline{h_b} \approx 0.087$m, and a bedform crest period of $\overline{T_b} \approx 7.7$ minutes. Mean flow depth at the location where the turbine was eventually placed was $\overline{h} = 0.306$m. Maximum cross-sectional channel depth was $h_{max} = 0.394$m.

Average bedform velocity, $\overline{U_b}$, was estimated through cross-correlation analysis of sequential streamwise sonar bed elevation measurements. Spatial correlation coefficients, $\rho(\Delta x)$, were averaged to find a peak correlation coefficient at $\Delta x = 0.04$m ($\rho(\Delta x) \approx 0.97$). Given the time difference, $\Delta t = 24.6$s, necessary to complete two sonar passes, the resulting average bedform velocity during baseline experiments was calculated to be $\overline{U_b} \approx 0.0016$ ms^{-1}. Using this velocity and the estimated bedform crest periodicity, T_b, the average bedform wavelength along the streamwise transect is $\lambda_b \approx 0.74$m. These bedform characteristics are quantified for the location at which the turbine was eventually placed. Due to varying bedform kinematic properties from the inner bank of the meander towards the outer bank, λ_b, h_b, and T_b may vary as qualitatively visualized in Figure 4.5a.

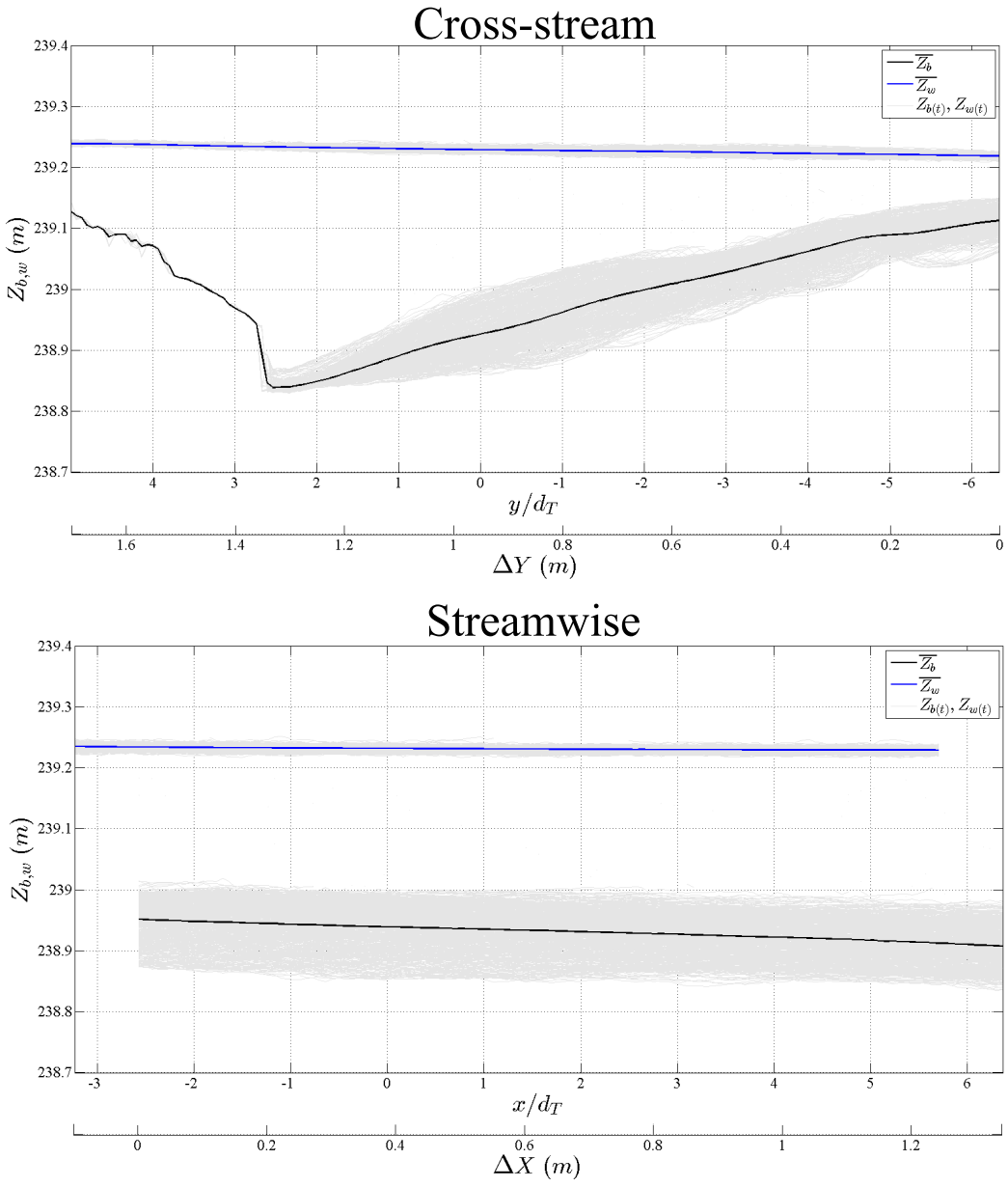

Figure 4.4: Instantaneous (light gray) and mean bed (solid black) and water surface (solid blue) elevation data in the cross-stream (top) and streamwise (bottom) directions collected during the baseline experiment.

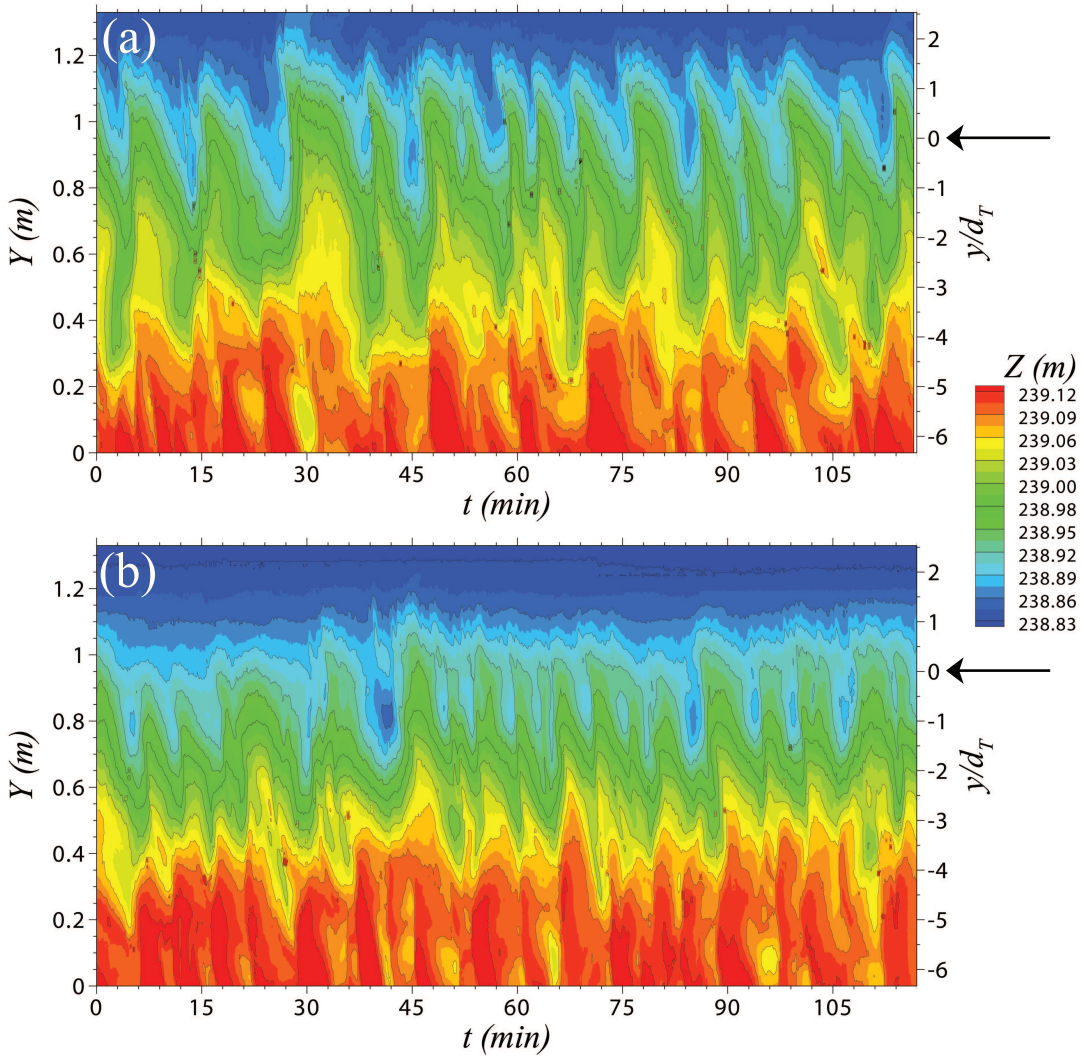

Figure 4.5: Space vs. time contours of the cross-stream sonar bed elevation data from the baseline (a) and turbine (b) experiments. Arrows at $y/d_T = 0$ indicate cross-stream location where bed elevation timeseries data are taken from and plotted in Figure 4.6.

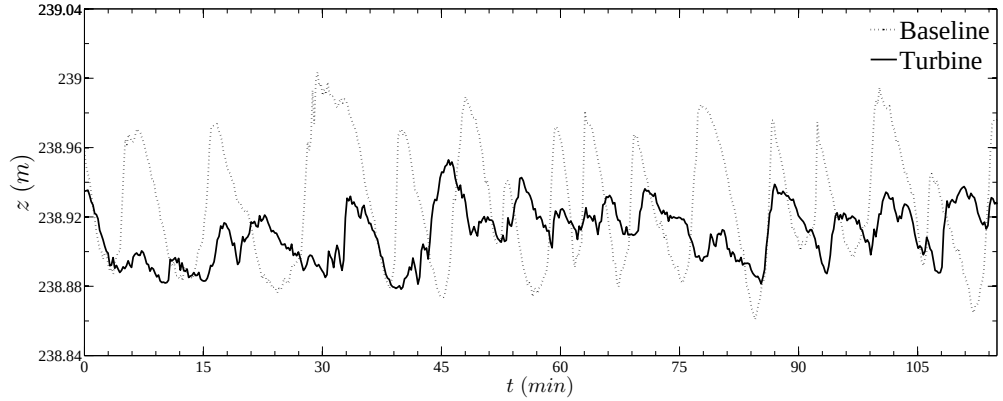

Figure 4.6: Bed elevation, z_b, timeseries comparison between baseline (dotted line) and turbine (solid line) experiments at $x/d_T \approx 1.4$ and $y/d_T = 0$.

Velocity Characteristics

Asymmetric channel cross-section geometry, migrating bedforms, and channel meandering in the OSL facility create a complex environment with turbulent characteristics affected by both local and non-local, steady and unsteady, topographic features. Locally, sediment grain roughness and bedform geometry introduce a strong variability in the streamwise direction, while non-local channel geometry such as sinuosity and asymmetric channel cross-sections give rise to secondary currents in the form of helical flow patterns and coherent circulation zones in the streamwise and cross-stream direction. Recent simulations of turbulent flow through the OSL channel using time-averaged bed topography with no mobile bedforms provide insight into these complex flow patterns in the OSL channel and highlight the development of two counter-rotating circulation cells around the middle meander, including the presence of a shear layer where these two cells merged [137]. However, it is likely that the presence of bedforms ($\overline{\lambda_b} \approx 0.74$m, $\overline{h_b} \approx 0.087$m) migrating through the OSL middle meander contaminate the signature of these secondary currents inducing strong fluctuations in the streamwise-vertical plane. Nonetheless, to characterize the flow in the region where the turbine would be placed, an ADV was placed at 3 streamwise locations (referred to as upstream, turbine, and downstream locations) to quantify mean and fluctuating 3D velocity characteristics, correlations between bed elevation of velocity direction and magnitude, and the dominant scales of turbulence in the flow along the meander. These measurements provide a baseline for comparison to any modifications induced by the presence of the axial-flow turbine model. Additionally, the comparison of baseline flow statistics at different locations is used to support the invariance of the results with respect to the turbine streamwise position within the meander, and thus the representativeness of this study.

Table 4.1: Summary of the mean ($\bar{U}$,$\bar{V}$,$\bar{W}$), fluctuating (σ_u,σ_v,σ_w), turbulent kinetic energy (k), and the integral time ($\mathcal{T}$) and length ($\mathcal{L}$) scales from the baseline (B) and turbine (T) experiments from three locations (US = upstream ($x/d_T \approx$ -2.9); Turb. = turbine ($x/d_T \approx$ 0.4), and DS = downstream ($x/d_T \approx 4.4$)) at the same elevation as the turbine hub height, h_{hub}. Statistics were calculated from 45 minute ADV records at each location. No data are available for the Turbine location during the Turbine experiment because model turbine was in the way of the ADV.

		$\bar{U}$ (m/s)	$\bar{V}$ (m/s)	$\bar{W}$ (m/s)	σ_u (m/s)	σ_v (m/s)	σ_w (m/s)	k (m^2/s^2)	$\mathcal{T}$ (s)	$\mathcal{L}$ (m)
US	B	0.658	0.055	-0.018	0.104	0.097	0.077	0.013	0.069	0.046
	T	0.673	0.109	-0.010	0.078	0.094	0.063	0.009	0.066	0.044
Turb.	B	0.676	-0.008	-0.006	0.103	0.095	0.074	0.013	0.067	0.045
	T	n/a	n/a	n/a	n/a	n/a	n/a	n/a	n/a	n/a
DS	B	0.696	-0.060	-0.002	0.096	0.083	0.070	0.011	0.069	0.048
	T	0.560	-0.027	-0.019	0.129	0.120	0.103	0.021	0.067	0.037

Table 4.1 summarizes the mean, $\overline{U_i}$, root-mean squared, σ_i, turbulent kinetic energy, k, and the integral time (T) and length (L) scales based on the velocity timeseries autocorrelation function for these three locations at the turbine hub height elevation. Because the ADV coordinate system was referenced to the DAQ carriage and turbine rotor plane and did not follow the curvature of the channel or rotate with the mean streamwise velocity direction, it is also valuable to assess the magnitude and direction of the velocity vector (Figure 4.7). Using the right-hand rule notation, the ADV coordinate system measured positive streamwise velocities, U, in the downstream direction, positive cross-stream velocities, V, towards the left bank of the OSL channel, and small but positive vertical velocities, W, upward towards the free surface. Positive horizontal angle direction, ϕ, indicates departure towards the left (outer) OSL bank, while positive vertical angle direction, θ, indicates departure towards the free surface. Table 4.2 summarizes the horizontal and vertical angles of the velocity vector at each location. The curvature of the channel has a small but noticeable effect in the baseline velocity horizontal direction, ϕ_B, switching from positive ϕ (towards left outer bank) to negative ϕ (towards right inner bank) further downstream. The flow is nearly orthogonal to the channel cross-section and turbine rotor plane where the turbine was located.

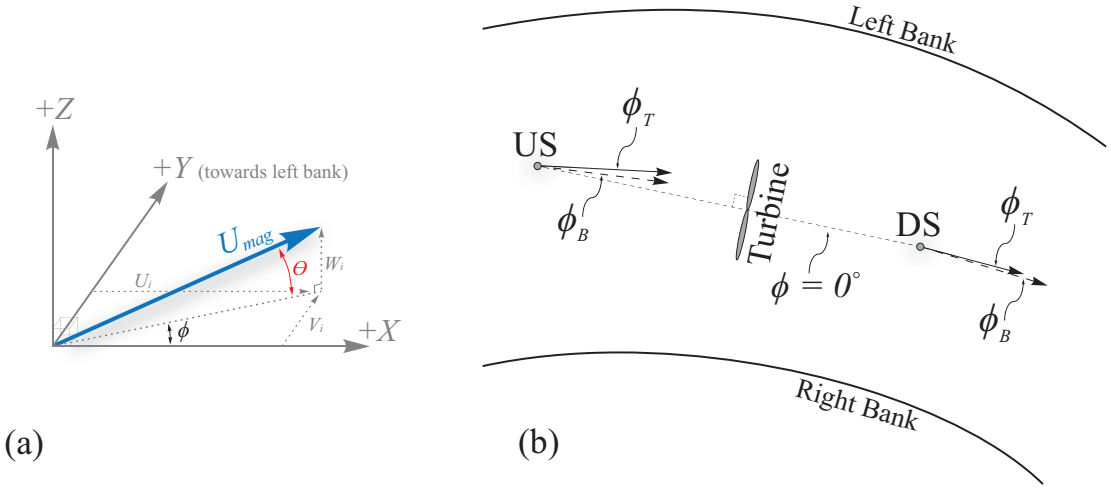

Figure 4.7: (a) Schematic of the ADV coordinate system and calculated velocity magnitude and direction ϕ (horizontal angle) and θ (vertical angle). (b) Schematic of the relative change in ϕ between baseline (subscript, B) and turbine (subscript, T) experiments, summarized in Table 4.2.

Table 4.2: Summary of the horizontal (ϕ), vertical (θ), and relative change in angle ($\Delta\phi$) of the velocity magnitude vector (U_{mag}) from the 3 ADV locations. Cross-correlation coefficients for lag zero (ρ_0) are summarized from the correlation analysis between bed elevations and velocity magnitude and direction.

Location	**Case**	ϕ (°)	θ (°)	$\Delta\phi$ (°)	$\rho_0\,(z_b : U_{mag})$	$\rho_0\,(z_b : \phi)$	$\rho_0\,(z_b : \theta)$
US	B	4.75	-1.46	n/a	0.23	-0.31	0.40
	T	9.09	-2.87	4.34	0.28	-0.04	0.11
Turb.	B	-0.74	-0.44	n/a	0.41	-0.20	0.32
	T	n/a	n/a	n/a	n/a	n/a	n/a
DS	B	-4.94	-0.14	n/a	0.70	-0.66	0.16
	T	-2.87	1.95	2.07	0.43	-0.33	0.05

Insight into the influence of bedform elevation (z_b) on the local velocity magnitude (U_{mag}) and direction (ϕ, θ) is illustrated in Figure 4.8. Simultaneous sonar and ADV measurements provide a 45 minute timeseries of bedform migration and velocity magnitude and direction at each of the three locations. Cross correlation analysis between the bed elevation timeseries, $z_b\,(t)$, and U_{mag}, ϕ, and θ are plotted in Figure 4.9, providing an even further understanding into the bedform influence on hydrodynamics at the location where the turbine would be installed.

In Figure 4.9, the cross correlation function between z_b and θ lags approximately $\Delta t \approx 1.5$ minutes behind the peak correlation of z_b and ϕ. Similarly, the peak correlation between z_b and U_{mag} appears another $\Delta t \approx 1.5$ minutes after the peak between z_b and θ. The distance between peaks in the correlation functions also provide an additional estimate for the bedform period. Because the peak correlations range between $0.45 < \rho < 0.6$, this indicates a relatively significant local effect on the hydrodynamics due to the bedforms. Table 4.2 summarizes these correlation coefficients, while further discussion on the implications of these synchronous bed elevation and velocity measurements is discussed in Section 4.4.2.

To further investigate the streamwise homogeneity of the flow in the region of interest, the integral time scale, $\mathcal{T}$, and the integral length scale, $\mathcal{L}$ of the flow (Table 4.1) are calculated from the autocorrelation function as:

$$\mathcal{T} = \int_0^\infty \rho(\tau)\, d\tau$$

and

$$\mathcal{L} = \overline{U}\mathcal{T}$$

where $\rho(\tau)$ is the auto-correlation function, defined as

$$\rho(\tau) = \frac{(u'(t)\, u'(t+\tau))}{{\sigma_u}^2}$$

where u' is the instantaneous velocity fluctuation and τ is the time lag. $\overline{U}$ is the local mean velocity.

Spectral analysis of the U, V, and W velocity components at the 3 locations during baseline experiments provides, in addition to integral scale values discussed above, further evidence that the characteristic turbulent scales were similar throughout the region of interest. Figure 4.10 illustrates the normalized velocity spectra. Here, the mean flow depth at the future turbine location ($\overline{h} = 0.306$m) and a turbulent kinetic energy velocity scale, defined as

$$u_k = \sqrt{\frac{1}{2}\left(\overline{{\sigma_u}^2} + \overline{{\sigma_v}^2} + \overline{{\sigma_w}^2}\right)}$$

were used for normalizing the calculated spectral energy density ($S(f)$, units of $\mathrm{m^2 s^{-1}}$).

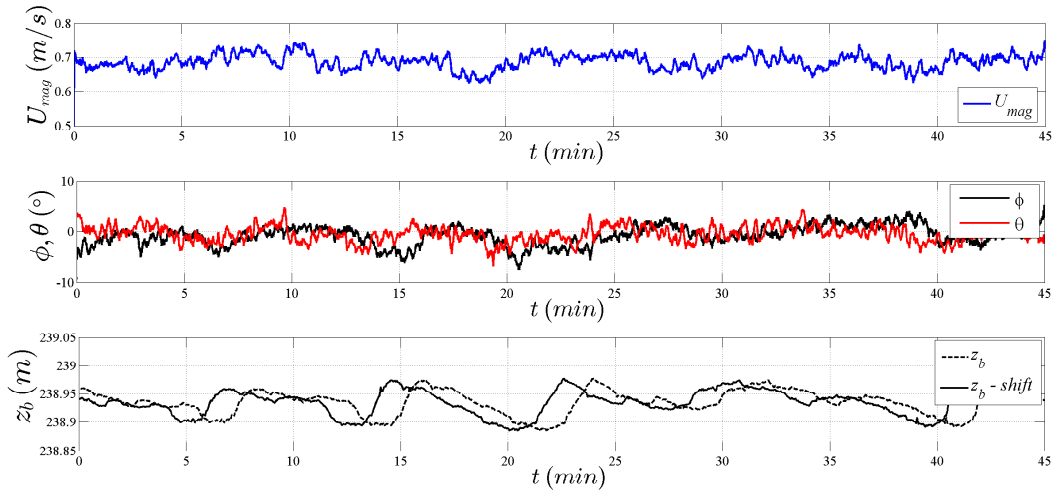

Figure 4.8: 45 minute timeseries of velocity magnitude, U_{mag} (top), horizontal ϕ (black) and vertical θ (red) angles (middle), and bed elevations z_b (bottom) from the future turbine location during the baseline experiment. Bed elevations were measured 0.13m downstream of ADV location. Raw data (dotted line) and shifted data (solid line) are presented as though the elevations were collected simultaneously directly under the ADV sampling location. Timeseries has been shifted using the mean bedform velocity, $\overline{U_b} \approx 0.0016\text{ms}^{-1}$ assuming minor bedform geometry distortion under relatively short travel times and lengths.

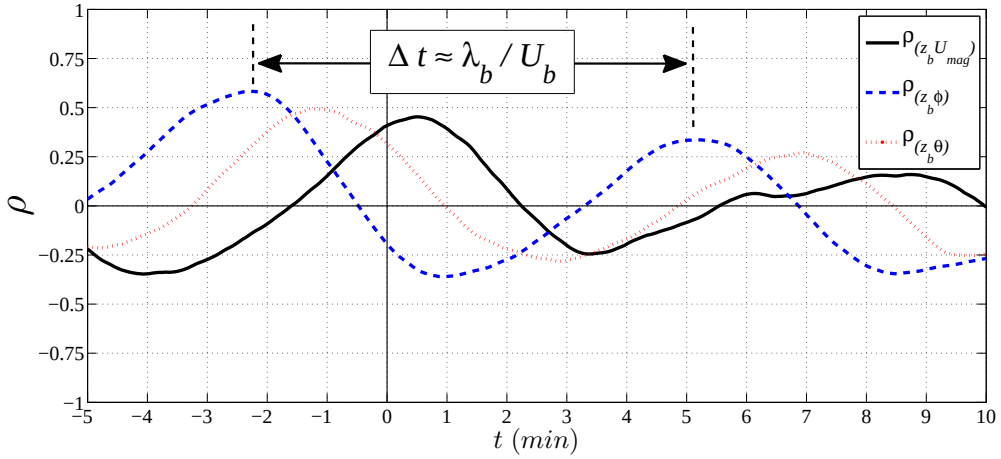

Figure 4.9: Temporal cross-correlation curves between the bed elevations and the velocity magnitude and direction timeseries presented in Figure 4.8. Data from baseline experiments at the location where the turbine was placed.

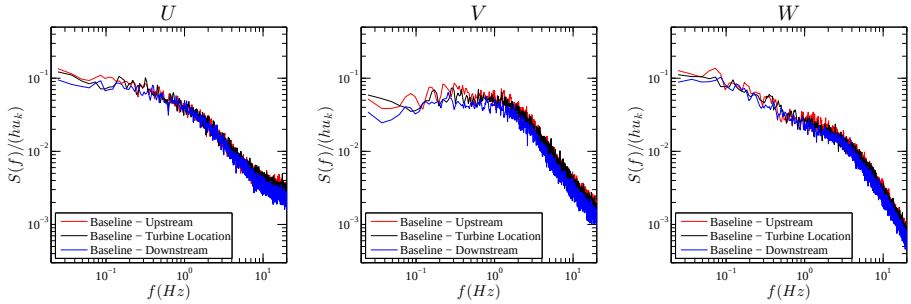

Figure 4.10: Velocity spectrum from the ADV measurements under baseline conditions at three locations: upstream (red), future turbine location (black), and downstream (blue). $S(f)$ is the calculated energy spectrum [$m^2 s^{-1}$]. The energy spectrum are normalized by the mean flow depth at the location of the turbine during baseline experiments ($\overline{h} = 0.306$m) and the turbulent kinetic energy velocity scale, u_k, from the upstream baseline timeseries data.

4.3.2 Turbine Experiment

Following the baseline experiment, a model axial-flow hydrokinetic turbine ($d_T = 0.15$m, $h_{hub} = 0.147$m) was installed near the apex of the middle meander bed approximately half way across

the channel cross-section in an area where the turbine was exposed to the combined effect of actively migrating dunes, incoming turbulence and secondary currents. This section highlights results on mean bed topography and both bedform and flow characteristics under the presence of the instream turbine in the OSL meander.

Morphodynamics

Cross-stream and streamwise continuous bed and water surface elevation measurements were collected along the same transects as during the baseline experiment, providing a method for monitoring the change in mean and fluctuating bed elevations induced by the turbine deployment (Figure 4.11). When compared to the baseline condition in the cross-stream direction (Figure 4.12), the presence of the turbine resulted in a slight lowering of the mean bed elevation (scour) between -2.5 $\approx y/d_T \approx$ 2.5 and an increase (deposition) towards the inner bank on the point bar within the meander ($y/d_T <$ -2.5). This configuration denotes a wide scour hole centered on the turbine location due to a slight flow acceleration around the rotor (the cross-section transect is $\approx 1.4 d_T$ downstream of the rotor). The increase in size of the high momentum region near the outer bank is balanced by a likely reduction in flow velocity in the proximity of the inner bank where deposition is observed. Comparisons between the baseline and turbine experiment root-mean squared (σ_{z_b}) values of the bed elevation profiles in the cross-stream direction are also provided in Figure 4.12. The largest reduction in σ_{z_b} due to the turbine was observed aligned with the center of the turbine position at $y/d_T = 0$. In general, σ_{z_b} stayed consistent between the baseline and turbine experiments inward of the mean bed elevation crossover location at $y/d_T \approx$ -2.5 (i.e. $y/d_T < -2.5$), while σ_{z_b} was substantially decreased under the presence of the turbine elsewhere. As observed in Figures 4.5, 4.6, and 4.11, such decreased variability is due to a reduction in height and wavelength of the incoming bedforms.

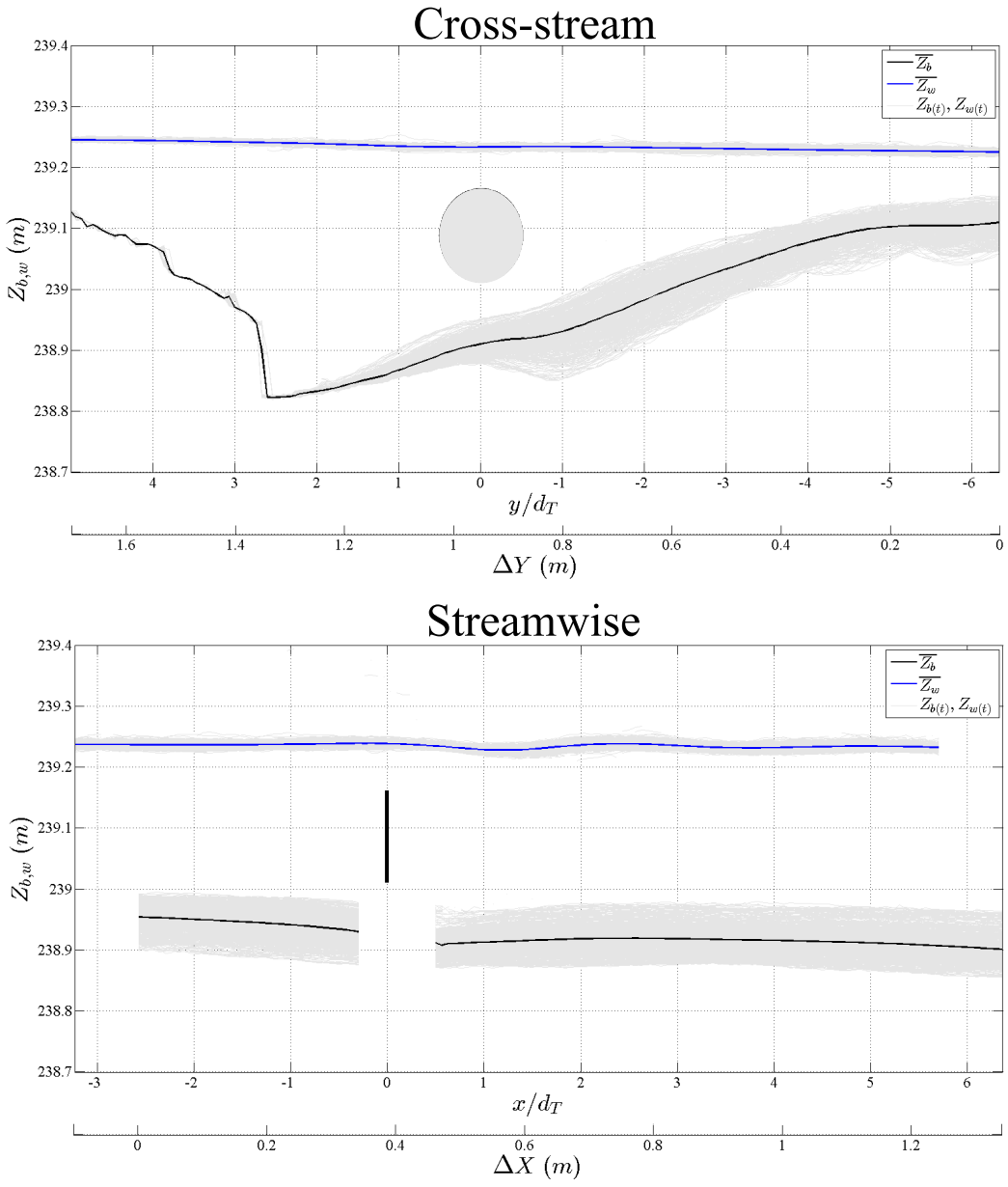

Figure 4.11: Instantaneous (light gray) and mean bed (solid black) and water surface (solid blue) elevation data in the cross-stream (top) and streamwise (bottom) directions collected during the turbine experiment. Turbine rotor area is represented gray circle at $y/d_T = 0$ in the top figure and by the solid black vertical line at $x/d_T = 0$ in the bottom figure.

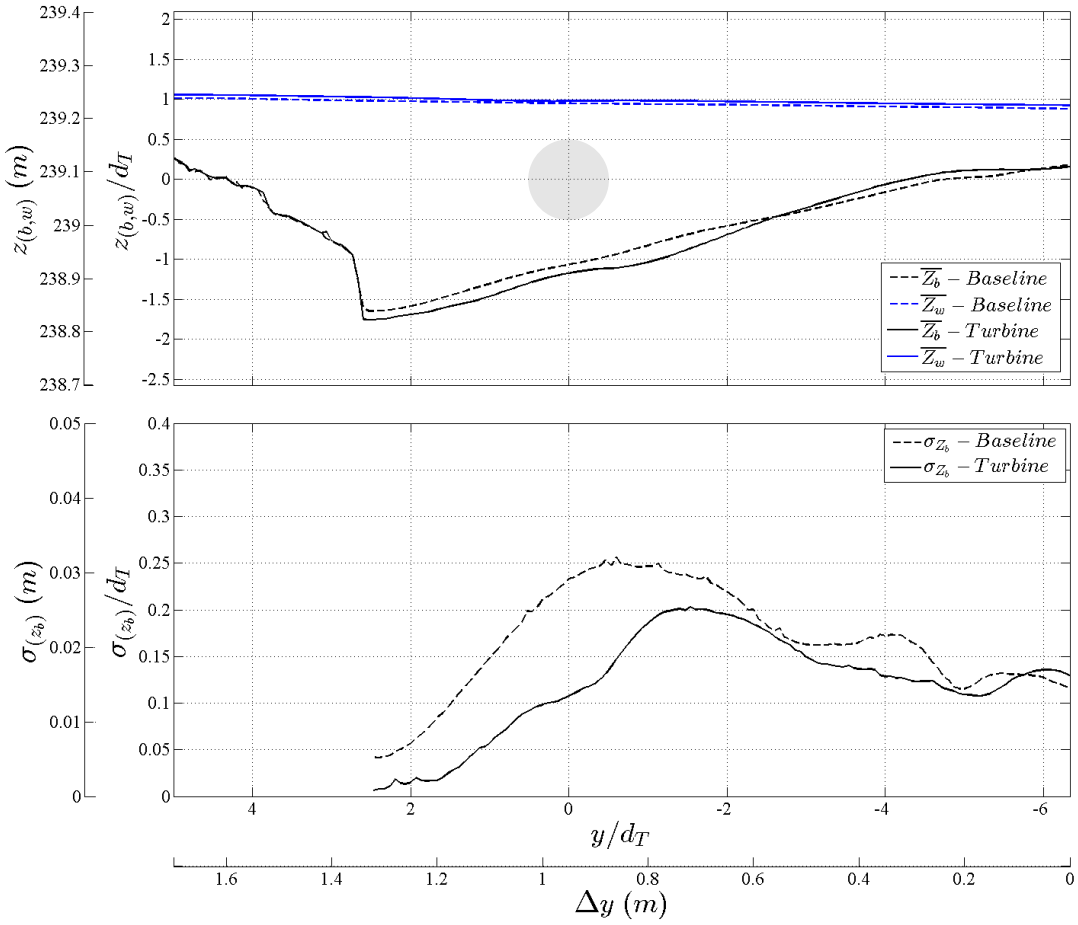

Figure 4.12: Comparison between the cross-stream mean bed and water surface elevations (top) and the root-mean squared elevations (bottom) for the baseline (dashed lines) and turbine (solid lines) experiments. Turbine rotor area is represented by the gray circle in the top figure. The X-axis is presented in both dimensional (m) and non-dimensional (y/d_T) units. The Y-axis is presented in both dimensional (m) and non-dimensional (z/d_T) units with $z/d_T = 0$ corresponding to the turbine hub height, h_{hub}.

Similar comparisons are made between the baseline and turbine experiments streamwise bed and water surface elevation profiles as illustrated in Figure 4.13. Most notable is the locally enhanced scour induced by the presence of the turbine up to $x/d_T \approx 2$ or 3 downstream of the turbine location. Local scour depths reached a maximum of $\Delta z_b \approx$ -0.023m ($z/d_T \approx 0.15$). Downstream from here ($x/d_T \approx 3$ or 4), the mean bed elevation profile asymptotes towards the baseline streamwise mean bed elevation profile. While mean bed elevations between baseline and

turbine experiments were similar upstream and farther downstream of the turbine, the variability in bed elevation σ_{z_b} was consistently observed to be approximately 65% of that measured during the baseline experiment.

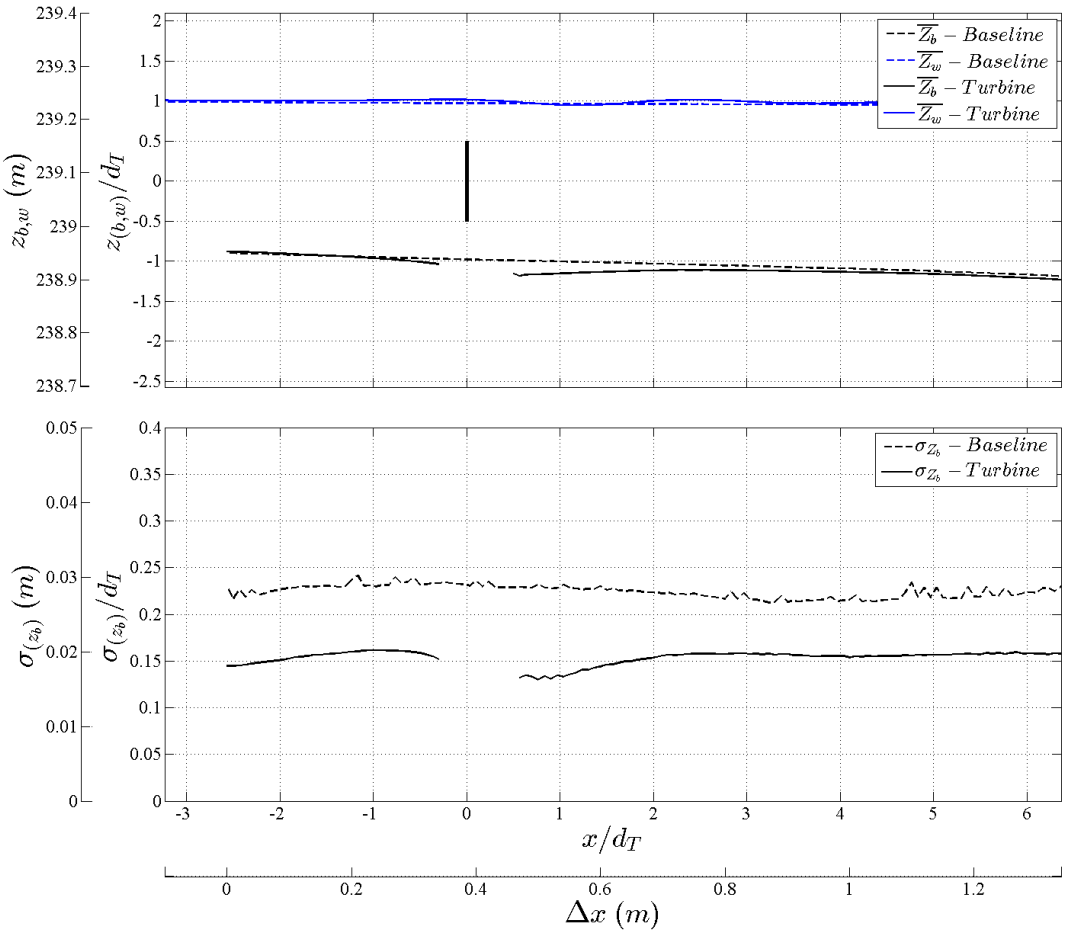

Figure 4.13: Comparison between the streamwise mean bed and water surface elevations (top) and the root-mean squared elevations (bottom) for the baseline (dashed lines) and turbine (solid lines) experiments. Turbine rotor area is represented by the vertical solid black line in the top figure. The X-axis is presented in both dimensional (m) and non-dimensional (x/d_T) units. The Y-axis is presented in both dimensional (m) and non-dimensional (z/d_T) units with $z/d_T = 0$ corresponding to the turbine hub height, h_{hub}.

The cross-stream space vs. time evolution contour illustrated in Figure 4.5b and the bed elevation timeseries data comparison at $x/d_T \approx 1.4$ in Figure 4.6 provide another comparison

between the baseline and the turbine-altered morphodynamic characteristics. In general, cross-stream bedform length has decreased, the slope between the inner point bar and the outer-bank thalweg is steeper, and the frequency of bedforms has increased while the bedform height is smaller. Distinguishing bedforms is more challenging in the wake region of the turbine at $x/d_T = 1.4$, yet approximately 17-20 smaller bedforms were observed during the same time period.

Velocity Characteristics

Mean and fluctuating 3D velocity characteristics in the OSL channel with the turbine are summarized in Table 4.1. The most noticeable effects of the turbine are in the decrease in the mean streamwise velocity, $\overline{U}$, the increase in each of the three turbulent fluctuating components (σ_u, σ_v, and σ_w), and the nearly doubling of the turbulent kinetic energy, k, resulting from the ADV measuring at $x/d_T \approx 4.4$ in the wake of the turbine. Additionally, the cross-stream component, V, at the upstream measurement location nearly doubled when the turbine was in the channel. With this increase in cross-stream velocity, the direction of the mean velocity vector upstream of the turbine was redirected outwards by $\Delta\phi \approx 4.3°$ towards the outer (left) bank of the OSL channel (Figure 4.7, Table 4.2). The horizontal direction, ϕ_T, in the wake of the turbine was also shifted by $\Delta\phi \approx 2.1°$ towards the outer bank of the OSL channel, indicating a straighter trajectory of the velocity magnitude vector at this position in the wake of the turbine compared to the baseline conditions (rather than following the channel curvature).

The characteristic length and time scales of the flow were again calculated using the integral time and length scales and compared to the baseline conditions (Table 4.1). In general, there were not noticeable modifications to these scales due to the presence of the turbine except in the downstream location in the wake of the turbine. Despite a similar time scale, $\mathcal{T}$, the length scale, $\mathcal{L}$, is lower due to the substantially lowered local mean streamwise velocity, $\overline{U}$. An investigation into the turbulent energy spectrum of the flow at the downstream location shows a noticeable increase in energy in all three components, particularly in V and W between $f \approx$ 0.7–3hz (Figure 4.14). This broad peak represents the added energy from the turbulent wake of the turbine. Similar to the baseline spectral characteristics shown in Figure 4.10, the mean flow depth from the baseline experiment at the turbine location ($\overline{h} = 0.306$m) and a turbulent kinetic energy velocity scale were used to normalize the spectra.

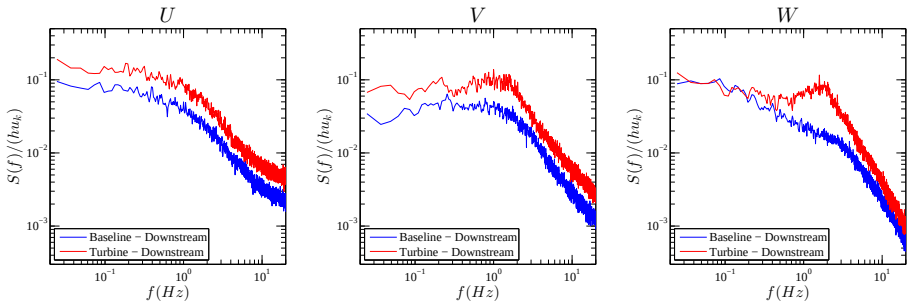

Figure 4.14: Comparison between the U, V, and W velocity spectrum from the downstream ADV measurements during the baseline (blue) and turbine (red) experiments. $S(f)$ is the calculated energy spectrum [m^2s^{-1}]. The energy spectrum are normalized by the mean flow depth at the location of the turbine during baseline experiments ($\overline{h}$ = 0.306m) and the turbulent kinetic energy velocity scale, u_k, from the upstream baseline timeseries data.

Traversing Wake Measurements

The turbulent wake region of the turbine was also characterized using a moving ADV traverse method, a method similar to that used for collecting moving boat ADCP (Acoustic Doppler Current Profiler) data to characterize the flow field within large rivers [148, 149, 150]. Data were collected along five cross-stream transects located at x/d_T = 1.4, 2.4, 3.4, 4.4, and 5.4 downstream of the turbine, spanning from approximately y/d_T = -1.5 to 1.2 in the cross-stream direction. The DAQ carriage moved the ADV in the cross-stream direction at a speed of U_{adv} = 0.001ms^{-1}. The total distance traveled was 0.4m, resulting in a total sampling duration of t = 400s for each profile. Using the estimated bedform velocity, $U_b \approx$ 0.0016ms^{-1} and bedform wavelength, $\lambda_b \approx$ 0.74m, it is assumed that approximately one complete bedform passed during each traverse, therefore providing a minimally adequate representation of the bedform-averaged turbulent flow field in the wake of the turbine. During post-processing, the ADV traversing speed, U_{adv}, was removed from the cross-stream ADV measurements, V. The timeseries collected during each traverse was averaged and assigned to a lateral position using a moving average window filter. The maximum size of this low pass filter was determined by the equation

$$n_{adv} = \frac{d_{adv} f_{adv}}{U_{adv}}$$

where, n_{adv} is the maximum number of samples for the low pass filter window, d_{adv} is the diameter of the ADV sampling volume, and f_{adv} is the ADV sampling frequency. In this scenario, n_{max} = 1200 samples. Figure 4.15 illustrates the application of this low pass filter to

determine (a) the mean streamwise velocity, $\overline{U}$, and (b) the turbulent fluctuations, u', at $x/d_T = 1.4$. Figure 4.16 combines the five traverses to illustrate (a) the mean streamwise velocity, $\overline{U}$, (b) the streamwise root-mean squared velocity fluctuations, u' or σ_u, and (c) the turbulent kinetic energy, k, in the near-wake region of the turbine. The gray-scale bathymetry contour is a "frozen" snapshot of the bedform geometry at the end of the turbine experiment.

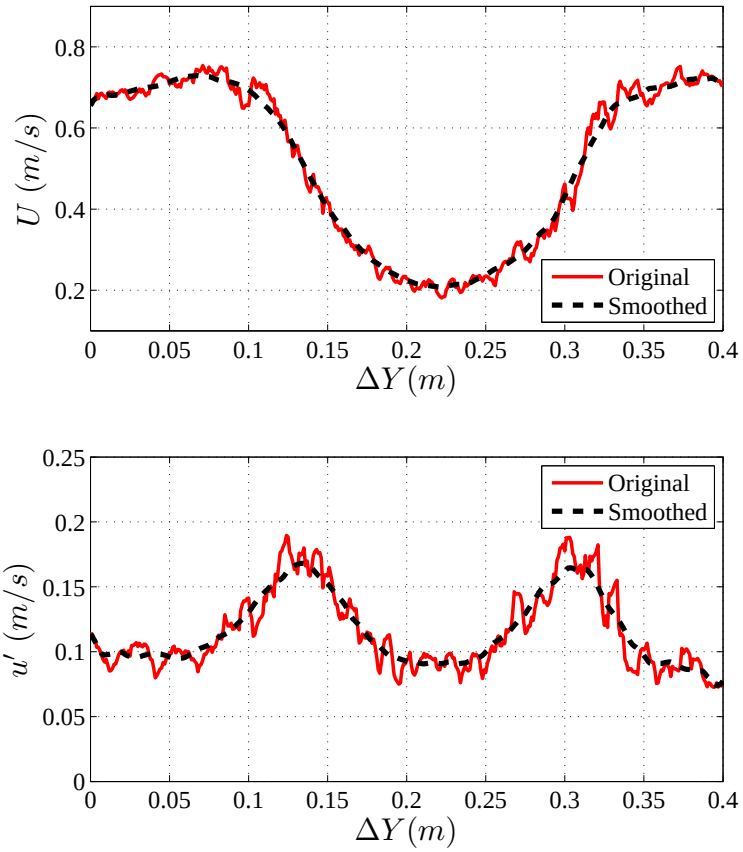

Figure 4.15: Comparison of the collected moving average window data (red, -) and the low-pass filtered data (black, –) for (a) the mean streamwise velocity, $\overline{U}$, and (b) the streamwise velocity fluctuations, u', in the wake of the turbine ($x/d_T = 1.4$) collected during the ADV moving traverse measurements.

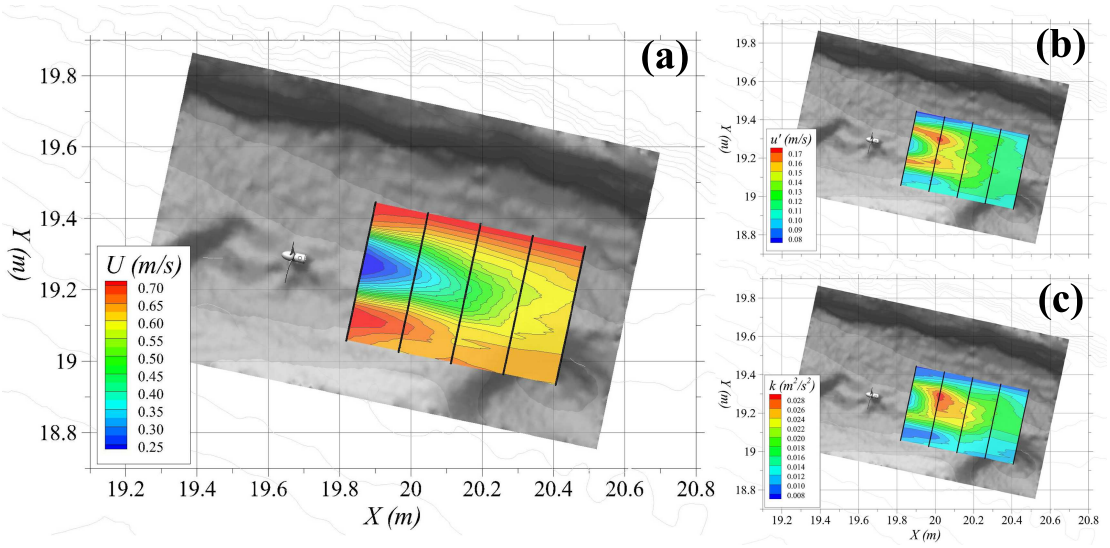

Figure 4.16: (a) Mean streamwise velocity, $\overline{U}$, (b) streamwise velocity fluctuations, u', and (c) turbulent kinetic energy, k, in the wake of the turbine (x/d_T = 1.4 to 5.4) collected during the ADV moving traverse measurements. The model turbine, d_T = 0.15m, is visible in each image at $(X, Y) \approx$ (19.7m,19.3m). Channel topography from the end of the turbine experiment is shown in gray-scale contoured background region. Moving traverse ADV transect locations illustrated by black lines spanning the velocity contour regions.

4.4 Discussion

4.4.1 Channel bathymetry and sediment transport

The simultaneous velocity and bed elevation measurements presented in Figure 4.8 provide useful insight into the dominant flow and bedform characteristics at the turbine location before the actual deployment. While the blockage of the turbine rotor ($\approx 4\%$) redirects the flow towards the outer (left) bank, this outward and downward shift observed in the bulk flow may be the driving factor to the overall scour experienced by the mean bed observed during the turbine experiment (Figure 4.12). Similar to results published from previous work [5, 42], the presence of the turbine in the OSL meandering channel exhibited locally enhanced scour. Interestingly, the magnitude and extent of local scour is similar to that found by [5] using the same scale turbine in a straight laboratory channel under both clear water and live bed sediment transport experiments at comparable flow depths (Figure 4.17). During the OSL experiments, maximum scour depths immediately downstream of the turbine were $z/d_T \approx 0.15$ (0.023m). Unlike the results found from the straight channel, there was no local deposition that occurred between

$x/d_T \approx 3$ to 7. It is hypothesized that the lack of deposition here is due to the outward mean flow pattern characterizing the turbine wake redirecting sediments toward the outer meander bank where they are transported downstream as a result of increased flow depth and bed shear stress. We acknowledge that the measurements from the OSL only allow observations along two transects, while it is likely that the scour, shear stress distribution, and deposition of the removed sediment is a highly 3D problem, especially in meandering channels. As local shear stress is increased due to the turbine rotor blockage and flow acceleration beneath the rotor, the sediment is likely to be transported further up onto the point bar (where deposition is indeed observed, Figure 4.12) or outwards towards the thalweg of the channel where such sediment is easily swept away downstream.

Initially, the decrease in bedform variability σ_{z_b} estimated from cross-stream sonar measurements and observed to align with the position of the turbine (see Figure 4.12) was thought to be a local effect in the near-wake region of the turbine. However, this phenomena was observed along the entire range of the streamwise sonar measurements. Interestingly, a similar phenomena was observed from experiments in a straight rectangular laboratory channel using the same sized turbine operating in conditions similar to the OSL (similar flow depth, h, bedform height, h_b, turbine hub height, h_{hub}, etc.) [42] (Figure 4.18). From the straight channel experiments, measurements recorded a decrease in σ_{z_b} upstream of the turbine location compared to the baseline (no turbine) experiment. Downstream, σ_{z_b} values recovered to the baseline condition approaching the far-wake region of the turbine, something that was not observed in the OSL meandering channel experiments. This is likely due to the fact that in the meandering channel, the far-wake downstream measurements were beginning to enter the deeper thalweg portion of the channel and any sediment located in this region is likely transported rapidly downstream due to higher bed shear stress (i.e. [144]) before reforming into appreciable bedforms. However, the similarity in upstream and downstream reduction in bedform σ_{z_b} values are strikingly similar between the straight and meandering channel experiments. Note that an extended region of reduced bedform variability in height and wavelength is potentially a favorable feature within larger multi-turbine deployments since bedform induced turbulence is known to have a strong effect on turbine performance, especially in terms of fluctuating power production and enhanced loads [42, 1].

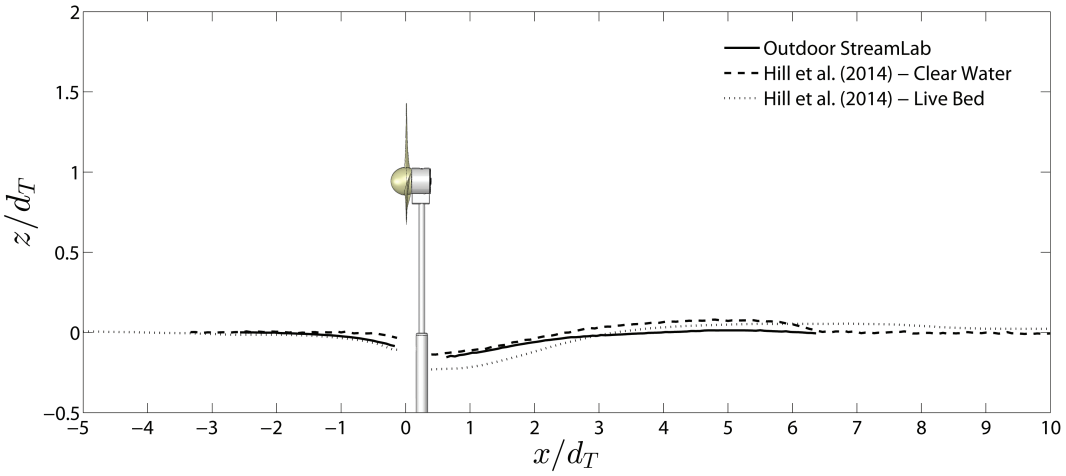

Figure 4.17: Comparison between the streamwise mean bed elevation from the OSL turbine experiments and the clear water and live bed experiments presented by [5].

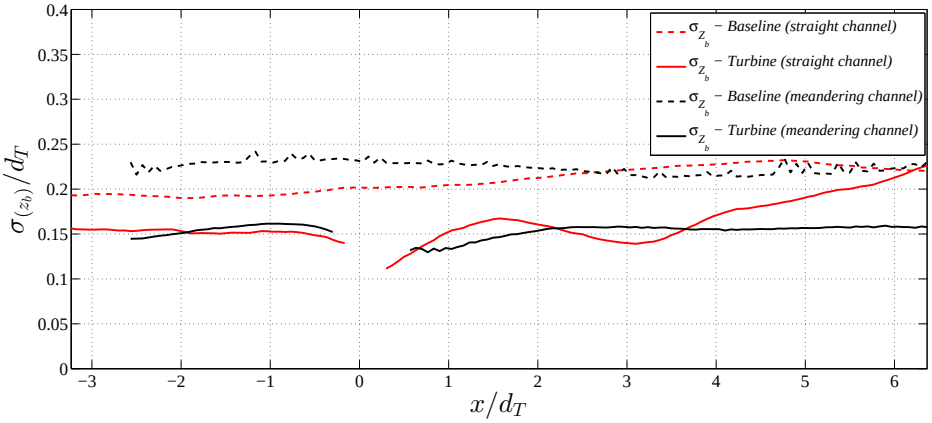

Figure 4.18: Comparison of the streamwise bed elevation root-mean squared values from baseline (dashed) and turbine (solid) experiments in both a straight laboratory channel (red) and the meandering natural channel in the OSL (black).

4.4.2 Flow field and wake characteristics

Measurements from the ADV at three locations during baseline conditions provide evidence that the region of interest within the OSL channel had fairly homogenous turbulent flow in the streamwise direction. Not only were the turbulent fluctuations and turbulent kinetic energy

levels similar (Table 4.1), but also the velocity spectrum at all 3 locations collapse onto one another (Figure 4.10) indicating similar distribution of turbulent kinetic energy across scales. Estimates of the integral time and lengths scales at the three streamwise locations corroborates this finding.

The most insightful measurements and analysis into the flow field where the turbine was installed comes from the cross correlation analysis between bed elevations, z_b, and the velocity magnitude and direction during the 45 minute ADV point measurements. Maximum correlation between z_b and U_{mag} occurs near a lag $\Delta t \approx 0$. Essentially, when the local depth is at a minimum due to an approaching bedform crest, z_b maximum, the confining effect induces an increase in local velocity. When the bedform crest (maximum z_b) is upstream of the ADV sensor, the peak correlation between z_b and θ occurs, preceded by the peak correlation between z_b and ϕ when the bedform crest is even further upstream from the ADV. This implies that an approaching dune in the meander bend induces first a horizontal flow diversion, directing the mean velocity towards the outer bank, and then a more local effect on the vertical velocity direction. The turbulent flow field properties above dunes studied over recent decades, summarized nicely by [95, 97], provides an indication as to the physical processes occurring governing these periodic and phase-shifted relationships illustrated in Figure 4.9. When the maximum correlation between z_b and ϕ occurs, the ADV sensor is likely measuring velocities above the stoss side (upstream, low slope side) of the dune where i) the flow is mostly being dictated by the non-local channel geometry, for example the sinuosity of the channel bend, and ii) the velocity magnitude vector maintains a deviation towards the outer (left) bank of the OSL (positive ϕ). The correlation between z_b and ϕ is at a minimum when the crest of the dune is beneath the ADV measurement location, indicating negative ϕ angles and a deviation of the flow towards the inner bank of the channel, possibly a clue that at this time the flow direction is mostly dictated by the local topography of the dune crest.

In general, flow throughout the meander is complex, especially considering the presence of the moving bedforms that can cause quasi-periodic fluctuations of the local velocity and introduce variability into the velocity spectrum measured, in this case, at hub height h_{hub} [91]. As shown by [1], these periodic fluctuations due to coherent eddies will likely impact the performance and wake structure of an axial-flow device in the channel. Although not entirely quantified here, the stability of the turbine wake visualized in Figure 4.16 is potentially disrupted by the coherent eddies shed by large-scale bedforms as well as any meander-induced circulating eddy structures convected through the meander bend. One method of assessing the stability of the wake, however, is to assess the velocity deficit in the downstream direction (Figure 4.19). Here, the velocity deficit at hub height perpendicular to the rotor plane is shown for the turbine in a straight non-erodible channel and the OSL meandering channel. The wake rapidly recovers in

the complex flow of the meandering OSL channel. By $5d_T$-$6d_T$ downstream of the turbine, the center wake velocity deficit is approximately 10%, similar to the velocity deficit at nearly $10d_T$ downstream of the same turbine operating in the straight, non-erodible channel. The large-scale bedforms migrating past the turbine combined with the coherent helical flow patterns around the meander bend likely increase turbulent mixing and the accelerated recovery in the wake in the meandering channel.

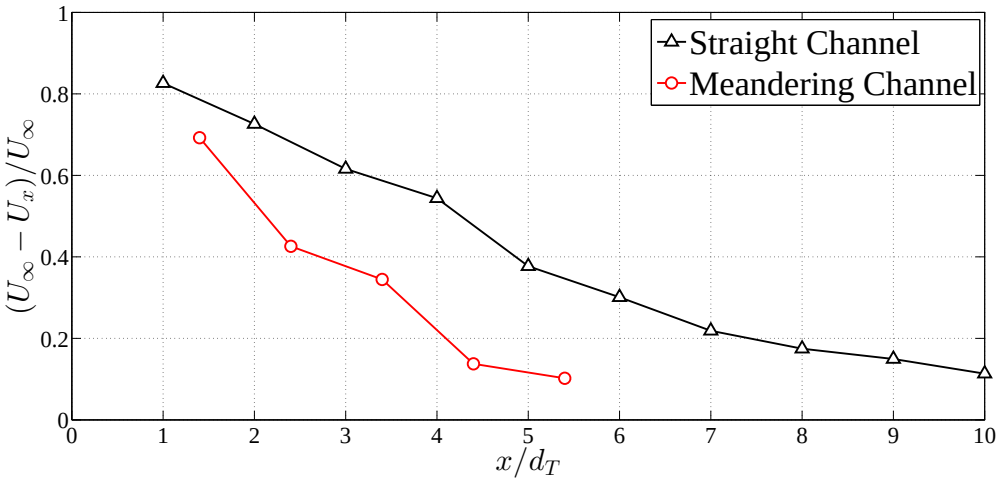

Figure 4.19: Comparison of the wake velocity deficit downstream of the axial flow turbine (d_T = 0.15m) from a straight non-erodible channel (black) and the meandering natural channel in the OSL (red).

4.4.3 Applications within MHK industry

As the MHK industry advances that proposed project sites will likely be among complex topography, mobile sediment and bedforms, and time-varying approach flow (both in terms of direction, magnitude, and length scales). These effects are actively studied and pursued within the wind industry through active yaw and blade pitch mechanisms incorporated into turbine designs. The effects of complex topography on wind turbine performance and wake characteristics is also being investigated through experiments and simulations [82, 81]. As demonstrated by the cross correlation analysis in Figure 4.9, the local bed elevation greatly influences the direction and magnitude of the inflow perceived by a device at that location. Possible strategies for maintaining optimal performance of MHK devices is to incorporate in-situ monitoring and feed these measurements into advanced control strategies, whether that be through controlled

yaw mechanisms, blade pitch control to maximize generator torque or minimize rotor fatigue from unsteady loading, or incorporating turbine designs that are less susceptible to performance deficiencies due to non-orthogonal inflow (i.e. vertical axis cross flow devices). What will remain a challenge, however, especially in curved channels, is where to measure the characteristic inflow velocities. Local morphodynamics can introduce extensive variability which may not be representative of the flow perceived by a device, while individual turbines can also exert an influence on the magnitude and direction of the flow, even up to $3d_T$ upstream of the rotor location.

The near-wake measurements provided from the OSL experiments illustrate how axial-flow turbine wake characteristics may vary slightly in meandering, asymmetric channel flow compared to straight, relatively smooth and fully developed turbulent channel flow. This slight curvature visible in the mean streamwise wake velocity and non-symmetric tip vortex σ_u levels illustrated in Figure 4.16 indicates that optimal layout of a turbine array within meandering channels, especially those with actively transported bedforms, will likely not rely on a simple uniform Cartesian grid of devices (staggered or aligned). Instead, site-specific bathymetric and hydrodynamic characterization should be considered to optimize multi-turbine deployments in these complex environments.

4.5 Conclusion

This study provides some of the first insight into the morphodynamic impact of an axial-flow hydrokinetic turbine operating in a meandering, asymmetric channel geometry under active sediment transport and migrating bedforms. Experiments were performed in the St. Anthony Falls Outdoor StreamLab (OSL) research facility using a turbine with rotor diameter $d_T = 0.15$m installed with hub height $h_{hub} = 0.147$m and occupied $\simeq$50% of the local depth with a total rotor blockage of the channel cross-section of approximately 4%. Measurements included continuous spatio-temporally resolved bed elevations to monitor migrating sand bedforms ($h_b \approx 0.087$m, $\lambda_b \approx 0.74$m, $U_b \approx 0.0016$ms^{-1}) and simultaneous velocity measurements to assess inflow conditions for the turbine and its wake characteristics. The cross-stream turbine location was defined to i) experience effects of both migrating dunes and secondary currents, ii) leave a signature on the erodible bed, iii) represent the transverse-slope geometry typical of point bars in meandering topographies, iv) qualitatively expose the turbine to the bulk of the flow (for high energy production) without enhancing erosion mechanisms on the outer bank (however, non-erodible in the current configuration), and v) have a hub height to depth ratio (h_{hub}:h) comparable with experiments performed in a straight flume under similar Froude number ($Fr = 0.39$) and bedform roughness dimensions (i.e., h_b).

Baseline measurements within the meander indicated streamwise homogeneity of the mean

and root-mean squared velocities, integral scales, and power spectral density, ensuring that the turbine effects studied here would represent its interaction with the hydrodynamics and morphodynamics of meandering channels. In particular, investigations focused on the simultaneous velocity and bed elevation measurements to demonstrate how approaching bedforms can locally and non-locally modulate the incoming flow field intersecting the turbine, first impacting the horizontal velocity direction, followed by the vertical velocity direction, and finally the velocity magnitude. The hydrodynamic and morphodynamic impact of the turbine can be summarized in the following:

- Local velocity magnitude and direction without a turbine is influenced by local (i.e. dune crest location and size) and non-local (i.e. channel sinuosity and asymmetric cross-section) topography. The turbine presence at the specific installed location in the channel redirected the orientation of both upstream approach velocity ($\Delta\phi \approx 4.3^\circ$ at x/d_T = -2.9) and turbine wake velocity ($\Delta\phi \approx 2.1^\circ$ at $x/d_T = 4.4$) toward the outer (left) bank (Figure 4.7 and Table 4.2).

- The low velocity in the turbine wake persisted beyond the measurement extent of $x/d_T =$ 5.4 (Figure 4.16), implying zones of higher velocity may concentrate between the wake and the outer bank. This is inferred to be a consequence of turbulent flow organization along the channel curvature, likely governed by the secondary currents. A two-fold increase in turbulent kinetic energy was measured at hub height in the wake of the turbine at $x/d_T =$ 4.4. Local and non-local bathymetry is expected to introduce large scale fluctuations in the perceived inflow at the turbine location and accelerate wake recovery by increasing turbulent mixing in the turbine wake.

- A local decrease (scour) of $\Delta z_b/d_T \approx 0.15$ ($\approx$ 0.023m) in the mean bed elevation, $\overline{z_b}$, was measured in the cross-stream direction $x/d_T \approx 1.4$ downstream of the turbine from -2.5 $\leq y/d_T \leq 2$. (Figure 4.12); the scour zone has extended in the downstream direction to $x/d_T \approx 3$ (Figures 4.13 and 4.17), supporting previously published results indicating that individual turbines have only local effects on the mean bathymetry of erodible channels. The local scour depth in the meandering channel was ≈30% less than the observed local scour depth in a straight channel. The presence of the turbine decreased the variability in bed elevation, quantified by temporal r.m.s. values, σ_{z_b}, both upstream and downstream of the rotor by ≈35%, a phenomena that has been measured in similarly scaled straight channel experiments (Figure 4.18). Secondary currents may explain why σ_{z_b} reduction was observed to be more persistent in meandering flow compared to a straight channel.

- Bedform heights, h_b, were decreased when the turbine was present while the frequency of bedforms passing the turbine increased (17-20 bedforms compared to 15 during baseline

experiments (Figure 4.6)). This turbine-induced modification to bedform evolution and sediment transport was also observed by the potential steepening of the transverse point bar slope (Figure 4.5) and increased deposition along the inner portion of the point bar resulting in a higher mean bed elevation (Figure 4.12). The steepening of the transverse point bar slope implies that sediment will likely be swept away in the non-erodible outer bank thalweg rather than forming large scale migrating bedforms along the banks. Further investigation is required for turbines operating in channels where the banks are erodible

Future experiments would benefit from more detailed wake characterization, especially in the far wake region of the turbine and further along the meander bend to understand wake recovery in complex topography and curving channels. Additionally, the interactions between multi-turbine arrays and complex topographic channels requires further investigating. Applications of these results should be considered by full-scale device developers during MHK site assessment and development. Recent research into the effects of large scale coherent turbulent structures on axial-flow turbine performance and wake characteristics, along with the findings from these OSL experiments, reiterate the necessity for complete site-specific hydrodynamic and bathymetric characterization for optimal design of single turbine placement and multi-turbine arrays, and the necessity for advanced turbine control strategies for maximizing energy production while minimizing device fatigue.

4.6 Notation used in Chapter 4

b = channel width, m
d_{adv} = ADV sampling volume diameter, m
d_T = turbine rotor diameter, m
d_{50} = mean sediment grain size, m
f = sampling frequency, Hz
h = flow depth, m
h_{adv} = ADV sampling volume height, m
h_b = bedform height, m
h_{hub} = hub height, m
k = turbulent kinetic energy, m^2s^{-2}
n = number of samples, #
Q_w = bulk flow rate, m^3s^{-1}
q_s = sediment supply rate, Ls^{-1}
SI = sinuosity index, or sinuosity, [-]
S_b = channel bed slope, %

$S(f)$ = spectral energy density, m^2s^{-1}
t = time, s
T_b = bedform period, s
$\overline{U}$ = mean streamwise velocity, ms^{-1}
U_{adv} = ADV traversing velocity, ms^{-1}
U_b = bedform velocity, ms^{-1}
U_{mag} = velocity magnitude, ms^{-1}
u' = streamwise velocity fluctuations, ms^{-1}
u_k = turbulent kinetic energy velocity scale, ms^{-1}
$\overline{V}$ = mean cross-stream velocity, ms^{-1}
v' = cross-stream velocity fluctuations, ms^{-1}
$\overline{W}$ = mean vertical velocity, ms^{-1}
w' = vertical velocity fluctuations, ms^{-1}
x = streamwise coordinate direction, m
y = cross-stream coordinate direction, m
z = vertical coordinate direction, m
z_b = bed surface elevation, m
z_{hub} = hub elevation, m
z_w = water surface elevation, m

Greek & Script symbols
λ_b = bedform wavelength, m
$\mathcal{L}$ = integral length scale, m
ϕ = horizontal velocity vector angle (subscripts: B = baseline, T = turbine), (°)
ρ = correlation coefficient, [-]
σ_i = root-mean squared ($i = u,v,w$ or 1,2,3).
τ = time-step lag, s
$\mathcal{T}$ = integral time scale, s
θ = vertical velocity vector angle (subscripts: B = baseline, T = turbine), (°)

Chapter 5

Morphodynamic impact of a hydrokinetic turbine

The following chapter is a work in progress with most content to be submitted for publication in the *Journal of Fluid Mechanics*.

Hill, C., Sotiropoulos, F., and Guala, M., (2015), Interactions between a morphodynamic channel and an axial-flow turbine, in preparation for *J. Fluid Mech.*.

5.1 Introduction

Tidal and instream turbines aim to mechanically convert kinetic to electrical energy in areas with naturally occurring currents. The design of such devices is challenging due to turbulence induced unsteady loading on rotor blades and structural components in these extremely harsh environments. Added challenges arise due to the hydrodynamic and topographic complexity in the natural environments these turbines will operate. Collectively referred to as hydrokinetic energy technologies, these emerging devices have been extensively studied in recent years using both experimental and numerical methods to investigate performance characteristics and both near and far-wake properties in straight rectangular, non-erodible channels (for example, [138, 27, 6, 29, 24, 116]). While these studies provide detailed performance and wake characteristics of axial-flow devices, it is unclear how similar devices will perform in complex topography, similar to the natural variability present at tidal and in-stream deployment locations.

As a first look into how axial-flow hydrokinetic turbines respond to hydrodynamic complexity, [1] studied the response of a model turbine interacting with various scales of von Kármán type

coherent vortices introduced by vertically-oriented cylinders placed upstream of the turbine. Results indicated direct coupling between the modified turbulence scales of the flow and turbine performance characteristics, as well as tip-vortex breakdown and accelerated wake recovery due to the presence of coherent eddies in the approach flow. Beyond this work, most of the investigations surrounding axial-flow devices and boundary layer flow above uneven complex terrain has stemmed from the wind energy industry and research community. Wind-tunnel experiments on the effects of boundary layer roughness on wind turbine wake characteristics were conducted by [151]. Here, the authors indicated departure from typically observed axisymmetric turbine wake structure as a result of increased shear in the boundary layer profile approaching the turbine. Numerically, [82] addressed the interactions of a wind turbine farm operating in complex terrain. [152] performed small-scale wind tunnel experiments to investigate the response of an axial-flow wind turbine ($d_T = 0.128$m) positioned in the wake of a Gaussian hill, which were subsequently modeled using LES to investigate a larger parameter space including upwind hill location and hill height [153]. Results from these simulations suggested that turbines can in fact be placed closer together in complex terrain environments to achieve higher power density compared to turbine farms in flat, open terrain.

The available literature on the interactions between hydrokinetic turbines and sediment transport is limited, yet becoming an area of increased interest as researchers aim to address uncertainties regarding hydrokinetic device interaction with the surrounding biological and morphological environment. Most studies have focused on large-scale numerical modeling of large turbine arrays off the coast of the United Kingdom [43, 44, 47]. The smallest grid sizes were larger than most hydrokinetic turbine rotors today, therefore unable to predict local effects on channel bathymetry. These studies have indicated a potential far-field effect on sediment transport in the vicinity of large-scale hydrokinetic turbine arrays (i.e. 300-400 devices). It remains unclear whether morphodynamic impacts of large turbine arrays is simply an accumulation of single turbine impacts.

Experimentally, work preceding this study investigated the near-field effects of a single turbine and two aligned turbines operating in both clear water (i.e. $\tau_b < \tau_{cr}$) and live bedload (i.e. $\tau_b > \tau_{cr}$) sediment transport conditions [5, 42]. Locally enhanced scour was observed near the turbine foundation and extended to approximately $2d_T$ downstream of the device, likely a result of the rotor blockage and acceleration of flow between the rotor bottom tip and sediment surface. Large-scale mobile bedforms were also shown to directly impact the performance of these turbines. The interactions between an axial-flow hydrokinetic turbine model and the hydrodynamics and morphodynamics in a realistic meandering channel were also studied [154]. Measurements identified potential curvature of the turbine wake that approximately follows the channel curvature. Beyond this study, little is known about how axial-flow hydrokinetic turbine

wake characteristics change in arbitrarily complex and mobile terrain.

A series of experiments were conducted to investigate the interactions between a model axial-flow hydrokinetic turbine and an erodible channel with active morphodynamics, beginning to develop an understanding of the scaling effects of such interactions. Details of the facility and experimental setup are provided in Section 5.2. Results and discussion into the key findings on the effects on turbine performance, wake characteristics, and the turbine-induced morphological changes are provided in Section 5.3, followed by a summary and concluding remarks given in Section 5.4.

5.2 Experimental Setup

The experiments were conducted in the St. Anthony Falls Laboratory (SAFL) main channel facility at the University of Minnesota (UMN) (Figure 5.1a). The concrete channel (85m long, 2.75m wide, 1.8m deep) was filled with uniform medium quartz sand ($d_{50} = 0.42$mm) to an average sediment depth of $\bar{h}_{sed} = 0.43$m from the channel inlet ($x = 0$m) to the sediment weighing system ($x \approx 59$m). The sediment weighing system, described in detail by [91], provided a means for weighing transported sediment in five pans (pan width = 0.55m) that spanned the total width of the channel. Accumulated sediment was stored in a holding pit and transported back upstream via auger and hydraulic pump to get reintroduced into the channel system ensuring sediment volumetric continuity during experiments. A series of baseline experiments was run after reaching equilibrium channel slope conditions ($S_b \approx 0.05\%$) to record characteristic hydraulic and bedform conditions (volumetric flow rate, $Q_1 = 1.65\text{m}^3\text{s}^{-1}$). Following baseline experiments, a model axial-flow hydrokinetic turbine was installed in the channel to investigate the morphodynamic impact of the turbine operating in close proximity to the channel surface (average hub height, $\bar{h}_{hub} = 0.425$m). Two phases of experiments were conducted; first, using similar hydraulic parameters as during baseline experiments, and second, a bedform regime transitional experiment during which the bulk flow rate was incrementally raised to two higher discharges, $Q_2 = 1.92\text{m}^3\text{s}^{-1}$ for approximately two hours and $Q_3 = 2.34\text{m}^3\text{s}^{-1}$ for appropriately two hours (Figure 5.2). Flow depth was maintained at $\bar{h} \approx 1.17$m for all experiments.

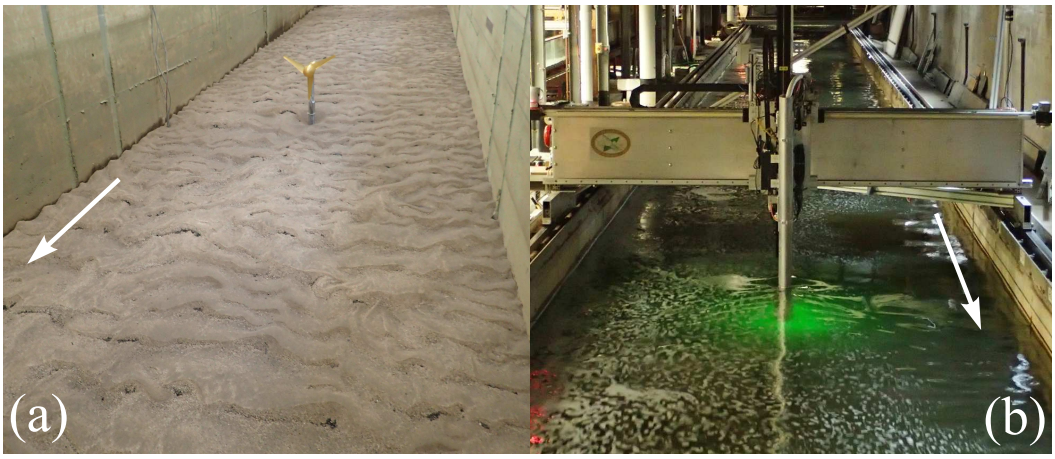

Figure 5.1: (a) Photograph of the St. Anthony Falls Laboratory (SAFL) main channel and turbine model. (b) Data acquisition (DAQ) carriage collecting spatio-temporal bedform topography data in SAFL main channel. Arrows indicate flow direction.

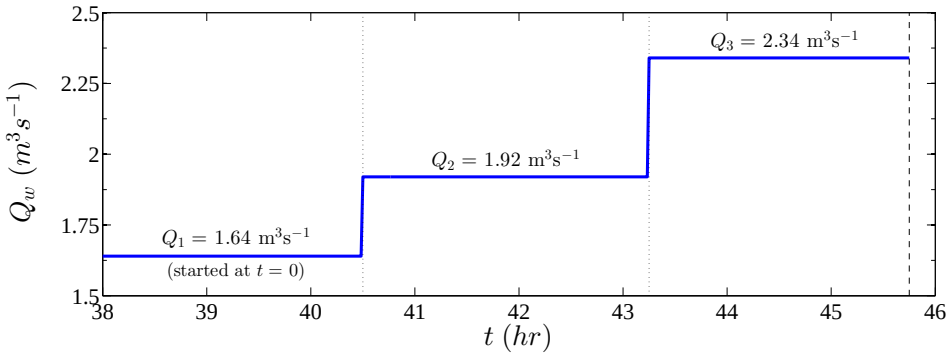

Figure 5.2: Volumetric flow rate hydrograph used during the experiments. Baseline experiments started at $t = 0$hrs. Turbine was installed at $t = 19.5$hrs.

The axial-flow three-bladed turbine with rotor diameter $d_T = 0.5$m was mounted in the center of the channel such that the average hub height was $\bar{h}_{hub} = 0.425$m above the mean sediment bed elevation, $\overline{z_b}$. Precise rotor angular velocity, ω, was controlled using a Danaher Powermax NEMA-23 stepper motor. An Interface Force 2Nm torque transducer provided instantaneous measurements of rotor torque, while a US Digital EM1 optical rotary encoder measured rotor angular position, θ, and provided verification of the angular velocity, ω, defined by the stepper motor (Figure 5.3). Blade pitch angles were manually adjusted and secured such that the tip

profile of each blade was at an angle of $\alpha = 0°$. Additional turbine and blade geometry details are available in [6] and [1].

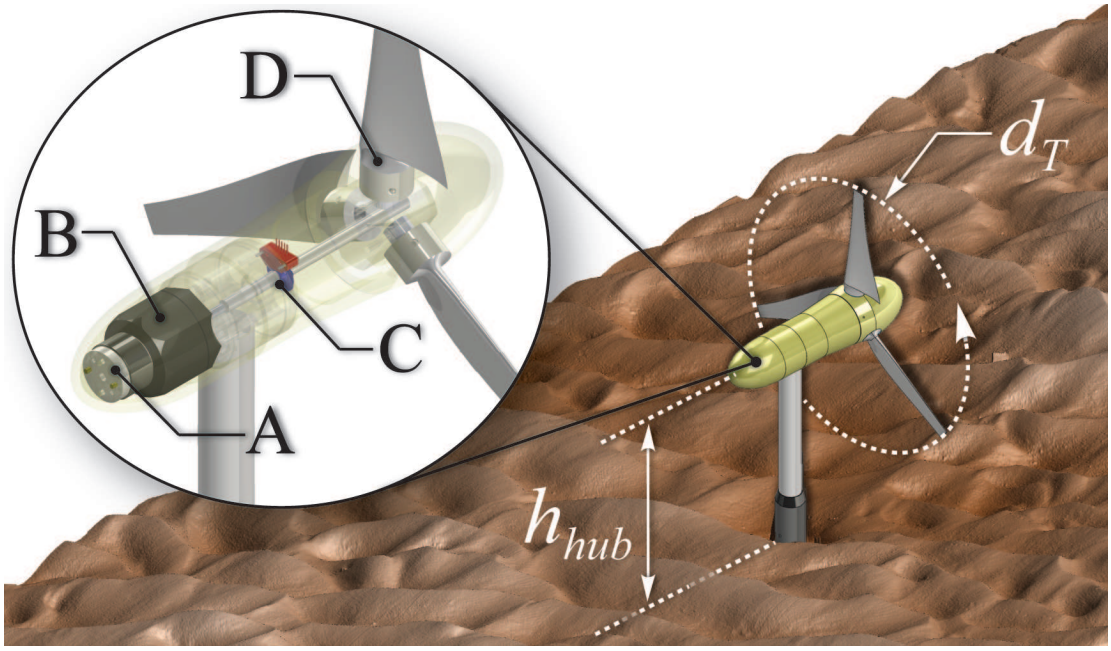

Figure 5.3: Schematic of the turbine installed in SAFL main channel. (A) Torque transducer, (B) rotor angular velocity speed control motor, (C) rotary encoder, and (D) manual blade pitch angle adjustment. Rotor diameter, $d_T = 0.5$m, average hub height, $\bar{h}_{hub} = 0.425$m, and average sediment depth, $\bar{h}_{sed} = 0.43$m.

An array of three Nortek Vectrino+ acoustic Doppler velocimeters (ADVs) were positioned throughout the flume using a computer automated data acquisition (DAQ) carriage (Figure 5.1b) and collected three-dimensional (3D) instantaneous flow velocity data to characterize the inflow and wake environment downstream of the turbine. All turbine and velocity data were recorded at 100Hz. Inflow conditions during baseline experiments were measured at a position approximately 5m upstream ($x/d_T \approx$ -10) from the location where the turbine was installed and compared to flow characteristics from preliminary studies completed to measure performance of the turbine in a smooth concrete rectangular channel cross section (Figure 5.4). While the bulk flow and hub height velocity differed between concrete channel and sediment experiments, characteristic inflow vertical profiles exposed the turbine energy extraction plane to similar mean shear and turbulence intensity across the rotor plane.

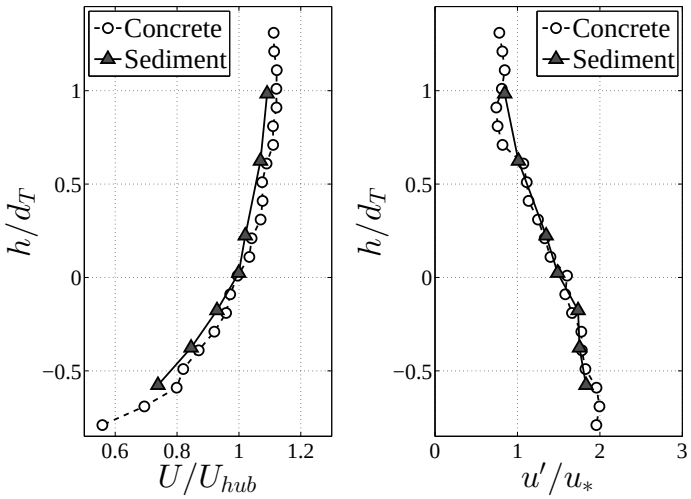

Figure 5.4: Vertical profiles of (a) U/U_{hub} and (b) u'/u_* from the concrete channel experiments (O) and sediment transport experiments (△). Normalization factors U_{hub} (concrete, U_{hub} = 0.45ms^{-1}; sediment, U_{hub} = 0.52ms^{-1}) and u_* are specific to each experiment (concrete, u_* = 0.033ms^{-1}; sediment, u_* = 0.04ms^{-1}). Data collected x/d_T = -5 and -10 upstream of the turbine for concrete channel and sediment transport experiments, respectively. The turbine rotor plane extends from h/d_T = -0.5 to 0.5, with the turbine hub height at h/d_T = 0.

A camera and laser imaging system provided a method for collecting spatio-temporally resolved bed elevation data, $z_b = z(x, y, t)$. Details of the topographic imaging system are published in [5]. Repeated streamwise oriented swaths ($\Delta y \approx$ 0.5m in the cross-stream direction and $\Delta x \approx$ 5m in the streamwise direction) of bed elevation data were collected during baseline and turbine sediment transport experiments (Figure 5.1b). Scans repeated every 212s during baseline experiments, and 202s (center wake bed profiles) or 218s (offset to turbine side) during turbine experiments. Dry channel high-resolution topography (2mm x 2mm) of the entire channel domain was collected upon completion of each experiment. Additional bed elevations measurement were collected using a submerged sonar transducer traversing the length of the flume, providing additional measurements of instantaneous bed elevation profiles, time-averaged bed slope, and additional methods for calculating bedform geometric and kinematic characteristics.

In work leading up to these experiments, a series of reference experiments were conducted. First, performance characteristics and wake velocity measurements were collected for the same turbine in the SAFL main channel prior to adding sediment, providing turbine baseline measurements in a rectangular, non-erodible channel. These experiments were similar to those reported

by [6], but provided a more recent characterization of the turbine model. Second, detailed measurements on the performance and wake characteristics of the turbine were measured downstream of vertically-oriented cylinders used to introduce coherent turbulent eddies upstream of the turbine location that would impact the turbine rotor plane. Detailed results and analysis from these measurements are reported in [1], while selected data are used within this paper to discuss hydrodynamic and morphodynamic interactions of the turbine operating in an erodible channel.

5.3 Results & Discussion

5.3.1 Turbine Performance

Instantaneous torque, τ, and rotor angular velocity, ω, provided methods for monitoring turbine power output, $P_T = \tau\omega$, and resulting power coefficient, $C_p = P_T/P_A$, where the available power approaching the rotor is $P_A = 0.5\rho A_T U_{hub}^3$ (A_T is the turbine rotor area), typically characterized by a point measurement of hub height velocity. A performance curve, C_p vs. λ, was generated during the experiments in a concrete rectangular channel without sediment, providing reference turbine power characteristics for comparison (Figure 5.5). Maximum turbine efficiency was observed at $\lambda \approx 0.52$ with $C_p \approx 0.42$. Similar performance data were measured during experiments with vertically-oriented cylinders [1] and during sediment transport experiments (Q_1, Q_2, and Q_3). Results demonstrate how added hydrodynamic and morphodynamic complexity in the channel make it difficult to simply achieve and maintain optimal performance. During sediment transport experiments with ripples (Q_1), the tip-speed ratio was maintained near $\lambda \approx 6.1$ ($\omega = 2\pi f_T \approx 12.6$). The resulting performance ranged from $C_p \approx 0.32$ to 0.35. During phase two of sediment transport experiments (Q_2 and Q_3) when hydraulic conditions promoted bedform regime transition from ripples ($\lambda_b \approx 0.3$m, $h_b \approx 0.03$m, $h_b/h \approx 0.026$) to dunes ($\lambda_b \approx 0.6$m, $h_b \approx 0.06$m, $h_b/h \approx 0.052$), turbine performance decreased to $C_p \approx 0.13$ to 0.20 across a range of tested tip-speed ratios, $\lambda \approx 5.6$ to 7.9. Details of individual turbine performance points are summarized in Table 5.1.

In an effort to understand the adjustment of performance during this transitional period from Q_1 to Q_2 to Q_3, the instantaneous centerline channel topography bed elevation profiles are plotted in Figure 5.6 as profiles t_1 to t_7, corresponding to points 1 (Q_2, ★) and 2 (Q_3, ◁) through 7 (Q_3, ◁) in the performance curve in Figure 5.5. Noticeably, the peak performance resulted during Q_2 (★1) when bedform dimensions were still relatively small and similar to those observed during Q_1 experiments. During Q_3, the turbine tip-speed ratio, λ, was incrementally adjusted by defining f_T such that the turbine was able to maintain a constant ω in hydraulic conditions that resulted in increased rotor generated torque. This adjustment of ω added complexity in

determining the real variability in C_p values reported in Figure 5.5 and Table 5.1. Limitations in sensor deployment resulted in λ being calculated using the bulk velocity, U_∞, rather than a more desirable instantaneous local hub height velocity, U_{hub}. As bedform dimensions grew during these transitional bedform experiments, U_{hub} was likely locally modified, exposing the turbine to increased variability in the mean and fluctuating flow-field. This variability in U is not taken into account in the λ; therefore, actual C_p locations in Figure 5.5 may have collapsed into a less-variable cluster if measurements of local λ would have been permitted. Regardless, there are certain trends shown in the performance measurements during Q_3. In general, points gradually increased in performance nearing $C_p \approx 0.2$ as λ was increased, eventually landing on the fit-curve of the characteristic performance curve ($\triangleleft$5). However, as bedform geometry continued to develop during Q_3, a larger dune formed immediately upstream of the turbine rotor location (profiles t_6 and t_7 in Figure 5.6). This topographic signature seemed to directly impact the turbine performance. With the crest of the dune located $x/d_T \approx$ -1 to -2 upstream of the turbine rotor plane, the turbine was likely operating in a region of increase local velocity with potentially increased turbulent kinetic energy emanating from the crest of the dune [95]. With slight adjustment of λ, turbine C_p was increased from 0.14 to 0.18 despite operating in very similar local topography. Dune geometric complexity and fixed blade pitch angle and rotor yaw position likely made it difficult to increase turbine performance beyond the observed range for the tested tip-speed ratios, indicating a need for future investigations into optimal power point tracking through advanced control systems integrated into axial-flow turbine designs. The performance measurements detailed in Figure 5.5 and Table 5.1 highlight the difficulty in addressing variability in the C_p in these complex environments, especially when local U_{hub} values are not available, thereby making it difficult to accurately control instantaneous and locally-defined λ.

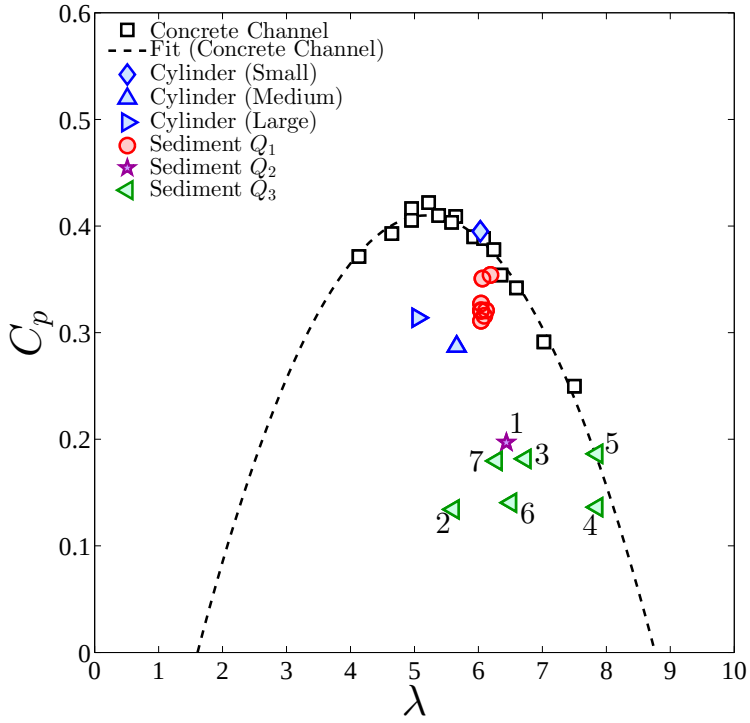

Figure 5.5: Turbine performance curve, C_p vs. λ for fixed bed concrete rectangular channel experiments without (□) and with cylinders (small = ◇; medium = △; large = ▷) and erodible sediment transport experiments (Q_1 = ○; Q_2 = ★; Q_3 =◁). Numbers by points refer to sonar traces in Figure 5.6 and data in Table 5.1.

Experiment	Fig 5.5 Symbol	U_∞ (ms^{-1})	$\omega = 2\pi f_T$ (rad s^{-1})	λ	C_p
Q_1	◯	0.52	12.6	6.06	0.35
	◯	0.52	12.7	6.09	0.32
	◯	0.52	12.7	6.12	0.32
	◯	0.52	12.9	6.19	0.35
	◯	0.52	12.6	6.04	0.32
	◯	0.52	12.6	6.04	0.32
	◯	0.52	12.6	6.04	0.31
	◯	0.52	12.6	6.04	0.33
Q_2	★1	0.60	15.7	6.44	0.20
Q_3	◁2	0.72	16.2	5.61	0.13
	◁3	0.72	19.4	6.73	0.18
	◁4	0.72	22.0	7.85	0.14
	◁5	0.72	22.0	7.85	0.19
	◁6	0.72	18.2	6.51	0.14
	◁7	0.72	17.6	6.28	0.18

Table 5.1: Performance measurement data during Q_1(○), Q_2(★), and Q_3(◁). Data refer to points plotted in Figure 5.5. U_∞ during Q_1 comes from hub height ADV measurement during vertical inflow profile measured during Baseline-Q_1 experiments (Figure 5.4). U_∞ during Q_2 and Q_3 is calculated from the cross-sectional area bulk velocity, $U_\infty = Q_w/(hb)$.

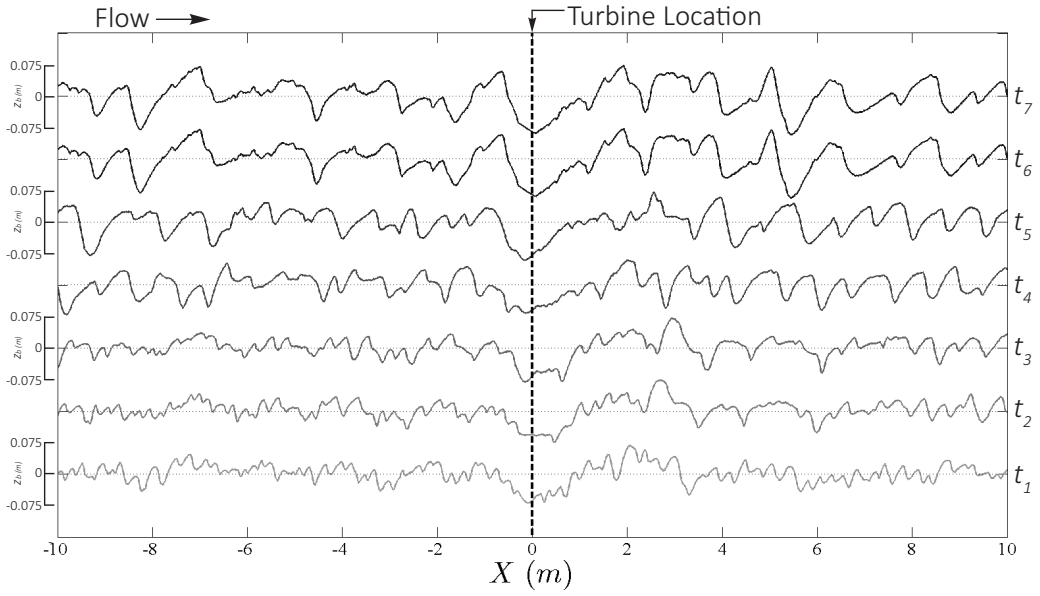

Figure 5.6: Sonar centerline bed elevation profiles t_1 to t_7 associated with numbered points 1 (Q_2, ★) and 2 (Q_3, ◁) through 7 (Q_3, ◁) in the turbine performance curve in Figure 5.5.

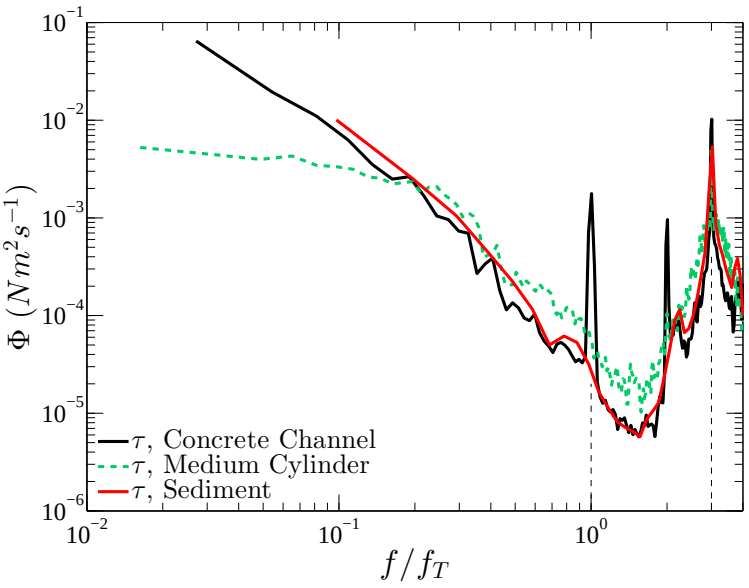

Figure 5.7: Turbine torque power spectra for the concrete channel, medium cylinder, and sediment channel experiments. The $x-$axis has been normalized by the experiment specific turbine rotational frequency ($f_T = 1.5$ for cylinder experiment; $f_T = 2.0$ for concrete channel and sediment experiments). Vertical dashed lines at $f/f_T = 1$ and 3 correspond to the turbine (f_T) and blade passing (f_B) frequency, respectively. Data from cylinder experiment presented in [1].

To gain further insight into the effects of fixed (i.e. cylinders) and mobile (i.e. ripples, dunes) hydraulic structures, fast-Fourier transformation (FFT) analysis was performed on the torque timeseries. [6] demonstrated the link between incoming flow turbulence and turbine response, showing low-frequency coupling between turbulent open-channel flow and turbine power, and a high-frequency region where the turbine is seemingly unresponsive to the small-scale fluctuations in the incoming flow. Further insight into this coupling was addressed by [1] illustrating the dominant effect large-scale coherent eddies have on turbine response, results that stemmed from the cylinder experiments also discussed in this paper. Here, the strong scale-to-scale interactions between flow turbulence and turbine power was shown to reflect itself by imprinting a modified broad range of frequency in the turbine power spectrum coupled to the cylinder-induced turbulent eddy frequencies. To reiterate this phenomenon and extend its application to turbine performance in complex topographic channels with mobile bedforms, similar analysis was conducted using turbine torque timeseries data from Q_1. Figure 5.7 compares the turbine torque power spectra for the same turbine operating in a concrete channel with unmodified approach flow ($\omega = 12.6$), the experiment when coherent eddies were introduced by a medium cylinder

(ω = 9.4) ([1]), and the sediment transport experiment with ripples (Q_1, ω = 12.6). A clear signature of the turbine operational frequency, f_T is seen when the approach flow is unmodified. However, as originally indicated by [1], this signature is lost when an obstacle introduce large-scale eddies upstream of the turbine. Interestingly, a small, yet broad peak is seen in the spectra from sediment transport experiments. Resonant frequencies exist in the turbine torque beyond the turbine cut-off frequency ($f/f_T \approx 1.5$). These lie within the high-frequency region unresponsive to equivalent scales of turbulent flow. Presumably, the small yet broad peak found near the turbine operational frequency during sediment transport experiments indicates that the turbulent boundary layer developed over mobile roughness (i.e. ripples) resulted in lower-frequency modulations that influenced the turbine performance. If the turbine would have been able to dynamically respond to the low-frequency modulations, it would have accordingly adjusted the operating tip-speed ratio.

Research has demonstrated that dune-generated vortices often develop into horseshoe or hairpin-shaped structures emanating from the crest of river dunes towards the free-surface [95]. The frequency of these macro-turbulent structures increases as dunes develop to a greater percentage of the flow depth [97, 155]. Relative dune roughness (i.e. dune height/flow depth) greater than ≈0.2 typically maintain a similar shedding frequency range (≈0.1–0.2Hz), yet visually appear more energetic as the vortex structure intersects the free surface and dune size becomes a larger percentage of the flow depth [97]. While bedforms during Q_1 remained small and likely resulted in less energetic, lower frequency vorticity generated from bedform heterogeneity, the transitional experiments during Q_2 and Q_3 would have resulted in an increase, both in size and frequency, of macro-turbulent vortices generated by the dunes. This increase in vorticity and more frequent interaction with the turbine rotor likely was the cause for decreased and more variable performance characteristics (Figure 5.5). In the case of a turbine operating in dune morphology, the hairpin vortices would occasionally intersect the rotor plane causing unsteady loading on turbine components and energetic bursts in the lower frequency range that is directly coupled to the turbine performance, as seen in Figure 5.7.

5.3.2 Wake Recovery

Wake recovery downstream of wind and marine turbines is typically quantified by the velocity deficit, $U_{def} = (U_\infty - U_x)/U_\infty$, and provides a method for determining optimal downstream placement of addition turbines. Near-wake velocity deficit can provide an indication of turbine efficiency, and has also been used to show the effect that large-scale coherent eddies have on wake recovery [1]. Using hub height ADV measurements aligned with the hub center, U_{def} was quantified up to $x/d_T = 10$ downstream of the turbine for all experiments. Similar characteristics are measured to those reported in previous wake studies (i.e. [6, 29], for example) in that rapid

wake recovery occurs before $5d_T$. For the turbine installed in the mobile sediment channel, near-wake velocity deficit was relatively low at $U_{def} \approx 0.6$. Beyond $x/d_T = 3$, the wake recovery is similar to all cases except for the medium cylinder experiment. Because the turbine was operating at off-peak performance, this implies that the operational characteristics of the turbine, i.e. λ, control the near-wake low-velocity core more directly than the turbulence scales in the surrounding flow. While large-scale coherent eddies accelerate tip-vortex breakdown [1], initiate more rapid onset of wake mixing, and as suggested by [116], are one factor that influences the location and onset of wake meandering along with the inner-core hub vortex dynamics, the near-wake more directly reflects if a turbine is operating at peak-performance. Because U_{def} during sediment ($\lambda \approx 6.1$, $C_p \approx 0.33$) experiments is similar to the off-peak performance operating turbine in an undisturbed concrete channel ($\lambda \approx 7.7$, $C_p \approx 0.32$), this suggests that the decrease from optimal performance was not necessarily due to the small-scale channel roughness (i.e. ripples). The size of the bedform roughness during the experiments was not large enough to modify the turbulent boundary layer and introduce periodic motions in the flow to result in accelerated tip vortex breakdown and accelerated wake velocity deficit recovery in both near and far-wake regions.

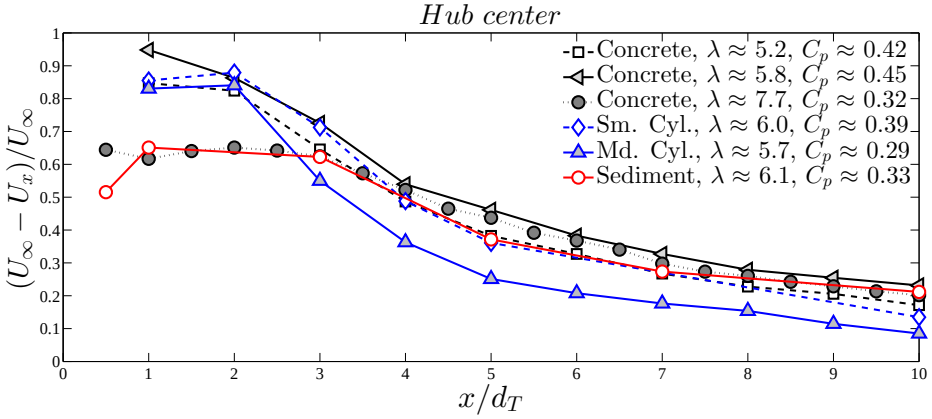

Figure 5.8: Velocity deficit comparison aligned with the hub center for fixed and erodible channels at several tip-speed ratios.

5.3.3 Near-Wake Vortices

During sediment transport experiments, wake measurements at $x/d_T = 0.5$ and 1 provide additional details on the near-wake vortex characteristics. Figure 5.9a focuses on the cross-stream velocity, v, at these two near-wake locations aligned with the blade tip. At $0.5d_T$, a clear signature of the turbine rotational frequency is found, along with an additional spectra peak

coincident with the blade passing frequency, $f_B = 3f_T$. At $1d_T$ however, both frequencies are lost, indicating a break down of the tip vortex by this location. The role that coherent eddies have on turbine wake characteristics, and specifically tip vortex breakdown, was discussed by [1]. Additional evidence that the near-wake vortex structure is preserved in both the tip and hub vortex is shown in Figure 5.9b, a plot of the pre-multiplied spectra of the cross-stream velocity, v, at $0.5d_T$ downstream of the turbine aligned with the hub center. Here the turbine rotational frequency, $f_T = 2.0$, is not observed in the center of the wake as it is at the tip-vortex location. However, a lower frequency signature is found at $f_H = 0.513$, an observation of the spiraling motion of the hub vortex. For wind turbines, hub vortices have been identified in wind tunnel experiments and characterized as having a Strouhal number, $St = (fd_T)/U_{hub} \approx 0.44$ to 0.81 ([152]). For the case of this axial-flow hydrokinetic turbine, $St \approx 0.49$ (where $f = f_H$, $d_T = 0.5$m, and $U_{hub} = 0.52\text{ms}^{-1}$), falling right within that range previously observed for axial-flow turbines. The signature of this hub vortex is also shown in Figure 5.10, a plot of the cross-stream, v', and vertical, w', fluctuation velocity components showing the near-wake spiraling motion in time.

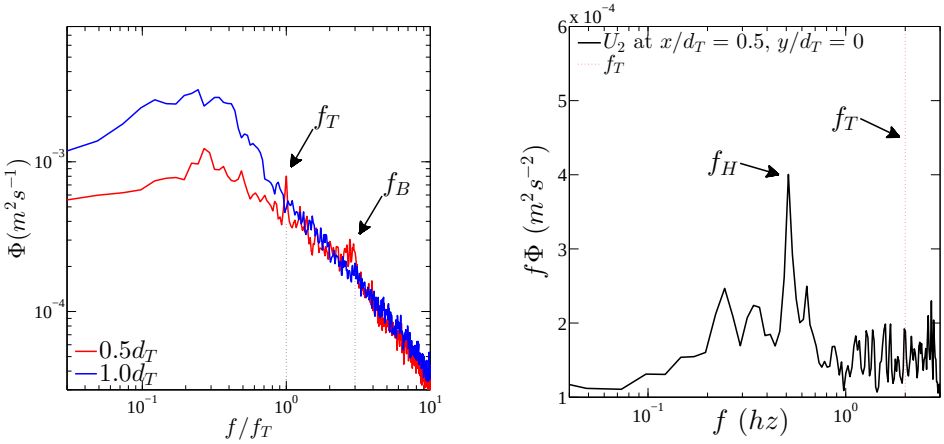

Figure 5.9: (a) Power spectra of the cross-stream velocity, v, at hub height $0.5d_T$ (red) and $1d_T$ (blue) downstream of the turbine aligned with the blade tip $y/d_T = 0.5$ for sediment transport experiments. (b) Pre-multiplied spectra of the cross-stream velocity, v, at hub height $0.5d_T$ downstream of the turbine. Turbine rotational frequency, $f_T = 2.0$hz ($\omega \approx 12.6\text{rad s}^{-1}$). Spectra peak at $f_H \approx 0.51$hz identifies hub vortex signature.

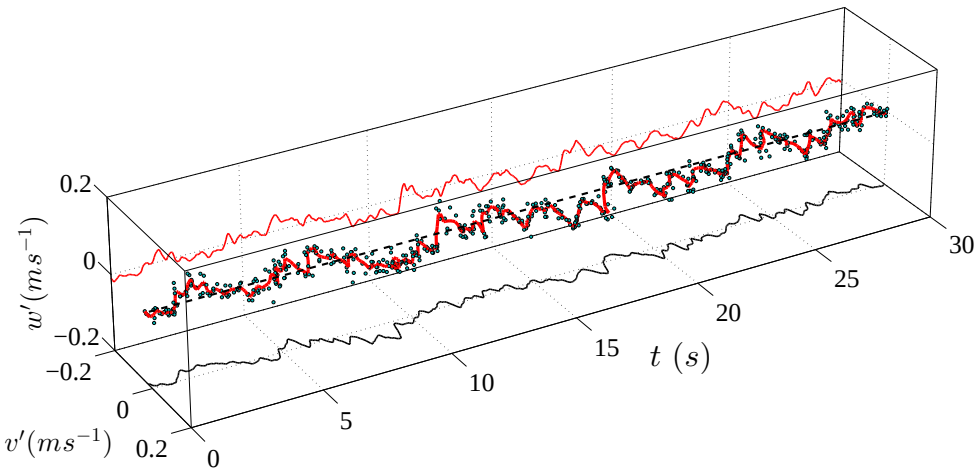

Figure 5.10: Timeseries of the fluctuating cross-stream, v, and vertical, w, velocity components at hub height $0.5d_T$ downstream of the turbine illustrating spiraling motion around the mean, $\bar{V}$ and $\bar{W}$.

5.3.4 Morphodynamics: Average characteristics

High-resolution topography from the end of each experiment is shown in Figures 5.11a-c. Baseline experiments consisted of similarly scaled ripples throughout the entire channel domain. Local turbine-induced scour was observed around the foundation during and after both sediment transport regimes, Q_1 (b) and Q_3 (c). The extent of the near-field scour zone reached to $y/d_T \approx \pm\ 1$ and $x/d_T \approx 2$, similar to local scour measured using the same sized model turbine under clear water sediment transport conditions (i.e. $\tau_b < \tau_{cr}$) [5], and small three-bladed axial-flow turbines studied under both clear water and live bed transport conditions [5, 42]. Similar to observations during those previous studies, deposition of sediment occurred in a wedge-like pattern between $x/d_T \approx 2$ to 5 when ripples were present, and between $x/d_T \approx 3$ to 11 during the dunes experiment.

Using average bed elevation measurements from the continuous sonar profiles along the center of the channel, the characteristics roughness scales can be quantified by calculating the interface width, a method that calculates the root-mean squared of roughness elements along the channel length and provide indications of the bedform wavelength, λ_b, and bedform height, h_b [2]. Figure 5.12 provides a comparison of these characteristics bedform quantities. During Q_2, little change was observed in the bedform geometry compared to the hydraulic conditions used during

baseline and initial turbine experiments. Only a small increase in λ_b and h_b was observed (Table 5.2). During the bedform transitional regime experiment Q_3, a noticeable increase in both occurred, and is easily observed in the ending topography of the channel (Figure 5.11c). Kinematic properties of the bedforms were also quantified using the repeating centerline sonar scans. Cross-correlation analysis performed on two successive longitudinal scans provided methods for calculating average bedform velocities during each experiments. Similar migration velocities were observed during both the baseline experiment and turbine experiment installed in ripples. Here, $U_b \approx 0.21\text{mh}^{-1}$ to 0.25mh^{-1}. During the bedform regime transitional experiment Q_2 phase, bedform velocity increased to $U_b \approx 0.54\text{mh}^{-1}$. During the bedform regime transitional experiment Q_3 phase, bedform velocity increased again to $U_b \approx 1.6\text{mh}^{-1}$. This increase in bedform velocity is also noticeable in the space-time plots using the channel centerline sonar data (Figure 5.13). Here, a noticeable increase in both bedform velocity, U_b (i.e. the slope of the contours in time), and bedform wavelength, λ_b, are visible. The longitudinal bed slope also increased at the from one experiment to the next. During baseline experiment, $S_b \approx 0.05\%$. When the turbine was installed among migrating ripples, the average bed slope adjusted to $S_b \approx 0.12\%$, and adjusted to an even steeper slope during the bedform regime transitional experiments to $S_b \approx 0.18\%$.

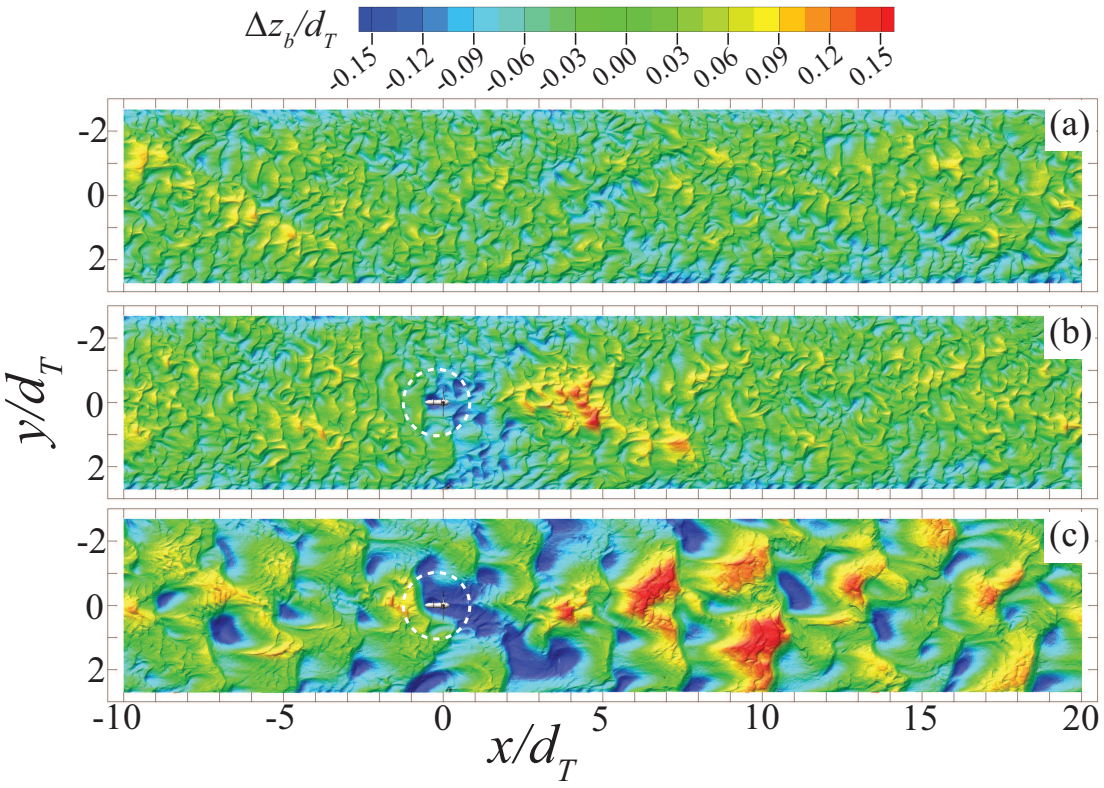

Figure 5.11: Normalized channel topography for (a) baseline ripples, (b) turbine with ripples, and (c) turbine with dunes experiments. Streamwise, x, cross-stream, y coordinates and vertical bed elevation z_b are normalized by the turbine rotor diameter, $d_T = 0.5$m. Turbine location ($x/d_T = 0$, $y/d_T = 0$) indicated by circle. Flow is left to right.

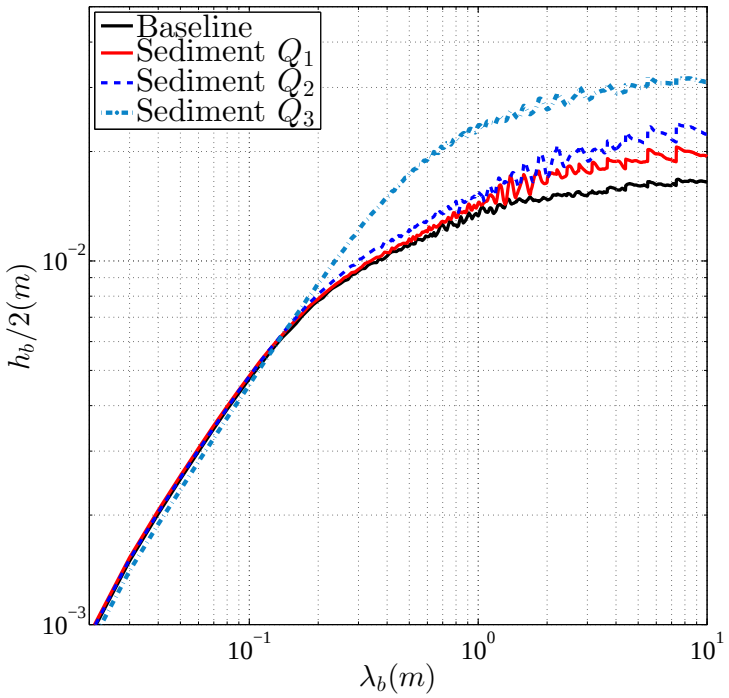

Figure 5.12: Interface width roughness characterization for the sediment transport experiments.

Table 5.2: Hydraulic and bedform characteristics estimated using the interface width approach for each phase of the experiments. Reynolds number, $Re = (U_\infty h)/\nu$. [2].

Experiment	Q_w (m^3s^{-1})	h (m)	Re (−)	Fr (−)	h_b (m)	λ_b (m)	S_b (−)
Baseline - Q_1	1.64	1.17	6.0x10^5	0.15	0.027	0.29	0.0005
Turbine - Q_1	1.64	1.17	6.0x10^5	0.15	0.032	0.32	0.0012
Turbine - Q_2	1.92	1.17	7.0x10^5	0.18	0.035	0.33	0.0014
Turbine - Q_3	2.34	1.18	8.5x10^5	0.21	0.058	0.59	0.0018

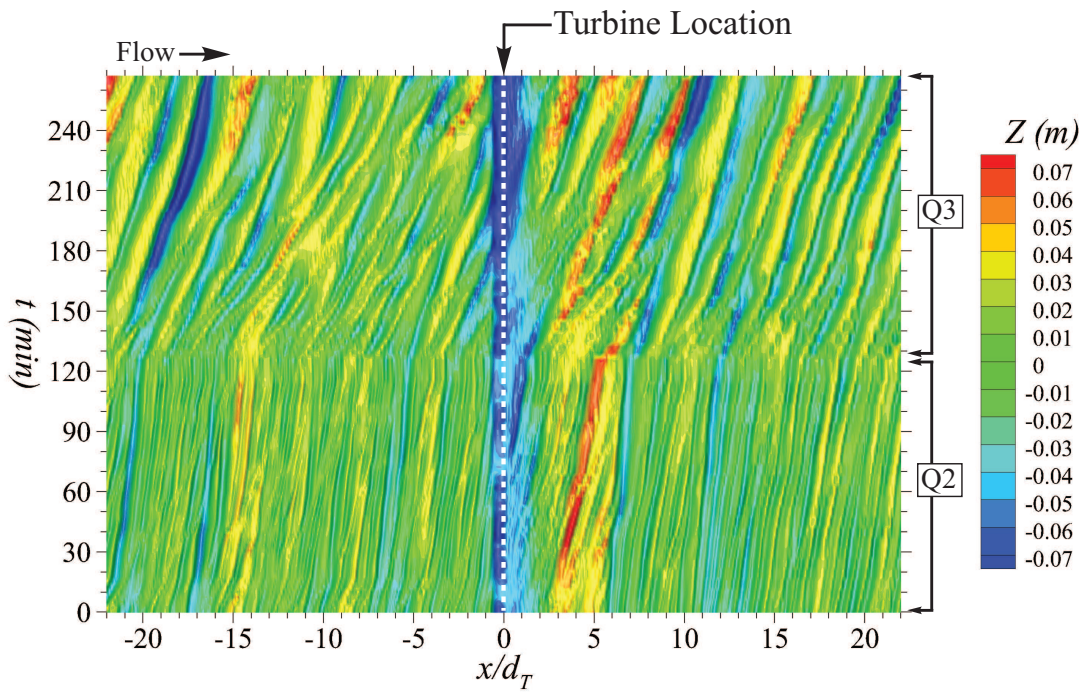

Figure 5.13: Space-time plot of bed elevations during the bedform transitional regime phase from ripples to dunes (Q_2 from $t \approx$ 0min to 125min; Q_3 from $t \approx$ 125min to 265min). Streamwise x coordinate is normalized by the turbine rotor diameter, $d_T = 0.5$m. Turbine located at $x/d_T = 0$. Flow is left to right.

Previously, turbine-induced scour and deposition in the near-field region had been normalized using the rotor diameter, d_T ([5, 42, 154]). However, after quantifying characteristic bedform scales (λ_b and h_b), it was found that similar zones of influence were found for two Reynolds number experiments, indicating Reynolds independent results (Figure 5.14). When the streamwise, x, and cross-stream, y, dimensions are normalized using the characteristic bedform wavelength, λ_b, from each experiment, the turbine zone of influence length, I_L, and width, I_B, collapse into a similar region. This region is a triangular, wedge-like shape that spreads at an angle of $I_\theta \approx 42°$ from the channel center aligned with the turbine hub for a region quantified as $I_L \approx 7\lambda_b$ and $I_B \approx 4\lambda_b$. The experiments from Q_1 ($Re \approx 6.0\text{x}10^5$) and Q_3 ($Re \approx 8.5\text{x}10^5$) begin demonstrating Reynolds independence. Further comparison between experiments at a range of Re is illustrated in Figure 5.15. Here, the average centerline bed elevation and local scour profiles are plotted from a range of Reynolds numbers, $Re \approx 9.2\text{x}10^4$ to $8.5\text{x}10^5$. The maximum scour observed in the near-field region extends from $\Delta z_b/d_T \approx$ -0.1 to -0.2.

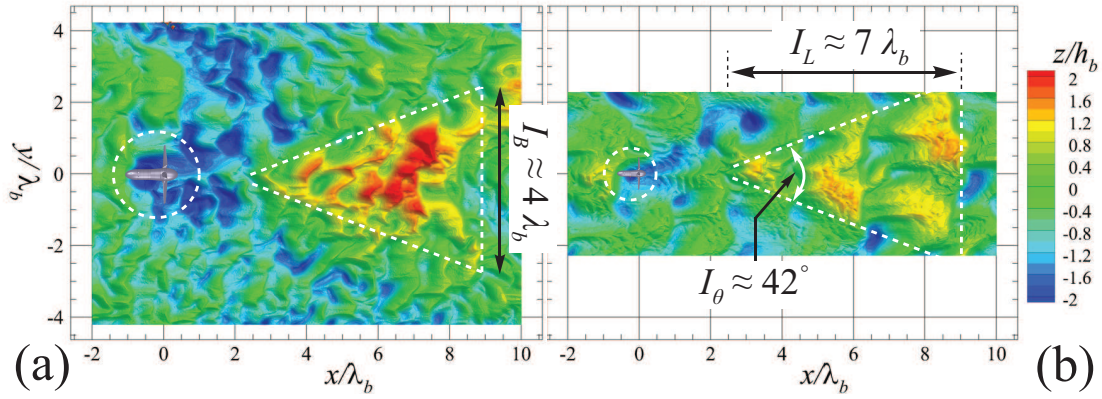

Figure 5.14: End topography of Turbine Q_1 (a) and Turbine Q_3 (b) experiments, normalized by characteristic bedform wavelength, λ_b, from each experiment. The turbine zone of influence length, $I_L \approx 7\lambda_b$ for each case, while the influence width, $I_B \approx 4\lambda_b$ for each case. The zone of influence spreading angle is consistent between the two cases, $I_\theta \approx 42°$. Triangular areas outlined by white dashed lines are equivalent zones in (a) and (b). Contour scale is normalized bedform height, z/h_b. Turbine location outlined by white dashed circle. Flow is left to right.

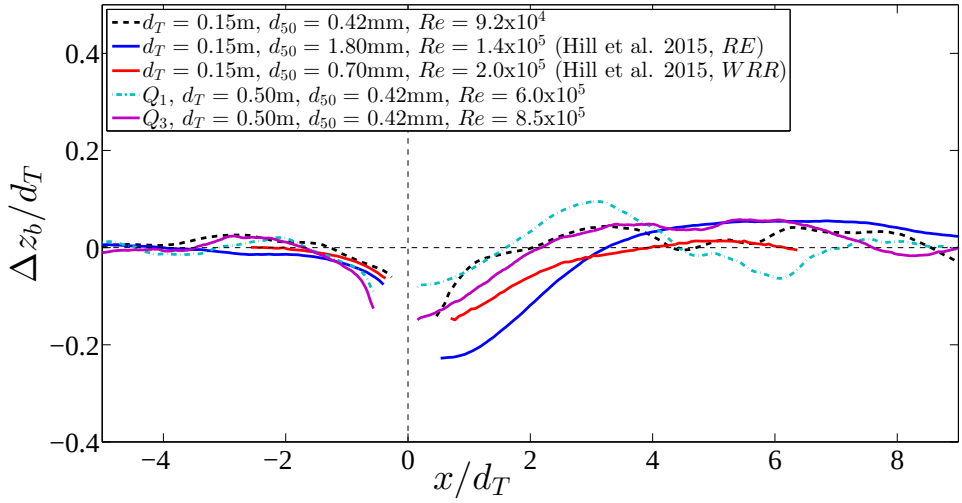

Figure 5.15: Centerline bed elevation profiles aligned with the turbine center plotting mean elevations and scour depth for a range of Reynolds numbers.

5.4 Summary & Conclusion

A series of experiments were conducted to investigate the interactions between uni-directional flow sediment bedforms, axial-flow hydrokinetic turbine performance and wake characteristics, and the effect of Reynolds number on the interactions between axial-flow turbines and sediment transport. In general, mobile bedforms decreased turbine performance compared to a similar experiment in a non-erodible channel. Measurements indicated preservation of key near-wake characteristics such at the tip and hub vortices, while near-wake velocity deficit was observed to be similar to the near-wake velocity deficit downstream of the same turbine in a concrete channel operating at off-peak performance. Far-wake velocity deficit remained similar to other published results for axial-flow turbines [6, 29]. These experiments added to previously published results on near-field turbine-induced scour [5, 42, 154], providing an indication that local scour depths may be Froude and Reynolds number independent, although there remains a large parameter space yet to be investigated (i.e. hub height, tip-speed ratio, sediment grain distribution, and a larger range of Re, for example). Key insights are summarized below relating to the turbine performance, wake characteristics, and channel topography.

Performance

- Turbines operating at similar λ experience reduced C_p when operating in channels with mobile bedforms compared to smooth, non-erodible channels, as shown in the performance curve, Figure 5.5. This reduction in performance is similar to results from experiments published by [1], reiterating that turbine performance responds to stationary and mobile features upstream of the turbine location.

- Transition to larger and faster bedforms reduces turbine performance to $C_p \approx 0.13$ to 0.2) for a range of λ tested ($\lambda \approx 5.6$ to 7.9). The variability in λ and C_p may represent the extremes since local and instantaneous U_{hub} measurements were not permitted, thereby requiring assumptions while prescribing ω.

- The introduction of coherent turbulent structures (i.e. von Kármán type vortices from vertical cylinders or hairpin-shaped vortex tubes emanating from bedforms) results in the loss of the turbine operational spectral peak in the low-frequency zone (Figure 5.7 and also identified by [1]). This broad, less distinct peak in the torque timeseries spectra during mobile sediment bed experiments indicates the channel roughness of this size had less of an impact compared to those reported by [1]. These results provide an indication that precise control of λ may provide improved performance by near-optimal efficiency.

Wake

- Off-peak performance influences the velocity deficit, U_{def}, in the near-wake, shown in the case of the turbine operating in bedforms (Q_1) with $\lambda \approx 6.1$ and in a smooth concrete channel at $\lambda \approx 7.7$ (Figure 5.8).

- Far-wake velocity deficit, U_{def}, is controlled more by channel boundary conditions and turbulent mixing which is increased due to large-scale coherent eddies in the approach flow.

- Evidence of typical scales of motion associated with axial-flow turbine near-wake characteristics, such as the tip vortices and evidence of a slowly rotating hub vortex at $x/d_T = 0.5$ (Figure 5.9).

- Wake characteristic data with dune bedform transport were not available, yet results suggest velocity deficit would recover more quickly, similar to the cylinder experiments where turbulent coherent eddies resulted in near-wake tip vortex breakdown and accelerated near and far-wake velocity deficit recovery [1].

Topography

- Local scour and deposition was observed during live bed sediment transport experiments (Q_1 and Q_3). The turbine region of influence at two Reynolds numbers is a triangular shaped region extending $I_L \approx 7\lambda_b$ in the streamwise direction and $I_B \approx 4\lambda_b$ in the cross-stream direction with a spreading angle of $I_\theta \approx 42°$ (Figure 5.14).

- Recent results suggest normalizing turbine-sediment interactions by the characteristic bedform dimensions (λ_b and h_b) is more appropriate that using the turbine diameter, d_T, as the normalization factor. Rotor diameter may still be the appropriate factor for normalizing scour depth, d_s.

- Small modifications in bedform geometric characteristics, λ_b and h_b, were measured between the baseline and turbine experiments in ripples (Q_1).

5.5 Notation used in Chapter 5

b = channel width, m
d_T = turbine rotor diameter, m
d_{50} = mean sediment grain size, m
f = sampling frequency, Hz
h = flow depth, m
h_b = bedform height, m

h_{hub} = hub height, m
Q_w = bulk flow rate, m^3s^{-1}
q_s = sediment supply rate, Ls^{-1}
S_b = channel bed slope, %
$S(f)$ = spectral energy density, m^2s^{-1}
t = time, s
$\overline{U}$ = mean streamwise velocity, ms^{-1}
U_{adv} = ADV traversing velocity, ms^{-1}
U_b = bedform velocity, ms^{-1}
U_{mag} = velocity magnitude, ms^{-1}
u' = streamwise velocity fluctuations, ms^{-1}
u_k = turbulent kinetic energy velocity scale, ms^{-1}
$\overline{V}$ = mean cross-stream velocity, ms^{-1}
v' = cross-stream velocity fluctuations, ms^{-1}
$\overline{W}$ = mean vertical velocity, ms^{-1}
w' = vertical velocity fluctuations, ms^{-1}
x = streamwise coordinate direction, m
y = cross-stream coordinate direction, m
z = vertical coordinate direction, m
z_b = bed surface elevation, m
z_{hub} = hub elevation, m
z_w = water surface elevation, m

Greek & Script symbols
λ_b = bedform wavelength, m
τ = turbine torque, Nm

Chapter 6

U.S. Department of Energy Reference Model 1

The following chapter is a work in progress to be submitted for publication in *Renewable Energy*. The planned citation is as follows.

Hill, C., Neary, V. S., Gunawan, B., Guala, M., and Sotiropoulos, F., (2015), Performance and wake characteristics of a laboratory scaled model hydrokinetic turbine: RM1 dual-rotor axial-flow turbine., in preparation for *Ren. Energy*.

6.1 Introduction

The Reference Model Project (RMP), sponsored by the U.S. Department of Energys (DOE) Wind and Water Power Technologies Program within the Office of Energy Efficiency & Renewable Energy (EERE), aims at expediting industry growth and efficiency by providing non-proprietary Reference Models (RM) of MHK technology designs as study objects for open-source research and development. As part of this program, MHK turbine models were tested in a large open channel facility at the University of Minnesotas St. Anthony Falls Laboratory (UMN-SAFL). Reference Model 1 (RM1) is a 1:40 geometric scale dual-rotor axial-flow horizontal axis device with counter-rotating rotors, each with a rotor diameter $d_T = 0.5$m. Precise blade angular position and torque measurements were synchronized with three acoustic Doppler velocimeters (ADV) aligned with each rotor and the midpoint for RM1. Flow conditions for each case were controlled such that depth, $h = 1$ m, and volumetric flow rate, $Q_w = 2.425\text{m}^3\text{s}^-1$, resulting in a hub height velocity of approximately $U_{hub} = 1.05\text{ms}^-1$ and blade chord length Reynolds

numbers of $Re_c \approx 3.0x10^5$. Vertical velocity profiles collected in the wake of each device from 1 to 10 rotor diameters are used to estimate the velocity recovery and turbulent characteristics in the wake, as well as the interaction of the counter-rotating rotor wakes. The development of this high resolution laboratory investigation provides a robust dataset that enables assessing turbulence performance models and their ability to accurately predict device performance metrics, including computational fluid dynamics (CFD) models that can be used to predict turbulent inflow environments, reproduce wake velocity deficit, recovery and higher order turbulent statistics, as well as device performance metrics.

6.2 Experimental Setup

Experiments for Reference Model 1 (RM1) were completed in the Main Channel facility at St. Anthony Falls Laboratory (SAFL) at the University of Minnesota (UMN), a 2.75m wide by 1.8m deep by 85m long concrete rectangular channel with controllable supply of Mississippi River water. An intake gate controls the discharge level within the flume while a mechanical tailgate weir controls flow depth, h, and monitors flow rate, Q_w. Water passed through two rows of vertically oriented baffles to break up any large scale turbulent structures before entering the test section of the channel. The RM1 model was located approximately 40m downstream of the baffles. RM1 is a 1:40 geometric scale dual-rotor axial-flow horizontal axis turbine with counter-rotating rotors, each with a rotor diameter $d_T = 0.5$m (Figures 6.1, 6.2, and 6.3). Geometric and experimental parameters are detailed in Table 6.1. The blade profile used for the SAFL RM1 turbine designs (NACA-4415) was modified from the original RM1 design blade profile (NACA 63(4)-24). This was done because of the lower Reynolds number flows used for the SAFL open channel experiments and the availability of low Reynolds number lift (C_L) and drag (C_D) coefficient data for the NACA-4415 profile (Figure 6.4, Table 6.2). The SAFL Main Channel is equipped with a data acquisition (DAQ) carriage that is capable of three-axis automated motion. This carriage was utilized during data collection to position various sensors to monitor the hydraulic environment around the RM1.

Velocity measurements were collected using three Nortek Vectrino acoustic Doppler velocimeters (ADVs). During performance measurements, the ADVs were positioned at hub height 3 rotor diameters ($3d_T$) upstream of the RM1 rotor location and sampled at 200Hz for 10 minutes for each rotor angular velocity. All three ADVs were synchronized with the turbine torque and angular position measurements. Vertical velocity profiles were collected at $1d_T$, $3d_T$ and $5d_T$ upstream of the RM2 location. Vertical point spacing was 5cm and measurements were collected at 200Hz for 3 minutes. A horizontal profile at hub height was collected at $1d_T$, $3d_T$ and $5d_T$

upstream and spanned the channel width. Wake vertical velocity profiles were collected downstream of the turbine from $1d_T$ to $10d_T$ with $1d_T$ streamwise spacing. One ADV was aligned with the axis of rotation for each rotor, and the third ADV was positioned at the mid-plane between the rotors centered on the vertical cylindrical support tower for RM1. Vertical point spacing was 2.5cm for all wake profiles, and measurements were collected for 5 minutes at each point at 200Hz. A horizontal plane was collected from $1d_T$ to $10d_T$ with $1d_T$ streamwise spacing. Cross-stream ADV point location varied, but provided enough spatial resolution to resolve key characteristics of the turbine wake. Prior to velocity measurements, the SAFL Main Channel was ponded with water and a towing test was performed to determine any rotation of the ADV measurement volume. All measurements had the resulting rotation matrix applied to the data before calculating flow statistics. Additionally, velocity timeseries measurements were filtered to remove any erroneous samples [156].

Torque measurements were collected from each rotor. Each rotor had an Interface Force 20Nm MRT miniature reaction torque sensor mounted inside the hub, thereby minimizing the torque losses in the system prior to measuring torque. Voltages from the torque transducer were transmitted to the data acquisition computer via a Rotary Systems SR003 series slip ring, through an Interface Force SGA signal conditioner to convert the millivolt signal to a 0-5V range, and then acquired at the analog to digital data acquisition board. A chain drive was used to connect the shaft of each rotor to the shaft of the system speed control. A Pacific Scientific stepper motor (model K42HRFM-LEK-M2-00) controlled by a Parker Zeta 6108 indexer drive provided accurate and precise control of rotor angular velocity. Angular position was measured using a single Automation Direct rotary encoder (model TRD-SH1000-VD) mounted to the motor shaft and referenced to the counter-rotating RM1 rotor blade position. All torque and angular position measurements were synchronized with the velocity measurements.

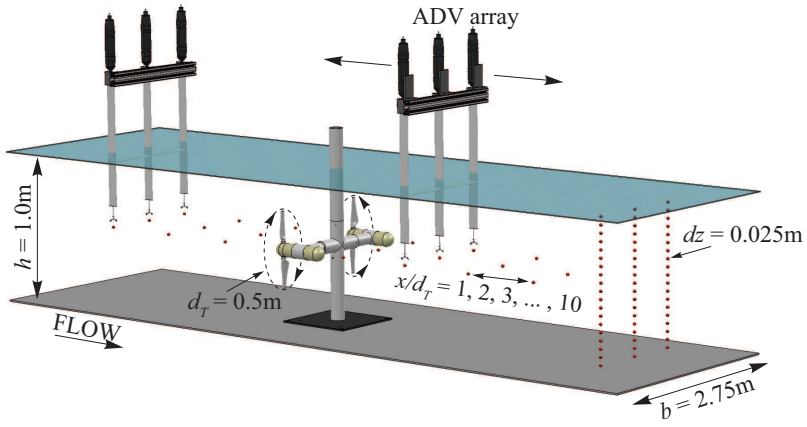

Figure 6.1: Experimental setup schematic of RM1 in the SAFL Main Channel Facility.

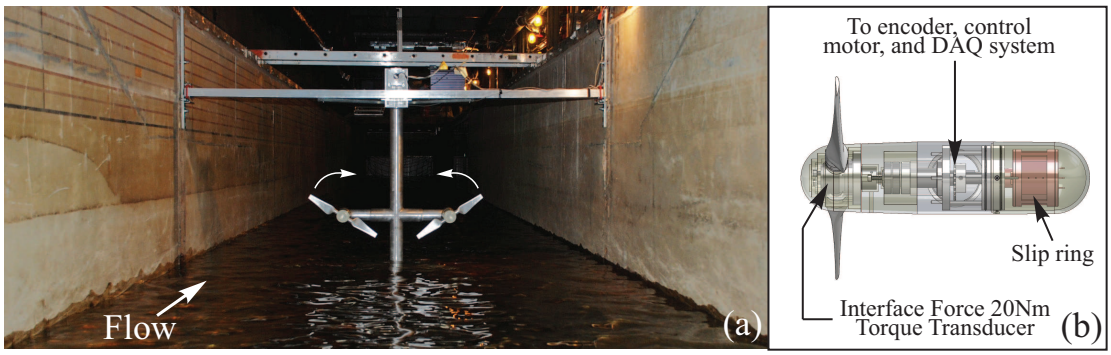

Figure 6.2: (a) Photo of RM1 installed in the SAFL Main Channel Facility. (b) CAD image showing internal instrumentation setup for data acquisition of turbine performance.

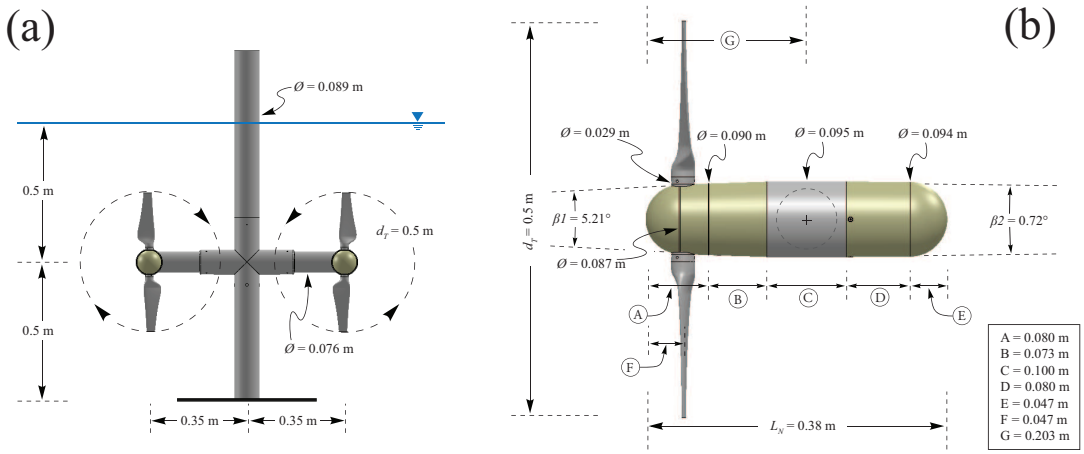

Figure 6.3: Detailed dimensions of the 1:40 scale RM1 turbine tested at SAFL.

Parameter	**SAFL RM1 Turbine**
Blade Profile	NACA-4415
Max Chord Length (c_{max})	0.0645m
Tip Chord Length (c_{tip})	0.0312m
Rotor Diameter (d_T)	0.5m
Hub Height (h_{hub})	0.5m ($1.0d_T$)
Hub Diameter (d_{hub})	0.087m ($0.174d_T$)
Hub Length (L_{hub})	0.080m
Nacelle Length (L_N)	0.380m
Nacelle Diameter (d_N)	0.095m ($0.19d_T$)
Cross Arm attachment position	L_N x 53.4%
Cross Arm Diameter	0.0762m
Vertical Tower diameter	0.0889m
Turbine Rotor Spacing (S_T)	0.7m ($1.4d_T$)
Submergence (S)	0.5m ($1.0d_T$)
Solidity	13.7%
Flow Depth (h)	1.0m ($2.0d_T$)
Volumetric Flow Rate (Q_w)	2.425m3s-1
Blockage ($= A_T/A$)	14.3%
Tip-Speed Ratios (λ)	1–9
Froude Number ($Fr = U_\infty/\sqrt{gh}$)	0.28 ($U_\infty \approx 0.88\text{ms}^{-1}$)
Reynolds Number ($R_c = (\lambda U_{hub} c)/\nu$)	$\approx$ 3.0x10^5

Table 6.1: Geometric and experimental parameters for RM1 experiments.

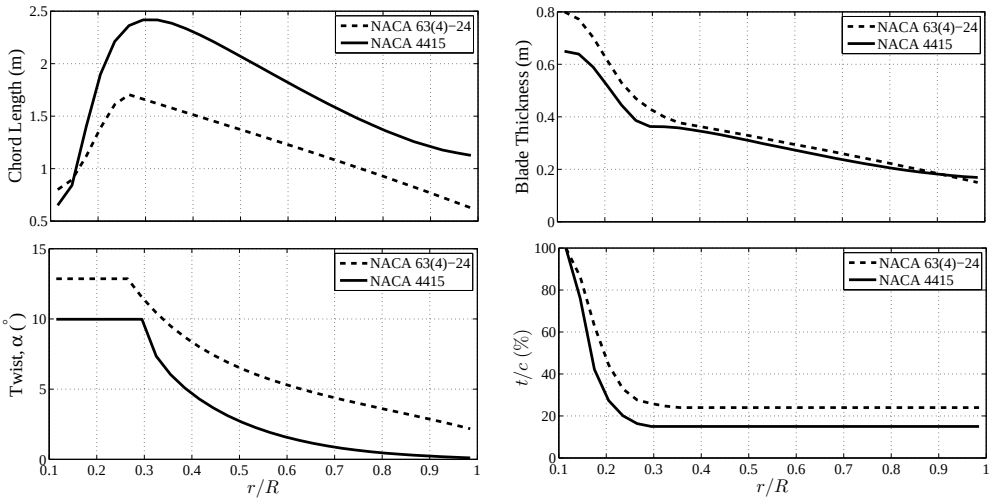

Figure 6.4: Comparison between full-scale blade geometric characteristics for the original RM1 blade design (NACA 63-series) and the modified design (NACA 44-series) for lower Reynolds number testing at SAFL.

r/R	c/R	t/c	$\alpha(^\circ)$
0.21	0.12	1.00	13.16
0.24	0.12	1.00	13.16
0.27	0.14	0.85	13.16
0.29	0.19	0.52	13.16
0.32	0.23	0.31	13.16
0.35	0.25	0.19	13.16
0.37	0.26	0.15	13.16
0.40	0.26	0.15	11.28
0.43	0.25	0.15	10.24
0.45	0.25	0.15	9.43
0.48	0.24	0.15	8.76
0.51	0.23	0.15	8.17
0.53	0.22	0.15	7.64
0.56	0.21	0.15	7.16
0.59	0.21	0.15	6.70
0.61	0.20	0.15	6.27
0.64	0.19	0.15	5.86
0.67	0.18	0.15	5.46
0.69	0.18	0.15	5.07
0.72	0.17	0.15	4.69
0.75	0.16	0.15	4.31
0.77	0.16	0.15	3.93
0.80	0.15	0.15	3.55
0.83	0.15	0.15	3.17
0.85	0.14	0.15	2.78
0.88	0.14	0.15	2.38
0.91	0.13	0.15	1.98
0.93	0.13	0.15	1.57
0.96	0.13	0.15	1.14
1.00	0.12	0.15	0.70

Table 6.2: Characteristics of the RM1 turbine blades (NACA-4415).

6.3 Data Reduction Methods

The following parameters were calculated during the processing of the velocity and turbine performance data collected during the RM1 experiments at SAFL.

Mean and fluctuating velocity fields

The 200Hz velocity data output from the three Nortek Vectrino velocimeters were filtered to remove any erroneous data (see [157], [156]). Through Reynolds decomposition, the velocity timeseries can be decomposed into the mean and fluctuation components,

$$U_i = \overline{U} + u'$$

The so calculated fluctuating velocity components are then used to calculate a number of flow statistics, which are described below.

Turbulence Intensity

The turbulence intensities are dimensionless parameters that describe the level of turbulence within the flow along each spatial direction, and are defined as the root-mean squared of the fluctuating velocity component divided by the mean velocity magnitude, where,

$$\overline{U}_M = \sqrt{\overline{U}^2 + \overline{V}^2 + \overline{W}^2}$$

and,

$$I_{u_i} = \sigma^2_{u_i} / \overline{U_M}$$

for i = 1, 2, 3.

Reynolds Stresses

The Reynolds stress tensor is defined as follows:

$$\tau_{ij} = \overline{u'_i u'_j}$$

When $i = j$, the results are the normal stresses ($\overline{u'u'}$, $\overline{v'v'}$, $\overline{w'w'}$), also known as the velocity variance, $\sigma^2_{u_i}$, and when $i \neq j$, the results are the shear stresses ($\overline{u'v'}$, $\overline{u'w'}$, $\overline{v'w'}$).

Turbulence Kinetic Energy

The turbulence kinetic energy (TKE), k, is defined as follows:

$$k = \frac{1}{2}\left(\overline{u'^2} + \overline{v'^2} + \overline{w'^2}\right)$$

Velocity Deficit

The streamwise velocity deficit is a common metric used to report the wake velocity recovery downstream of a turbine, and is defined as follows:

$$U_{def} = \frac{|U_\infty - U_x|}{U_\infty}$$

where U_∞ is the upstream approach velocity at hub height, or rotor height center in the case of RM1, and U_x is the hub height velocity at position x downstream of the turbine. Here, U_∞ is measured at x/d_T = -5.

Turbine Performance

Using the synchronous velocity, torque and rotor position measurements, various turbine parameters could be calculated. The rotor position was used to calculate the turbine angular velocity, ω. Turbine power, P_T, was calculated using the measured torque and angular velocity using,

$$P_T = \tau\omega$$

where τ is the measured torque and ω is the calculated angular velocity that was applied via the stepper motor and measured using the positional encoder integrated with the drive system. The available power within the approaching flow was calculated using the synchronous velocity measurements upstream of the RM1 location using,

$$P_A = \frac{1}{2}\rho A_T U^3$$

where P_A is the calculated available power, ρ is the density of water ($\approx$ 1 kg/m^3) dependent on water temperature (typically between 18.0°C and 20.5°C during the RM1 tests), A_T is the flow cross sectional area covered by the device ($A_T = \left(\pi {d_T}^2\right)/4$), and $\bar{U}$ is the approach flow mean velocity from the measured data using the three ADVs at hub height $3d_T$ upstream of RM1. Both time-averaged turbine power ($\overline{P_T} = f(\tau)$) and available power ($\overline{P_A} = f\left(\overline{U}^3\right)$) as well as instantaneous turbine power ($P_{Ti} = f(\tau_i)$) and available power ($P_{Ai} = f\left({U_i}^3\right)$) were calculated. With these power calculations, the coefficient of performance, C_p, is calculated by applying the above defined values to the equation,

$$C_p = \frac{P_T}{P_A}$$

This parameter describes the fraction of power extracted from the approaching flow by the turbine. An additional dimensionless parameter used to describe the turbine performance characteristics is the tip-speed ratio, λ, defined as the ratio of the rotor tip speed to the speed of the approaching flow,

$$\lambda = \frac{\omega d_T}{2\overline{U}}$$

Uncertainty Analysis

In experimental measurements, both systematic and random measurement error exists [158]. Systematic error in the torque sensors was determined during torque sensor calibration by applying known torque values and comparing measured against expected values. The results of the calibration tests are summarized in Table 3 and represent the systematic (constant) error associated with the torque sensors during RM1 experiments. This systematic error was removed prior to calculating and reporting of the additional experimental measurement uncertainty. Uncertainty values for the ADVs and optical encoder were used from manufacturers reported values and incorporated into the error propagation from measurements into the calculations of turbine performance, C_p. Additionally, extended datasets were collected to assess the uncertainty in the mean values of each instrument. Results showed that the uncertainty in the torque, τ, was $U_\tau/\tau = 1.92\%$. Uncertainty in the angular velocity, ω, was $U_\omega/\omega = 2.5\%$. Uncertainty in the velocity measurements, U, was $U_U/U = 0.78\%$. Methods outlined by [158] were used to calculated the combined uncertainty from the measured variables used in calculating $C_p = \mathrm{f}(\tau, \omega, U^3)$. The uncertainty in calculated C_p values is given by;

$$\frac{U_{C_p}}{C_p}^2 = \frac{U_\tau}{\tau}^2 + \frac{U_\omega}{\omega}^2 + (-3)^2 \frac{U_{\bar{u}}}{\bar{u}}^2$$

Using the uncertainty values reported above, the uncertainty in calculated C_p values is approximately U_{C_p} 3.9%.

6.4 Results & Discussion

6.4.1 Inflow Characteristics

Inflow vertical (Figure 6.5) and horizontal (Figure 6.6) velocity profiles were collected at three rotor diameters ($3d_T = 1.5$m) upstream of the RM1 rotor locations. The three ADV mount described in the Experimental Setup section was used to collect synchronous ADV measurements at these locations. Average hub height streamwise velocity, $U_{hub} = 1.05\mathrm{ms}^{-1}$. Turbulence intensity in the region of the RM1 rotors was approximately 5%. The shear velocity, u_*, in open channel flow is an important parameter in characterizing the near-wall stresses imposed by the flow on the channel boundaries. This parameter can be estimated using velocity profiles and the logarithmic law of the wall equation,

$$\frac{\overline{U}}{u_*} = \frac{1}{\kappa} ln\left(\frac{z}{z_0}\right)$$

where $\bar{U}$ is the mean velocity at z, the distance from the wall, κ is the von Kármán constant ($\kappa = 0.41$), and z_0 is the hydrodynamic roughness length. Using this method, the friction velocity

was found to be, $u_* = 0.033\text{ms}^{-1}$.

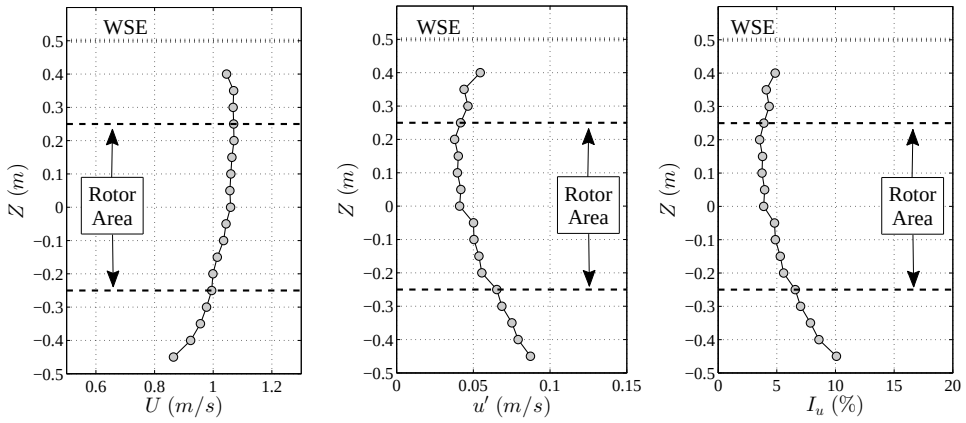

Figure 6.5: Inflow vertical profile characteristics in the center of the channel at $3d_T$ upstream of the RM1 rotors: mean streamwise velocity, $\bar{U}$ (left), streamwise velocity root-mean squared, u' (center), and streamwise turbulence intensity, I_u (right). Area between dashed lines -0.25m $\leq Z \leq$ 0.25m indicates RM1 rotor energy extraction plane. Mean water surface elevation (WSE) indicated by dashed line at $Z = 0.5$m.

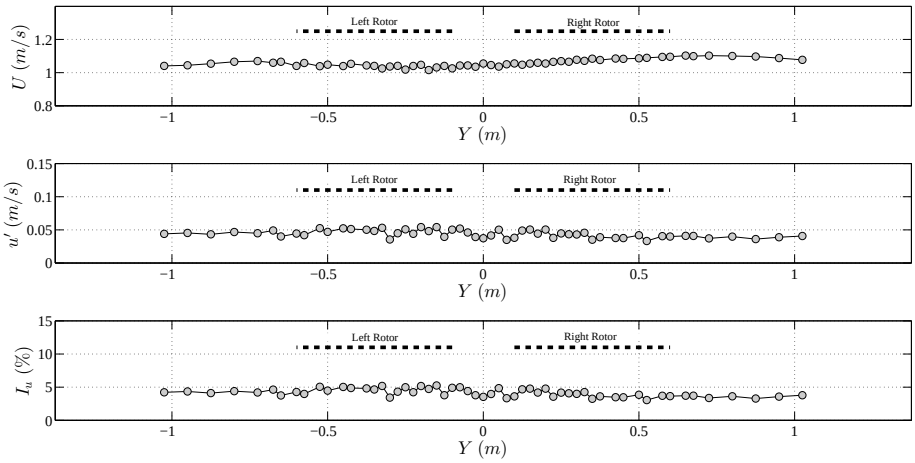

Figure 6.6: Inflow horizontal profile characteristics at hub height, h_{hub}, from $3d_T$ upstream of the RM1 rotors: mean streamwise velocity, $\bar{U}$ (top), streamwise velocity root-mean squared, u' (center), and streamwise turbulence intensity, I_u (bottom). Y-axis distance shows full channel width, $b = 2.75$m.

6.4.2 Turbine Performance

Performance curves for both the left and right rotors are shown in Figure 6.7. These plots show the coefficient of power, C_p, against tip-speed ratio, λ. Optimal performance occurred at approximately $\lambda = 5.1$ with a corresponding $C_p = 0.48$ for the right rotor and $C_p = 0.43$ for the left rotor. For comparison, [39] observed optimal performance at approximately $\lambda = 6.5$ with a corresponding $C_p = 0.41$ for a single scaled model RM1 rotor in a large towing tank facility at the United States Naval Academy. The turbine model for the Naval Academy test consisted of a 0.8m diameter rotor with a NACA 63-618 blade cross section. The blades are twisted from 13◦ at the root to 2◦ at the tip and tapered from a maximum chord length of 0.07m to a minimum of 0.025cm. The two rotors performed differently, although both had relatively high performance (i.e. greater than $C_p = 0.4$). The complexity of flow in the SAFL open channel facility and slight asymmetry in the approach flow may have been a factor in this observed difference. In addition to the measurement uncertainty reported in Figure 6.7, possible differences could result from asymmetric flow. Because turbine performance is a function of velocity cubed, $C_p = f\left(U^3\right)$, a difference of 0.03-0.05ms^{-1} ($\approx$ 3-5% in the RM1 experiments case) from one side of the channel to the other could result in C_p values varying by approximately 9-15%. The resulting performance curves do show differences at optimal tip speed ratio, λ, of approximately

10%. During performance tests, ADVs were positioned upstream at $3d_T$ and aligned with the rotor center. These velocity values were used in calculating instantaneous C_p values; however, additional asymmetry in the approach flow that may have existed to the left or right of the ADV, yet still within the turbine energy extraction plane region, may have propagated and added to the difference in calculated C_p values. During performance testing, instantaneous rotor torque, τ_i (Nm), and angular position, $\theta_i(^\circ)$, were collected, providing data to calculate average torque values based on rotor angular position (Figure 6.8).

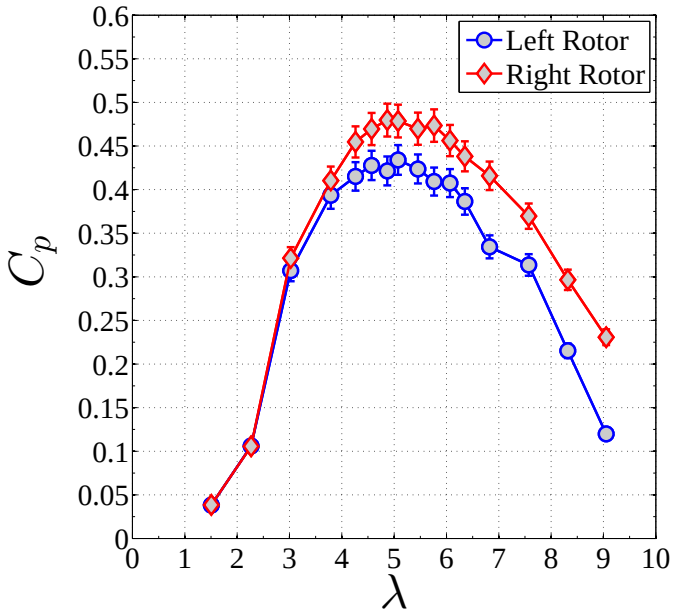

Figure 6.7: Calculated C_p vs. λ (coefficient of power vs. tip-speed ratio) for the left (blue) and right (red) RM1 rotors. Vertical error bars represent mean C_p value measurement uncertainty. Maximum C_p occurs near $\lambda \approx 5.1$ (right rotor $C_p = 0.48$; left rotor $C_p = 0.43$). Results have not been corrected for channel blockage; therefore, maximum C_p may slightly decrease after blockage corrections have been applied.

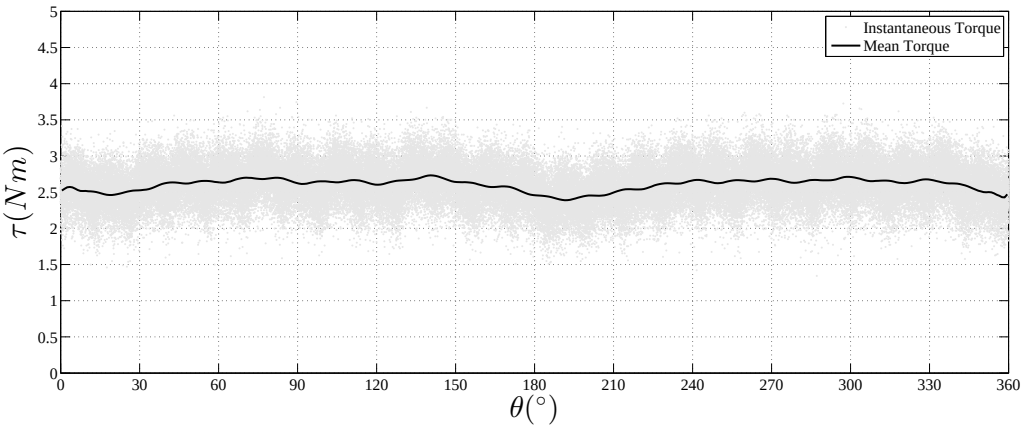

Figure 6.8: Instantaneous torque (light gray dots) measurements, τ_i vs. instantaneous rotor blade angular position, $\theta_i(^\circ)$. Solid black line illustrates mean torque value, $\bar{\tau}$ vs. rotor blade angular position, $\theta(^\circ)$. Measurements collected from right rotor while turbine was operating at $\omega = 3.4$rps ($\lambda \approx 5.1$). RM1 blades are offset 180° on each rotor but were rotating in symmetry.

Blade Pitch Adjustment

Initial performance testing of the RM1 rotors revealed a C_p vs. λ curve as shown in Figure 6.7. It was hypothesized that the pitch of the blades on the left rotor were misaligned, thereby creating the lowered performance compared to the right rotor. To investigate this hypothesis, performance measurements at several pitch angles for the left rotor were measured to verify that the blades were at the optimal angle. After collecting performance measurements at a turbine rotational speed of $\omega = 3.4$ rps ($\lambda \approx 5.1$), it was found the optimal pitch angle was $\alpha = 0^\circ$ for the initial performance tests completed. Therefore, other factors, not identified in this study, caused decreased performance of the left rotor. A full round of performance testing was repeated. These are the results shown in Figure 6.7.

6.4.3 Wake Characteristics

Mean and RMS velocity

Turbine wake velocity profiles were collected downstream of the RM1 rotor locations from $1d_T$ to $10d_T$ at $1d_T$ streamwise spacing. These data were collected along three vertically oriented (XZ) planes aligned with each rotor center and the mid-plane between the two rotors, as well as a horizontal (XY) plane aligned with the rotor hub height. Contour plots for the velocity deficit within the horizontal hub height plane and three vertical planes aligned with each rotor

and center support tower are shown in Figure 6.9. Additionally, the normalized values of turbulent kinetic energy in these same planes are illustrated in Figure 6.10. In general, the largest velocity deficit occurs in the near wake region at the center between the two rotors, immediately downstream of the center cylindrical vertical and horizontal support arms. The relatively high blockage (14.3%) forces flow acceleration to the outside of each rotor, as well as above and below each rotor location, visible in Figure 6.9. It should be noted that the results reported here have not yet been corrected for channel blockage. The wake of each RM1 rotor quickly joins with the disturbance created by the center tower and forms a horizontally expansive wake that propagates far downstream and remains approximately the width of the entire RM1 device while slowly diffusing and mixing with the surrounding flow. Elevated levels of turbulent kinetic energy are present in the downstream environment, particularly in the region aligned with the center support tower extending to approximately $2d_T$. Additionally, the tip vortices shed from the blades create elevated regions of turbulent kinetic energy, evident in Figure 6.10 aligned with the top-tip elevation of each rotor. Between approximately $2d_T$ and $4d_T$, the TKE values begin to spread vertically and horizontally.

The streamwise velocity deficit previously defined is plotted at the RM1 rotor hub height, along with streamwise root-mean squared values, ${\sigma_u}^2$, and streamwise turbulence intensity, I_u, in Figures 6.11, 6.12, and 6.13, respectively. The RM1 rotors begin affecting inflow velocities up to approximately $2.5d_T$ to $3d_T$, at which point the flow decelerates by approximately 10% by the time it is one blade length upstream of the rotor energy extraction plane. The largest velocity deficit occurs in the wake of the center support tower (approximately 100%), which strong instabilities occurring here in the form of von Kármán type vortices shed from the cylinder. Near wake ($\approx 1d_T$) velocity deficit in the wake of each rotor is approximately 30% and increases up to about $3d_T$ to $4d_T$, at which point it begins to gradually recover. The relatively large blockage by the two rotors and center cylinder support tower generate a large wake that propagates far downstream. Hub height velocity measurements were collected up to $24d_T$, at which point the velocity deficit had recovered to only about 5% in the wake of each rotor, while the center of the wake was still nearly 15% deficient. Neither turbulent fluctuations nor the streamwise turbulence intensity recovered to the undisturbed upstream equivalent values as far downstream as $24d_T$.

Wake characteristics from previous experiments using a single three-bladed axial-flow turbine with the same diameter, $d_T = 0.5$m, were reported by [6] and wake recovery was discussed by [29]. The rotor for this turbine was located on the downstream side of the support tower ($d_{tower} = 0.038$m), whereas the RM1 dual-rotor turbine rotors were located on the upstream side of the horizontal cross arm supports. Results presented in [29] show a similar behavior in the velocity deficit, with a peak velocity deficit occurring around $x/d_T = 3$. The near wake velocity deficit for

the RM1 turbine is lower than the single rotor turbine, possibly due to the larger size, proximity, and downstream near-wake location of the horizontal cross arm support. The flow instability generated by this support structure could increase mixing, thereby increasing wake mixing and decreasing recovery distance. Far wake ($\geq x/d_T = 5$) velocity deficit is similar between the single rotor and dual-rotor turbines ($\approx$ 10%-20%). Similar behavior is also noticed in the RMS values, with peak intensity occurring around $x/d_T = 5$; however, single rotor turbine values are approximately twice that of the RM1 dual-rotor turbine. Turbulence intensity, I_u, values are similar for distances greater than $x/d_T = 5$, but lower in the near wake region closer than $x/d_T = 5$.

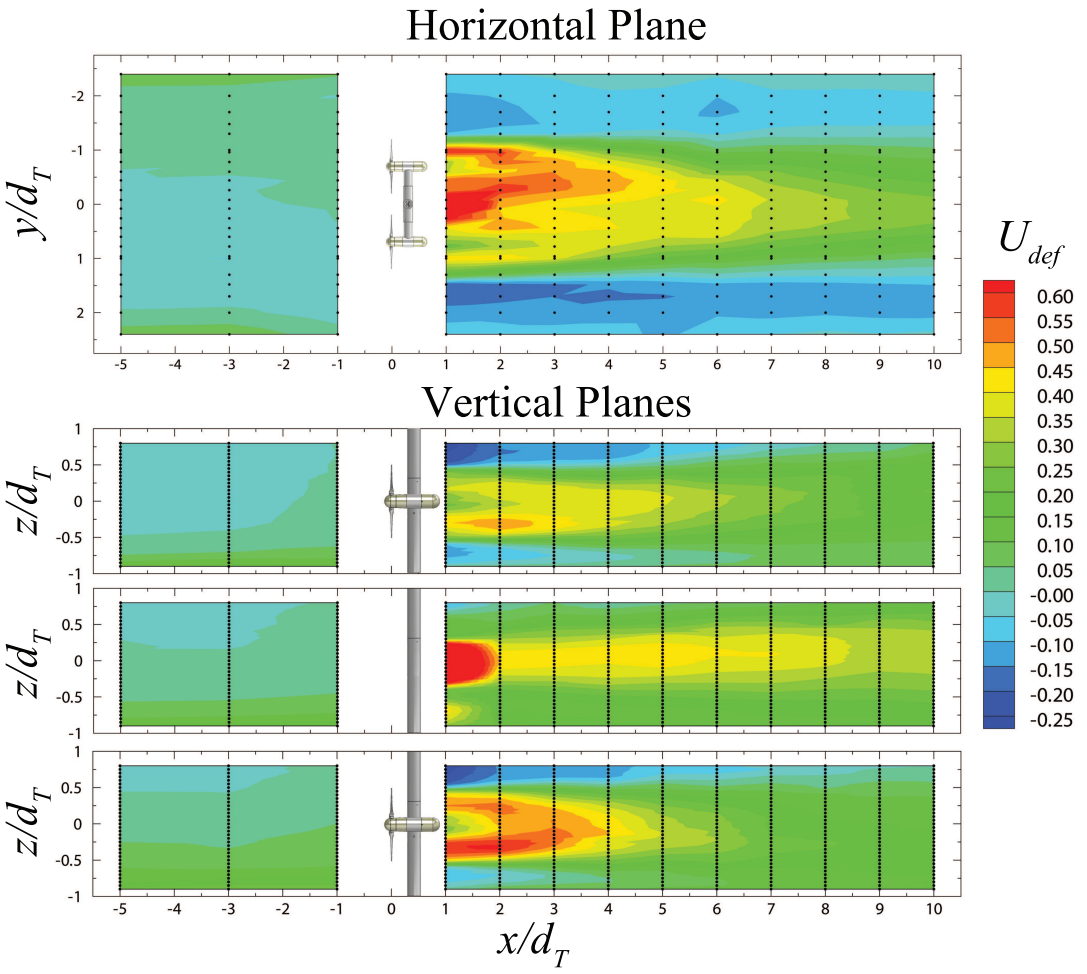

Figure 6.9: Velocity deficit horizontal (XY) and vertical (XZ) plane contours upstream and downstream of RM1 in the SAFL Main Channel. Vertical plane y-axis, z/d_T, shows full water depth during the experiment ($h = 1.0$ m). Horizontal plane y-axis, y/d_T, shows full channel width ($b = 2.75$ m). Horizontal and vertical dotted black lines indicate actual ADV measurement profile locations. ADV vertical point spacing $\Delta z = 0.025$ m ($z/d_T = 0.05$). Horizontal spacing varied. Measurements collected at $\lambda \approx 5.1$ ($\omega = 3.4$ rps). Flow is left to right.

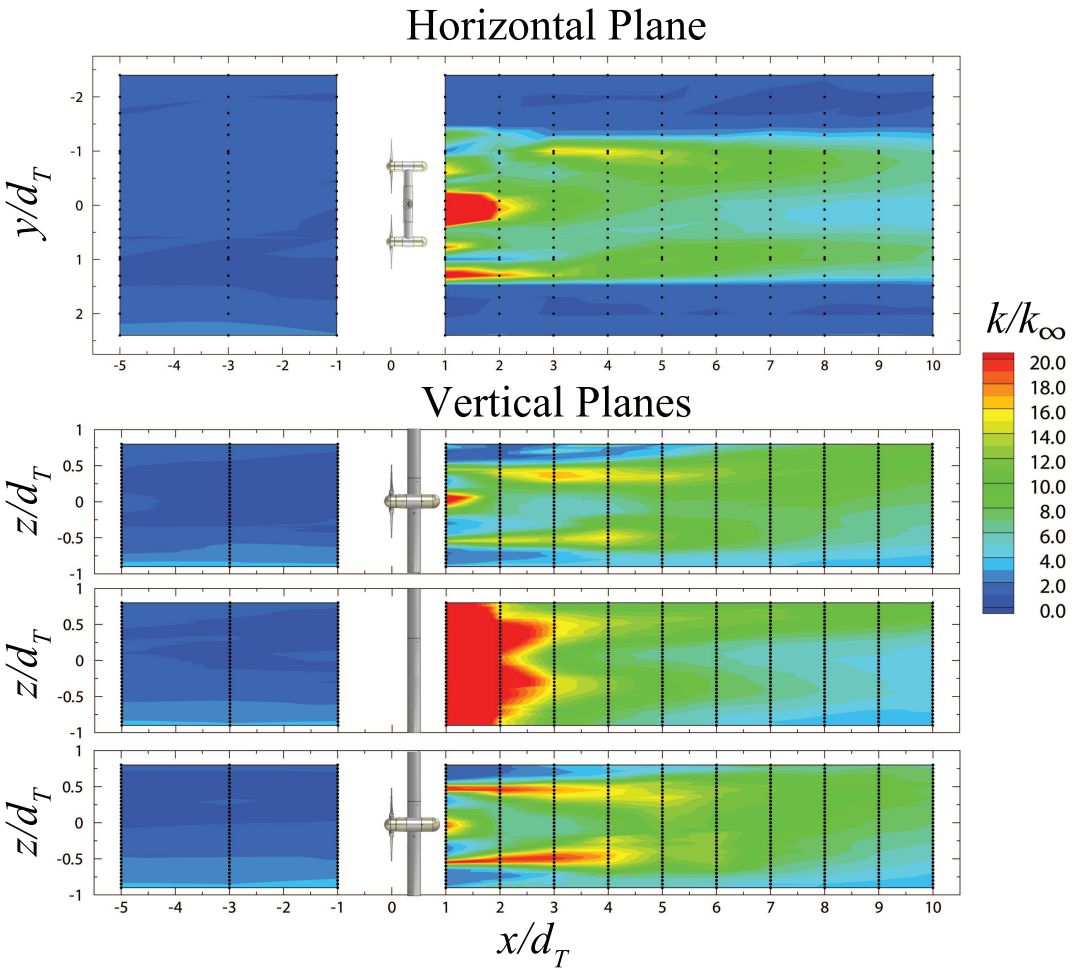

Figure 6.10: Normalized turbulent kinetic energy, k/k_∞, horizontal (XY) and vertical (XZ) plane contours upstream and downstream of RM1 in the SAFL Main Channel. Vertical plane y-axis, z/d_T, shows full water depth during the experiment ($h = 1.0$ m). Horizontal plane y-axis, y/d_T, shows full channel width ($b = 2.75$ m). Horizontal and vertical dotted black lines indicate actual ADV measurement profile locations. ADV vertical point spacing $\Delta z = 0.025$ m ($z/d_T = 0.05$). Horizontal spacing varied. Measurements collected at $\lambda \approx 5.1$ ($\omega = 3.4$ rps). Flow is left to right.

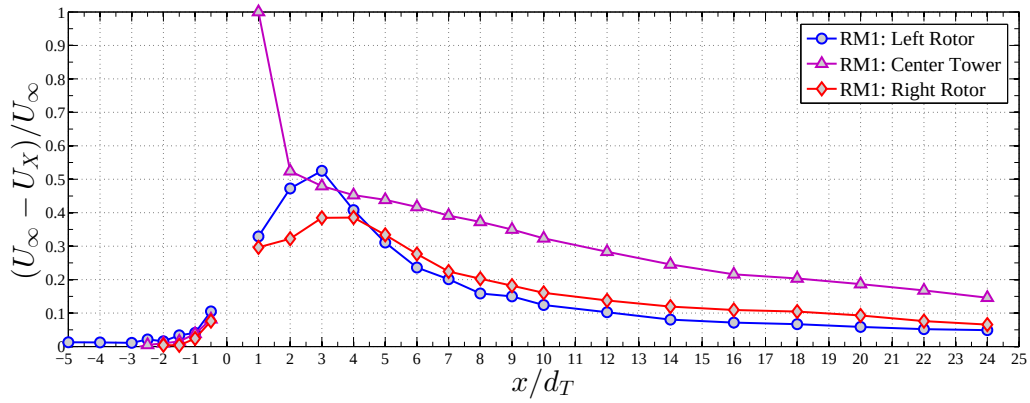

Figure 6.11: Hub height velocity deficit. RM1 rotors located at $x/d_T = 0$. Measurements collected at $\lambda \approx 5.1$ ($\omega = 3.4$ rps).

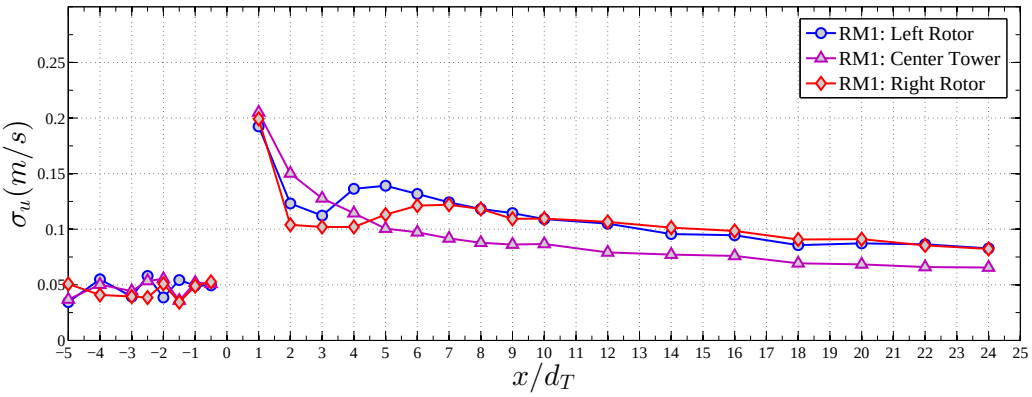

Figure 6.12: Hub height streamwise root-mean squared ($\sigma_u = \sqrt{\overline{u'^2}}$). RM1 rotors located at $x/d_T = 0$. Measurements collected at $\lambda \approx 5.1$ ($\omega = 3.4$ rps).

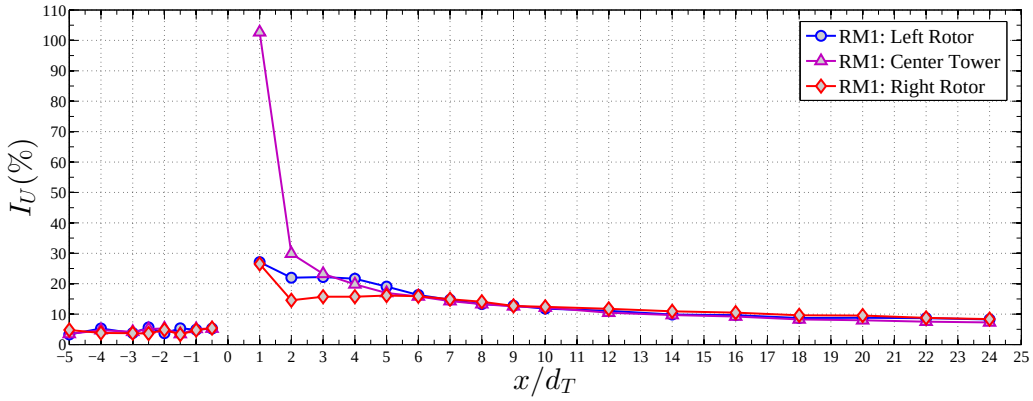

Figure 6.13: Hub height streamwise turbulence intensity, I_u. RM1 rotors located at $x/d_T = 0$. Measurements collected at $\lambda \approx 5.1$ ($\omega = 3.4$ rps).

6.5 Summary & Conclusions

The Reference Model 1 (RM1), a 1:40 geometrically scaled horizontal axis axial-flow hydrokinetic turbine designed by the U.S. DOE for tidal environments, was tested in the St. Anthony Falls Laboratory Main Channel facility at the University of Minnesota. Detailed performance and velocity measurements were collected to assess the interaction of RM1 with the surrounding environment. A robust data-set resulted from these experiments, providing exceptional data for model validation. Maximum C_p was found to occur near $\lambda \approx 5.1$ with values of $C_p = 0.48$ for the right rotor and $C_p = 0.43$ for the left rotor. Slight asymmetries in the approach flow environment may have caused the different turbine performance characteristics, but the root cause or causes were not determined. Detailed wake velocity measurements provide an indication of the turbulent wake environment, showing elevated levels of turbulent kinetic energy in the near wake environment, particularly resulting from the instabilities induced by the center support tower cylinder. Tip vortices also inject high turbulence levels that propagate up to approximately $4d_T$. Further investigations into the RM1 experimental data may reveal the mechanics of the near wake environment and the influence of von Kármán frequencies shed from the center vertical and horizontal support arms have on the near wake structure of each rotor. What remains unknown is the effect of the proximity of the rotor plane to the horizontal support arm downstream of each rotor and the cross arm effect on turbine performance. This structural feature likely does disrupt the near wake velocity and induce mixing more rapidly than other turbine configurations.

6.6 Notation used in Chapter 6

A = flow cross-sectional area, m^2
A_T = turbine rotor area, $(= d_T h_T)$, m^2
b = channel width, m
c = blade chord length, m
C_p = coefficient of power, [-]
d_T = turbine rotor diameter, m
f_T = turbine rotational frequency, Hz
Fr = Froude number, $(= U_\infty/\sqrt{hg})$, [-]
g = gravitational constant, ms^{-2}
h = flow depth, m
h_{hub} = hub height, m
I_u = streamwise turbulence intensity, %
k = turbulence kinetic energy, $\mathrm{m}^2\mathrm{s}^{-2}$
P_A = available power, W
P_T = turbine power, W
Q_w = volumetric flow rate, $\mathrm{m}^3\mathrm{s}^{-1}$
Re_c = blade chord Reynolds number, $(= \lambda U_\infty c/\nu)$
Re_d = rotor diameter Reynolds number, $(= U_\infty d_T/\nu)$
S_T = turbine rotor spacing, m
U_{hub} = hub height velocity, ms^{-1}
U_∞ = bulk velocity, ms^{-1}
x = streamwise coordinate, m
y = cross-stream coordinate, m
z = vertical coordinate, m

Greek symbols
η = turbine blockage ratio, $(= A_T/A)$
λ = tip speed ratio, $(= \omega d_T/2U_{hub})$
ν = kinematic viscosity, $\mathrm{kg(sm)}^{-1}$
ω = turbine rotor tip speed $(= 2\pi f_T)$, rad s^{-1}
ρ = fluid density, kgm^{-3}
σ = solidity, $(= Nc/\pi d_T)$
τ = turbine torque, Nm

Chapter 7

Additional Results and Future Directives

7.1 Additional Results

The following sections briefly present several other projects I was involved in leading up to and during my Doctoral research program. Except for a few exceptions, most of the descriptions and images presented below are not currently in published peer-reviewed journals. However, they provide some interesting results regarding the hydrodynamics and morphodynamic interactions of hydrokinetic devices, and will hopefully serve as a starting point for future analysis and both experimental and computational investigations.

7.1.1 Axial-flow turbine arrays & sediment transport

A series of experiments was completed in the SAFL tilting bed flume (0.9m wide x 15m long) to investigate small-scale axial-flow turbine interactions with medium grained sand ($d_{50} = 0.42$mm) and migrating ripples. The experiments were designed to further investigate the near and far-field effects of turbines on sediment transport characteristics, and to determine if smaller scale roughness features on the channel bottom have as strong an impact on turbine performance, similar to the experiments conducted and reported in Chapter 3. Both a two-turbine aligned configuration and an array of turbines were used. For the two-turbine installation, the turbines were positioned $7d_T$ apart in the streamwise direction and aligned with the center of the channel. For the multi-turbine array experiments, seven turbines were used and installed with a staggered configuration with a streamwise spacing of $x/d_T = 3.5$ between each staggered row ($x/d_T = 7$ between aligned turbines) and a cross-stream spacing of $y/d_T =$ +/- 1.5 (Figure 7.1). Voltage

data were collected from each of the seven turbines to investigate the change in performance due to migrating ripple bedforms, providing some interesting results on the difference in performance when a turbine is installed in a fixed bed concrete channel vs. an erodible sand channel. Similar to results from small and large-scale model axial-flow turbine experiments operating in clear water or live bed conditions in straight and meandering erodible channels (see Chapter 2 Figures 2.4, 2.5, and 2.14, Chapter 3 Figure 3.11, and Chapter 4 Figures 4.13 and 4.17, for reference), local scour and deposition was observed downstream of each of the seven turbines in the mean bed elevation profiles (Figure 7.2). Maximum scour depth was observed downstream of Turbine 4 in the center of the seven turbine array to a depth of $\Delta z/d_T \approx 0.2$ below the mean bed elevation. Maximum scour depths were consistently observed $0.5d_T$ downstream of each turbine, ranging from $\Delta z/d_T \approx 0.07$ downstream of Turbine 1 at the upstream end of the array, to $\Delta z/d_T \approx 0.2$, with an average of $\Delta z/d_T \approx 0.15$, consistent with results from other experiments discussed in previous chapters.

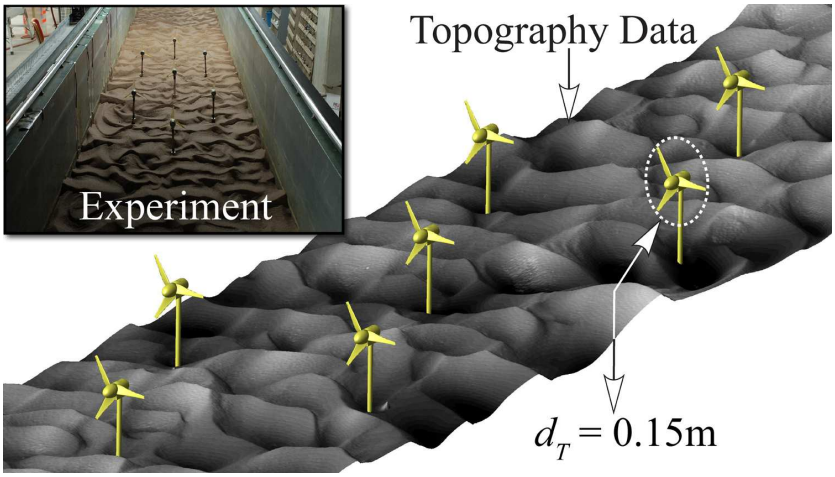

Figure 7.1: Topography of seven turbine staggered array installed in migrating sand ripple topography ($d_{50} = 0.42$mm). Inset shows photograph of experiment. Flow is left to right (top to bottom in inset image).

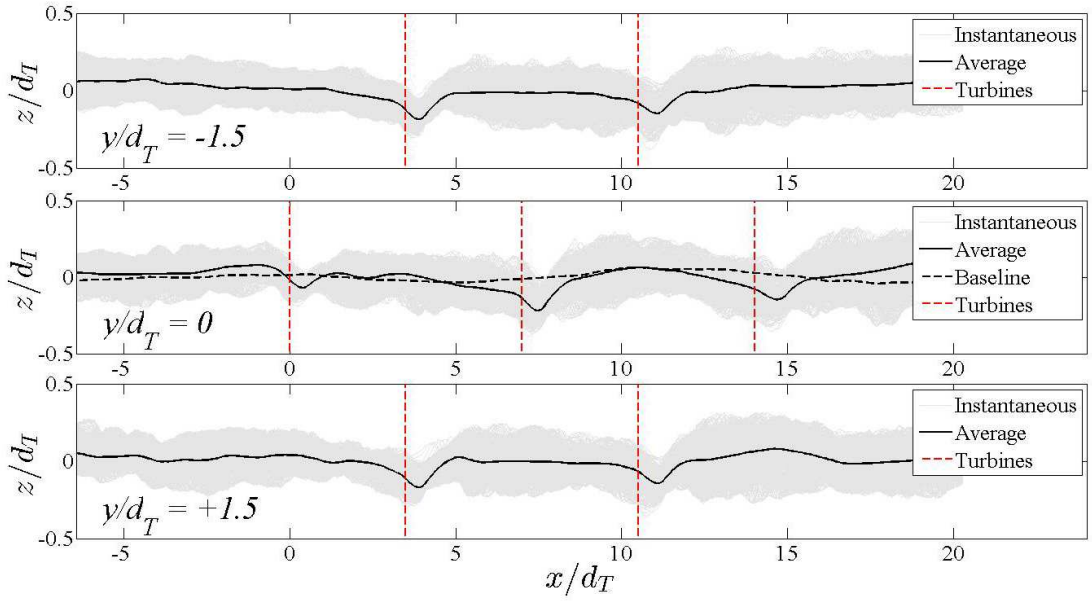

Figure 7.2: Instantaneous (light gray lines) and mean bed elevation profiles (solid black lines) along three streamwise sonar transects (top: right side of channel; center: middle of channel; bottom: left side of channel) during the seven turbine staggered array experiments. Vertical red dashed lines indicate locations of the seven turbines. Flow is left to right.

Voltage data collected during the experiments provided a method of investigating the impact the migrating ripples had on turbine performance, similar to the analysis performed in Chapter 3 and highlighted in Figure 3.9. Similar results from cross-correlation analysis were found during the small-scale roughness experiments with migrating ripples (Figure 7.3). Here, the peak elevation of ripple crests show a similar impact on turbine voltage output. Specifically, when ripple crest peak elevations are $x/d_T \approx$ -0.7 upstream of the rotor location, the corresponding voltage output is at a maximum. Despite showing a similar trend to that found with larger scale dunes as shown in Chapter 3, the effect smaller scale ripples had on turbine voltage output was not quite as prominent, suggesting the turbines were mounted high enough above the roughness elements to not have a major impact on their performance. Regardless, a signature of the bedform wavelength is observed in both the dune and ripple experiments (Figure 7.3). Presumably hub height above the mean bed elevation influences this relationship, and requires further investigation into the relationships between turbine hub height, roughness height and wavelength, proximity to prominent topographic features, and the resulting near-field scour and far-field sediment transport modifications.

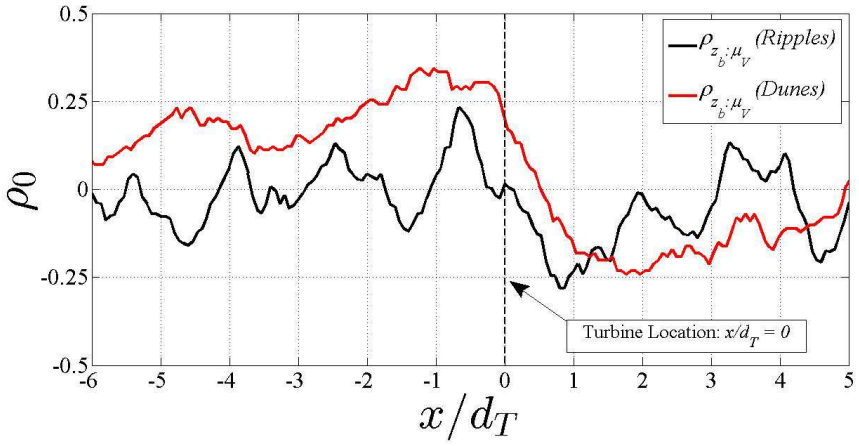

Figure 7.3: Cross-correlation coefficients, ρ_0, between bed elevation, z_b, and turbine voltage as a function of normalized streamwise distance x/d_T. Black lines shows relationships from ripples experiment, while the red line shows results from dunes experiments presented for a single turbine in Chapter 3.

As described in Chapter 3 Figure 3.4, FFT analysis of the voltage data from the rotating turbine provides a method of monitoring the turbine operating conditions by identifying spectral peaks associated with the turbine rotational frequency, thereby providing a method of calculating the turbine tip-speed ratio, $\lambda = (\pi f_T d_T)/U_{hub}$, where the turbine frequency, f_T, is identified from the first peak in the power spectral plots resulting from FFT analysis. Figure 7.4 compares this spectral analysis for Turbine 1, the most upstream turbine in the seven-turbine array for experiments completed with a fixed bed (i.e. rectangular flume with no sediment) and an erodible sediment bed with actively migrating bedforms. Distinct spectral peaks are present in the spectral plots resulting from voltage data originating from the fixed bed experiments, providing indicating that the turbine maintained consistent tip-speed ratios throughout the experiment and the large-scale turbulence in the flow did not have a major impact on the turbine operating [6]. However, when similar analysis was performed on the voltage data from the sediment experiments, the distinct spectral peaks disappear. This result suggests that the added roughness on the channel bottom alters the turbulent boundary layer enough to impact the turbine operation. Specifically, the turbine tip-speed ratio is constantly modulated based on the roughness (i.e. ripples) size and location, which locally impact the mean flow, U and the turbulent fluctuations, u', and turbulent kinetic energy levels, k. Similar analysis was performed for Turbine 7 at the downstream end of the seven-turbine array. The spectra at low frequencies show added energy in the signal, likely a result of the accumulated turbulent energy from the

upstream six turbines, whereas the high frequency end of the spectrum contains lower amounts of energy. Similar to the results for Turbine 1, the sediment experiments modulate the turbine tip-speed ratio across a range of frequencies, removing any signature of a distinct peak and constant λ. These results provide indication that advanced control strategies implemented into turbine designs could potential provide increased efficiency and decreased susceptibility to structural fatigue by providing constant λ control.

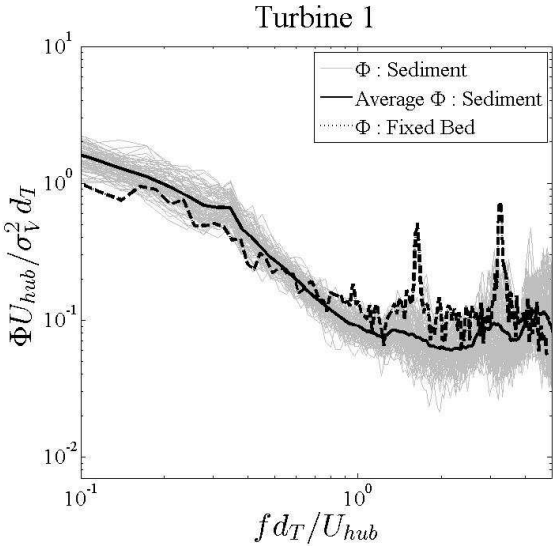

Figure 7.4: Voltage spectra from Turbine 1 (upstream center turbine in seven turbine array) for both fixed bed and erodible channel experiments. Light gray lines show 5-minute interval voltage spectra during the erodible channel experiments, while the solid black line illustrates the average of those instantaneous spectral functions. The dashed black line shows the voltage spectra from the same turbine during fixed bed experiments. Spectra have been normalized using the corresponding hub height velocity, U_{hub}, rotor diameter $d_T = 0.15$m, and timeseries variance, σ_v^2.

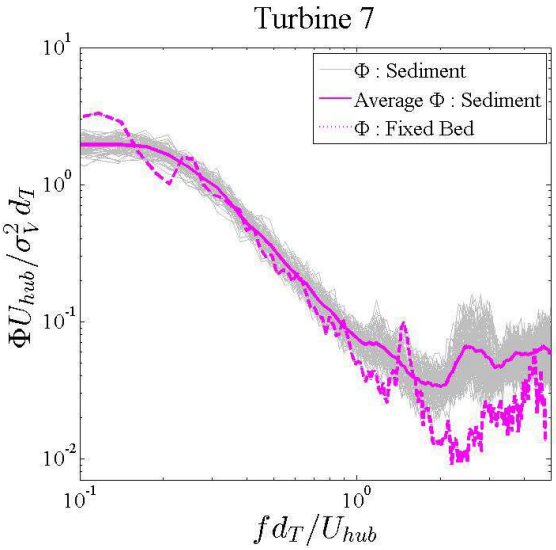

Figure 7.5: Voltage spectra from Turbine 7 (downstream center turbine in seven turbine array) for both fixed bed and erodible channel experiments. Light gray lines show 5-minute interval voltage spectra during the erodible channel experiments, while the solid purple line illustrates the average of those instantaneous spectral functions. The dashed purple line shows the voltage spectra from the same turbine during fixed bed experiments. Spectra have been normalized using the corresponding hub height velocity, U_{hub}, rotor diameter $d_T = 0.15$m, and timeseries variance, σ_v^2.

While single turbine wake characteristics have been extensively studied over recent years (see Chapter 1), the impacts of accumulated turbine wakes has yet to be examined, and will likely have a major role in determining the operational strategies of larger turbine power plant arrays. Preliminary analysis from the voltage data from the seven-turbine array experiments provided some indication of the aggregation of individual turbine wakes into a larger-scale turbulent feature that impacts downstream turbines. Figure 7.6 illustrates the pre-multiplied voltage spectra from Turbines 1, 4, and 7 (the upstream, middle, and downstream turbine, respectively, in the seven-turbine array). Additionally, the power spectra from a velocity time-series located at $7d_T$ downstream in the wake of a single turbine is plotted to show the increase in energy occurring near a frequency of $f \approx 0.5$Hz. Interestingly, this large-scale frequency motion, $f_m \approx 0.5$Hz, coincides with the occurrence of a spectral peak present in the downstream turbines, Turbine 4 and Turbine 7. This frequency results in a similar Strouhal number, $St \equiv (f_m d_T/U_{hub}) \approx 0.24$-0.28, reported by [6] as the characteristic motion scale in the wake of an axial-flow hydrokinetic turbine. An additional distinct peak at an even lower frequency starts to appear in the spectral

plot for Turbine 4, and dominates the spectral plot for the downstream Turbine 7. This distinct peak, occurring near approximately $f_m = 0.3$Hz, potentially indicates the aggregation of multiple turbine wakes that are merging to form a "'super-wake"' and impacting the turbines near the downstream end of the array. None of these spectral peaks are observed in the voltage spectra from the upstream Turbine 1, providing re-assurance that this turbine was exposed to the undisturbed fully-developed turbulent boundary layer profile and that the peaks observed in the downstream turbines are a result of the turbulent wakes.

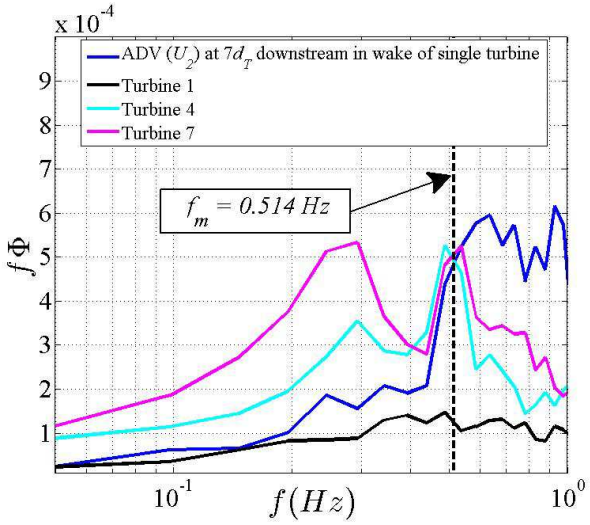

Figure 7.6: Pre-multiplied voltage spectra from the seven turbine staggered array experiment during fixed bed conditions for the three turbines in the center of the channel (Turbine 1 = upstream; Turbine 4 = middle; Turbine 7 = downstream). Dark blue lines shows pre-multiplied spectra of the hub height flow velocity at seven rotor diameters ($7d_T$) downstream of a single turbine during fixed bed experiments.

7.1.2 Verdant Power and the RITE site

Wake characterization: Large-scale turbine experiments

As a research engineer, I assisted Dr. Leonardo P. Chamorro in experiments in the SAFL main channel to characterize the wake downstream of a $d_T = 0.5$m axial-flow turbine, originally based on the Verdant Power design, although modified in several ways to not be a complete representation of the Verdant Power turbine. More detailed analysis of the power and wake characteristics are provided in the following publication.

Chamorro, L. P., Hill, C., Morton, S., Ellis, C., Arndt, R. E. A., and Sotiropoulos, F., (2013), On the interaction between a turbulent open channel flow and an axial-flow turbine, *J. Fluid Mech.*, 716, 658-670, doi:10.1017/jfm.2012.571 (PDF).

The following figures provide details of the wake characteristics downstream of the axial-flow turbine up to $15d_T$ downstream of the turbine. Data were collected at the turbine's optimal operating condition ($C_p \approx 0.45$ at $\lambda = 5.8$). Turbine model hub height was $h_{hub} = 0.425$m and the flow depth was $h = 1.15$m. See [6] for additional details on turbine geometric characteristics and in-depth experimental results. Figures 7.7, 7.8, and 7.9 illustrate the mean U, V, and W velocity components, respectively, in a vertical plane aligned with the center of the turbine from $-2 < x/d_T < 15$. Figures 7.10, 7.11, and 7.12 illustrate the fluctuating velocity components u', v', and w', respectively, in the same region, followed by the Reynolds stress, $u'w'$, illustrated in Figure 7.13. These figures provide detailed visualizations of time-averaged flow-quantities in the wake of a turbine, and provide high-resolution data for computational model validation [116]. These data illustrate the low velocity core of the near-wake extending downstream to $x/d_T \approx 3$ (Figure 7.7), the rotational characteristic in the near-wake region in the transverse velocity component (Figure 7.8), the elevated regions of turbulent fluctuations originating from the turbine tip vortices and extending downstream to $x/d_T \approx 6$ and creating a zone of rapid growth of turbulent kinetic energy, k, that coincides with the region of tip-vortex breakdown, merging of the inner and outer wake regions, and downstream wake meandering [116] (Figures 7.10, 7.11 and 7.12), and an increase in near-bed Reynolds stresses which can influence local scour and sediment transport characteristics (Figure 7.13).

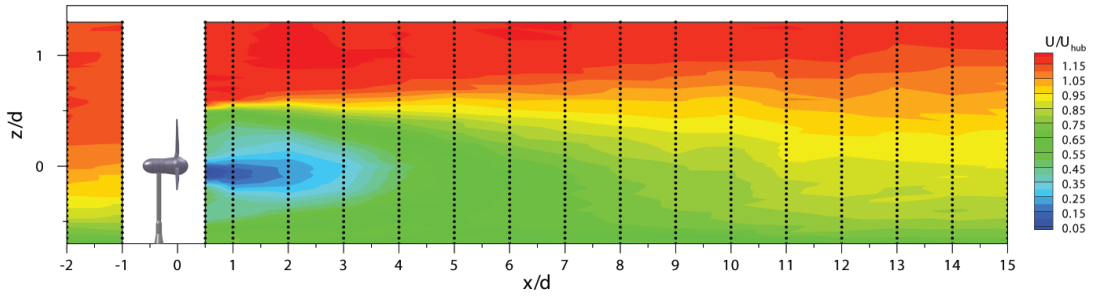

Figure 7.7: Mean streamwise velocity, U, normalized by the hub height velocity, U_{hub}, in a vertical plane aligned with the turbine center from -2 $< x/d_T <$ 15. Measurements collected using a Nortek Vectrino+ acoustic Doppler velocimeter (ADV) at locations indicated by black dots (18 vertical profiles x 41 measurements locations each profile = 738 total points). Data collected with turbine operating at optimal condition ($C_p \approx 0.45$ at $\lambda = 5.8$) [6].

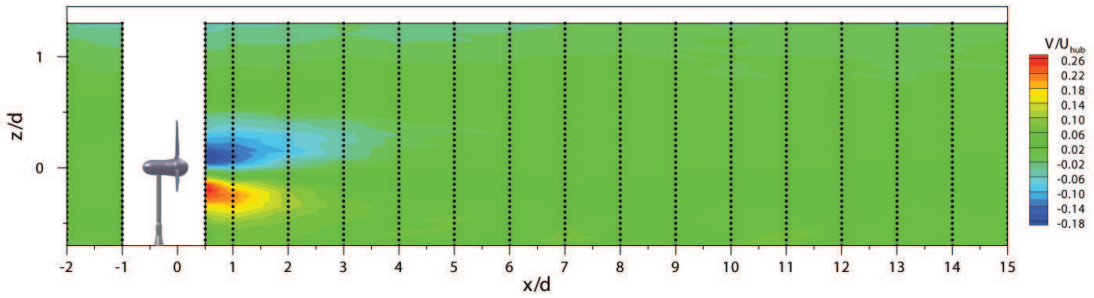

Figure 7.8: Mean cross-stream velocity, V, normalized by the hub height velocity, U_{hub}, in a vertical plane aligned with the turbine center from -2 $< x/d_T <$ 15. Measurements collected using a Nortek Vectrino+ ADV at locations indicated by black dots. Data collected with turbine operating at optimal condition ($C_p \approx 0.45$ at $\lambda = 5.8$) [6].

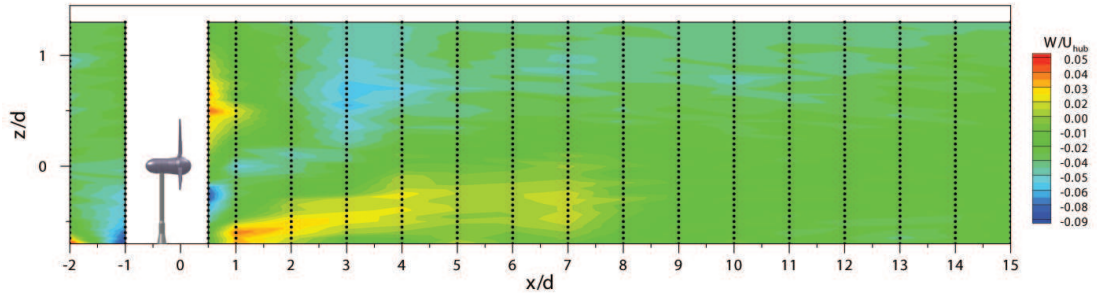

Figure 7.9: Mean vertical velocity, W, normalized by the hub height velocity, U_{hub}, in a vertical plane aligned with the turbine center from -2 $< x/d_T <$ 15. Measurements collected using a Nortek Vectrino+ ADV at locations indicated by black dots. Data collected with turbine operating at optimal condition ($C_p \approx 0.45$ at $\lambda = 5.8$) [6].

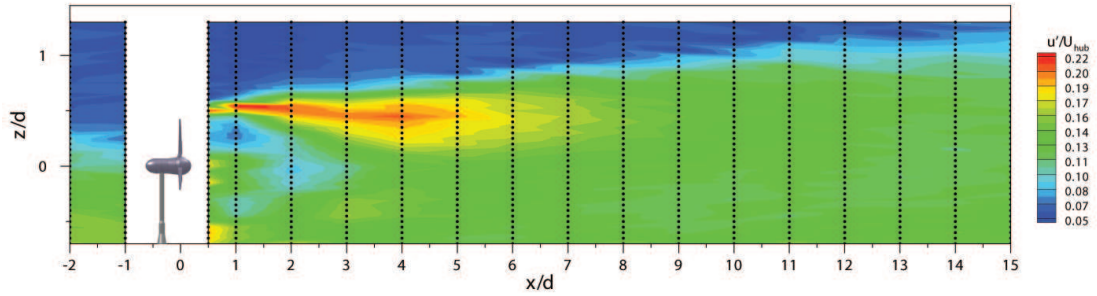

Figure 7.10: Root-mean squared (RMS) streamwise velocity, u', normalized by the hub height velocity, U_{hub}, in a vertical plane aligned with the turbine center from -2 $< x/d_T <$ 15. Measurements collected using a Nortek Vectrino+ ADV at locations indicated by black dots. Data collected with turbine operating at optimal condition ($C_p \approx 0.45$ at $\lambda = 5.8$) [6].

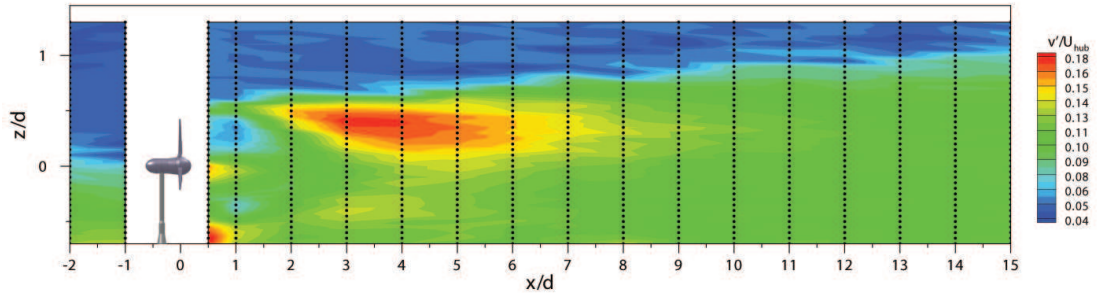

Figure 7.11: RMS cross-stream velocity, v', normalized by the hub height velocity, U_{hub}, in a vertical plane aligned with the turbine center from -2 $< x/d_T <$ 15. Measurements collected using a Nortek Vectrino+ ADV at locations indicated by black dots. Data collected with turbine operating at optimal condition ($C_p \approx 0.45$ at $\lambda = 5.8$) [6].

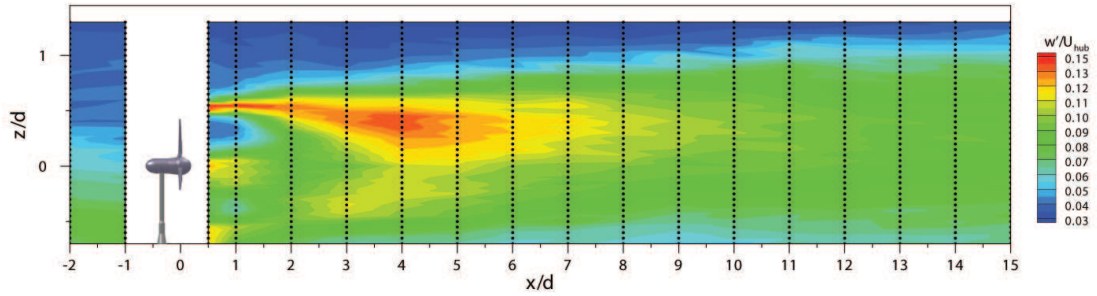

Figure 7.12: RMS vertical velocity, w', normalized by the hub height velocity, U_{hub}, in a vertical plane aligned with the turbine center from -2 $< x/d_T <$ 15. Measurements collected using a Nortek Vectrino+ ADV at locations indicated by black dots. Data collected with turbine operating at optimal condition ($C_p \approx 0.45$ at $\lambda = 5.8$) [6].

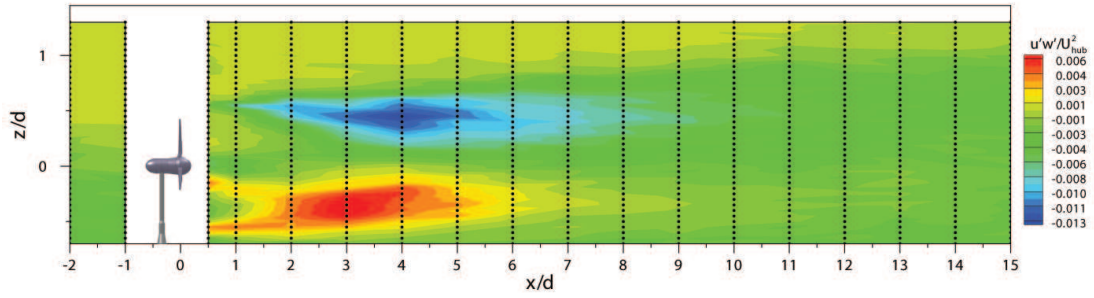

Figure 7.13: Reynolds stress, $u'w'$, normalized by the hub height velocity squared, U_{hub}^2, in a vertical plane aligned with the turbine center from -2 $< x/d_T <$ 15. Measurements collected using a Nortek Vectrino+ ADV at locations indicated by black dots. Data collected with turbine operating at optimal condition ($C_p \approx 0.45$ at $\lambda = 5.8$) [6].

Velocity Deficit: Small-scale turbine experiments

During a recent project funded by the National Science Foundation (NSF), a small-scale experiment was carried out in the SAFL tilting bed flume above a non-erodible bed using model axial-flow turbines with rotor diameter $d_T = 0.15$m to compare wake characteristics between a single turbine, similar to that shown in Figures 7.7 through 7.13 above, with detailed wake measurements downstream of a tri-frame arrangement of turbines. Verdant Power is considering to use a tri-frame configuration for installation 10 sets of three turbines for their Roosevelt Island Tidal Energy (RITE) site in New York City. As part of the NSF project, we were tasked with characterizing their new blade designs and investigating the interactions of turbines in a tri-frame configuration. Much of the work is being done through CFD simulations, however, several experiments were conducted to provide validation data to the CFD modeling group at SAFL. For these small-scale experiments, turbine hub height $h_{hub} = 0.135$m, flow depth $h = 0.28$m, bulk flow velocity $U_\infty = 0.27$m/s, and Reynolds number based on turbine diameter, d_T, was $Re_{d_T} = 4.1$ x 10^4. The following presents preliminary results on the velocity deficit and turbulent kinetic energy comparison between the two cases.

NOTE: The data presented below are currently being submitted for publication as the following reference, although they are presented in a different format and used as validation for CFD simulations. Please refer to the *Physics of Fluids* publication for future and additional details.

Chawdhary, S., Hill, C., Yang, X., Guala, M., and Sotiropoulos, F. (2015). Wake structure

of a tri-frame of hydrokinetic turbines. Under review, *Phys. Fluids.*

Figure 7.14 illustrates the velocity deficit, $U_{def} = (U_\infty - U_x)/U_\infty$, within a plane at hub height from $1 < x/d_T < 10$ downstream of a single turbine. Typical characteristics of a single turbine wake are observed, including near-wake $U_{def} \approx$ 80%-90%, rapid near-wake recovery, maintained far-wake $U_{def} \approx 10\%$ near $x/d_T = 10$, and gradual lateral wake expansion in the downstream direction. Figure 7.15 shows the velocity deficit for a tri-frame configuration of turbines along a hub height, wall-parallel plane. Similar near and far-wake characteristics are observed for each of the three turbines in the tri-frame configuration. The most notable difference is in the wake of the center, upstream turbine. The wake is confined between the two downstream turbines, therefore is not allowed to expand and actually becomes narrower that a typical single turbine wake. This phenomenon is easily observed in the hub height spanwise velocity deficit profile comparisons in Figure 7.16, especially at $4d_T$ downstream of the first turbine.

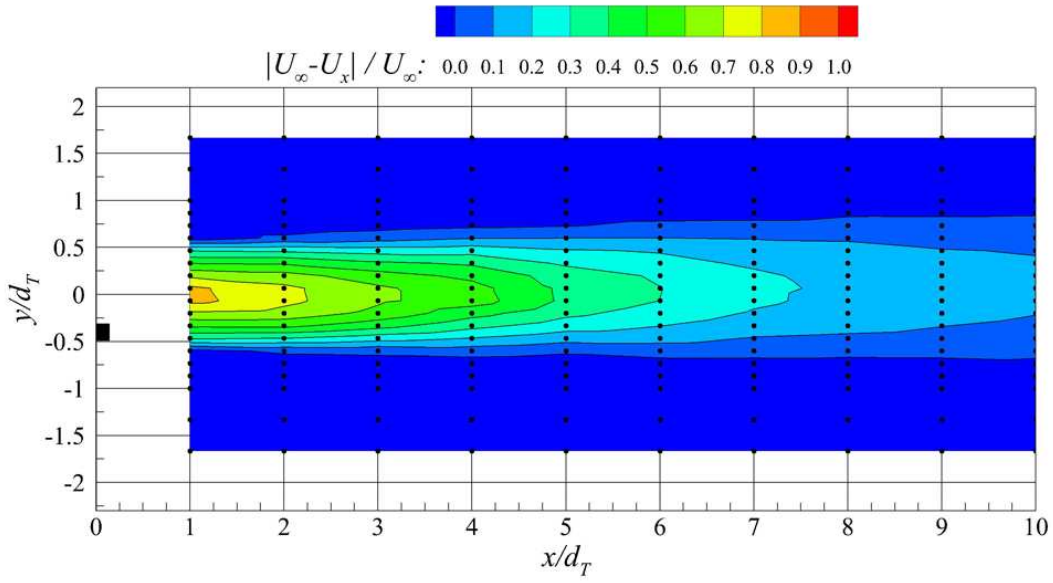

Figure 7.14: Velocity deficit, $U_{def} = (U_\infty - U_x)/U_\infty$, within a plane at hub height from $1 < x/d_T < 10$ downstream of a single turbine, $d_T = 0.15$m operating at $\lambda \approx$ 4.5-4.6.

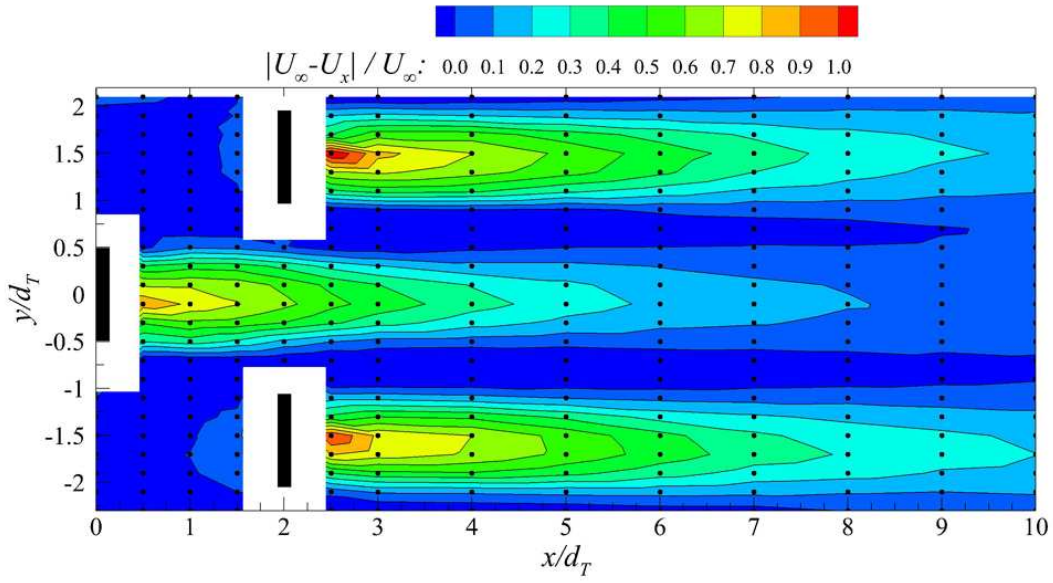

Figure 7.15: Velocity deficit, $U_{def} = (U_\infty - U_x)/U_\infty$, within a plane at hub height from 1 $< x/d_T <$ 10 downstream of a tri-frame turbine arrangment, $d_T = 0.15$m operating at $\lambda \approx$ 4.5-4.6.

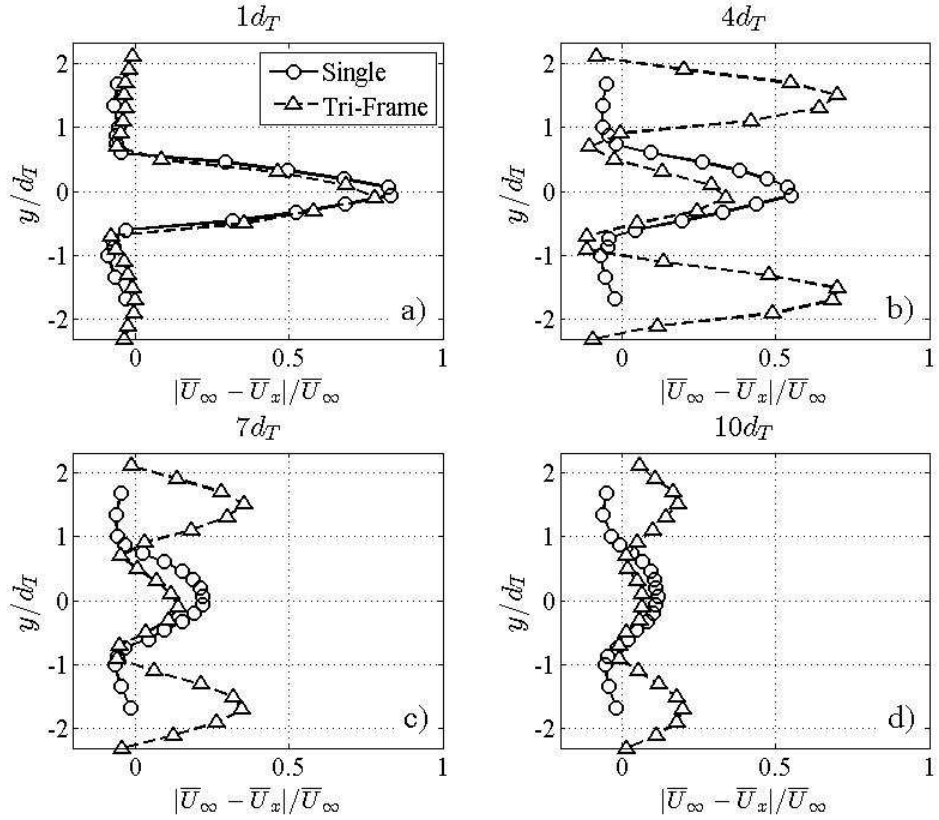

Figure 7.16: Spanwise comparison of velocity deficit, $U_{def} = (U_\infty - U_x)/U_\infty$, between a single turbine wake (O) and a tri-frame turbine configuration wake (Δ) at x/d_T = 1(a), 4(b), 7(c), and 10(d).

When designing multi-turbine arrays, an important parameter to consider is the downstream velocity deficit recovery aligned with each turbine. This parameter assists in determining streamwise spacing, as it is desirable to have maximum available power for each turbine. One possibility is to arrange turbines in a staggered configuration, similar to the tri-frame arrangement or the experiments presented earlier in this chapter. However, the characterization of the hub height velocity deficit is still critical. Figure 7.17 illustrates the hub height velocity deficit for five scenarios: a single turbine, the central upstream turbine in the tri-frame configuration, and two turbines spaced at $4d_T$, $7d_T$, and $10d_T$. A few notable features are visible in this figure. First, the turbines begin affecting the flow $x/d_T \approx$ -2 to -3 upstream of their location, seen by the deceleration of the hub height velocity (i.e. $\approx$ 10% velocity deficit upstream). In all cases, the wake recovery exhibits similar behaviour in the downstream environment, showing rapid

recovery in the near-wake region up to approximately $5d_T$, and recovering $U_{def} \approx 10\%$-15% at $10d_T$. One notable difference is the slightly slower recovery of the single turbine compared to the multi-turbine experiments. Additional turbines introduces turbulence and coherent structures into the flow, which result in increased turbulent mixing and faster near-wake velocity recovery, as discussed by [1]. Although not particularly illustrated in Figure 7.17, velocity deficit downstream of $x/d_T = 10$ is very gradual.

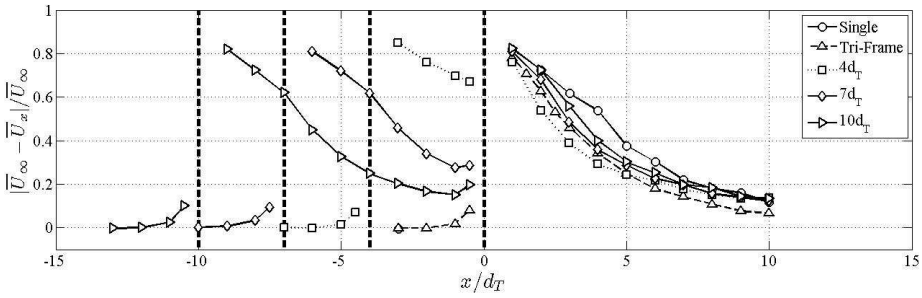

Figure 7.17: Velocity deficit, $U_{def} = (U_\infty - U_x)/U_\infty$, comparison at hub height in the streamwise direction between five configurations: Single turbine (O), tri-frame turbines (Δ), and two turbines spaced at $4d_T$ ($\square$), $7d_T$ ($\diamond$), and $10d_T$ ($\triangleright$).

Turbulent kinetic energy: Small-scale turbine experiments

Figure 7.18 illustrates the normalized turbulent kinetic energy, k/u_*^2, within a plane at hub height from $1 < x/d_T < 10$ downstream of a single turbine. As expected, the wake region downstream of the turbine elevates the levels of k, with the highest levels aligning with the rotor tip vortices and occurring in a region between $x/d_T = 2$ to 6. Figure 7.19 shows the normalized turbulent kinetic energy for a tri-frame configuration of turbines along a hub height, wall-parallel plane. Similar near and far-wake characteristics are observed for each of the three turbines in the tri-frame configuration. The most notable difference is in the wake of the center, upstream turbine. Because the wake is confined and accelerated between the two downstream turbines, there is not a prominent region of elevated k values associated with the tip vortices of the upstream turbines. These regions do still exist in the wake of the two downstream turbines. The difference in k between the single turbine and the central, upstream turbine in the tri-frame configuration is easily observed in the hub height spanwise normalized turbulent kinetic energy profile comparisons in Figure 7.20, especially from $4d_T$ and beyond.

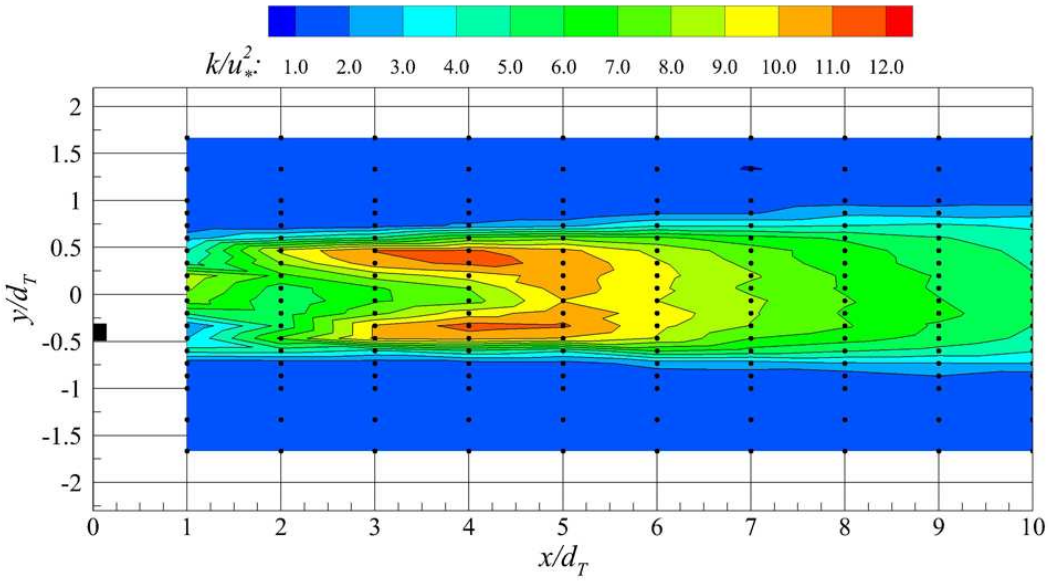

Figure 7.18: Normalized turbulent kinetic energy, k/u_*^2, within a plane at hub height from 1 $< x/d_T <$ 10 downstream of a single turbine, $d_T = 0.15$m operating at $\lambda \approx$ 4.5-4.6.

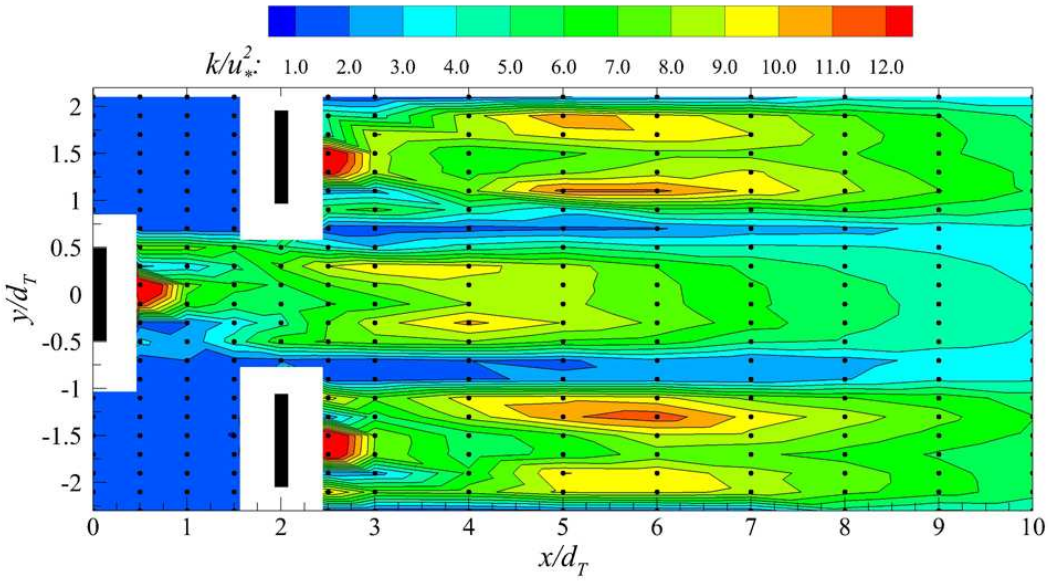

Figure 7.19: Normalized turbulent kinetic energy, k/u_*^2, within a plane at hub height from 1 $< x/d_T <$ 10 downstream of a tri-frame turbine arrangment, $d_T = 0.15$m operating at $\lambda \approx$ 4.5-4.6.

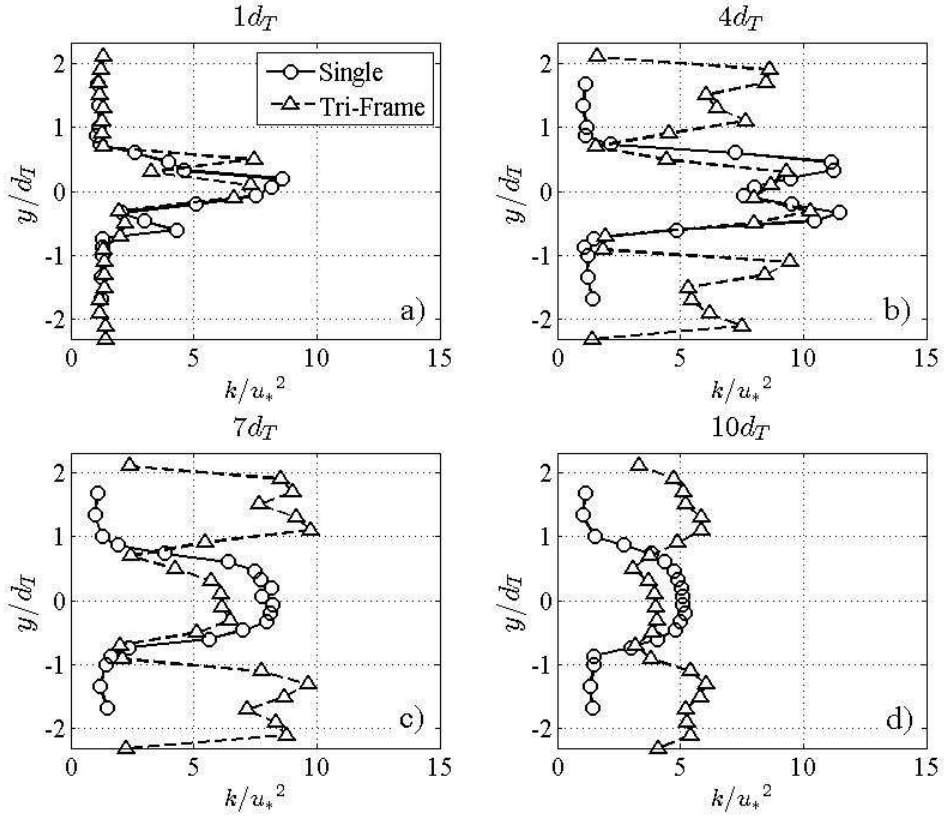

Figure 7.20: Normalized turbulent kinetic energy, k/u_*^2, comparison in the spanwise direction at hub height between a single turbine wake (O) and a tri-frame turbine configuration wake (Δ) at $x/d_T = 1$(a), 4(b), 7(c), and 10(d).

Figure 7.21 illustrates the normalized turbulent kinetic energy, k/u_*^2, from the five scenarios presented early in Figure 7.17 (a single turbine, the central upstream turbine in the tri-frame configuration, and two turbines spaced at $4d_T$, $7d_T$, and $10d_T$). The differences among the five scenarios are noticeable in the wake of the turbine, where the maximum levels of k vary from $x/d_T \approx 2$ to 5 depending on the configuration. As was shown by [116], the wake characteristics and interactions of the inner and outer wake regions, and the tip vortices, impact the downstream wake environment, especially the meandering characteristics. Because maximum k/u_*^2 values change location based on multi-turbine configuration, this has direct implications for design and operation of turbines in a larger deployment configuration.

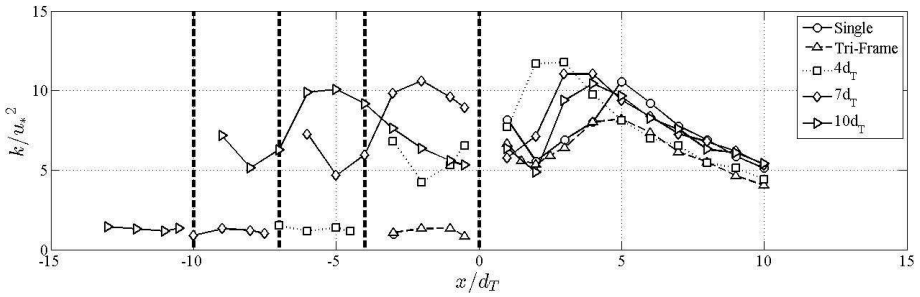

Figure 7.21: Normalized turbulent kinetic energy, k/u_*^2, comparison at hub height in the streamwise direction between five configurations: Single turbine (O), tri-frame turbines (Δ), and two turbines spaced at $4d_T$ ($\square$), $7d_T$ ($\diamond$), and $10d_T$ ($\triangleright$).

7.1.3 U.S. Department of Energy Reference Model 2

In addition to the U.S. Department of Energy Reference Model 1 presented in Chapter 6, I also worked on testing a scaled model of the Reference Model 2 (RM2), a 1:15 geometric scale, dual-rotor, counter-rotating, vertical axis cross-flow turbine (Figure 7.22). The experimental protocol was similar to that discussed for RM1 in Chapter 6 (Figure 7.23). Data processing was the same as described in the Data Reduction Methods section in Chapter 6. Rotor diameter $d_T = 0.43$m and rotor height, $h_T = 0.323$m. Blade profiles and horizontal strut support arms used NACA-0021 profiles. RM2 is a river turbine designed for a site modeled after a reach in the Lower Mississippi River near Baton Rouge, Louisiana [159]. Detailed performance and velocity measurements were collected to assess the interaction of RM2 with the surrounding environment. A robust dataset resulted from these experiments, providing data for CFD model validation, available through the U.S. Department of Energy and Sandia National Laboratories Reference Model Project website. Performance of the dual-rotor device was found to be relatively low, possibly due to the low chord Reynolds numbers during the experiments. Maximum $C_p = 0.05$ at a tip-speed ratio of $\lambda \approx 2.2$. Detailed wake velocity measurements show the greatest velocity deficit extending to approximately $4d_T$ downstream of RM2, while evidence of the wake extends to $10d_T$ and beyond (Figures 7.24 and 7.25). At $10d_T$, the wake velocity has only recovered to approximately 80% of the upstream flow value, similar to that reported for axial-flow devices [29]. The lower near wake velocity deficit for RM2 compared to axial-flow devices likely is a result of the much lower performance. The interaction of the dual-rotor wakes is strongly evident between $3d_T$ and $6d_T$ (Figures 7.26 and 7.27). The range of angles of attack for the RM2 turbine causes the blades to operate under dynamic stall. This is a Reynolds number dependent phenomenon. For these experiments, the chord Reynolds number, $Re_c \approx 10^4$, was

likely below the threshold needed to properly scale stall (and lift) characteristics. For a 3-bladed cross-flow turbine of similar geometry, but different with NACA-0020 foils and a solidity $Nc/(\pi d_T) = 13.4\%$, [160] reported that $Re_c \equiv (\lambda U_\infty c)/\nu \approx 2.1$ x 10^5 was required to achieve Reynolds number independence.

Figure 7.22: Photo of the RM2 dual-rotor model in the SAFL Main Channel.

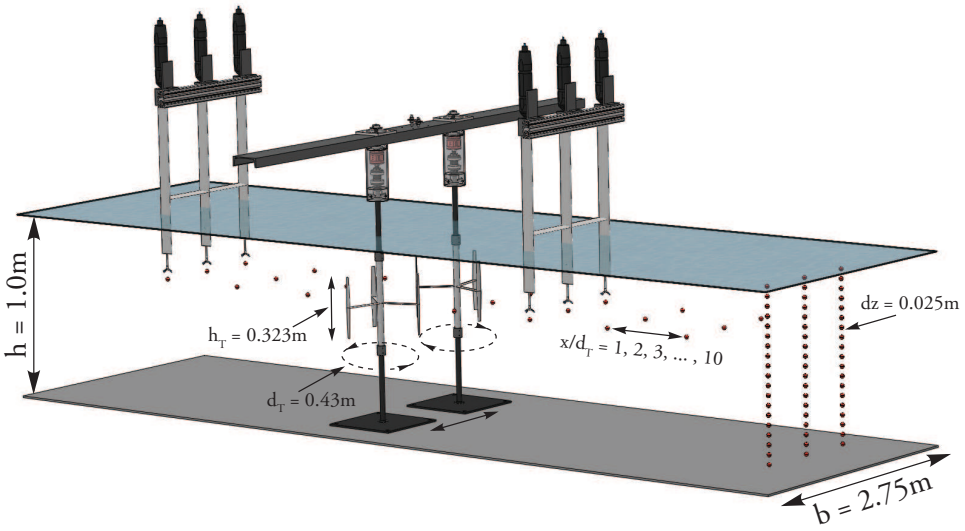

Figure 7.23: Schematic of the RM2 experimental setup and ADV collection locations in the SAFL Main Channel facility. Flow is from left to right.

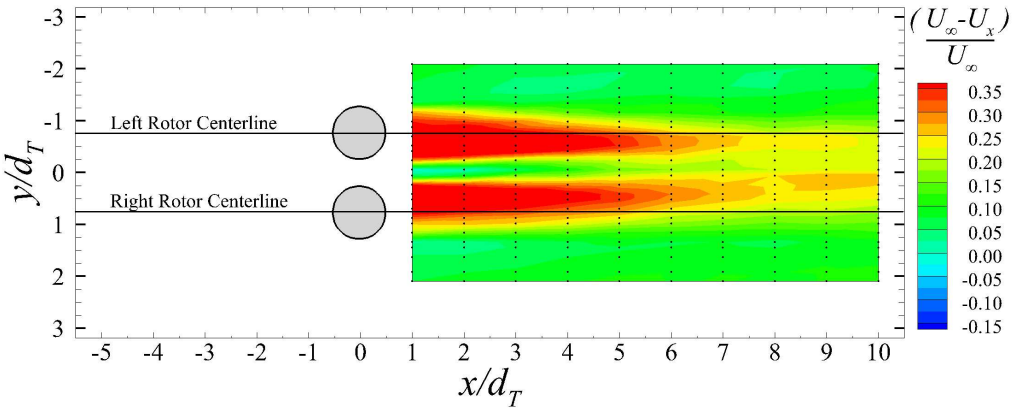

Figure 7.24: Velocity deficit downstream of RM2 in the SAFL Main Channel in a plane parallel to the channel bottom at turbine center height. Turbine location indicated by the two circles at $x/d_T = 0$. Vertical axis, y/d_T, shows full SAFL Main Channel width ($b = 2.75$m). Black dots indicate actual ADV measurement locations. Measurements collected with dual-rotors in-phase and $\lambda \approx 2.2$ ($\omega = 2.0$rps). Flow is left to right.

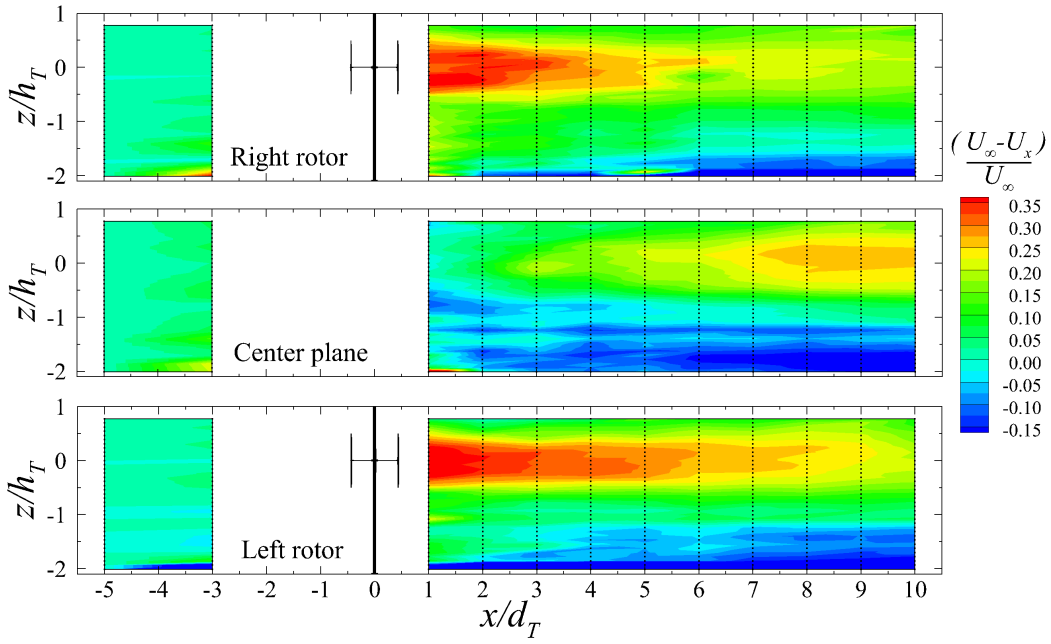

Figure 7.25: Velocity deficit upstream and downstream of RM2 in the SAFL Main Channel in vertical planes aligned with the right rotor (top), midway between the two rotors (middle), and the left rotor (bottom). Turbines located at $x/d_T = 0$. Vertical axis, z/d_T, shows full water depth during experiments ($h = 1.0$m). Black dots indicate actual ADV measurement locations. Measurements collected with dual-rotors in-phase and $\lambda \approx 2.2$ ($\omega = 2.0$rps). Flow is left to right.

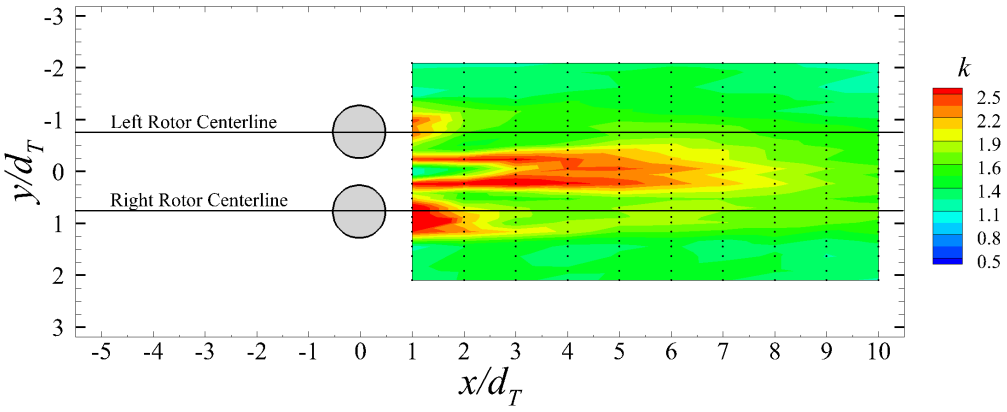

Figure 7.26: Normalized turbulent kinetic energy, k/k_∞, downstream of RM2 in the SAFL Main Channel in a plane parallel to the channel bottom at turbine center height. Turbine location indicated by the two circles at $x/d_T = 0$. Vertical axis, y/d_T, shows full SAFL Main Channel width ($b = 2.75$m). Black dots indicate actual ADV measurement locations. Measurements collected with dual-rotors in-phase and $\lambda \approx 2.2$ ($\omega = 2.0$rps). Flow is left to right.

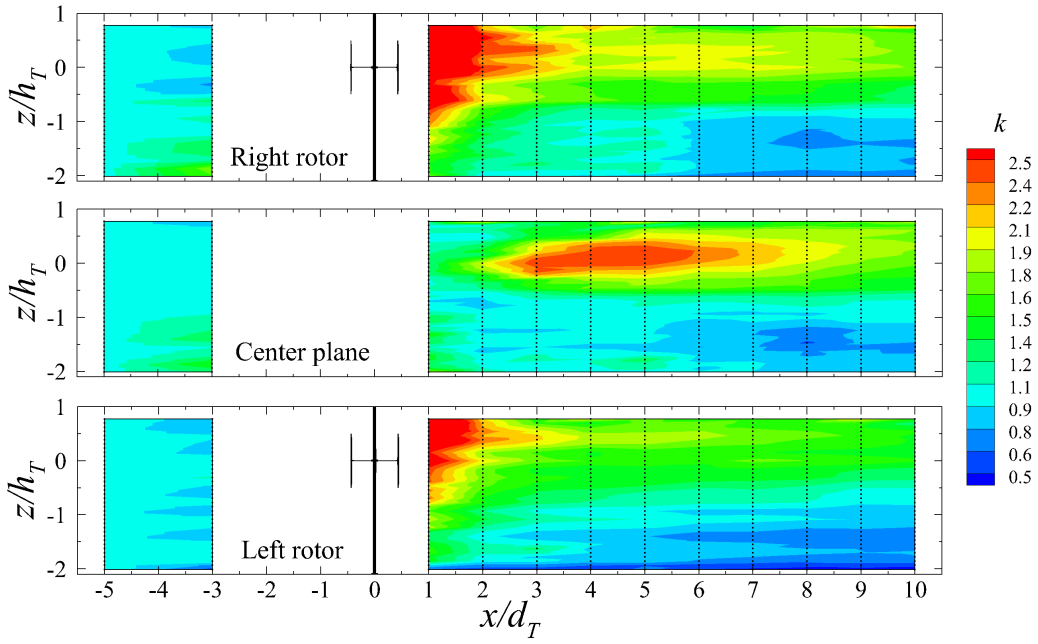

Figure 7.27: Normalized turbulent kinetic energy, k/k_∞, upstream and downstream of RM2 in the SAFL Main Channel in vertical planes aligned with the right rotor (top), midway between the two rotors (middle), and the left rotor (bottom). Turbines located at $x/d_T = 0$. Vertical axis, z/d_T, shows full water depth during experiments ($h = 1.0$m). Black dots indicate actual ADV measurement locations. Measurements collected with dual-rotors in-phase and $\lambda \approx 2.2$ ($\omega = 2.0$rps). Flow is left to right.

7.1.4 Particle Image Velocimetry (PIV) using bedform topography

Particle Image Velocimetry (PIV) is a technique that is commonly used to develop detailed spatial resolution of a flow-field. This practice is common to use in wind tunnels and water channels to monitor the complex turbulent flow fields above sedimentary dunes, downwind of model wind turbines, within various sized roughness patches to assess boundary layer development and stability, and a variety of other uses. More recently, the techniques have been extended to large-scale PIV by mapping snow particle trajectories in the wake of a full-scale 2.5MW wind turbine at the University of Minnesota [161]. This technique now shows promise as a method for mapping local bedform velocities using the laser imaging topographic mapping system developed at St. Anthony Falls Laboratory and discussed in the previous chapters. During the experiments presented in Chapter 5, repeated bed topography scans were collected at various regions and times during the experiment. Using the topographic grid points as particles, the

data fields can be used in existing PIV analysis software to calculate instantaneous and time-averaged bedform velocities. This technique, currently in proof-of-concept stage, was tested on data collected along the side of the axial-flow turbine. Figure 7.28 illustrates the technique using two subsequent topography scans, t_1 and t_2 (sub-figures (a) and (b), respectively). The time between these scans was approximately 212 seconds. By subtracting t_2 from t_1, a difference map is generated showing regions of active erosion and deposition during this time-span (Figure 7.28c). Here, there are two regions that show most movement of sediment: First, upstream of the turbine, and second, downstream of the turbine between approximately $1d_T$ and $2.5d_T$, both shown circled. After applying PIV techniques to track the correlation between the two time-frame topographic images, instantaneous bedform velocities are generated (Figure 7.28d). As one would expect, the fastest bedform velocities occur in the regions were the most erosion and deposition occurred. By applying this PIV technique to all of the repeated topographic scans over the course of the experiment, a time-averaged bedform velocity map is generated for the region upstream and downstream of the the turbine location, revealing a bit more on the dynamics of bedforms as they approach, bypass, and move farther downstream of the turbine (Figure 7.28e).

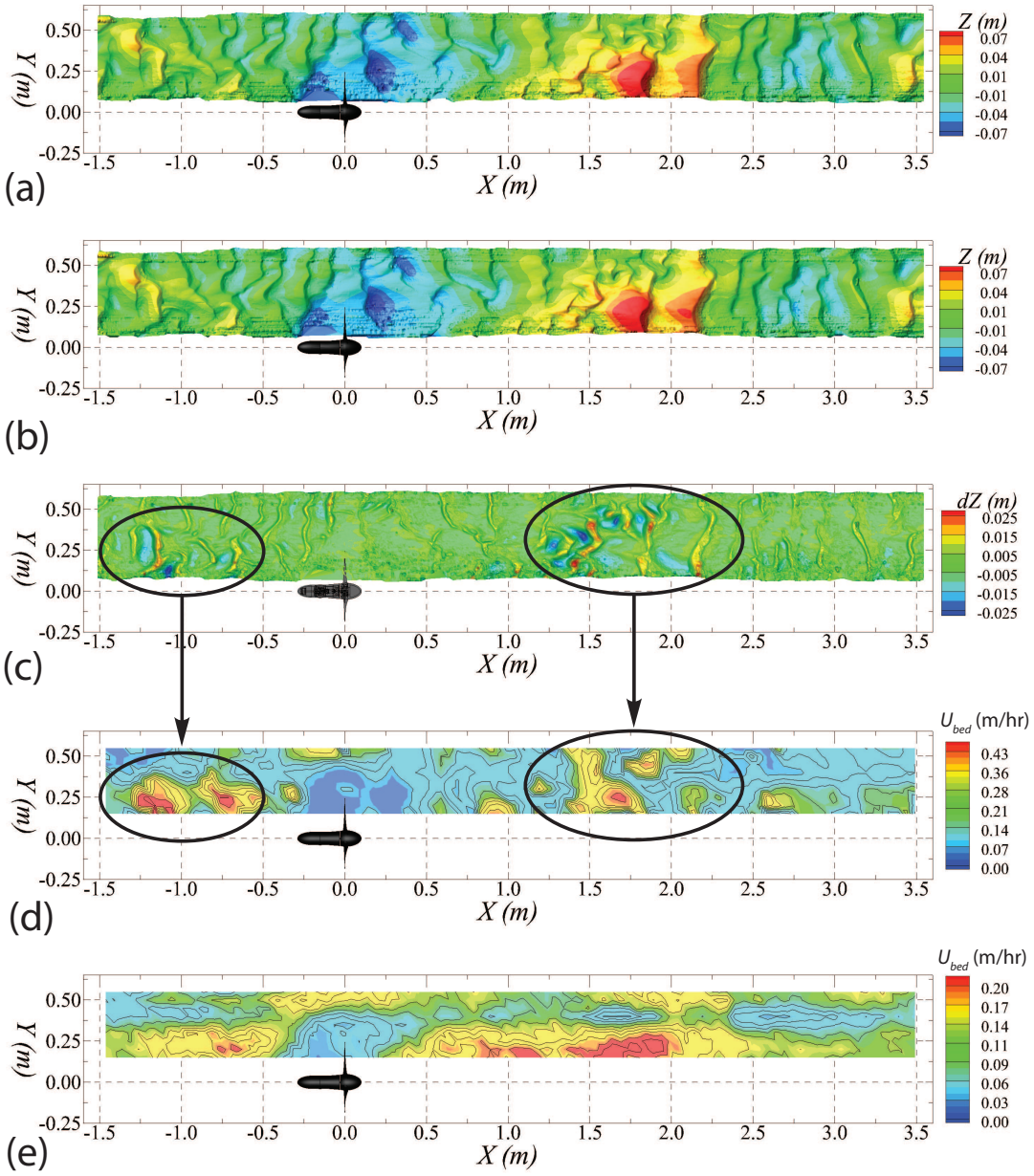

Figure 7.28: Demonstration of particle image velocimetry being applied to sediment topography data. Instantaneous bed elevation data for (a) $t_1$and (b) t_2 can be used to determine local areas of (c) erosion and deposition (i.e. $\Delta z_b = t_2 - t_1$). Using elevation nodes as particles, the correlation between the data from (a) and (b) can be analyzed using PIV algorithms to calculate instantaneous local bedform velocities (d). Averaging all time-steps together enables determining a regional map of average bedform velocities (e). Flow is left to right in all images.

7.2 Future Directives

As the hydrokinetic energy industry advances towards commercial viability, continued collaboration among industry companies, government agencies, and academic institutions will remain a necessity to continue addressing challenges and uncertainties at the forefront of developing new ideas and strategies for implementing, operating, and maintaining MHK devices in complex hydrodynamic and morphodynamic environments. The research discussed in the previous chapters provides useful information for several areas of study, including adaptive and advanced device control strategies, numerical model validation, and regulatory agency education to continually update and modify the permitting processes for emerging companies. In general, the MHK industry will benefit from open-access and standardized data, providing resources for permitting agencies to compare and assess emerging technologies and their potential interactions with the environment. Reference Model (RM) development by the U.S. Department of Energy provide the groundwork in this direction by supporting research testing of reference designs that can be used in. Future studies can expand these RM data-sets by investigating their interactions with the biological and morphological environments.

Until the experiments and results originating from this research program, much of the turbine-sediment interaction research has used numerical models to evaluate the impacts of MHK devices on sediment [43, 44, 48, 45, 46, 47]. The data generated during these studies now provide exceptional CFD validation data-sets that can be used to further investigate the parameter space, including additional turbine designs (i.e vertical and horizontal axis cross-flow devices, wave energy devices, and numerous other axial-flow device designs), rotor height above the sediment bed, operational strategies (i.e. tip-speed ratio), and a variety of grain size distributions and sediment transport rates. Incorporating grid-refining strategies, such as those currently under development at St. Anthony Falls Laboratory in the CFD research group of Dr. Fotis Sotiropoulos, can provide methods of using higher resolution coupled hydro-morphodynamic models near the turbine location. While these efforts are currently still computationally expensive, it will certainly become achievable in the near future as the rate of computational resources and supercomputing technologies continue to advance at rapidly.

Development of active and passive control strategies should evolve with the understanding of device interactions with their natural environments. Device geometry and operating principles will influence control strategies, for example, whether it is an axial-flow device with asymmetric, lift generating blades, or a cross-flow device utilizing symmetric blades in either a straight-bladed or helical (i.e. Gorlov) arrangement. The MHK industry will benefit from previous research in control strategies and implementation in the wind industry [107, 108, 109, 110, 111]. In the case of axial-flow devices, possible active control strategies could aim to achieve maximum power point tracking for specific devices (Figure 7.29). Additionally, control strategies may focus on

minimizing individual blade, rotor, or entire turbine and support structure fatigue. Due to the scale of laboratory devices, these goals may be achievable purely through controlling rotational velocity of the rotor. With larger scale rotors having a much larger moment of inertia, such as at field scale, the likelihood of active control based on a feed-forward approach using in-situ measurements of turbulent flow-fields may be less feasible, and approaches may shift to focus on slower response control when large-scale topographic changes occur or sensors indicate a local presence of marine life or other structures (i.e. ships) moving nearby. At field-scale, active pitching of blades will likely be incorporated into designs, similar to what is used in the wind industry. In environments where the dominant approach flow direction changes (i.e. tidal flows, mobile channel substrates with 3D bedforms), incorporating yaw control will improve performance [112]. To date, little work has been completed for active control of MHK devices. [113] experimented with closed-loop PI (Proportional Integral) and H_∞ LPV (Linear Parametric Varying) speed control of a straight-bladed vertical axis hydrokinetic turbine. Here, the authors attempted to incorporate a maximum power point tracking feedback control system and had reasonable success. Unlike wind energy systems, MHK systems typically operated at lower tip speed ratios, λ, a possible benefit for the control systems community. Regardless, non-linearities in the MHK systems (i.e. C_P or C_T vs. λ) often introduce complexity when considering control operations, and the inherent energy in environments these devices are designed for will require both low-pass and high-pass filters to reduce noise from environmental variables.

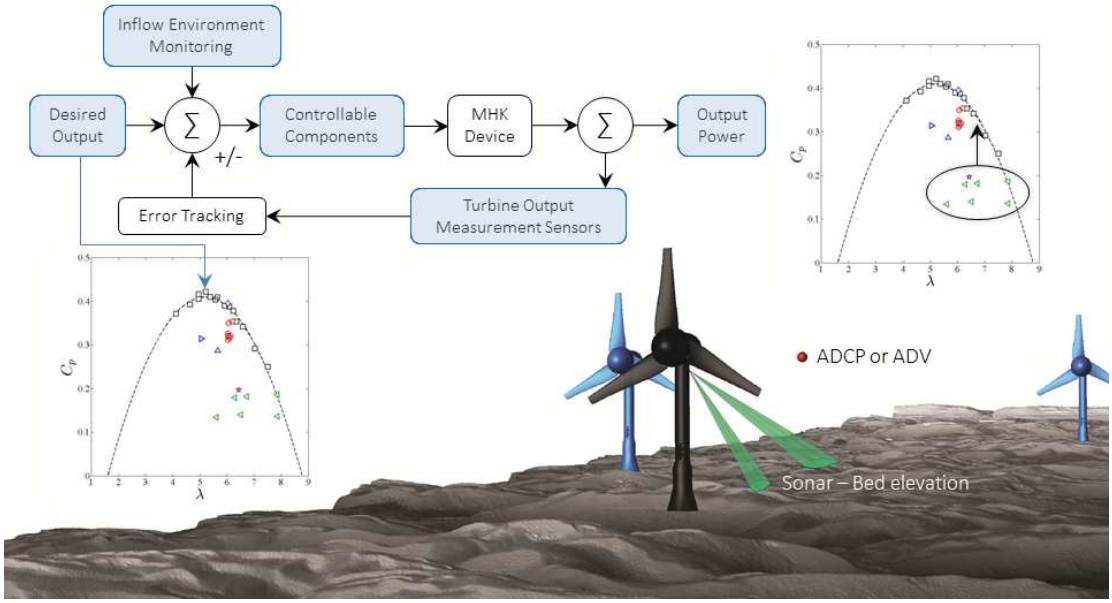

Figure 7.29: Feedback and feed-forward loop diagram schematic for advanced control strategies for the next generation MHK devices.

Additional future research should systematically address the interactions between the turbulent flow-field above bedform features in channels. Ideally this would begin with a detailed laboratory study using frozen or rigid non-erodible and non-mobile bedform features. To gain a better understanding of how the dune-influenced hydrodynamics impact turbine performance and wake characteristics, a larger parameter space needs to be investigated. This could be achieved by using particle image velocimetry (PIV) techniques to map the upstream flow field and downstream interaction with the turbine wake (Figure 7.30). By changing the rotor location in the streamwise direction with respect to the location of the dune crest, the impacts of the topography on turbine performance could be better understood. Additionally, adjust hub height above the mean bed elevation would provide meaningful results for the MHK industry. PIV techniques would allow for very detailed flow-field studies on how increased turbulent kinetic energy levels may impact loading on turbine components, while also providing in-depth results on near and far-wake turbulent mixing. A detailed laboratory research program using this systematic approach would greatly improve the MHK communities understanding of how these devices respond to complex topography, similar to the channels and hydrodynamic environments they will ultimately be installed in.

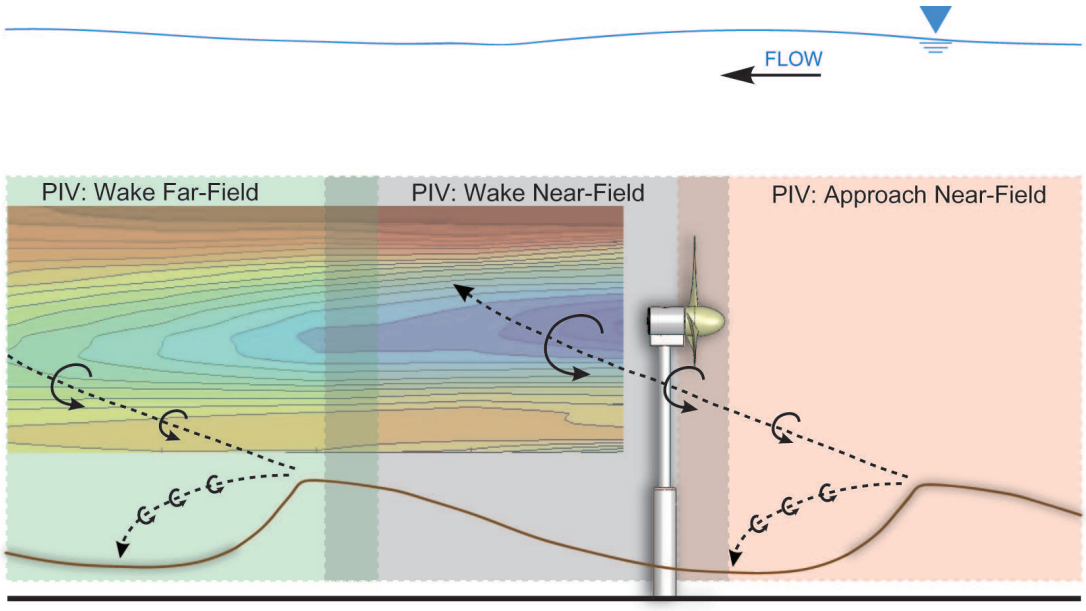

Figure 7.30: Schematic experimental setup for future studies on the interactions between dune generated turbulence and axial-flow hydrokinetic turbines to study to role dune size and location has on turbine performance and the associated near and far-wake characteristics.

Chapter 8

Summary & Conclusions

The research program carried out during my Doctoral degree at St. Anthony Falls Laboratory (SAFL), University of Minnesota, utilized multi-scale physical experiments to study the interactions between axial-flow hydrokinetic turbines, turbulent open channel flow, sediment transport, turbulent turbine wakes, and complex hydro-morphodynamic processes in open channel flow. Model axial-flow current-driven three-bladed turbines (rotor diameters, $d_T = 0.15$m and 0.5m) were installed in open channel flumes with both erodible and non-erodible substrates. Device-induced local scour was monitored over several hydraulic conditions and material sizes. Synchronous velocity, bed elevation and turbine performance measurements provided an indication into the effect channel topography has on device performance. Results provide the foundation for investigating advanced turbine control strategies for optimal power production in non-stationary environments, while also providing a robust data-set for computational model validation for further investigating the interactions between energy conversion devices and the physical environment. The results obtained from experiments in this research program provide some of the first insights into these interactions. While each individual chapter preceding this point summarizes key results in the context of that chapter, important insights are summarized below in sections relating to turbine performance, turbine wake characteristics, and sediment transport in complex topographic channels, followed by suggestions for future research directions and applications of these results towards the MHK industry and governmental regulatory agencies.

Turbine Performance

- Axial-flow hydrokinetic turbines are typically characterized by a parabolic shaped performance curve, with peak efficiency occurring somewhere below the maximum Betz limit

level of approximately 60%. The operational condition of this optimal efficiency point is governed both by the blade geometric characteristics (i.e. twist and pitch along the length of the blade) and the tip-speed ratio, $\lambda = (\omega d_T) / (2U_{hub})$. Turbines operating at similar λ experience reduced C_p when operating in channels with mobile bedforms compared to smooth, non-erodible channels, as shown in the performance curve, Figure 5.5. This reduction in performance is similar to results from experiments published by [1], reiterating that turbine performance responds to stationary and mobile features upstream of the turbine location.

- In channels with active bedload transport, approaching bedforms reach a critical zone within approximately $2d_T$ upstream of the turbine, where the bed elevation profile is closely correlated to the turbine performance (in terms of voltage output, in the case of the experiments reported in Chapter 3). Within this nearby region, mean voltage output tends to increase, as well as voltage intensity levels (i.e. the range of fluctuations, similar to turbulence intensity in the flow). These effects are likely related to the evolution of specific turbulent flow regions associated with bedform migration, as summarized by [97].

- In the case of large-scale sediment transport experiments with dunes (Chapter 5), transition to larger and faster bedforms reduces turbine performance to $C_p \approx 0.13$ to 0.2) for a range of λ tested ($\lambda \approx 5.6$ to 7.9) (Figure 5.5). The variability in λ and C_p may represent the extremes since local and instantaneous U_{hub} measurements were not permitted, thereby requiring assumptions while prescribing ω. The increase in topographic variance subjects the turbine rotor to a broader range of turbulence scales, which in turn can imprint these fluctuations in the turbine power signature.

- The introduction of coherent turbulent structures (i.e. von K*árm*án type vortices from vertical cylinders or hairpin-shaped vortex tubes emanating from bedforms) results in the loss of the turbine operational spectral peak in the low-frequency zone (Figure 5.7 and also identified by [1]). This broad, less distinct peak in the torque time-series spectra during mobile sediment bed experiments indicates the channel roughness of this size had less of an impact compared to those reported by [1]. These results provide an indication that precise control of λ may provide improved performance by near-optimal efficiency.

- In summary, the presence of both additional turbines and/or bedforms results in decreased performance of the turbine, and turbine-bedform interactions are expected to be amplified by higher or steeper bedforms, or by a larger rotor positioned closer to the sediment layer. Turbines operating in complex hydrodynamic and morphodynamic channels need to be able to withstand more frequent turbulent fluctuations across a broader range of scales.

- Preliminary work that served as the foundation for this research program indicated that large-scale coherent turbulent structures directly modulate the wake and performance characteristics of axial-flow turbines in open channel flow [1]. Experiments indicated that stationary obstacles positioned upstream of a turbines location modulate a broad range of turbulence frequency, which in turn have a direct scale-to-scale modulation of the turbine power characteristics (Figure 1.5). While these structures (i.e. bridge piers, bridge abutments, or large-scale boulders, for example) introduce added turbulence into the approach flow, their upstream location and coherence plays a more important role in near-wake velocity recovery. Specifically, large-scale coherent turbulent structures accelerate tip-vortex breakdown and accelerated near-wake velocity recovery up to approximately $x/d_T = 5$ to 7 when compared to turbines operating in unimpeded approached flow (Figure 1.8).

- Off-peak performance influences the velocity deficit, U_{def}, in the near-wake, shown in the case of the turbine operating in bedforms (Q_1) with $\lambda \approx 6.1$ and in a smooth concrete channel at $\lambda \approx 7.7$ (Figure 5.8) as discussed in Chapter 5. Far-wake velocity deficit, U_{def}, is controlled more by channel boundary conditions and turbulent mixing which is increased due to large-scale coherent eddies in the approach flow. Wake characteristic data with dune bedform transport were not available, yet results suggest velocity deficit would recover more quickly, similar to the cylinder experiments where turbulent coherent eddies resulted in near-wake tip vortex breakdown and accelerated near and far-wake velocity deficit recovery [1].

- Experiments highlighted evidence of typical scales of motion associated with axial-flow turbine near-wake characteristics, such as the tip vortices and evidence of a slowly rotating hub vortex at $x/d_T = 0.5$ (Figure 5.9 and 5.10). Additionally, signatures of upstream turbine wakes, as well as a possible aggregation of an array super wake was found in the turbine performance spectra (Figure 7.6), suggesting that turbine-array power plant operational strategies may in fact be different to accommodate the altered hydrodynamic environment imposed by upstream turbines.

- In a field-scale realistic meandering channel, local velocity magnitude and direction without a turbine is influenced by local (i.e. dune crest location and size) and non-local (i.e. channel sinuosity and asymmetric cross-section) topography. With a turbine present at that same specific location in the channel, the orientation of both upstream approach velocity and turbine wake velocity is redirected toward the outer banks of the channel (Figure 4.7). Despite the redirection of flow, there is evidence that the wake of a turbine will follow the

curvature of a channel, impacting the downstream location of an additional turbine, and potentially allowing closer spacing of turbines in meandering channels. The evidence of flow redirection also indicates a need for post-project monitoring of erodible channel banks to monitor for signs of degradation and lateral movement in the channel boundary.

- The low velocity in the turbine wake persisted beyond the measurement extent of $x/d_T = 5.4$ (Figure 4.16) in a meandering channel, implying zones of higher velocity may concentrate between the wake and the outer bank. This is inferred to be a consequence of turbulent flow organization along the channel curvature, likely governed by the secondary currents. Local and non-local bathymetry is expected to introduce large scale fluctuations in the perceived inflow at the turbine location and accelerate wake recovery by increasing turbulent mixing in the turbine wake.

Turbine Interactions with Sediment Transport and Topography

- Turbines operating in erodible channels typically under clear water scour conditions (i.e. bed shear stress below a critical threshold required for incipient sediment transport, $\tau_b < \tau_{cr}$) cause locally amplified scour, especially when compared to bridge pier scour (Figures 2.4 and 2.5). Existing bridge scour prediction guidelines were inadequate at estimating equilibrium scour depth when a single turbine rotor was present ([126, 127], for example). Near-turbine scour zones rapidly develop and extend $2d_T$ downstream and up to $1.5d_T$ to either side of the turbine. Maximum scour depths were measured between 15% (small-scale experiments) and 35% (large-scale experiments) of the rotor diameter, d_T (Figure 2.6). The local scour depth in the meandering channel was ≈30% less than the observed local scour depth in a straight channel. The presence of the turbine decreased the variability in bed elevation, quantified by temporal r.m.s. values, σ_{z_b}, both upstream and downstream of the rotor by ≈35%, a phenomena that has been measured in similarly scaled straight channel experiments (Figure 4.18). Secondary currents may explain why σ_{z_b} reduction was observed to be more persistent in meandering flow compared to a straight channel.

- Results suggest normalizing turbine-sediment interactions by the characteristic bedform dimensions (λ_b and h_b) is more appropriate that using the turbine diameter, d_T, as the normalization factor. Rotor diameter may still be the appropriate factor for normalizing scour depth, d_s. In the case of large-scale experiments with a turbine rotor diameter $d_T = 0.5$m, the turbine region of influence at two Reynolds numbers is a triangular shaped region extending $I_L \approx 7\lambda_b$ in the streamwise direction and $I_B \approx 4\lambda_b$ in the cross-stream direction with a spreading angle of $I_\theta \approx 42°$ (Figure 5.14).

- Downstream of the turbine(s) location in a region spanning from near-field (approximately $1d_T$ to far-field (approximately $33d_T$), bedform detection techniques revealed that median values for bedform wavelength, $\bar{\lambda}_b$, and bedform height, h_b, only slightly vary within the range of values encountered in undisturbed baseline experiments; therefore, the presence of turbine(s) does not seem to impact the far-field sediment transport or morphodynamic characteristics of the channel under the aligned turbine configuration tested thus far.

- Regardless of large bedforms with respect to the turbine hub height, no blade damage was observed in any of the experiments, implying that the annular shear layer and local acceleration below the bottom tip responsible for the increased scour surrounding the device also acts to protect the rotor from potential impacts with the incoming bedforms. Additionally, preliminary work using PIV techniques with spatio-temporally resolved bed elevation measurements, as demonstrated in Figure 7.28, show that bedforms accelerate upstream of the turbine likely due to the increased local bed shear stress and locally accelerated flow beneath the rotor. PIV analysis shows low bedform velocities below the turbine due to lack of any recognizable bedform features because they are sheared off from accelerated flow and rapidly transported downstream. This serves as additional evidence that devices may protect themselves from potential blade contact with large-scale mobile topographic features.

Future Research Directives

- There remains a need for a systematic investigation on turbine-sediment interactions based on the turbine hub height, h_{hub}, and tip-speed ratio, λ, and proximity to the nearest upstream bedform crest location (Figure 7.30). Research should investigate these parameters in-depth to gain a better understand on how it effects the mean and variability in turbine performance coefficients, C_p, and the turbine near and far-wake velocity deficit, U_{def}. Additionally, these parameters should be further investigated to assess their control on local scour depths and lateral areas of influence. While these studies focused primarily on axial-flow hydrokinetic devices, research should expand to incorporate additional device designs.

- Incorporating real-time sensing networks such as upstream ADCPs and ADVs, topographic measurement systems, and turbine operational sensors should be utilized to begin development of advanced control strategies for hydrokinetic devices. Using feedback and feedforward control algorithms, there is promise for maintaining optimal efficiency operating conditions for devices operating in non-stationary complex hydrodynamic and morphodynamic environments (Figure 7.29).

- The challenge of where to appropriately measure upstream velocities in complex hydrodynamic environments should be investigated to understand how to better estimate the available power in the approach flow, how to calculate the local tip-speed ratio, and how to assess the unsteady turbulent fluctuations that will impact the turbine rotor. Today, the industry standard is to use the hub height velocity at approximately 3-5d_T upstream of the turbine location. Because these are typically either point measurements or lower resolution vertical profiles, the data do not always capture the asymmetry of the flow, especially downstream of obstacles in the channel (i.e. bridge foundation structures, rock ledges, mobile bedforms, upstream turbines, etc.). Any error and asymmetry in the flow will compound in the estimated available power to the turbine, and the definition of the turbine tip-speed ratio, which in turn can influence operational strategies being employed to maintain peak performance.

- As the knowledge on turbine-sediment interaction grows, scaling from laboratory to field-scales needs to be further address, as well as how these interactions change as the MHK industry moves beyond single device design and testing towards multi-turbine installations, and ultimately large utility-scale deployments.

The experiments discussed above provide preliminary insights into the interaction between hydrokinetic turbines and the surrounding geomorphic environment. Continued assessment of these interactions is a critical prerequisite for accelerating the environmental permitting processes currently acting as a barrier towards continued implementation of such devices. Ideally these results can readily be extended for suggestions for device developers on optimal siting of turbines at field locations with either stationary or mobile large-scale topographic features. With proper dissemination of these results, the MHK research community can provide confidence for permitting agencies during the Environmental Impact Statement and permitting processes, thereby reducing the cost to device developers and ultimately the levelized cost of energy, providing a way for marine and hydrokinetic energy technologies to serve as an economically viable and sustainable method for contributing renewable energy to our Nation's electrical network.

For questions pertaining to the work presented in the preceding chapters or discussion on projects related to hydrokinetic turbine interactions with the environment, please feel free to contact me, Craig Hill, at hillx154@umn.edu.

References

[1] L.P. Chamorro, C. Hill, V.S. Neary, B. Gunawan, R.E.A. Arndt, and F. Sotiropoulos. Effects of energetic coherent motions on the power and wake of an axial-flow turbine. *Phys. Fluids*, 27:055104, 2015.

[2] D. Jerolmack and D. Mohrig. A unified model for subaqueous bed form dynamics. *Water Resour. Res.*, 41:W12421, 2005.

[3] B. Polagye, B. Van Cleve, A. Copping, and K. Kirkendall. Environmental effects of tidal energy development. Technical report, U.S. Dept. Commerce, NOAA Tech. Memo., F/SPO-116, 2011.

[4] J. Nittrouer, M. Allison, and R. Campanella. Bedform transport rates for the lowermost Mississippi River. *J. Geophys. Res.*, 113:F03004, 2008.

[5] C. Hill, M. Musa, L.P. Chamorro, C. Ellis, and M. Guala. Local scour around a model hydrokinetic turbine in an erodible channel. *J. Hydraul. Eng.*, 140(8):04014037, 2014.

[6] L.P. Chamorro, C. Hill, S. Morton, C. Ellis, R.E.A. Arndt, and F. Sotiropoulos. On the interaction between a turbulent open channel flow and an axial-flow turbine. *J. Fluid Mech.*, 716:658–670, 2013.

[7] Ocean Renewable Energy Coalition. U . S . Marine and Hydrokinetic Renewable Energy Roadmap. Technical Report November, Ocean Renewable Energy Coalition, 2011.

[8] R. Bedard. Prioritized research, development, deployment and demonstration (RDD&D) needs: Marine and other hydrokinetic renewable energy. Technical report, Electric Power Research Institute, 2008.

[9] M.S. Güney and K. Kaygusuz. Hydrokinetic energy conversion systems: A technology status review. *Renew. Sustain. Energy Rev.*, 14(9):2996–3004, 2010.

[10] M.J. Khan, G. Bhuyan, M.T. Iqbal, and J.E. Quaicoe. Hydrokinetic energy conversion systems and assessment of horizontal and vertical axis turbines for river and tidal applications: A technology status review. *Appl. Energy*, 86(10):1823–1835, 2009.

[11] R.M. Baxter. Environmental effects of dams and impoundments. *Annu. Rev. Ecol. Syst.*, 8:255–283, 1977.

[12] D. Leary and M. Esteban. Renewable energy from the ocean and tides : A viable renewable energy resource in search of a suitable regulatory framework. *Carbon Clim. Law Rev. Renew. Energy from Ocean Tides*, 4:417–426, 2009.

[13] K.W. Ng, W.H. Lam, and K.C. Ng. 2002–2012: 10 years of research progress in horizontal-axis marine current turbines. *Energies*, 6(3):1497–1526, 2013.

[14] F. O'Rourke, F. Boyle, and A. Reynolds. Tidal energy update 2009. *Appl. Energy*, 87(2):398–409, 2010.

[15] M. Previsic, J. Epler, M. Hand, D. Heimiller, W. Short, and K. Eurek. The future potential of wave power in the United States. Technical Report August, ReVision Consulting LLC, 2012.

[16] G.W. Boehlert and A.B. Gill. Environmental and ecological effects of ocean renewable energy development: A current synthesis. *Oceanography*, 23(2):68–81, 2008.

[17] G. Cada, J. Ahlgrimm, M. Bahleda, T. Bigford, S.D. Stavrakas, D. Hall, R. Moursund, and M. Sale. Potential impacts of hydrokinetic and wave energy conversion technologies on aquatic environments. *Fisheries*, 32(4):174–181, 2007.

[18] A. Copping, C. Smith, L. Hanna, H. Battey, J. Whiting, M. Reed, J. Brown-Saracino, P. Gilman, and M. Massaua. Tethys: Developing a commons for understanding environmental effects of ocean renewable energy. *Int. J. Mar. Energy*, 3-4:41–51, 2013.

[19] E. Foufoula-Georgiou, M. Guala, and F. Sotiropoulos. Marine-hydrokinetic energy and the environment: Observations, modeling, and basic processes. *Eos*, 93(10):111, 2012.

[20] M. Mueller and R. Wallace. Enabling science and technology for marine renewable energy. *Energy Policy*, 36(12):4376–4382, 2008.

[21] R. Bucher and S.J. Couch. Adjusting the financial risk of tidal current projects by optimising the installed capacity/capacity factor-ratio already during the feasibility stage. *Int. J. Mar. Energy*, 2:28–42, 2013.

[22] A.S. Bahaj, L.E. Myers, G. Thompson, and N. Jorge. Characterising the wake of horizontal axis marine current turbines. In *7th Eur. Wave Tidal Energy Conf.*, 2007.

[23] L.P. Chamorro, D.R. Troolin, S.J. Lee, R.E.A. Arndt, and F. Sotiropoulos. Three-dimensional flow visualization in the wake of a miniature axial-flow hydrokinetic turbine. *Exp. Fluids*, 54(2):1–12, 2013.

[24] S. Kang, I. Borazjani, J.A. Colby, and F. Sotiropoulos. Numerical simulation of 3D flow past a real-life marine hydrokinetic turbine. *Adv. Water Resour.*, 39:33–43, 2012.

[25] F. Maganga, G. Germain, J. King, G. Pinon, and E. Rivoalen. Experimental characterisation of flow effects on marine current turbine behaviour and on its wake properties. *Ren. Power Gen.*, 4(6):498–509, 2010.

[26] L. Myers and A.S. Bahaj. Wake studies of a 1/30th scale horizontal axis marine current turbine. *Ocean Eng.*, 34:758–762, 2007.

[27] L.E. Myers, B. Keogh, and A.S. Bahaj. Experimental investigation of inter-array wake properties in early tidal turbine arrays. *OCEANS 2011*, pages 1–8, 2011.

[28] L.E. Myers and A.S. Bahaj. An experimental investigation simulating flow effects in first generation marine current energy converter arrays. *Ren. Energy*, 37(1):28–36, 2012.

[29] V.S. Neary, B. Gunawan, C. Hill, and L.P. Chamorro. Near and far field flow disturbances induced by model hydrokinetic turbine : ADV and ADP comparison. *Ren. Energy*, 60:1–6, 2013.

[30] G. Pinon, P. Mycek, G. Germain, and E. Rivoalen. Numerical simulation of the wake of marine current turbines with a particle method. *Ren. Energy*, 46:111–126, 2012.

[31] T. Stallard, R. Collings, T. Feng, and J. Whelan. Interactions between tidal turbine wakes: Experimental study of a group of three-bladed rotors. *Philos. Trans. A. Math. Phys. Eng. Sci.*, 371, 2013.

[32] A.S. Bahaj, W.M.J. Batten, and G. McCann. Experimental verifications of numerical predictions for the hydrodynamic performance of horizontal axis marine current turbines. *Ren. Energy*, 32(15):2479–2490, 2007.

[33] A.S. Bahaj, A.F. Molland, J.R. Chaplin, and W.M.J. Batten. Power and thrust measurements of marine current turbines under various hydrodynamic flow conditions in a cavitation tunnel and a towing tank. *Ren. Energy*, 32(3):407–426, 2007.

[34] L. Myers and A.S. Bahaj. Power output performance characteristics of a horizontal axis marine current turbine. *Ren. Energy*, 31(2):197–208, 2006.

[35] L.E. Myers and A.S. Bahaj. The effect of boundary proximity upon the wake structure of horizontal axis marine current turbines. *27th Int. Conf. Offshore Mech. Arct. Eng.*, 134:709–719, 2008.

[36] C. Faudot and O.G. Dahlhaug. Prediction of wave loads on tidal turbine blades. *Energy Procedia*, 20:116–133, 2012.

[37] P.W. Galloway, L.E. Myers, and A.S. Bahaj. Studies of a scale tidal turbine in close proximity to waves. *3rd Int. Conf. Ocean Energy*, 1:1–6, 2010.

[38] L. Luznik, K.A. Flack, E.E. Lust, and K. Taylor. The effect of surface waves on the performance characteristics of a model tidal turbine. *Ren. Energy*, 58:108–114, 2013.

[39] E.E. Lust, L. Luznik, K.A. Flack, J.M. Walker, and M.C. Van Benthem. The influence of surface gravity waves on marine current turbine performance. *Int. J. Mar. Energy*, 3-4:27–40, 2013.

[40] J. Giles, L. Myers, Abu B. B., and J. ONians. An experimental study to assess the potential benefits of foundation based flow acceleration structures for marine current energy converters. *Power*, 3, 2009.

[41] L. Chen and W.-H. Lam. Methods for predicting seabed scour around marine current turbine. *Renew. Sustain. Energy Rev.*, 29:683–692, 2014.

[42] C. Hill, M. Musa, and M. Guala. Interaction between instream axial flow hydrokinetic turbines and uni-directional flow bedforms (accepted for publication). *Ren. Energy*, 2015.

[43] S.P. Neill, E.J. Litt, S.J. Couch, and A.G. Davies. The impact of tidal stream turbines on large-scale sediment dynamics. *Ren. Energy*, 34(12):2803–2812, 2009.

[44] S.P. Neill, J.R. Jordan, and S.J. Couch. Impact of tidal energy converter (TEC) arrays on the dynamics of headland sand banks. *Ren. Energy*, 37(1):387–397, 2012.

[45] P.E. Robins, S.P. Neill, and M.J. Lewis. Impact of tidal-stream arrays in relation to the natural variability of sedimentary processes. *Ren. Energy*, 72:311–321, 2014.

[46] I. Fairley, I. Masters, and H. Karunarathna. The cumulative impact of tidal stream turbine arrays on sedimnet transport in the Pentland Firth. *Ren. Energy*, 80:755–769, 2015.

[47] R. Martin-Short, J. Hill, S.C. Kramer, A. Avdis, P.A. Allison, and M.D. Piggott. Tidal resource extraction in the Pentland Firth, UK: Potential impactson flow regime and sediment transport in the Inner Sound of Stroma. *Ren. Energy*, 76:596–607, 2015.

[48] X. Yang, S. Kang, and F. Sotiropoulos. Toward a simulation based approach for optimizing mhk turbine arrays in natural waterways. *1st Marine Energy Technology Symposium*, 2013.

[49] A. Khosronejad, S. Kang, and F. Sotiropoulos. Experimental and computational investigation of local scour around bridge piers. *Adv. Water Resour.*, 37:73–85, 2012.

[50] A. Khosronejad, C. Hill, S. Kang, and F. Sotiropoulos. Computational and experimental investigation of scour past laboratory models of stream restoration rock structures. *Adv. Water Resour.*, 54:191–207, 2013.

[51] J. Baltazar and J.A.C. Falcao de Campos. Hydrodynamic analysis of a horizontal axis marine current turbine with a boundary element method. *J. Offshore Mech. Arct. Eng.*, 133(4):883–893, 2011.

[52] W.M.J. Batten, A.S. Bahaj, A.F. Molland, and J.R. Chaplin. Experimentally validated numerical method for the hydrodynamic design of horizontal axis tidal turbines. *Ocean Eng.*, 34(7):1013–1020, 2007.

[53] W.M.J. Batten, A.S. Bahaj, A.F. Molland, and J.R. Chaplin. The prediction of the hydrodynamic performance of marine current turbines. *Ren. Energy*, 33(5):108–1096, 2008.

[54] D. Fallon, M. Hartnett, A. Olbert, and S. Nash. The effects of array configuration on the hydro-environmental impacts of tidal turbines. *Ren. Energy*, 64:10–25, 2014.

[55] M. Lawson, Y. Li, and D. Sale. Development and verification of a computational fluid dynamics model of a horizontal-axis tidal current turbine. *ASME 2011 30th Int'l Conf. Ocean, Off. Arctic Eng.*, pages 711–720, 2011.

[56] Y. Li, B.J. Lence, and S.M. Calal. Modeling the energy output from an in-stream tidal turbine farm. *J. Comput.*, 4(4):288–294, 2009.

[57] Y. Li, B.J. Lence, and S.M. Calal. An integrated model for estimating energy cost of a tidal current turbine farm. *Energy Convers. Manag.*, 52(3):1677–1687, 2011.

[58] A.J. MacLeod, S. Barnes, K.G. Rados, and I.G. Bryden. Wake effects in tidal current turbine farms. In *Int'l Conf. on Marine Ren. Energy*, pages 49–53, 2002.

[59] P. Mycek, B. Gaurier, G. Germain, G. Pinon, and E. Rivoalen. Numerical and experimental study of the interaction between two marine current turbines. *Int. J. Mar. Energy*, 1:70–83, 2013.

[60] X. Sun, J.P. Chick, and I.G. Bryden. Laboratory-scale simulation of energy extraction from tidal currents. *Ren. Energy*, 33(6):1267–1274, 2008.

[61] F. Sotiropoulos and X. Yang. Immersed boundary methods for simulating fluid–structure interaction. *Prog. Aero. Sci.*, 2013.

[62] S.C. James, E. Seetho, C. Jones, and J. Roberts. Simulating environmental changes due to marine hydrokinetic energy installations. *Oceans 2010*, pages 1–10, 2010.

[63] Y. Li and S.M. Calal. Modeling of twin-turbine systems with vertical axis tidal current turbines: Part I – Power output. *Ocean Eng.*, 37(7):627–637, 2010.

[64] Y. Li and S.M. Calal. Three-dimensional effects and arm effects on modeling a vertical axis tidal current turbine. *Ren. Energy*, 35(10):2325–2334, 2010.

[65] Y. Li and S.M. Calal. Modeling of twin-turbine systems with vertical axis tidal current turbine: Part II – Torque fluctuation. *Ocean Eng.*, 38(4):550–558, 2011.

[66] Y. Li and S.M. Calal. Numerical analysis of the characteristics of vertical axis tidal current turbines. *Ren. Energy*, 35(2):435–442, 2010.

[67] J.C. Murray and M. Barone. The development of CACTUS, a wind and marine turbine performance simulation code. In *49th AIAA Aerosp. Sci. Meet.*, pages 1–21, 2011.

[68] V.S. Neary. Reference inflow characterization for river resource reference model: Reference Model 2 (RM2). Technical report, Oak Ridge National Laboratory, 2011.

[69] P. Bachant and M. Wosnik. Experimental investigation of helical cross-flow axis hydrokinetic turbines, including effects of waves and turbulence. In *ASME 2011 Jt. Fluids Eng. Conf.*, pages 1895–1906. ASME, 2011.

[70] P. Bachant and M. Wosnik. Performance and near-wake measurements for a vertical axis turbine at moderate Reynolds number. In *ASME 2013 Fluids Eng. Div. Summer Meet.* ASME, 2013.

[71] J. Zanette, D. Imbault, and A. Tourabi. A design methodology for cross flow water turbines. *Ren. Energy*, 35(5):997–1009, 2010.

[72] A.H. Birjandi, J. Woods, and E.L. Bibeau. Investigation of macro-turbulent flow structures interaction with a vertical hydrokinetic river turbine. *Ren. Energy*, 48:183–192, 2012.

[73] K. McCaffrey. *Characterization of turbulence anisotropy, coherence, and intermittency at a prospective tidal energy site: Observational data analysis.* PhD thesis, University of Colorado-Boulder, 2014.

[74] V.S. Neary, B. Gunawan, and D.C. Sale. Turbulent inflow characteristics for hydrokinetic energy conversion in rivers. *Renew. Sustain. Energy Rev.*, 26:437–445, 2013.

[75] V.S. Neary and D. Sale. Flow characteristics of river resources for hydrokinetic energy conversion. In *Hydrovision Int. 2010*, 2010.

[76] E. Nelson. Developing an Instrumentation Package for in-Water Testing of Marine Hydrokinetic Energy Devices. In *Ocean. 2010*, pages NREL/CP–500–49004, 2010.

[77] J.B. Richard, J. Thomson, B. Polagye, and J. Bard. Method for identification of Doppler noise levels in turbulent flow measurements dedicated to tidal energy. *Int. J. Mar. Energy*, 3-4:52–64, 2013.

[78] J. Thomson, B. Polagye, M. Richmond, and V. Durgesh. Quantifying turbulence for tidal power applications. *Oceans 2010*, pages 1–8, 2010.

[79] J. Thomson, B. Polagye, V. Durgesh, and M. C. Richmond. Measurements of turbulence at two tidal energy sites in Puget Sound, WA. *IEEE J. Ocean. Eng.*, 37(3):363–374, 2012.

[80] R.J. Barthelmie, E.S. Politis, J. Prospathopoulos, K. Rados, S.T. Frandsen, O. Rathmann, K. Hansen, D. Cabezon, S.P. Van Der Pijl, J. Schepers, W. Schlez, J. Phillips, and A. Neubert. Flow and wakes in large wind farms in complex terrain and offshore. In *Eur. Wind Energy Conf.*, 2008.

[81] K.B. Howard, J.S. Hu, L.P. Chamorro, and M. Guala. Characterizing the response of a wind turbine model under complex inflow conditions. *Wind Energy*, 2014.

[82] E.S. Politis, J. Prospathopoulos, D. Cabezon, K.S. Hansen, P.K. Chaviaropoulos, and R.J. Barthelmie. Modeling wake effects in large wind farms in complex terrain: the problem, the methods and the issues. *Wind Energy*, 15:161–182, 2012.

[83] J.M. Prospathopoulos, E.S. Politis, and P.K. Chaviaropoulos. Modelling wind turbine wakes in complex terrain. In *EWEC*, 2008.

[84] G.C. Larsen, H.A. Madsen, K. Thomsen, and T.J. Larsen. Wake meandering: A pragmatic approach. *Wind Energy*, 11(4):377–395, 2008.

[85] N. Hutchins and I. Marusic. Large-scale influences in near-wall turbulence. *Philos. Trans. A. Math. Phys. Eng. Sci.*, 365(1852):647–64, 2007.

[86] S.J. Bennett and J.L. Best. Mean flow and turbulence structure over fixed, two-dimensional dunes: implications for sediment transport and bedform stability. *Sedimentology*, 42(3):491–513, 1995.

[87] D. Jerolmack and D. Mohrig. Interactions between bed forms: Topography, turbulence, and transport. *J. Geophys. Res.*, 110(F2):F02014, 2005.

[88] T.B. Maddux. Turbulent flow over three-dimensional dunes: 1. Free surface and flow response. *J. Geophys. Res.*, 108(F1):6009, 2003.

[89] T.B. Maddux. Turbulent flow over three-dimensional dunes: 2. Fluid and bed stresses. *J. Geophys. Res.*, 108(F1):6010, 2003.

[90] J.M. Nelson, S.R. McLean, and S.R. Wolfe. Mean flow and turbulence fields over two-dimensional bed forms. *Water Resour. Res.*, 29(12):3935–3953, 1993.

[91] A. Singh, F. Porté-Agel, and E. Foufoula-Georgiou. On the influence of gravel bed dynamics on velocity power spectra. *Water Resour. Res.*, 46(4):W04509, 2010.

[92] A. Singh, S. Lanzoni, P.R. Wilcock, and E. Foufoula-Georgiou. Multiscale statistical characterization of migrating bed forms in gravel and sand bed rivers. *Water Resour. Res.*, 47(12), 2011.

[93] D.G.E. Grigoriadis, E. Balaras, and A.A. Dimas. Large-eddy simulations of unidirectional water flow over dunes. *J. Geophys. Res.*, 114(F2):F02022, 2009.

[94] T. Stoesser, C. Braun, M. García-Villalba, and W. Rodi. Turbulence Structures in Flow over Two-Dimensional Dunes. *J. Hydraul. Eng.*, 134(1):42–55, January 2008.

[95] J. Best. Kinematics, topology and significance of dune-related macroturbulence: some observations from the laboratory and field. *Spec. Publs int. Ass. Sediment*, 35:41–60, 2005.

[96] J.G. Venditti and B.O. Bauer. Turbulent flow over a dune: Green river, colorado. *Earth Surf. Proc. Landforms*, 30(3):289–304, 2005.

[97] J. Best. The fluid dynamics of river dunes: A review and some future research directions. *J. Geophys. Res.*, 110(F4):F04S02, 2005.

[98] M. Guala, A. Singh, N. Badheartbull, and E. Foufoula-Georgiou. Spectral description of migrating bedforms and sediment transport. *J. Geophys. Res. Earth Surf.*, 119(2):123–137, 2014.

[99] R.L. Martin and D.J. Jerolmack. Origin of hysteresis in bed form response to unsteady flows. *Water Resources Research*, 49(3):1314–1333, 2013.

[100] B. McElroy and D. Mohrig. Nature of deformation of sandy bed forms. *J. Geophys. Res.: Earth Surface (2003–2012)*, 114(F3), 2009.

[101] D.J. Harbor. Dynamics of Bedforms in the Lower Mississippi River. *J. Sediment. Res.*, 68(5):750–762, 1998.

[102] R. Kostaschuk, P. Villard, and J. Best. Measuring velocity and shear stress over dunes with acoustic Doppler profiler. *J. Hydr. Engrg.*, 130:932–936, 2004.

[103] R.K. Kropp. Biological and existing data analysis to inform risk of collision and entanglement hypotheses environmental effects of marine and hydrokinetic energy. Technical report, US DOE Pacific Northwest National Laboratory, 2013.

[104] P. Schweizer, G. Cada, and M. Bevelhimer. Estimation of the Risks of Collision or Strike to Freshwater Aquatic Organisms Resulting from Operation of Instream Hydrokinetic Turbines. Technical Report May, Oak Ridge National Laboratory ORNL/TM-2011/133, 2011.

[105] Energy Efficiency and Renewable Energy. Report to Congress on the Potential Environmental Effects of Marine and Hydrokinetic Energy Technologies. Technical report, U.S. Department of Energy, 2009.

[106] R. Inger, M.J. Attrill, S. Bearhop, A.C. Broderick, J.W. Grecian, D.J. Hodgson, C. Mills, E. Sheehan, S.C. Votier, M.J. Witt, and B.J. Godley. Marine renewable energy: potential benefits to biodiversity? An urgent call for research. *J. Appl. Ecol.*, 46:1145–1153, 2009.

[107] F.D. Bianchi, H. DeBattista, and R.J. Mantz. *Wind turbine control systems: principles, modelling and gain scheduling design.* Springer, 2006.

[108] I. Houtzager. *Towards Data-Driven Control for Modern Wind Turbines.* PhD thesis, Dutch Institute of Systems and Control, 2011.

[109] K.E. Johnson, L.Y. Pao, M.J. Balas, and L.J. Fingersh. Control of variable-speed wind turbines: Standard and adaptive techniques for maximizing energy capture. *IEEE Control Syst. Mag.*, pages 70–81, 2006.

[110] E.B. Muhando, T. Senjyu, A. Yona, H. Kinjo, and T. Funabashi. Disturbance rejection by dual pitch control and self-tuning regulator for wind turbine generator parametric uncertainty compensation. *Control Theory & App.*, 1(5):1431–1440, 2007.

[111] T. Senjyu, S. Tamaki, E. Muhando, N. Urasaki, H. Kinjo, T. Funabashi, H. Fujita, and H. Sekine. Wind velocity and rotor position sensorless maximum power point tracking control for wind generation system. *Ren. Energy*, 31(11):1764–1775, 2006.

[112] W.M.J. Batten and A.S. Bahaj. Comparing energy yields from fixed and yawing horizontal axis marine current turbines in the English channel. In *27th Int. Conf. Offshore Mech. Arct. Eng.*, pages 1–10. ASME, 2008.

[113] V.J. Ginter and J.K. Pieper. Robust gain scheduled control of a hydrokinetic turbine. *IEEE Trans. Control Syst. Technol.*, 19(4):805–817, 2011.

[114] U. Fey, M. König, and H. Eckelmann. A new strouhalreynolds-number relationship for the circular cylinder in the range $47 < re < 2 \times 10^5$. *Phys. Fluids*, 10(7):1547–1549, 1998.

[115] V. L. Okulov and J. N. Sørensen. Stability of helical tip vortices in a rotor far wake. *J. Fluid Mech.*, 576:1–25, 4 2007.

[116] S. Kang, X. Yang, and F. Sotiropoulos. On the onset of wake meandering for an axial flow turbine in a turbulent open channel flow. *J. Fluid Mech.*, 744:376–403, 2014.

[117] B.W. Melville and A.J. Sutherland. Design Method for local scour at bridge piers. *J. Hydraul. Eng.*, 114(10):1210–1226, 1988.

[118] B.W. Melville and Y. Chiew. Time Scale for local scour at bridge piers. *J. Hydraul. Eng.*, 125(1):59–65, 1999.

[119] B.W Melville and S.E. Coleman. *Bridge Scour*. Water Resources, LLC, Colorado, USA, 2000.

[120] L.C. van Rijn. Sediment Transport, Part I: Bed Load Transport. *J. Hydraul. Eng.*, 110(10):1431–1456, 1984.

[121] F.M. Exner. ber die wechselwirkung zwischen wasser und geschiebe in flssen. *Akad. Wiss. Wien Math. Naturwiss. Klasse*, 134(2a):165–204, 1925.

[122] A. Siviglia, R. Repetto, G. Zolezzi, and M. Tubino. River bed evolution due to channel expansion: General behaviour and application to a case study (kugart river, kyrgyz republic). *River Res. Applic.*, 2008.

[123] G. Oliveto and W.H. Hager. Temporal Evolution of Clear-Water Pier and Abutment Scour. *J. Hydraul. Eng.*, 128(9):811–820, 2002.

[124] G. Oliveto and W.H. Hager. Further results to time-dependent local scour at bridge elements. *J. Hydraul. Eng.*, 131(2):97–105, 2005.

[125] U.C. Kothyari, W.H. Hager, and G. Oliveto. Generalized Approach for Clear-Water Scour at Bridge Foundation Elements. *J. Hydraul. Eng.*, 133(11):1229–1240, 2007.

[126] B.W. Melville. Pier and Abutment Scour: Integrated Approach. *J. Hydraul. Eng.*, 123(2):125–136, 1997.

[127] S. Dey, R.V. Raikar, and A. Roy. Scour at Submerged Cylindrical Obstacles under Steady Flow. *J. Hydraul. Eng.*, 134(1):105–109, 2008.

[128] M.A. Shields, D.K. Woolf, E.P.M. Grist, S.A. Kerr, A.C. Jackson, R.E. Harris, M.C. Bell, R. Beharie, A. Want, E. Osalusi, S.W. Gibb, and J. Side. Marine renewable energy: The ecological implications of altering the hydrodynamics of the marine environment. *Ocean Coastal Mgmt.*, 54:2–9, 2011.

[129] G. Seminara. Fluvial sedimentary patterns. *Ann. Rev. Fluid Mech.*, 42:43–66, 2010.

[130] A. Singh, E. Foufoula-Georgiou, F. Porte-Agel, and P.R. Wilcock. Coupled dynamics of the co-evolution of bed topography, flow turbulence and sediment transport in an experimental flume. *J. Geophys. Res.*, 117:F04016, 2012.

[131] C.F. van der Mark, A. Blom, and S. Hulscher. Quantification of variability in bedform geometry. *J. Geophys. Res.*, 113(F3):F03020, 2008.

[132] N. Barltrop, K.S. Varyani, A. Grant, D. Clelland, and X.P. Pham. Investigation into wave-current interactions in marine current turbines. *Proc. Inst. Mech. Eng. Part A - J. Power Energy*, 221(2):233–242, 2007.

[133] P. Julien and G. Klaassen. Sand-dune geometry of large rivers during floods. *J. Hydr. Engrg.*, 121(9):657–663, 1995.

[134] A. Copping, H. Battey, J. Brown-Saracino, M. Massaua, and C. Smith. An international assessment of the environmental effects of marine energy development. *Ocean Coast. Mgmt.*, 99:3–13, 2014.

[135] A. Copping, L. Hanna, B. Van Cleve, K. Blake, and R.M. Anderson. Environmental risk evaluation system - an approach to ranking risk of ocean energy development on coast and estuarine environments. *Estuaries and Coasts*, 38(1):S287–S302, 2015.

[136] G.B. Zydlewski, A.E. Copping, and A.M. Redden. Special issue: Renewable ocean energy development and the environment. *Estuaries and Coasts*, 38(1):S156–S158, 2015.

[137] S. Kang, A. Lightbody, C. Hill, and F. Sotiropoulos. High-resolution numerical simulation of turbulence in natural waterways. *Adv. Water Resour.*, 34(1):98–113, 2011.

[138] S.C. Tedds, I. Owen, and R.J. Poole. Near-wake characteristics of a model horizontal axis tidal stream turbine. *Renew. Energy*, 63:222–235, March 2014.

[139] P. Bachant and M. Wosnik. Characterising the near-wake of a cross-flow turbine. *J. Turb.*, 16(4):392–410, 2015.

[140] A.S. Bahaj and L.E. Myers. Shaping array design of marine current energy converters through scaled experimental analysis. *Energy*, 59:83–94, 2013.

[141] M.J Churchfield, Y. Li, and P.J. Moriarty. A large-eddy simulation study of wake propagation and power production in an array of tidal-current turbines. *Philos. Trans. A. Math. Phys. Eng. Sci.*, 371:20120421, 2013.

[142] T. Blackmore, W.M.J. Batten, and A.S. Bahaj. Influence of turbulence on the wake of a marine current turbine simulator. *Phil. Trans. R. Soc. A.*, 470:20140331, 2014.

[143] M.L. Palmsten, J.L. Kozarek, and J. Calantoni. Video observations of bedform morphodynamics in a meander bend (accepted). *Water Resour. Res.*, 2015.

[144] S. Kang and F. Sotiropoulos. Flow phenomena and mechanisms in a field-scale experimental meandering channel with a pool-riffle sequence: Insights gained via numerical simulation. *J. Geophys. Res.*, 116:F03011, 2011.

[145] S. Kang and F. Sotiropoulos. Assessing the predictive capabilities of isotropic, eddy viscosity reynolds-averaged turbulence models in a natural-like meandering channel. *Water Resour. Res.*, 48:W06505, 2012.

[146] A. Khosronejad, J.L. Kozarek, M.L. Palmsten, and F. Sotiropoulos. Numerical simulation of large dunes in meandering streams and rivers with in-stream rock structures. *Adv. Water Res.*, 81:45–61, 2015.

[147] W.E. Dietrich and J.D. Smith. Bed load transport in a river meander. *Water Resourc. Res.*, 20(10):1355–1380, 1984.

[148] R.L. Dinehart and J.R. Burau. Averaged indicators of secondary flow in repeated acoustic doppler current profiler crossings of bends. *Water Resourc. Res.*, 41(9):W09405, 2005.

[149] L.C. Sime, R.I. Ferguson, and M. Church. Estimating shear stress from moving boat acoustic doppler velocity measurements in a large gravel bed river. *Water Resourc. Res.*, 43(3):W03418, 2007.

[150] R. Tsubaki, Y. Kawahara, Y. Muto, and I. Fujita. New 3-d flow interpolation method on moving adcp data. *Water Resourc. Res.*, 48(5):W05539, 2012.

[151] L.P. Chamorro and F. Porté-Agel. A Wind-Tunnel Investigation of Wind-Turbine Wakes: Boundary-Layer Turbulence Effects. *Boundary-Layer Meteorol.*, 132(1):129–149, 2009.

[152] K.B. Howard, A. Singh, F. Sotiropoulos, and M Guala. On the statistics of wind turbine wake meandering: An experimental investigation. *Phys. Fluids*, 27:075103, 2015.

[153] X. Yang, K.B. Howard, M. Guala, and F. Sotiropoulos. Effects of a three-dimensional hill on the wake characteristics of a model wind turbine. *Phys. of Fluids*, 27:025103, 2015.

[154] C. Hill, J. Kozarek, F. Sotiropoulos, and M. Guala. Hydrodynamics and sediment transport in a meandering channel with a model axial-flow hydrokinetic turbine (under review). *Water Resourc. Res.*, 2015.

[155] C.S. Babakaiff and E.J. Hickin. Coherent flow structures in squamish river estuary, british columbia, canada. *Coherent flow structures in open channels*, pages 321–342, 1996.

[156] B. Gunawan, V.S. Neary, and J. McNutt. ORNL ADV post-processing guide and MATLAB algorithms for MHK site flow and turbulence analysis. Technical report, Wind and Water Power Program, Office of Energy Efficiency and Renewable Energy, U. S. Department of Energy, Washington, DC, 2011. ORNL/TML-2011/338.

[157] D.G. Goring and V.I. Nikora. Despiking acoustic Doppler velocimeter data. *J. Hydraulic Eng.*, 128(1):117–126, 2002.

[158] H.W. Coleman and W.G. Steele. *Experimentation, Validation, and Uncertainty Analysis for Engineers*. John Wiley & Sons, Inc., 3 edition, 2009.

[159] M. Barone, T. Griffith, and J. Berg. Reference Model 2: Rev 0 Rotor Design. Technical report, Sandia National Laboratories, Albuquerque, New Mexico, 2014. SAND2011-9306.

[160] P. Bachant and M. Wosnik. Reynolds number dependence of cross-flow turbine performance and near-wake characteristics. *Proc. of the 2nd Mar. Energy Tech. Sym.*, 2014.

[161] J. Hong, M. Toloui, L.P. Chamorro, M. Guala, K.B. Howard, S. Riley, J. Tucker, and F. Sotiropoulos. Natural snowfall reveals large-scale flow structures in the wake of a 2.5-MW wind turbine. *Nature Communications*, 5:4216, 2014.